Spring 2024

TAU LEPTONS IN THE SEARCH FOR CHARGED HIGGS BOSONS

Juan Carlos Cardenas Jr
University of Texas at Arlington

TAU LEPTONS IN THE SEARCH FOR CHARGED HIGGS BOSONS

Author: Juan Carlos Cardenas Jr.

Supervisor: Dr. Haleh Hadavand
Advisor: Dr. Blake Burghgrave

A DISSERTATION SUBMITTED
IN PARTIAL FULFILLMENT OF THE REQUIREMENTS
FOR THE DEGREE OF

DOCTOR OF PHILOSOPHY

AT THE UNIVERSITY OF TEXAS AT ARLINGTON
DEPARTMENT OF PHYSICS

May 2024
Arlington, Texas

Abstract

Tau Leptons In The Search For Charged Higgs Bosons

Juan Carlos Cardenas Jr.
The University of Texas At Arlington, 2024

The Standard Model (SM) of particle physics, a gracefully crafted collection of particle theories, has made an astounding number of accurate predictions about the properties of particles and the fundamental laws that govern our universe. Among its long list of remarkable successes are the unification of the electromagnetic and weak forces, the prediction of elementary particles such as the Higgs boson, and its ability to precisely predict a wide range of particle cross-sections and branching fractions which have been verified experimentally.

Yet despite its immense predictive power, some major problems with the standard model are its failure to accommodate dark matter and the gravitational force, as well as its inability to provide sources of CP violation large enough to produce the observed baryon asymmetry of our universe. It is apparent that extensions to the SM are required to account for these observed phenomena. Particle theorists have developed a plethora of such extensions to account for these observations, some of which include additional scalar particles as part of an extended Higgs sector. Extending the SM by adding a second Higgs doublet either as an independent theory via Two Higgs Doublet Models (2HDM)s, or as part of a more expansive framework like Super Symmetry helps accommodate for some of these observed phenomena. Additionally, an observed tension in lepton flavor universality giving rise to an excess of tau leptons can be explained by the existence of charged Higgs bosons decaying via $H^{\pm} \to \tau\nu$.

Because of its large branching fraction throughout a range of 2HDM parameter space, $H^{\pm} \to \tau\nu$ is an attractive decay channel for 2HDM-related searches. This thesis presents the search for charged Higgs bosons in a model-independent manner with a hypothesized mass between 80 and 3000 GeV through the ($H^{\pm} \to \tau\nu$) decay mode, as well as presents the contributions made in the development of the ATLAS collaboration's Tau Identification Neural Network (TauID), a tool used by all the on collaboration to identify hadronically decaying taus.

Dedication

To the reader, dear friend, or stranger, I hope this dissertation I have put so much effort into assembling helps you understand the physics I have spent so much of my life contemplating. To all my dear friends and family, in California, Texas, Geneva, thank you for all of your support and kindness, you have played a bigger role in my completion of graduate school than you know. To my friend Hector Carranza, thank you for loving this subject as much as I do, and for the countless discussions about physics over the years, I've learned a lot from you. To everyone who supported me financially when I broke my clavicle, I honestly can't thank you enough.

Acknowledgments

There have been so many people who have helped me become the physicist I am today, but first and foremost I would like to thank Dr. Haleh Hadavand and Dr. Blake Burghgrave. You both have been with me though this almost 8 year journey every step of the way, through the difficulty and the moments of awe, you have supported me and helped guide me to think like a scientist. I am eternally grateful for the knowledge you have shared with me, and am eternally grateful for the opportunity to have had you both in my life in a professional capacity, and as friends. Thank you, for it all. And to my fellow researchers who have helped me find insight in the physical processes I was stumped by. To all members of the Tau Working group for your insights and help in understanding all things tau related. To California State University Dominguez Hills, for being the only undergraduate university to grant me acceptance, and to the professors there that helped me begin my physics journey. To Dr.John Price and MBRS RISE, thank you for my first research experience. To the UTA college of science for providing me with the financial support through the Maverick Science Graduate Research Fellowship. To all of my UTA professors for teaching me well. To Danny Rodriguez, for introducing me to the word physics, and Mr.Hoang, for helping me understand it. And finally to Mr Feliciano, for not shying away from the concept of quantum mechanics in a 6th grade classroom. Thank you.

Contents

1 Introduction **1**
1.1 Introduction . . . 1

2 The Large Hadron Collider **2**
2.1 The LHC . . . 2
2.1.1 The LHC Accelerators . . . 3
2.1.2 Accelerating the protons . . . 3
2.1.3 The LHC bunch structure . . . 4
2.1.4 The LHC Hardware . . . 4
2.1.5 Proton collisions and new particles . . . 4

3 The ATLAS Detector **6**
3.1 The ATLAS coordinate system . . . 6
3.2 The Inner Detector . . . 8
3.2.1 Silicon Pixel Detectors . . . 8
3.2.2 Silicon Micro-strip Detectors . . . 8
3.2.3 The Straw Tube TRT . . . 9
3.3 ATLAS Calorimeters . . . 9
3.3.1 The Electromagnetic Calorimeter . . . 10
3.3.2 The Hadronic Calorimeter . . . 10
3.4 ATLAS Muon Spectrometer . . . 11
3.4.1 Monitored Drift Tube (MDT) Chambers . . . 11
3.4.2 Cathode-Strip Chambers . . . 12
3.4.3 Resistive Plate Chambers . . . 12
3.4.4 Thin Gap Chambers . . . 12
3.5 The Data Acquisition (DAQ) System . . . 12
3.5.1 Level 1 Trigger (L1 Trigger) . . . 13
3.5.2 High-Level Trigger (HLT) . . . 13
3.5.3 The Trigger Menu . . . 14

4 The Standard Model **15**
4.1 The Electro-Magnetic force . . . 16
4.2 The Weak Force . . . 16
4.3 The Strong Force . . . 17
4.4 The Electro-Weak Force . . . 18
4.5 The role of the Higgs Boson . . . 19
4.6 QFT Mass terms . . . 19
4.7 Spontaneous symmetry breaking . . . 19
4.8 The Higgs Mechanism . . . 21

4.9 Fermion Masses 21

5 The Two Higgs Doublet Model and other extensions to the Standard Model 23
5.1 The Two Higgs Doublet Model 23
5.1.1 Theoretical Motivations 23
5.1.2 The 2HDM as a theoretical framework 24
5.1.3 $H^{\pm}$ Production 25
5.2 SuperSymmetry (SUSY) 27
5.2.1 The MSSM and hMSSM 28
5.2.2 Grand Unified Theories (GUT)s 28

6 Event Reconstruction 29
6.0.1 Track Reconstruction 29
6.0.2 Topo-Cluster Reconstruction 30
6.0.3 Electron Reconstruction 31
6.0.4 Muon Reconstruction 32
6.0.5 Tau Reconstruction 33
6.0.6 Missing Transverse Energy (MET) (E_T^{Miss}) Reconstruction . . 34
6.0.7 Jet Reconstruction 35
6.0.8 b-Jet Reconstruction 35

7 The Tau Identification Algorithm 37
7.1 The Tau ID: A Summary 37
7.2 The Tau ID: An In-Depth Look 38
7.2.1 The TauID Network Architecture (RNN) 39
7.2.2 Tau ID Training Environments 40
7.2.3 Monte Carlo Training and Evaluation Samples 40
7.2.4 Creation of the HDF5 datasets 40
7.2.5 Signal and Background Selection Definitions 41
7.2.6 Training and Testing Sets 42
7.2.7 Recurrent Neural Networks (RNN) TauID Input Variables . . 42
7.2.8 Re-weighting procedure 44
7.2.9 Score Flattening 44
7.2.10 Tau Identification Performance 45
7.3 The 2p TauID 46
7.3.1 2p Network Results RNN 46

8 The Deepset TauIDs And Other Experimental Networks 48
8.1 The Deepset Architecture 48
8.2 Decay Mode Neural Nets 49
8.2.1 Decay Mode Network Architectures 50
8.2.2 Tau Decay Modes And My Qualification Task 50
8.2.3 Decay Mode Net Training and Testing data sets 50
8.2.4 Inclusive vs Decay mode Networks 51
8.2.5 RNN vs. Deepset, a pleasant surprise 51
8.3 The Deepset Tau ID with Track RNN variables 52
8.3.1 Equivalent Performance: Track (Deepset vs RNN) TauID . . 53
8.3.2 Track Deepset TauID Performance 54

8.3.3 Deepset TauID Training environment 55

9 The $H^{\pm} \to \tau\nu$ analysis **56**
9.0.1 $H^{\pm} \to \tau\nu$ a summary 56
9.1 $H^{\pm}$ Production 57
9.2 Final State Particle Objects 57
9.2.1 Selections on final state particle objects 58
9.2.2 Jet selections 58
9.2.3 b-Jet selections 58
9.2.4 Taus (τ) jet selections 59
9.2.5 Electrons (e) selections 59
9.2.6 Muons (μ) selections 59
9.2.7 Missing Transverse Energy (E_T^{miss}) selections 59
9.2.8 Overlap Removal 60
9.3 Signal Region Definitions:
Tau+Jets, Tau+Lep 60
9.4 The Tau+Jets Channel 61
9.4.1 E_T^{miss} (MET) Trigger 61
9.4.2 Selections for the Tau+Jets SR 61
9.5 The Tau+Lep Channel 62
9.5.1 Single Lepton Trigger 62
9.5.2 Selections for the Tau+Lep SR 62
9.6 Signal region and TTBar Control region Orthogonalization 63
9.7 Control/Validation Region Definitions 65
9.7.1 E_T^{miss} (MET) Control Region 65
9.7.2 TTBar Tau+Jets Control/Validation Region 65
9.7.3 TTBar Tau+Lep Control Region 65
9.7.4 b-Veto (e, μ) Control/Vaidation Regions 66
9.7.5 b-Tag Control Region $(e + \mu)$ 66
9.7.6 Anti-τ Control Region 66
9.7.7 Multi-Jet Control Region 67
9.7.8 W+Jets Control/Validation Region 67
9.7.9 Same Sign (e,μ) Control Region 67
9.7.10 Inclusive Control Region 68
9.7.11 b-Veto MT100 Control/Validation Region 68
9.7.12 Z-ee Control Region 68
9.7.13 Pre-Selection Control/Validation Region 69
9.7.14 Summary of Control/Signal/Validation regions [111] 70
9.8 Background Modeling and Validation 71
9.8.1 TTBar and W+Jets Sample Re-Weighting 71
9.8.2 Trigger Efficiency Scale Factors 74
9.8.3 Misidentified Leptons faking τ candidates 75
9.8.4 Misidentified Jets faking τ candidates 77
9.8.5 The Fake Factor Method 79
9.8.6 The MultiJet and W+Jets Fake Factors 79
9.8.7 Combined Fake Factors for signal regions FF_{SR} 81
9.9 Systematic Uncertainties 83
9.9.1 Detector related uncertainties 83

9.10 Effect of systematic uncertainties on final PNN distributions 83
9.11 Fake Factor Uncertainties 85
9.11.1 Scale Systematic on W+Jets 86
9.12 Impact of uncertainty types on Asimov limits 87
9.13 Data Samples 88
9.13.1 Signal Monte Carlo 88
9.13.2 Background Monte Carlo 89
9.13.3 Observed Data 90
9.14 The Parameterized Neural Network 90
9.14.1 PNN Architecture 90
9.14.2 PNN Training 91
9.14.3 The k-Fold training method 91
9.14.4 PNN Training Variables 92
9.15 Statistical Analysis 95
9.15.1 Description of Fit Model 95
9.15.2 Binning Schemes 95
9.15.3 Minimum Number of Entries 96
9.15.4 Symmetrization 96
9.15.5 Pruning 97
9.15.6 Fit Procedure 97
9.15.7 Limit setting procedure 97
9.15.8 Signal Injection Studies 98
9.16 Staged Unblinding: $36fb^{-1} H^{\pm} \rightarrow \tau\nu$ result 101
9.17 $140fb^{-1}$ Results 102
9.18 Interpretation 109
9.19 Conclusion 109

10 Additional Studies **110**
10.1 The Deepset based Tau ID As A Region Classifier 110

A Appendices **112**
A.1 Data Samples GRL 112
A.2 Good Run Lists 112
A.3 TauID related results 113
A.4 Decaymode net results 113
A.5 Tau ID Variable Descriptions [86][71] 116
A.5.1 High Level TauID Variable descriptions 116
A.5.2 Track TauID Variable descriptions 117
A.5.3 Cluster TauID Variable descriptions 118
A.5.4 Decay mode Network Input Variables 119
A.6 Systematic Used 120
A.7 Systematic List 120
A.7.1 Luminosity 120
A.7.2 Trigger Uncertainties 120
A.7.3 Tau Uncertainties 120
A.7.4 Jet Uncertainties 120
A.7.5 Electron Uncertainties 121
A.7.6 Muon Uncertainties 121
A.7.7 MET Uncertainties 122

A.7.8 SingleTop Uncertainties . . . 122
A.7.9 Fake Factor Uncertainties . . . 122
A.7.10 $t\bar{t}$ Modelling uncertainties . . . 122
A.7.11 W/Z+Jets Modelling Uncertainties . . . 122
A.7.12 Cross section Uncertainties . . . 123
A.7.13 H+ Signal uncertainties . . . 123
A.8 HTaunu Additional Results . . . 124
A.8.1 Cross Section Limit Tables . . . 127
A.9 Final Bin Arrays for Htaunu . . . 130
A.10 Starting arrays for TauLep channel . . . 130
A.11 Final Binning Arrays . . . 130
A.12 Statistical Methods . . . 132
A.13 Pruning Methods . . . 132
A.14 Post-fit plots . . . 133
A.14.1 Post Fit plots for JetTau Channel Observed . . . 133
A.14.2 Post Fit plots for ElTau Channel Observed . . . 137
A.14.3 Post Fit plots for MuTau Channel Observed . . . 141
A.15 Nuisance Parameter Ranking Plots . . . 145

Acronyms **150**

Bibliography **152**

Chapter 1

Introduction

1.1 Introduction

The discovery of the Higgs boson in 2012 represents one of the great triumphs in particle physics and provides us with yet another example of the standard model's extraordinary ability to predict the behavior of the particles and forces that shape our universe. Although the standard model has been nothing short of an incredible success, we know that it cannot be the overarching theory of our universe. Dark matter, the gravitational force, evidence of the breaking of lepton universality, and the observed baryon asymmetry of our universe are among the list of topics that manage to evade explanation by the standard model. Theories that include additional scalar particles as part of an extended Higgs sector such as 2 Higgs Doublet models (2HDMs) attempt to accommodate for the shortcomings of the standard model. This thesis presents the results of the search for charged Higgs bosons via $H^{\pm} \rightarrow \tau\nu$ in a mass range of 80GeV to 3000GeV, using 140.0 ± 0.83 of data collected by the ATLAS experiment in Run 2 of the Large Hadron Collider in chapter [9]. An overview of the Large Hadron Collider is given in chapter [2], followed by an overview of the ATLAS detector in chapter [3] and a summary of the standard model of particle physics in chapter [4]. Chapter [5] gives an overview of the theoretical framework of 2HDMs, and chapter [6] provides a summary of the particle reconstruction methodologies used to produce particle physics objects for analysis. Chapters [7] and [8] detail my contributions to ATLAS via the development of the Recurrent Neural Network and Deepset based tau identification algorithms, and this thesis concludes with chapter [10], where I show additional studies that I began and that will be continued by the $H^{\pm} \rightarrow \tau\nu$ group at the University of Texas at Arlington.

Chapter 2

The Large Hadron Collider

2.1 The LHC

The Large Hadron Collider (LHC) is an underground[1] circular proton accelerator [1] located near Geneva, Switzerland that is designed to accelerate bunches of protons to a center of mass energy $\sqrt{s}$ of 14TeV. These proton bunches are then collided every 25 nano-seconds at 4 points along the LHC's 27km circumference, where the detectors are located. These four detectors are the A Torioidal LHC Apparatus (ATLAS) [2], Compact Muon Solenoid (CMS) [3], A Large Ion Collider Experiment (ALICE) [4] and Large Hadron Collider Beauty (LHCb) [5] detectors. Data from these detectors is collected in a series of 4-year intervals called "LHC Runs". The latest run is Run 3 which began in July of 2022. The data in these runs, collected from their respective experiments, is distributed to different analysis groups who wish to undergo searches for new physics processes, or for precision studies to better our understanding of the processes and particles that we are aware of.

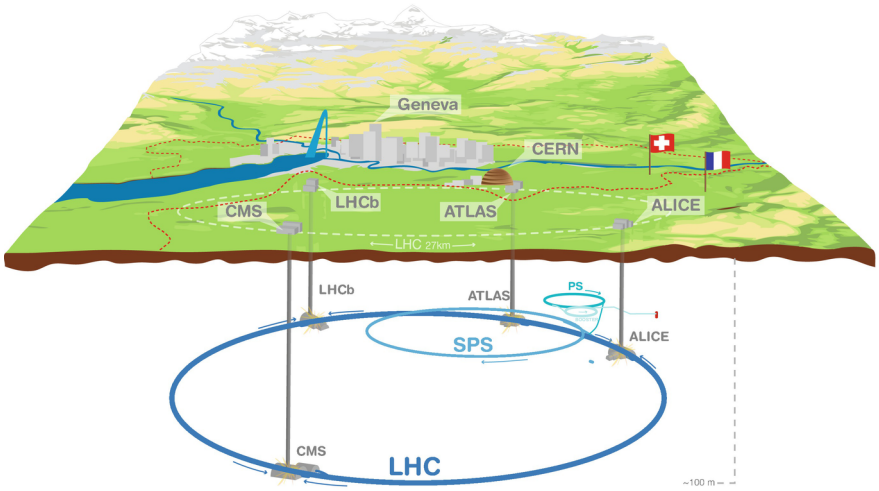

Figure 2.1: The Large Hadron Collider in its geographic location, CERN [6]

[1]The LHC tunnel is located 100 meters underground.

2.1.1 The LHC Accelerators

The LHC does not exist as a stand-alone 27-kilometer accelerator but is rather composed of many accelerators that were constructed beginning in 1950s. Together this group of accelerators is known as the CERN Accelerator Complex. This complex houses many experimental apparatuses used for many physics research operations in a range of particle energies. The complex is used to accelerate and collide low-energy isotope beams in ISOLDE (Isotope mass Separator online facility) as well as collides bunches of protons at the highest energies in the world in the Large Hadron Collider. Proton bunches used in particle physics experiments such as ATLAS go through acceleration in a succession of larger and larger accelerator rings until they reach their final collision energy. Figure 2.2 shows the various booster rings used to accelerate the proton bunches.

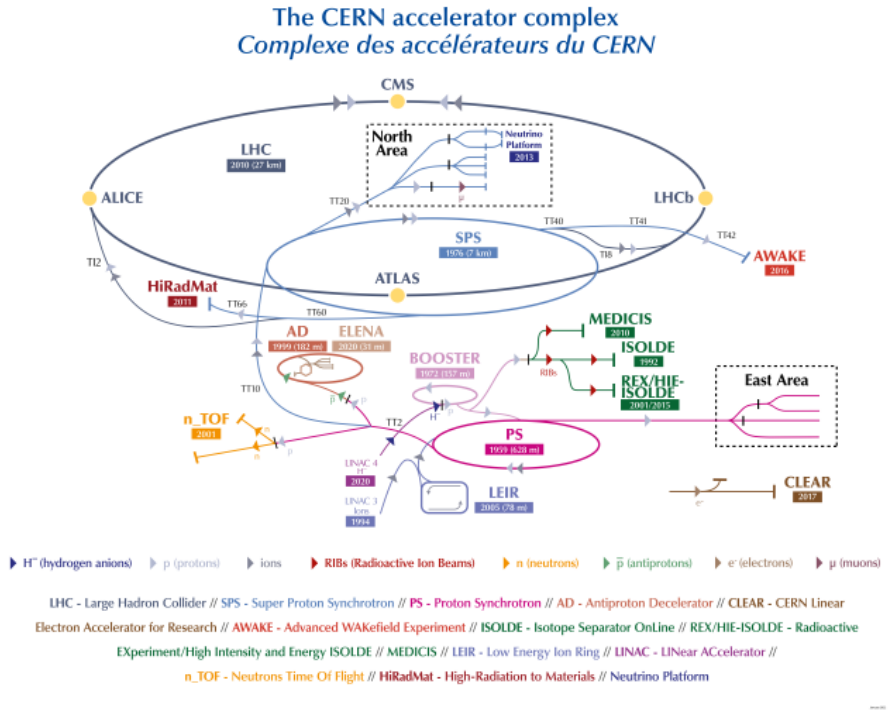

Figure 2.2: The CERN Accelerator Complex [7]

2.1.2 Accelerating the protons

Protons begin their acceleration process at a linear accelerator in the CERN accelerator complex called LINAC4 [8], where hydrogen ions are accelerated to an energy of 160 MeV. From here electrons are removed from the ions to obtain protons which enter the Proton Synchrotron Booster (BOOSTER) where they are accelerated to an energy of 2 GeV [9] and injected into the Proton Synchrotron (PS). The PS then accelerates these bunches of protons up to 26 GeV and then to 450 GeV by the Super Proton Synchrotron (SPS) [10]. At this point proton bunches are injected into the two beam pipes of the LHC ring where they circulate in opposite directions, taking them up to 20 minutes [1] to reach their final energy of 6.5 TeV after which they are collided for physics data.

2.1.3 The LHC bunch structure

When proton bunches enter the LHC beam pipe, they do so in a precise and predetermined manner. Inside of each beam pipe are Radio Frequency (RF) envelopes that act as a bucket in which to store and accelerate the bunches of protons as they circulate in the LHC. Each filled RF bucket contains approximately 1.15×10^{11} protons and receives a Bunch Crossing Identifier (BCID) from 0 to 3,563 to keep track of which RF buckets are empty and which are full. A bunch group tag is also used to keep track of what the RF bucket will be used for. There are 16 types of bunch group tags, four are most commonly used for physics analysis. A bunch group with a tag of "Paired" indicates that this bunch of protons is set to collide for physics data purposes, "CalReq." indicates that the bunch will be used for calibration requests for the Tile Calorimeter, bunches tagged as "Empty" means that there are no protons present in that RF bucket, and so no collisions will take place and bunches tagged as "BCRVeto" Stand for Bunch Counter Reset Veto, which leaves a short amount of time between bunch crossings for detector electronics to reset before the next crossing. [11]

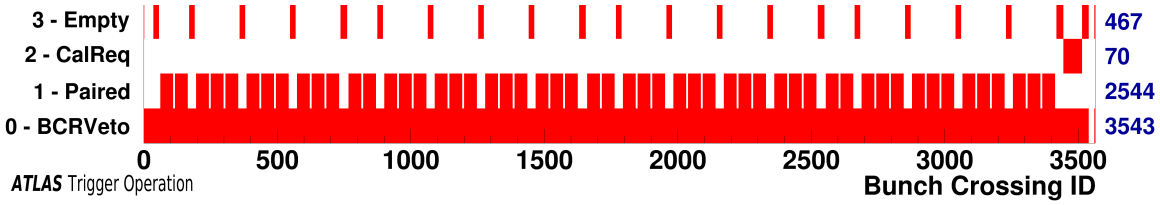

Figure 2.3: Bunch Crossing Identifiers used in the ATLAS fill cycle [11]

2.1.4 The LHC Hardware

The Large Hadron collider [1] is composed of eight arc and eight straight sections that contain 1,232 main dipole magnets with a "twin bore" design, as can be seen in figure 2.4. This twin-bore design allows them to store up to 2,808 proton bunches in two anti-circulating proton beams for eventual collision. These 1,232 dipole magnets are cooled to below 2 degrees kelvin by superfluid helium to allow them to make use of the superconducting properties of their NbTi Rutherford cables. Two types of magnets are used in the LHC beam line, dipole magnets for proton acceleration, and quadrupole magnets for steering of the beams.

2.1.5 Proton collisions and new particles

After proton collisions, we can quantify how many particles of interest we expect to produce before taking into account detector acceptance, instrument efficiencies, and signal region selection cuts. As an exercise, we will calculate the number of expected charged Higgs bosons created in the whole of the ATLAS run 2 dataset, and call this number N. To calculate N we must first become familiar with a few important quantities that are used in particle physics to determine this expected number. These quantities are the integrated luminosity L, cross-section σ, and branching fraction $\mathcal{BF}$. When coupled together, they yield the expected number of particles produced.

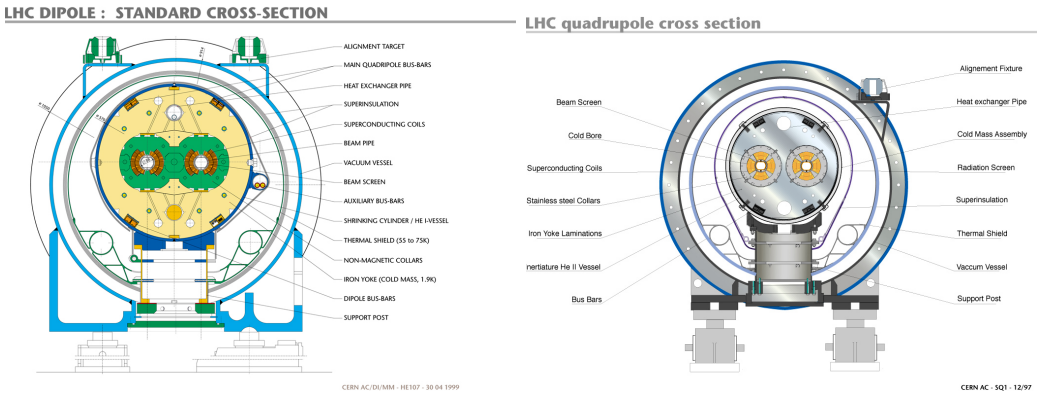

(a) (b)

Figure 2.4: (a) Cross section of LHC Dipole Magnet, CERN [12], (b) Cross section of LHC Quadrupole Magnet, CERN [13]

$$N = L \times \sigma \times \mathcal{BF} \tag{2.1}$$

Instantaneous luminosity can be thought of as a sort of particle beam density. This quantity is used to approximate the amount of data that is collected in a given period by integrating it over time. It is measured in units of inverse barns b^{-1}, that represents a physical area of meters squared m^2 where $1b^{-1} = 10^{-28}m^2$. The LHC was designed to have an instantaneous luminosity of $L = 10^{34}cm^{-2}s^{-1}$ [1]. ATLAS Run2 data amounts to an integrated luminosity of $140fb^{-1}$.

The cross-section σ is a property that all particles and their decay processes have, that represents the probability of producing a desired particle or physical process. For instance $\sigma_{pp\to btH^{\pm}}$ represents the probability of a proton-proton collision resulting in a charged Higgs alongside a top and bottom quark. Cross-section is measured in barns as opposed to inverse barns.

In a 2 Higgs Doublet Model framework with the following parameters, $m_{H^{\pm}} = 160\text{GeV}$, $tan(\beta) = 8$[2], $\mathcal{BF}(H^+ \to \tau\nu) = .7$ and $\sigma_{pp\to btH^{\pm}} = 0.943 \times 10^{-12}$ barns [14], we expect the LHC to have produced 92,414 Charged Higgs.

[2] $tan(\beta)$ is the ratio of the vacuum expectation values $(\frac{v_2}{v_1})$ for 2 Higgs fields in a 2 Higgs Doublet Model, see section 5 for more details.

Chapter 3

The ATLAS Detector

The ATLAS Detector [2] is a cylindrical general-purpose particle detector located at point 1 of the LHC ring that is designed to explore a broad range of physics domains. ATLAS is 44 meters long, 25 meters in diameter, and is located approximately 100 meters underground, it has a number of sub-detectors, each dedicated to the optimal detection of different particles. The main sub-detectors in ATLAS are the Tracking Detectors (3.2), the Calorimeters (3.3), and the Muon Spectrometer (3.4).

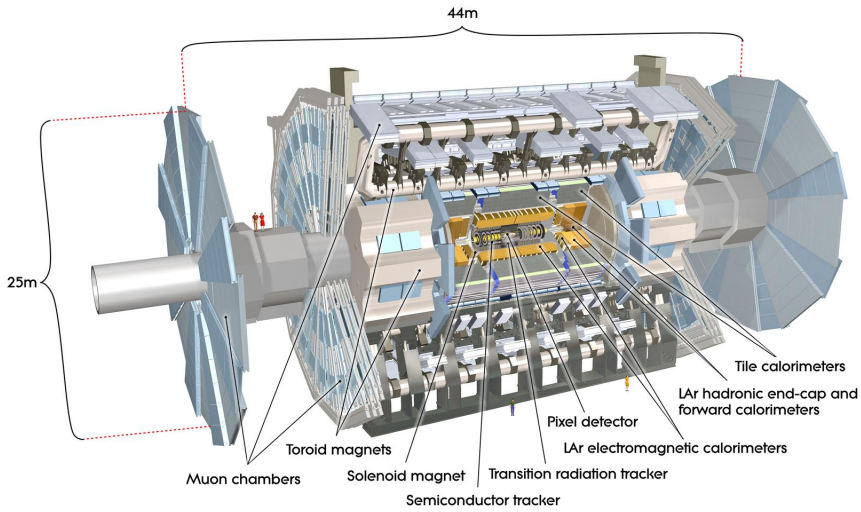

Figure 3.1: The ATLAS Detector, CERN [15]

3.1 The ATLAS coordinate system

The ATLAS collaboration uses 2 coordinate systems to describe particle as well as sub-detector locations, a right-handed Cartesian coordinate system (x, y, z), and a cylindrical coordinate system (r, ϕ, η) [16]. Knowing that ATLAS is situated on the LHC ring, the x-axis of our coordinate system points inward towards the center of the ring, the y-axis points towards the surface of the earth, and the z-axis then points along the beam pipe. The x and y planes define what is called the transverse plane, and are used to define the component of the momentum $p_t = \sqrt{p_x^2 + p_y^2}$,

and missing transverse momentum E_T^{Miss} that is along this plane when particles are created after proton collisions.

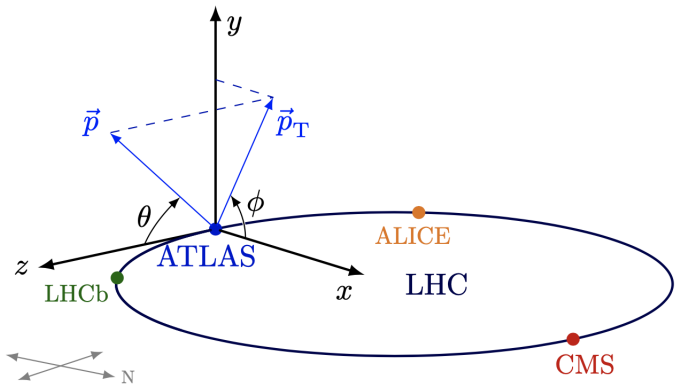

Figure 3.2: The ATLAS coordinate system [17]

This cartesian coordinate system then forms the basis in which we can define the cylindrical coordinate system (r, η, ϕ), where r defines the radial distance of the object of interest $\vec{p}$ [1] from the Interaction Point (IP)[2]. ϕ is defined as the angle subtended beginning at the origin of the x-axis in the transverse plane. The pseudo-rapidity $\eta = -ln(tan(\frac{\theta}{2}))$ is used in place of the angle θ to introduce a Lorentz invariant quantity $\Delta\eta$ that is able to measure the relative angular position of particles in ultra-relativistic conditions.

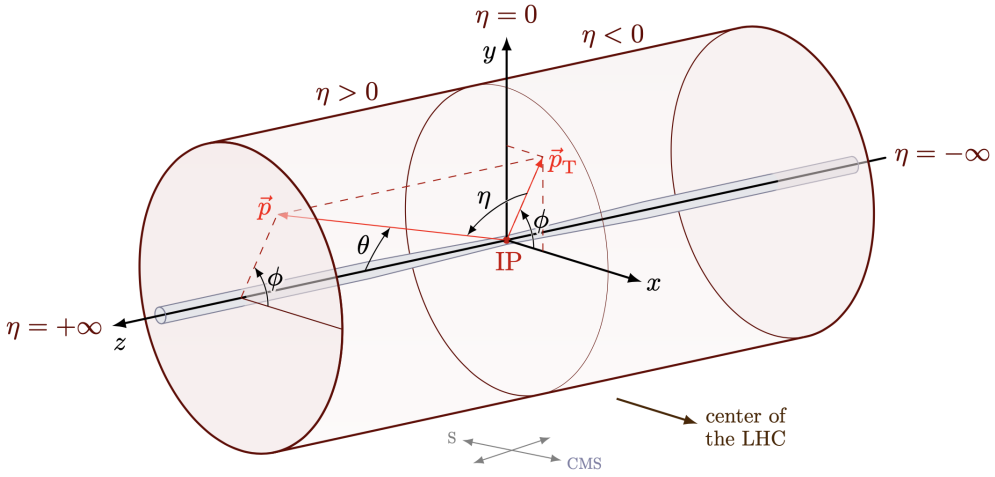

Figure 3.3: The ATLAS cylindrical coordinate system, modified using code here [17]

More generally, η is an approximation of the rapidity y, used to describe low momentum objects, and is defined as $y = \frac{1}{2}ln(\frac{E+p_z}{E-p_z})$. It is also important to introduce the quantities R and ΔR used to describe the angular position of an object in η and ϕ space defined as $R = \sqrt{\eta^2 + \phi^2}$.

[1] Usually a particle track or energy deposition
[2] Where the proton-proton collision that produced the object of interest is located

3.2 The Inner Detector

The Inner Detector (ID) is contained in a cylindrical holder approximately $\pm 3.5m$ in length and 1.1m in radius [2][18]. The ID is composed of three types of tracking detectors, Silicon Pixel detectors, Silicon Microstrip Trackers (SCT) and a Straw Tube Transition Radiation Tracker (TRT). These three tracking detectors are encased by a 2-Tesla superconducting solenoid magnet whose magnetic field permeates the entire ID. This magnetic field paired with the array of tracking detectors allows us to discern the transverse momentum of charged particle tracks above a threshold of .5 GeV over the range of $|\eta| < 2.5$. They also allow us to determine the IP at which the particles originated. Figures 3.4 and 3.5 show specifically the placement of the components in the ID.

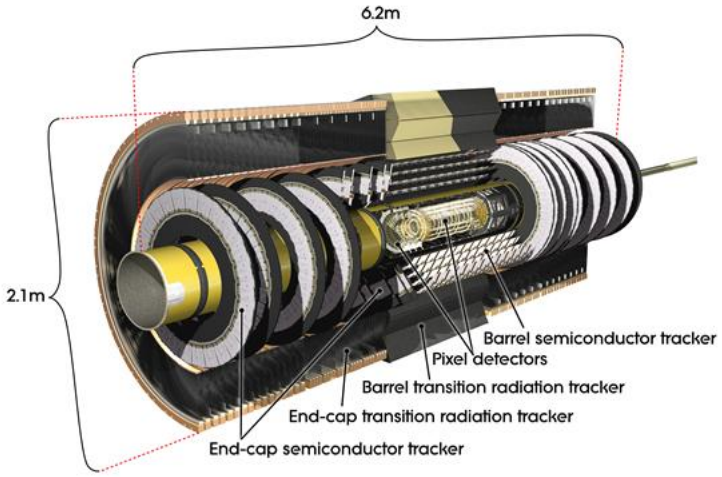

Figure 3.4: Complete ATLAS Inner Detector, CERN [19]

3.2.1 Silicon Pixel Detectors

The Silicon Pixel Detectors are located at a radial distance of $50.5mm$ to $122.5mm$ from the beam line. There are 3 layers of detector forming concentric cylinders around the beam line. In the end cap regions, there are three more disks, symmetric in ϕ and perpendicular to the beam line. In the barrel region, there are 1,744 pixel sensors of dimensions[3] $19 \times 63mm^2$, with 47,232 pixels of dimensions $50 \times 400\mu m^2$ $(R - \phi \times z)$ on each sensor. These pixel detectors yield a spatial resolution to determine track location of $10\mu m$ $(R - \phi)$ and $115\mu m(z)$. In the end cap regions, the pixel detectors have a spatial resolution of $10\mu m$ $(R - \phi)$ and $115\mu m(R)$.

3.2.2 Silicon Micro-strip Detectors

A bit further out from the Silicon Pixel detectors at a radius of $299mm$ to $514mm$ are the SCTs. There are 4 cylindrical layers of silicon micro-strips in the barrel region, and 9 disk detectors in the end cap regions. The SCTs consist of 4088 modules in the barrel and end cap regions, 2112 modules in the barrel, and 1976 in the end caps. The spatial resolutions of the Silicon Micro-strips in the barrel region

[3]Here R represents the radial direction and $R - \phi$ represents the asimuthal direction. [2]

are $17\mu m$ in $(R-\phi)$ with $580\mu m$ in the z-direction. In the end cap region, the disks have a spatial resolution of $17\mu m$ in $(R-\phi)$ and $580\mu m$ in (R).

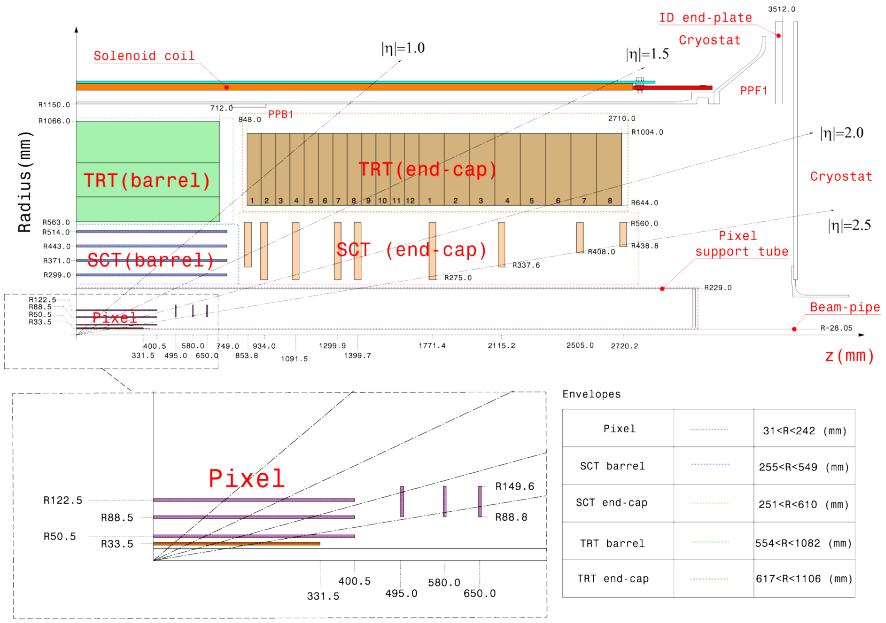

Figure 3.5: Cross section of a quadrant of the ATLAS Inner Detector describing the orientation and placement of components [2]

3.2.3 The Straw Tube TRT

The Straw Tube TRT is a tracking detector located at a radial distance of $554mm$ to $1082mm$ from the beam line, and is composed of about 300,00 drift tubes that have a spatial resolution of $130\mu m$ in $R-\phi$. In the barrel region the TRT is composed of 52,544 straw tubes arranged in 3 rings, as denoted by the segments in the green region in figure 3.5, the straws run parallel to the beamline and are 4mm in diameter and 144 cm in length. In each end cap, the TRT consists of 122,880 straw tubes arranged in 2 wheels, with 12 and 8 modules respectively, here the straws are arranged radially and are 37cm long. These drift tubes are filled with a gas mixture of 70% Xe, 27% CO_2 and 3% O_2 where the wall of the drift tubes are kept at a potential of -14,000V [20]. The TRT functions as a drift chamber similar to the Electromagnetic calorimeter described in section (3.3.1) but with a gas mixture used in place of Liquid Argon.

3.3 ATLAS Calorimeters

The ATLAS detector is comprised of two kinds of calorimeters, the Electromagnetic Calorimeter, and the Hadronic Calorimeter whose electronic signals are designed to identify charged and neutral particles as well as jets and measure their energy. The section below gives a brief description of the calorimeters and how they work.

3.3.1 The Electromagnetic Calorimeter

The Electromagnetic Calorimeter (ECAL) is designed to absorb and measure the energy of electrons, positrons, photons, and other light electro-magnetically interacting particles that come as a result of electromagnetic showers [21]. It has full ϕ coverage around the beam axis and is divided into a barrel part, and two end cap parts, that have a coverage of $|\eta| < 1.475$ and $1.375 < |\eta| < 3.2$ respectively. The EM calorimeter is made of alternating layers of accordion-shaped lead (Pb) plates sandwiched between two stainless steel sheets[4], and Liquid Argon (LAr) chambers. Here the Pb plates act as absorber material to produce EM showers, and the LAr chambers as an active material to drift charged particles through. The LAr-filled chambers have 3 copper planes within them, where the outer layers are held at high voltage, allowing the inner layer to collect electrons emitted when particles ionize the LAr [2].

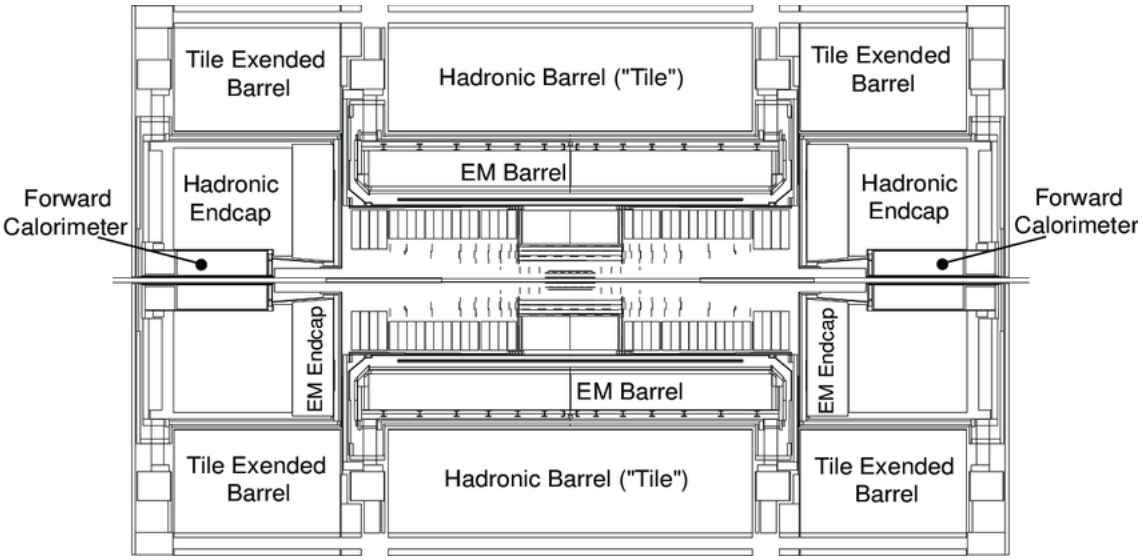

Figure 3.6: LAr and Tile Calorimeter Arrangement in ATLAS [22]

3.3.2 The Hadronic Calorimeter

Heavier particles like pions ($\pi^{\pm,0}$), protons, kaons ($K^{\pm,0}$), etc. that make it past the ECAL traverse the absorber material of the Hadronic Calorimeter (HCAL). The HCAL is located just after the ECAL and is divided into three parts, the central barrel, the extended barrels, and the Forward Calorimeterss (FCALs) that have an η coverage of $|\eta| < 1.7$, $1.5 < |\eta| < 3.2$, and $3.1 < |\eta| < 4.9$. The barrel region of the HCAL is also known as the Tile calorimeter because it is made of alternating layers of steel and dyed plastic scintillating tiles. When particles hit the tiles, they emit ultraviolet scintillation light which is then captured by optical wave shifting fibers that lead to photo-multiplier tubes that ultimately allow us to determine the energy of the particles that transverse it [2][23]. The Hadronic End Cap Calorimeters (HECs) are copper/liquid-argon sampling calorimeters that work on the same principles as the ECAL. The FCALs are also liquid argon sampling calorimeters that are split into three modules, FCal 1,2,3. FCal 1 uses copper as the

[4]The lead plates are sandwiched between stainless steel sheets to provide stability.

absorber material to optimize resolution and heat removal, while FCals 2 and 3 use tungsten as the absorbing material to reduce the spread of the resulting hadronic showers.

3.4 ATLAS Muon Spectrometer

Located just outside of the Hadronic calorimeters is the Muon spectrometer [2][24], which is designed to measure the charge and momentum of particles that traverse the material in the ECAL and HCALs. The Muon spectrometer has a measurement range of $|\eta| < 2.7$ and can measure the momenta of particles down to about 3GeV. In order to measure the momentum of muons in this region, the spectrometer deflects muon tracks using superconducting air-core toroid magnets, that generate the magnetic field in which charged particle tracks can bend. There are magnets placed in 2 regions of eta space that generate different magnetic field strengths, in the barrel region $0 < |\eta| < 1.4$ the magnets generate a 1.5 to 5.5 Tm field, while in the end cap regions defined by the η range of $1.6 < |\eta| < 2.7$, produce a field of 1 to 7.5 Tm. The field strength where the two regions overlap $1.4 < \eta < 1.6$, called the transition region, is weaker than in either region. Like the HCAL, the sub-components of the Muon Spectrometer can be divided into two parts, the barrel chambers and the end cap chambers. In most of the η space, $|\eta| < 2.0$, the momentum is measured by Monitored Drift Tube chambers (MDT's). From $2.0 < |\eta| < 2.7$, covering the forward region, Cathode-Strip Chambers (CSCs) are used. The purpose of these tracking chambers is to measure the coordinates of the tack in the bending (η) plane. Below is a description of the MDTs and CSCs, as well as a brief description of the Resistive Plate Chambers and Thin Gap Chambers.

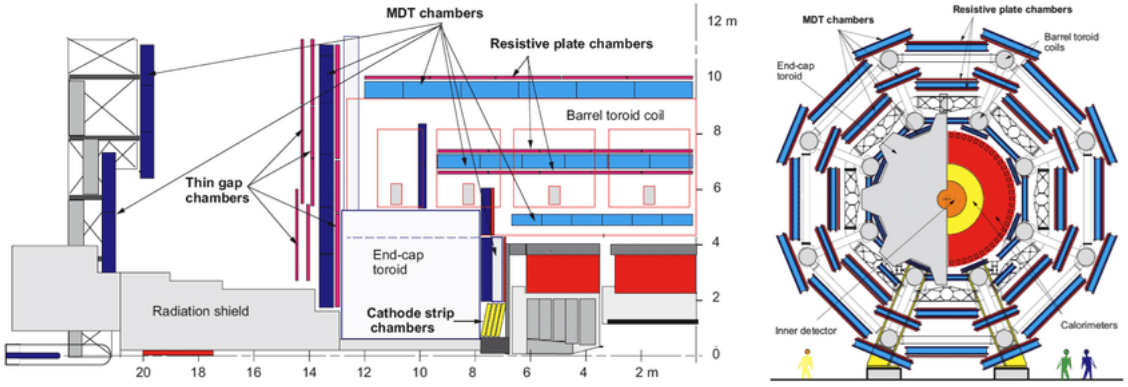

Figure 3.7: Schematic of the Muon Spectrometer [25]

3.4.1 Monitored Drift Tube (MDT) Chambers

In the barrel region, the chambers are arranged in three concentric but offset shells spanning from 5 meters to 10 meters away from the beam line [2]. These chambers contain 3 to 8 layers of drift tube which are about 30mm in diameter and are filled with Ar/CO2 gas pressurized to 3 bar. Particles that are created from the ionization of the gas are collected at a central wire in the drift tubes held at a potential of 3080V. These MDTs can be used to determine the position of a charged track to

a maximum resolution of $35\mu m$ with a sagitta [5] resolution of $\Delta S = 45\mu m$ and a resolution of $\frac{\delta p}{p} = \Delta S * \frac{p}{500\mu m}$ where p is given in units of TeV.

3.4.2 Cathode-Strip Chambers

Due to the high particle flux and a high number of muon tracks expected to traverse the forward region, $2.0 < |\eta| < 2.7$, Cathode-Strip Chambers (CSC) are used instead of MDTs because of their higher rate capability and time resolution. These CSCs are located in the forward region of the ATLAS detector and consist of two disks with eight chambers each symmetric about ϕ. These chambers contain wires oriented in the radial direction that are held at a potential of 1900V and operate on a mixture of Ar/CO2 (80/20) gas a a drift medium. The maximum resolution in the CSCs are $40\mu m$ in the plane in which the track bends representing η , and $5mm$ in the ϕ direction.

3.4.3 Resistive Plate Chambers

The Resistive Plate Chambers (RPCs) are located in the barrel region of ATLAS and are arranged in three layers covering a pseudo rapidity range of $\eta < 1.0$. These RPCs are used as trigger chambers to expand the ATLAS trigger system as much as possible and can trigger on high/low p_t tracks that have a momenta from $9 - 35GeV$ and $6 - 9GeV$ for the outermost and 2 innermost RPCs respectively [2]. These RPCs are composed of plastic laminate filled with a gaseous mixture of $C_2H_2F_4/Iso - C_4H_{10}/SF_6$ in the following proportions (94.7%/5%/0.3%). Because of its overlapping orientation, a single track traversing the RPCs can provide up to 6 measurements in η and ϕ with a space-time resolution of $1cm \times 1ns$.

3.4.4 Thin Gap Chambers

The Thin Gap Chambers (TGCs) are located in the end caps of the muon spectrometer and exist to provide further muon triggering capabilities and to provide an azimuthal coordinate ϕ to the MDTs. The TGCs are wire chamber detectors that operate on a gaseous mixture of CO_2 and $n - C_5H_{12}$[6] and cover an η range of $1.05 < |\eta| < 2.4$ [2].

3.5 The Data Acquisition (DAQ) System

On average, a single event[7] in ATLAS will produce about 1Mb of data, with data being collected every 25ns [26], this amounts to 40 Tb of data a second, or at a rate of 40 MHz. This is an impossibly large amount of data that cannot be stored in its entirety on the disks available at our tier 1 computing centers. So the ATLAS collaboration implements a skimming process to this incoming data so that only the data that could contain interesting physics is kept. This skimming is done by a set of 2 triggers called the Level 1 Trigger (L1) and the High Level Trigger (HLT)

[5] The distance from the midpoint of the arc to the chord of the arc.
[6] n - pentane
[7] An event is described as a single pp collision in a bunch crossing.

[11], and the decision on what events should be kept is made by a so called "Trigger Menu" [26][27].

3.5.1 Level 1 Trigger (L1 Trigger)

The first step in the data skimming process comes from the L1 [28]. This is a hardware-based trigger that makes a decision to keep high p_t leptons, photons, jets, and events with high MET. This trigger can be divided into 3 types called the L1Calo, the L1 Muon, and the L1Topo triggers. L1Calo takes in information from the Tile as well as Liquid Argon Calorimeters and has set energy thresholds for photons, jets, and high MET events. The L1Muon trigger takes input from the Muon subsystems As of 2017 [29], the L1Topo trigger system makes use of Field Programmable Gate Array (FPGA) processors to select interesting events by placing kinematic and angular requirements on electromagnetic clusters, jets, leptons, and the missing transverse energy. The L1Topo takes input from both the L1Calo and the L1Muon triggers to allow for topological selections to be made on objects of interest, such as determining the width of a jet cone (dR), or determining the invariant mass of a system of particles. All of these triggers pass information to the Central Trigger Processor (CTP) which applies pre-scales [8] to the data and creates what we call a Region of Interest (ROI) to determine the geometric area where objects that have been deemed as interesting make contact with ATLAS. After passing the L1 trigger, the rate of potential events that we will store has been reduced from 40MHz to about 100kHz at maximum, resulting in about 10 Gb of data every second.

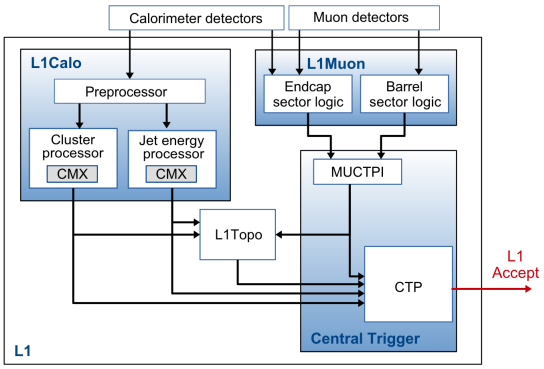

Figure 3.8: The ATLAS Trigger System used for Run 2 and Run 3 [29]

3.5.2 High-Level Trigger (HLT)

The HLT is a software-based trigger that performs online reconstruction of the physics objects in the ROIs passed to it by the L1 Trigger algorithm and makes a determination on weather it should be processed for long-term storage. On average, the rate of the events that are written to disk by this trigger system is 1 to 1.5kHz. This corresponds to a storage rate of 1-1.5 Gb/s.

[8] A pre-scale is a filter that only allows a certain number of events to go through, ex. every 5th event we trigger on.

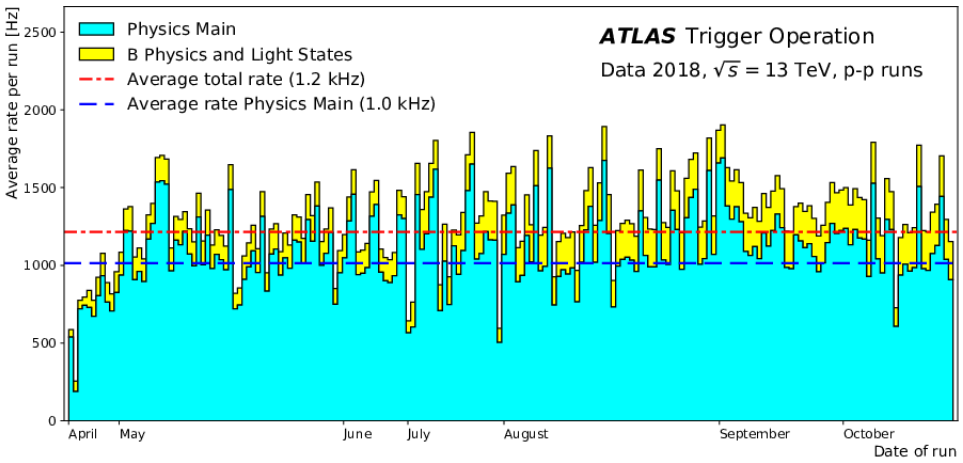

Figure 3.9: Data collection rate by the HLT for the entirety of 2018 [26]

Because of the software nature of the HLT and the requirement that trigger objects be reconstructed, the HLT has its own CPU computing farm to process these more CPU-intensive tasks. The HLT uses a so called "trigger menu", defined in the following section, to make a decision on weather an event should be stored.

3.5.3 The Trigger Menu

Together, all of the selections that make up the L1 Trigger and reconstruction algorithms of the HLT triggers and their pre-scales, make up the trigger menu. The trigger menu represents a set of criteria that must be fulfilled by multiple objects in an event, or single objects of an event, in the case of a trigger level analysis[9]. Selection criteria in the L1 trigger typically represent loose cuts on specific objects, such as single leptons or jets. When events that have passed the L1 triggers move on to the HLT, tighter cuts, as well as cuts that require online reconstruction of the objects are calculated by the CPU farm and then taken into consideration to be tagged for long-term storage and offline reconstruction. During the data-taking period of 2018, ATLAS triggered on events with 1, 2, or 3 leptons, single or di-photon events, events with a single jet, events with 1 or 2 b-jets, events with 4-6 jets, events with a $MET > 200GeV$, and B-Physics events which consist of events that contain 2 muons with at $p_t \geq 6GeV$ and a system mass of $2.5GeV < m(\mu, \mu) < 12GeV$ [26].

Trigger	Offline Selection	L1 Selection	HLT Selection
Single Lepton	1 e, $pT > 61GeV$	22 GeV	60 GeV
Single Photon	1 $\gamma, pT > 145GeV$	24 GeV	140 GeV
E_T^{Miss}	$E_T^{Miss} > 200$	50 GeV	110 GeV
b-Jets	Two $b(\epsilon = 60\%), pT > 185, 70GeV$	$100GeV$	$175, 60GeV$

Table 3.1: A simplified display of the 2018 trigger menu items

[9] A trigger level analysis is a kind of event trigger, where only the objects that are reconstructed and pass the selection criteria are stored

Chapter 4

The Standard Model

The Standard Model is the most accurate scientific achievement to date, beautifully linking all of the known particles and their interactions together in a mathematical formalism that is physically accurate. It is an $SU(3)_C \times SU(2)_L \times U(1)_Y$ [1] quantum field gauge theory that provides descriptions of 3 of the 4 known fundamental forces, the strong force, the weak force, and the electro-magnetic force, and describes how the elementary particles in our universe interact through these forces. The 17 elementary particles in the standard model are 12 spin $\frac{1}{2}$ particles that we call fermions, divided into 6 quarks and 6 leptons, and 4 spin 1 vector bosons which act as force mediators to the other particles in the standard model, and a single scalar (spin-0) particle.

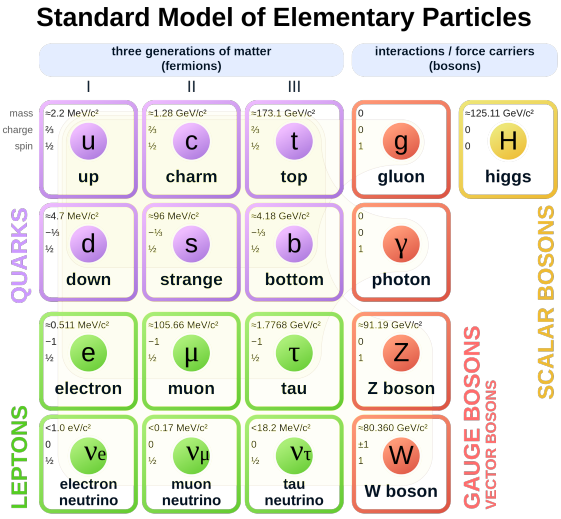

Figure 4.1: Graphical representation of the Standard Model of Particle Physics [30]

The theory describes these particles and their interactions via the standard model Lagrangian shown below

$$\mathcal{L} = -\frac{1}{4}F_{\mu\nu}F^{\mu\nu} + i\bar{\psi}\not{D}\psi + h.c. + \bar{\psi}_i y_{ij}\psi_j\phi + h.c. + |D_\mu\phi|^2 - V(\phi) \tag{4.1}$$

[1] Here C indicates color charge. L indicates the weak force couples to left-handed particles. Y indicates weak hypercharge.

4.1 The Electro-Magnetic force

The mathematical framework that is used to describe all particles that have an electric charge and therefore interact electromagnetically is called Quantum Electro-Dynamics (QED). The electromagnetic force is mediated by the photon (A^μ), and is brought about by making the Dirac Lagrangian invariant under local $U(1)$ transformations. Consider the $U(1)$ local transformation on a massive electromagnetically interacting fermion ψ which transforms as

$$\psi(x) \rightarrow \psi^{'} = e^{iQK(x)}\psi(x) \tag{4.2}$$

governed by the Dirac Lagrangian

$$\mathcal{L} = i\overline{\psi}\gamma^\mu\partial_\mu\psi - m\overline{\psi}\psi \tag{4.3}$$

by choosing the following transformations on the ∂_μ and A_μ such that

$$\partial_\mu \rightarrow D_\mu = \partial_\mu + iqA_\mu \tag{4.4}$$

$$A_\mu \rightarrow A^{'}_\mu = A_\mu - \partial_\mu K(x) \tag{4.5}$$

And adding in the lagrangian for a free photon $\mathcal{L}_{\mathcal{EM}} = -\frac{1}{4}F^{\mu\nu}F_{\mu\nu}$, we arrive at the gauge invariant QED Lagrangian

$$\mathcal{L}_{\mathcal{QED}} = i\overline{\psi}\not{D}\psi - m\overline{\psi}\psi + Q\overline{\psi}\gamma^\mu\psi A_\mu - \frac{1}{4}F_{\mu\nu}F^{\mu\nu} \tag{4.6}$$

After performing this gauge invariant transformation, we find a coupling constant Q appears between fermions and the photon in the third term of the Lagrangian, we interpret this physically as electric charge (e). Any particle that possesses an electric charge interacts electromagnetically. The EM force is now known to be part of the electroweak symmetry group $SU(2)_L \times U(1)_Y$ that when broken produces the EM force.

4.2 The Weak Force

The weak force is mediated by the $W^\pm$ bosons, as well as the neutral Z boson, and is responsible for nuclear decay. Charged current interactions come about by making the Dirac Lagrangian invariant under $SU(2)$ transformations. Experimental evidence for parity violation in nuclear decay by Wu [31] forces the weak interaction vertex to be a V-A interaction[2], placing chiral projection operators (P_L, P_R) in the vertex interaction for weak decay. This requires that particles (anti-particles) undergoing a weak interaction must be left chiral (right chiral). Since the weak interaction has been observed to couple left-handed particles differing by one unit of electric charge, and since the generators of SU(2) are 2×2 matrices, the spinors of the theory must be placed into a weak iso-spin doublet

$$\psi_L = \begin{pmatrix} \nu_{\tau L} \\ \tau_L \end{pmatrix}_L \tag{4.7}$$

[2]Vector minus Axial Vector

Since the right-handed component of fermions do not interact weakly, they are placed in weak iso-spin singlets. $\psi_R = (\tau_R)$

In order for weak interactions to occur, we must make the Dirac Lagrangian invariant under the $SU(2)$ transformation. This is done by requiring the following transformations

$$\psi_L \to \psi_L^{'} = e^{\frac{1}{2} i g_w \alpha(\mathbf{x}) \cdot \sigma} \psi_L \tag{4.8}$$

$$\partial_\mu \to D_\mu = \partial_\mu + \frac{1}{2} i g_W \sigma \cdot \mathbf{W}_\mu \tag{4.9}$$

$$\mathbf{W}_\mu \to \mathbf{W}_\mu^{'} = \mathbf{W}_\mu - \partial_\mu \alpha(\mathbf{x}) - g_W \alpha(\mathbf{x}) \times \mathbf{W}_\mu \tag{4.10}$$

Here g_W is the weak coupling constant, $\alpha(x)$ represent the phases that ψ transforms under, σ are the 2×2 Pauli spin matrices which are the generators of the $SU(2)$ group and $\mathbf{W}_\mu$ is a vector of the three gauge fields associated with the $SU(2)$ gauge group. Introducing this symmetry yields a conserved quantity called weak isospin (I) with a third component represented by $I_W^{(3)}$ given as either $\pm\frac{1}{2}$ depending on the particle's placement in the SU(2) doublet. Because right-handed components of particles are placed in a singlet, their $I_W^{(3)} = 0$. The physical $W^\pm$ bosons can be built out of linear combinations of two of the three W gauge fields as shown below

$$W_\mu^\pm = \frac{1}{\sqrt{2}} (W_\mu^{\mathbf{x}} \mp i W_\mu^{\mathbf{y}}) \tag{4.11}$$

Where the third component of $\mathbf{W}$ field $W^{\mathbf{z}}$ cannot correspond to the Z boson. In this SU(2) transformation $W^{\mathbf{z}}$ is a gauge field that only interacts with left-handed fermions, whereas the Z can interact with both left and right-handed fermions. We can obtain the physical Z boson field through the unification of the electro and weak gauge fields (4.4) where the photon A_μ and Z_μ can be represented as linear combinations of the fields generated by $SU(2) \times U(1)$.

4.3 The Strong Force

The quantum field theory of the strong force and the particles that interact through it is called Quantum Chromo-Dynamics (QCD). It is mediated by 8 massless spin $\frac{1}{2}$ gluons, these gluons are introduced by making the Dirac Lagrangian gauge invariant under transformations of the SU(3) symmetry group. This is done by requiring the following transformations

$$\psi \to \psi^{'} = e^{\frac{1}{2} i g_s \alpha(\mathbf{x})_\mathbf{k} \lambda^\mathbf{k}} \psi \tag{4.12}$$

$$\partial_\mu \to D_\mu = \partial_\mu + \frac{1}{2} i g_s G_\mu^k \lambda^k \tag{4.13}$$

$$G_\mu^k \to G_\mu^{k'} = G_\mu^k - \partial_\mu \alpha(x)_k - g_s f_{ijk} \alpha(x)_i G_\mu^j \tag{4.14}$$

Here the index "k" runs over all 8 gluons, where $\alpha(x)_k$ represent phases by which ψ transforms, λ^k represent the 3×3 Gell-Mann matrices which are the generators of

the $SU(3)$ group, G_μ^k indicate the gluon fields and g_s is the strong coupling constant. Introducing the $SU(3)$ gauge group leads to a conserved quantity analogous to that of electric charge but specific to the strong force that is called "color". Color charge comes in 6 distinct varieties, Red, Green, Blue and its anti-color counterparts, Anti-Red, Anti-Blue, and Anti-Green. Only particles that possess this color charge can interact via gluon exchange. In particular, leptons do not possess color change and so do not interact via the strong force. In contrast, quarks **do** possess color charge which allows them to couple to gluons. Because the generators of the $SU(3)$ group are 3×3 matrices, quarks spinors have an additional piece to include color interactions and can be written as

$$\psi_q^{'} = \begin{pmatrix} r \\ g \\ b \end{pmatrix} \psi_q \tag{4.15}$$

4.4 The Electro-Weak Force

Just as in classical physics when the Electric and Magnetic forces were thought to be separate, but then discovered to be one and the same, this joining of forces has once again been discovered to be present in the Electromagnetic and the Weak force. In the standard model, the $SU(2)$ gauge group of the Weak force, and the $U(1)$ gauge group of the electromagnetic force was first shown to be one unified Electroweak gauge group represented by $SU(2) \times U(1)$ in the Glashow-Salam-Weinberg (GSW) model. Only when spontaneous symmetry breaking of the electro-weak symmetry occurs, do these forces become distinct from each other. This breaking of symmetry is done via the Higgs mechanism described in section (4.5). To make the Dirac Lagrangian invariant under $SU(2) \times U(1)$ we can introduce gauge fixing terms by requiring the covariant derivative to be replaced with

$$\partial_\mu \rightarrow D_\mu = \partial_\mu + \frac{1}{2} i g_W \sigma \cdot \mathbf{W}_\mu + i g^{'} \frac{Y}{2} B_\mu \tag{4.16}$$

Here a $U(1)$ gauge field B_μ has been introduced that yields a conserved quantity called weak hypercharge Y with a coupling strength $g^{'}$ that can be related to the electric charge (Q) of the electromagnetic force through

$$Y = 2(Q - I_W^{(3)}) \tag{4.17}$$

This gauge transformation allows us to identify the physical field manifestations of the photon (A_μ) and Z boson (Z_μ) as a linear combination of $W_\mu^{\mathbf{z}}$ and B_μ, although they still lack mass terms.

$$A_\mu = B_\mu cos(\theta_W) + W_\mu^{\mathbf{z}} sin(\theta_W) \tag{4.18}$$

$$Z_\mu = -B_\mu sin(\theta_W) + W_\mu^{\mathbf{z}} cos(\theta_W) \tag{4.19}$$

where θ_W called the weak mixing angle characterizes their degree of mixing. It can also be shown that the interaction vertex associated with the Z now allows it to interact with both left and right-handed particles.

4.5 The role of the Higgs Boson

The Higgs boson is the most recently discovered elementary particle in the standard model. It was first theorized in 1964 and has a spin of 0, making it the only scalar particle in the standard model, and has been experimentally verified to have a mass of 125 GeV in 2012 by the ATLAS [32] and CMS collaborations [33]. The Higgs boson plays a critical role in the standard model because it provides the theory with an avenue by which particles can gain mass through spontaneous symmetry breaking while respecting an $SU(3) \times SU(2) \times U(1)$ local gauge symmetry.

4.6 QFT Mass terms

Mass in Quantum Field Theory (QFT) is represented by a constant preceeding quadratic field terms

$$\frac{1}{2}m_W^2 W_\mu W^\mu \tag{4.20}$$

In the pre-Higgs standard model mass terms for gauge bosons such as the W and Z are absent because they are not gauge invariant under a local $U(1)$, $SU(2)$ or $SU(3)$ transformations. Additionally, mass terms for fermions are not present because they do not respect $SU(2)$ gauge transformations when they are split into their left and right-handed components.

Consider the $U(1)$ local transformation on a massive electromagnetically interacting field W which transforms as

$$W(x) \rightarrow W(x)^{'} = W(x) - \partial_\mu K \tag{4.21}$$

If gauge invariant, the mass term shown by equation 4.20 once transformed should yield the same quantity, but it yields extra terms

$$\frac{1}{2}m_W^2 W_\mu W^\mu \rightarrow \frac{1}{2}m_W^2 (W_\mu + \partial_\mu K)(W^\mu + \partial^\mu K)$$

$$\frac{1}{2}m_W^2 W_\mu W^\mu \rightarrow \frac{1}{2}m_W^2 W_\mu W^\mu + \frac{1}{2}m_W^2 (W_\mu \partial^\mu K + \partial_\mu K W^\mu + \partial_\mu K \partial^\mu K)$$

And so mass terms for bosons must be added to the Lagrangian in a clever way to maintain gauge invariance. Spontaneous symmetry breaking provides such a way.

4.7 Spontaneous symmetry breaking

For simplicity, we will consider symmetry breaking in the context of a complex scalar field. We begin with a complex scalar field

$$\phi = \frac{1}{\sqrt{2}}(\phi_1 + i\phi_2) \tag{4.22}$$

with a Lagrangian of the form

$$\mathcal{L} = \partial_\mu \phi^\mu \partial^\mu \phi_\mu + V(\phi) \tag{4.23}$$

and potential

$$V(\phi) = \mu^2\phi^*\phi + \lambda(\phi^*\phi)^2 \tag{4.24}$$

Notice that this lagrangian is invariant under a $\mathcal{Z}_2$ symmetry transformation $\phi \to -\phi$. By taking the minimum of potential $V(x)$ and requiring μ be less than zero we can show that it has a ring of degenerate non-zero vacuum states we will call v shown by figure (4.2). Taking the minimum we find

$$\phi_1^2 + \phi_2^2 = v^2 = \frac{-\mu^2}{\lambda}; \quad v = \sqrt{\frac{-\mu^2}{\lambda}}$$

If we choose one of the points along this ring to be the physical vacuum, let's say on the real axis ϕ_1 such that $\phi_2 = 0$, and expand our function via Taylor series along that axis such that $\phi_1(x) = v + \chi(x)$ and plugin. We reveal that our potential and therefore Lagrangian is no longer symmetric under $\mathcal{Z}_2$ due to the introduction of a cubic term, this is spontaneous symmetry breaking.

$$V(\chi, \phi_2) = \lambda v^2\chi^2 + \lambda v\chi^3 + \lambda v\chi\phi_2^2 + \frac{1}{2}\lambda\chi^2\phi_2^2 + O^4(v, \chi, \phi_2) \tag{4.25}$$

Notice that this breaking of symmetry has produced a massive scalar boson χ as indicated by the first term I the potential[3], and a mass-less scalar ϕ_2 called a goldstone boson. As it turns out, symmetry breaking can enable mass-less gauge bosons to gain mass. In the context of a broken $SU(2) \times U(1)$ symmetry, it allows the $W^{\pm}$ and Z boson to gain mass. And the couplings of the Higgs field to fermions when it undergoes spontaneous symmetry breaking allows fermions to gain mass terms as well.

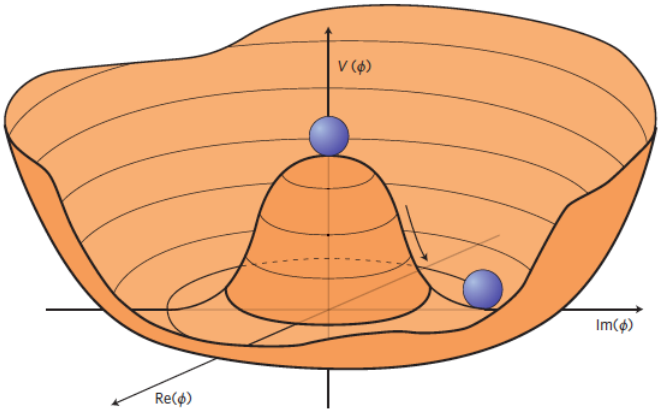

Figure 4.2: The Higgs potential often called a "Mexican Hat" or "Wine Bottle" potential, shows a ring of stable points along the rim of the surface, with a single stable point located at the origin of the imaginary and real plane.[34]

[3]since if $\mu < 0$ it can no longer be interpreted as mass, Important when trying to produce the massive scalar boson that is the Higgs

4.8 The Higgs Mechanism

In the standard model, the $W^{\pm}$ and Z bosons gain mass through the breaking of the $SU(2) \times U(1)_Y$ gauge symmetry. This is done with a Higgs field made of 2 complex scalar fields in $SU(2)_L$ doublet with hypercharge Y=1.

$$\phi = \begin{pmatrix} \phi^+ \\ \phi^o \end{pmatrix}, \quad \phi = \begin{pmatrix} \phi_1 + i\phi_2 \\ \phi_3 + i\phi_4 \end{pmatrix} \tag{4.26}$$

We begin with the same lagrangian and potential as in section (4.7)

$$\mathcal{L} = \partial_\mu \phi^\mu \partial^\mu \phi_\mu + V(x) \tag{4.27}$$

$$V(\phi) = \mu^2 |\phi^\dagger \phi| + \lambda (|\phi^\dagger \phi|)^2 \tag{4.28}$$

taking the minimum of the potential $V(x)$, and again requiring that $\mu^2 < 0$ we then arrive at the non zero vacuum expectation value v

$$(\phi_1^2 + \phi_2^2 + \phi_3^2 + \phi_4^2) = v^2 = \frac{-\mu^2}{\lambda} \;\; ; \;\; v = \sqrt{\frac{-\mu^2}{\lambda}} \tag{4.29}$$

Choosing to Taylor expand about the minima along ϕ_3 and choosing the vacuum state to be purely in this direction we find, after a unitary gauge transformation

$$\phi = \frac{1}{\sqrt{2}} \begin{pmatrix} 0 \\ v + H \end{pmatrix} \tag{4.30}$$

If we then choose the appropriate $SU(2)_L \times U(2)_Y$ gauge transformation for the covariant derivative

$$\partial_\mu \rightarrow D_\mu = \partial_\mu + \frac{1}{2} i g_W \sigma \cdot \mathbf{W}_\mu + i g^{'} \frac{Y}{2} B_\mu \tag{4.31}$$

and plug in equations 4.31 and 4.30 into our lagrangian 4.27 we obtain the mass terms for the $W^{\pm}, Z, A$ and Higgs boson.

$$m_{W^\pm} = \frac{1}{2} g_W v, \;\; m_Z = \frac{1}{2} v \sqrt{g_W^2 + g^{'2}}, \;\; m_A = 0, \;\; m_H = \sqrt{2\lambda} v$$

4.9 Fermion Masses

As discussed in (4.7) fermions can acquire mass through their coupling to the Higgs field ϕ and its conjugate ϕ_c. Because the addition of a mass term for fermions via $m\overline{\psi}\psi$ would break the $SU(2)$ gauge invariance of the Dirac Lagrangian, we cannot add it in outright. But the addition of a so-called Yukawa term allows for the preservation of $SU(2) \times U(1)$ symmetry while generating mass for the fermions. This term takes the form

$$\mathcal{L}_{m_f} = -y_f (\bar{\psi}_L \phi \psi_R + \bar{\psi}_R \phi^\dagger \psi_L) \tag{4.32}$$

Because left-handed fermions are placed in a weak-iso spin doublet, and right-handed fermions are placed in a weak-iso spin singlet, in the case of up and down quarks we can write

$$\psi_L = \begin{pmatrix} u_L \\ d_L \end{pmatrix}, \quad \psi_R = d_R \tag{4.33}$$

Where L and R indicate the left and right-handed components of the particle wave function, and u and d play the double duty of indicating the up and down quark spinors as well as representing the "up" and "down" components of the doublet. If we then choose to represent the Higgs field in the unitary gauge given by

$$\phi = \frac{1}{\sqrt{2}} \begin{pmatrix} 0 \\ v + H \end{pmatrix} \tag{4.34}$$

and plug in equations (4.33) and (4.34) into (4.32), we get two terms, one of which represents the down quark's coupling to the Higgs field, and the other

$$\frac{-y}{\sqrt{2}} v(\overline{d}_L d_R + \overline{d}_R d_L), \quad \overline{d}d = \overline{d}_L d_R + \overline{d}_R d_L \tag{4.35}$$

representing the mass term for the down quark [4]. Here the mass of the down quark is given by

$$m_d = \frac{y}{\sqrt{2}} v \tag{4.36}$$

where y is the Yukawa coupling. Because of the choice of gauge, the Higgs field only has the ability to give mass to particles in the lower part of the weak isospin doublet ("down" type particles). The Higgs conjugate with the same choice of gauge is needed to generate masses for the up-type particles,

$$\phi_c = \frac{1}{\sqrt{2}} \begin{pmatrix} v + H \\ 0 \end{pmatrix} \tag{4.37}$$

Alternatively, through the introduction of a second Higgs doublet with a weak hypercharge of Y=-1, a representation of it in the unitary gauge would give it the same form as equation (4.37) but provide an alternative mode by which particles can gain mass. One framework by which the second doublet couples to up-type particles and the first to down-type and charged leptons is called a Type-2 2HDM.

[4] Recall that spinors can be decomposed into their left and right-handed components, $\eta = P_L\eta + P_R\eta$

Chapter 5

The Two Higgs Doublet Model and other extensions to the Standard Model

As all-encompassing as the Standard Model (SM) may seem, it is still incomplete. It fails to address the purported observation of dark matter [35], and cannot accommodate for the observed mass of the Higgs boson through quantum loop corrections [36]. Additionally, it has no explanation for the anomalous magnetic moment of the muon [37], for evidence of flavor violation in the Higgs sector via $h \to \mu\tau$ [38][39], or for emerging evidence for the breaking of lepton universality from additional decays to τs [40][41]. Some of these discrepancies can be accounted for through the addition of a second Higgs doublet, or by more expansive extensions that include a 2 Higgs Doublet Model (2HDM) within it.

5.1 The Two Higgs Doublet Model

5.1.1 Theoretical Motivations

Publications by the multiple collaborations indicate a significant deviation in the quantity $R(D)$ and $R(D^*)$ with respect to its SM prediction [42][43][44]. These deviations represent the potential breaking of lepton universality in b quark decays due to excess production of taus [40], and can be explained by contributions to b quark decay modes from additional scalar bosons such as those in 2HDMs [45][46]. Additionally, purported flavor violation in the Higgs sector via $h \to \mu\tau$, and the deviation of the muon magnetic moment from SM predictions can be accommodated in a 2HDM [47]. Furthermore, scalar Higgs bosons in some versions of the 2HDM [48] can provide additional sources of CP violation that would improve the SMs inability to produce the degree of baryon asymmetry that we observe in our universe. Experimental results given by the $H^+ \to cb$ group in ATLAS show a local excess of 3σ at 130 GeV. This seems to be best explained by a charged Higgs [49]. The discovery of a singly charged Higgs boson would provide strong evidence of a second Higgs doublet. Given that a second Higgs doublet can exist as a stand-alone theory as well as part of other models, searches for additional Higgs particles are well motivated.

5.1.2 The 2HDM as a theoretical framework

In general, 2HDMs contain the standard model Higgs doublet[1] (Φ_1) that produces a non-zero vev [2] (v_1), the Higgs, as well as the $W^{\pm}$ and Z bosons, and a second doublet (Φ_2) that produces a second vev (v_2), and 4 additional Higgs particles. These particles are a scalar Higgs (H or h) either heavier or lighter than the SM Higgs, a pseudo scalar Higgs particle (A) and scalar charged Higgses ($H^{\pm}$) which are the focus of this search. When discussing 2HDMs there are 4 that are most common due to their natural flavor conservation. The Type-1 2HDM describes a model where all fermions couple to one of the 2 doublets. The Type-2 2HDM describes a model in which one doublet couples to up-type quarks and the second doublet couples to down-type quarks and leptons. The Type-X 2HDM also known as the lepton-specific model, is a framework where all leptons couple to one of the doublets and all quarks couple to the second doublet, and finally the Type-Y model also known as the flipped model, describes a model in which one doublet couples to the up-type quarks and leptons, and the other doublet couples to only down-type quarks.

Model	Type-I	Type-II	Type-X (Lepton-specific)	Type-Y(Flipped)
Φ_1	-	d, ℓ	ℓ	d
Φ_2	u, d, ℓ	u	u, d	u, ℓ

Table 5.1: A table representing the Higgs doublets (Φ_1, Φ_2) and their different couplings to quarks and leptons in the various 2HDM types. [50]

This analysis searches for the existence of a charged Higgs in a model-independent manner, but results are interpreted to exclude regions of $tan(\beta)$ and $m_{H^{\pm}}$ or m_A within the hMSSM model [51]. Here $tan(\beta)$ is the ratio of the vacuum expectation values $\frac{v_2}{v_1}$ for each doublet. In order to give an idea of the mathematical structure of 2HDM framework despite its extremely rich nature, equation 5.1 along with table 5.2 shows the most general Yukawa couplings for charged Higgs for 2 Higgs doublet models of types 1, 2, X, and Y [52][53] with the simplifying requirement that there are no flavor changing neutral currents. In equation 5.1 V_{ud} is the element of the CKM matrix corresponding to the charge $+\frac{2}{3}$ u quarks and the charge -$\frac{1}{3}$ d quarks, u and d are spinors of all the charged $\frac{2}{3}$,-$\frac{1}{3}$ quarks, m_u and m_d are mass terms for the u and d spinors, P_L and P_R are left and right handed chiral projection operators, l_R and $\overline{v}_L$ are lepton and neutrino spinors, m_ℓ is the lepton mass term, and $h.c.$ represents the hermitian conjugates of the objects in the Lagrangian.

$$L_{H^{\pm}} = -H^{+}(\frac{\sqrt{2}V_{ud}}{v}\overline{u}(m_u X P_L + m_d Y P_R)d + \frac{\sqrt{2}m_l}{v} Z \overline{v}_L l_R) + h.c \tag{5.1}$$

[1] A doublet is defined as a 2-component column vector with complex entries
[2] Vaccume expectation value

	Type I	Type II	Type X (Lepton-specific)	Type Y (Flipped)
X	cot β	cot β	cot β	cot β
Y	cot β	-tan β	cot β	-tan β
Z	cot β	-tan β	-tan β	cot β

Table 5.2: X, Y and Z input parameters for $L_{H^\pm}$ for each of the 2HDM types. [52]

5.1.3 $H^\pm$ Production

There are many production modes for the charged Higgs boson, each depending on what the mass of the charged Higgs is suspected to be relative to the top quark mass. In all cases relating to this analysis, charged Higgs bosons are produced via collisions of quark anti-quark, or gluon-gluon pairs in colliding protons. Other production modes, such as those due to vector boson fusion are outside of the scope of this analysis. All Feynman diagrams relating to charged Higgs production used in this analysis are shown in figure 5.1.3.

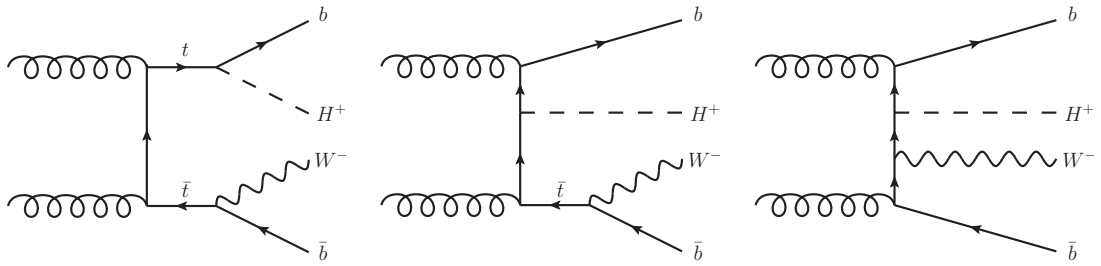

Figure 5.1: Leading-order Feynman diagrams contributing to the production cross-section of charged Higgs bosons: (a) double-resonant top-quark production dominating in the low mass regime and up to the top quark mass, (b) single-resonant top-quark production dominating in the intermediate mass regime with contributions from diagrams a and c, and (c) non-resonant top-quark production dominating in the high mass regime with contributions from b. [54]

The branching fractions of the charged Higgs bosons depend on their proposed mass, 2HDM type, and $tan(\beta)$. Figure 5.2 demonstrates that the $H^+ \to \tau\nu$ decay mode accounts for a significant branching fraction across a range of charged Higgs masses, 2HDM Types and $tan(\beta)$ and so this search is well motivated. In the examples shown below the dominant decay mode for charged Higgs with masses above 200GeV is $H^+ \to tb$, although this search channel suffers from large backgrounds due to the large high production of t and b quarks in pp collisions. $H^+ \to bc$ also represents a promising decay mode as its BR is still significantly large up to 200GeV.

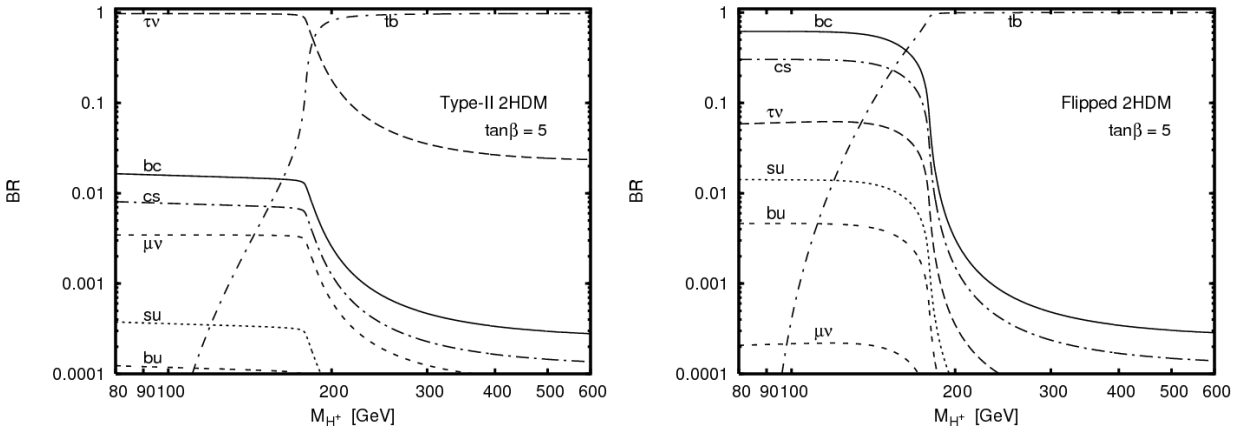

(a) (b)

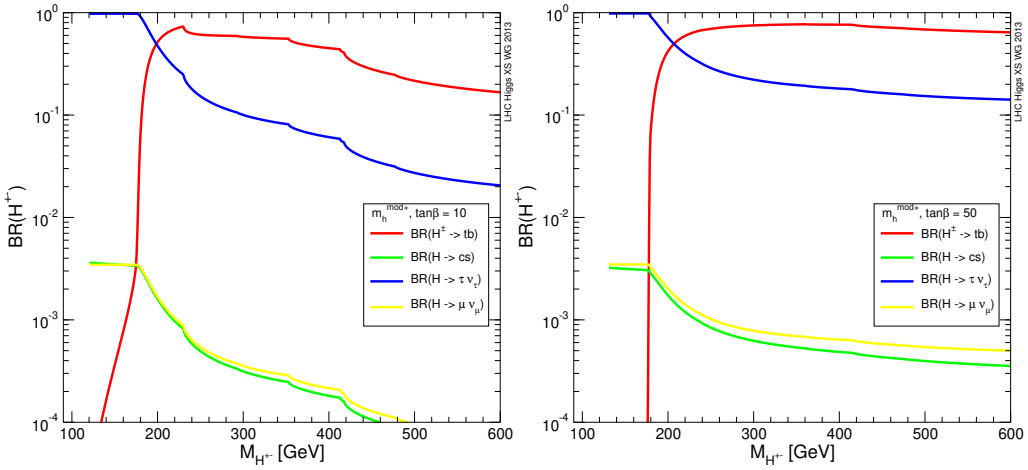

(c) (d)

Figure 5.2: Branching fractions for the various decay modes of the charged Higgs for (a) $tan(\beta) = 5$ in a Type-2 2HDM, and (b) $tan(\beta) = 5$ in a Flipped 2HDM [50], (c) in the context of the m_h^{mod+} hMSSM with a $tan(\beta) = 10$, (d) in the context of the m_h^{mod+} hMSSM with a $tan(\beta) = 50$ [55]

Setting upper bounds on the production cross section and branching fraction for charged Higgses allows us to exclude models from parameter space. Thus far, certain regions of the $tan(\beta)$ vs m_A phase space of the hMSSM have been excluded by various searches, as seen in figure 5.3. Given the exclusion space, we focus our search on the so-called wedge region, where the value of $tan(\beta)$ is about 6 and the m_A mass is greater than 500GeV.

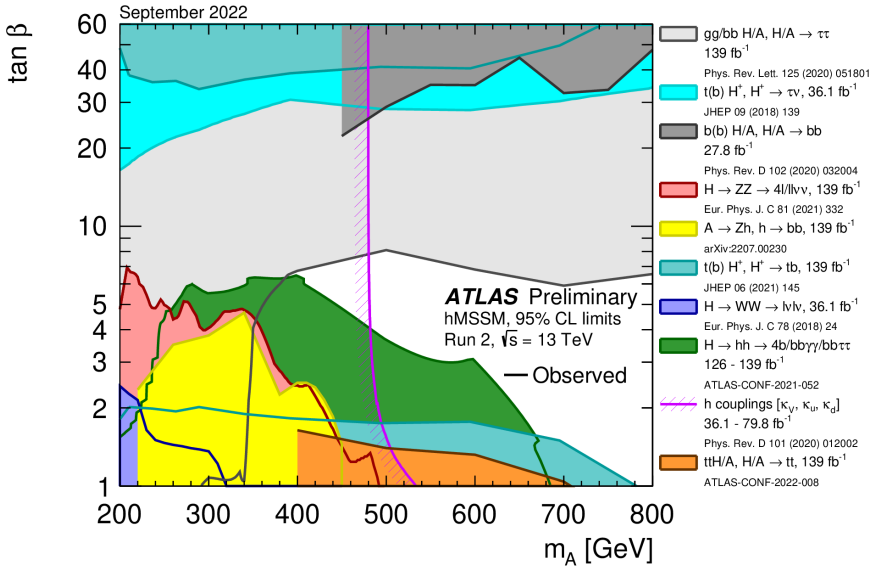

Figure 5.3: Exclusion plot in m_A and $tan(\beta)$ space in the context of the hMSSM.[56] Exclusion plots for the hMSSM are usually shown with respect to the mass of the pseudo scalar A (m_A) instead of $m_{H^\pm}$ or any other parameters because the higgs sector of the hMSSM can be fully defined by m_A and $tan(\beta)$ [51].

5.2 SuperSymmetry (SUSY)

The general premise of Super Symmetry (SUSY) is to introduce additional "super-partner" particles for each fermion and boson in the SM such that they differ by a half-integer spin. Spin $\frac{1}{2}$ fermions gain super partner spin 1 bosons called sqarks or sleptons, and spin 1 gauge bosons gain super partner spin $\frac{1}{2}$ fermions called gaugi-nos. Spin 0 Higgs bosons gain spin $\frac{1}{2}$ fermions called higgsinos. The existence of one or more charged Higgs bosons as part of an extended Higgs sector is critical to many supersymmetric theories since at least a second Higgs doublet is required to couple to the additional particles that SUSY introduces. But what is the theoretical mo-tivation for SUSY? As mentioned in the heading of this chapter [5], the SM cannot accurately calculate the mass squared of the SM Higgs via quantum loop corrections. Super partner particles are introduced to neatly cancel the contributions of the loop integrals from particles in this calculation. Drawing from SUSY primer [36] we can see that loop corrections coming from fermions add a correction proportional to Λ^2_{UV} which is on the order of the Planck scale $O(10^{19})$GeV. With no loop corrections to cancel out contributions of this magnitude, we are left with an untenable situation where m_h^2 is orders of magnitude larger than is observed. Because loop corrections

from fermions and bosons yield opposite signs, loop corrections from superpartner particles cancel out these large contributions.

5.2.1 The MSSM and hMSSM

The Minimal Super Symmetric Model (MSSM) [57] is a particular version of SUSY that has the simplest theoretical framework to allow for the existence of superpartners. In light of the discovery of the Higgs boson in 2012 [32][33] and the non-observation of supersymmetric particles with identical masses to those in the SM, we must exclude some parameter space of the MSSM, this is the hMSSM. Many Beyond Standard Model (BSM) searches in ATLAS, including this one, do the interpretations of their results in context of an MSSM or habemus MSSM (hMSSM) model given that these models require a Type-2 2HDM.

5.2.2 Grand Unified Theories (GUT)s

Another theoretical framework which attempts to resolve some of the problems with the standard model are Grand Unified Theories (GUT)s. These are theoretical frameworks in which the SM Lagrangian obeys a larger symmetry group such as the $SU(5)$ and $SO(10)$ gauge groups in place of the $SU(3) \times SU(2) \times U(1)$ which is the current gauge symmetry group of the SM. With GUT theories, the strong, weak, and electromagnetric forces all become one at very high energies. Additionally SUSY can fit within certain GUT frameworks, allowing for a combination of solutions from many fronts. 2HDMs also fit within these theoretical frameworks in part to grant mass to additional particles that arise from the larger symmetry group.

Chapter 6

Event Reconstruction

The ATLAS collaboration uses a software package called Athena [58], to do everything from reconstructing physics objects to creating input for event visualizations for proton collisions. Particle objects that physics analysis groups use are derived from various electrical signals called "hits". These hits are registered when the particles created in pp collisions or subsequent processes in ATLAS deposit their energy and momentum into the inner detector material (3.2). The process by which algorithms construct particle objects like jets, tracks, energy clusters, electrons (e), photons (γ), muons (μ), taus (τ), and MET (E_T^{Miss}) from the so-called "cell" level information and "hits" is called reconstruction. The following section briefly describes the algorithms responsible for resolving energy and momentum information into the particles that we use to conduct the analysis defined in section (9.2).

6.0.1 Track Reconstruction

The reconstruction of charged particle tracks is important for the reconstruction of many particle objects that are used in physics analysis. Tracks help identify charged particles, and primary vertices, aid in the removal of pileup events, and are useful in jet flavor tagging. The track reconstruction algorithm has two main methods called the inside-out method and the outside-in method [59][60][61]. Track reconstruction begins by gathering so-called 3-dimensional "space points" that correspond to where particles have deposited energy in either the pixel or the SCT layers. Sets of three space points are then gathered to trace the likely paths that a charged particle traversed. A minimum of 3 space points are used to define a 'track seed', that serves as a template to calculate a smooth path that the charged particle likely traversed. The characteristics of the tracks such as the transverse and longitudinal impact parameters (d_0, z_0) are estimated by fitting the track seeds with a perfectly helical particle trajectory made by a charged particle moving through a uniform magnetic field [59].

The Inside-Out Method

At times, multiple track seeds can share space points, and lead to ambiguities of the track shape, as well as which track seeds correspond to 'real' or 'fake' particle tracks. In this case, the inside-out ambiguity solver method is used by extrapolating the track paths in question into the TRT to see if they match with any tracks there

[61]. This method is useful for identifying "promptly created" charged particles that are created at or very near the interaction point.

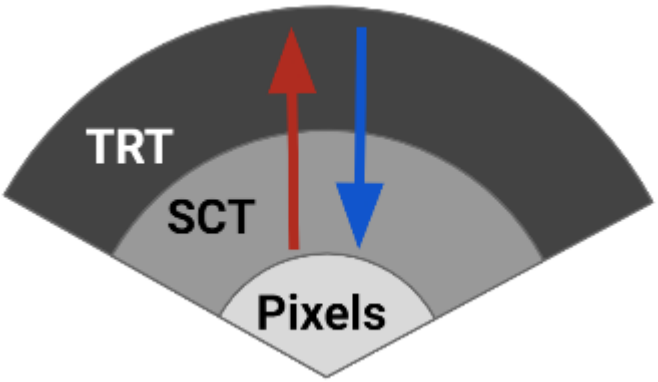

Figure 6.1: A graphic representing the inside-out track (red arrow) and outside-in (blue arrow) track reconstruction methods used by the ATLAS track reconstruction algorithms [62]

The Outside-In Method

The outside-in track resolution method is useful for identifying tracks that come from displaced vertices, such as charged particle tracks from B or Kaons that have a long enough lifetime to traverse a larger part of the detector material before decaying [61]. Displaced particle vertices can also come from electrons that form particle showers. This method begins by gathering space points starting from the TRT compatible with the Region of interest 3.5.1 defined in the EM calorimeter, and moving its way back to the interaction point to connect with track seed candidates.

Neural Network Track Reconstruction

In addition to the Inside-out and Outside-In track ambiguity solving methods described in the sections above, ATLAS uses a neural network based ambiguity solver [63] to estimate the probability that an energy cluster deposited in the calorimeters can be split into 2 energy cluster belonging to separate tracks, further improving track reconstruction.

6.0.2 Topo-Cluster Reconstruction

Topo-Clusters are topographically linked depositions of particle energies into the EM and or Hardonic calorimeters. These topo-clusters are primarily used to reconstruct, jets, hadrons, and Missing ET (E_T^{Miss}). Topo-cluster reconstruction is done via a seed-and-collect method that constructs and merges 3-dimensional energy depositions in the calorimeters based on predetermined criteria defined in [64]. Energy clusters are formed based on a "cell signal significance" defined as the ratio of the cell signal to the average expected noise for a given cell of the calorimeter.

$$\xi = \frac{E^{EM}_{cell}}{\sigma^{EM}_{Noise,cell}} \tag{6.1}$$

Calorimeter cells with the largest significance are then used as "seeds" into which surrounding cells with a smaller significance are added. In cases where the growing algorithm produces a very large cluster of energy such that there are multiple cells with $E^{EM}_{cell} > 500$ MeV, the cluster is split into sub-clusters.

Topo-Cluster Calibration

Topo-clusters must be calibrated to accurately determine their energy, and are calibrated depending on their probability of being electromagnetic or hadronic in nature. The energy of the topo-clusters is initially calculated using the EM scale, this is a scale used to accurately determine the energy deposition of electrons/positrons and photons in ATLAS but does not accurately calculate contributions from hadrons, pileup effects[1], and deposition of particle energies into dead material [64]. A dedicated calibration scheme used to account for energy depositions from these sources is called the Local Hadronic Cell Weight Calibration (LCW) scheme [65].

6.0.3 Electron Reconstruction

The reliable reconstruction of electrons is important for our analysis since one is used to define the Tau+e (9.5.2) signal region. An electron[2] is defined in this context as an object consisting of a topo-cluster matched to a track in the inner detector (3.2) [66]. Electrons are reconstructed based on topo-clusters defined within the EM calorimeter and are required to have an $E_{EM} > 400$MeV. A track is matched to a topo-cluster by requiring the following criteria, $|\Delta\eta| < 0.05$ and $-0.10 < q \times (\phi_{track} - \phi_{topoclus}) < 0.05$, where q refers to the reconstructed charge of the track. These matched topo-cluster and track pairs are then passed to a super-clustering algorithm before the final electron candidates are passed to their identification algorithm. Details on the workflow followed in the event that multiple tracks can be matched to a given topo-cluster are shown in [66].

e Identification

The electron reconstruction algorithm has no capability within it to differentiate between true, promptly created electrons in pp collisions, and other charged particles that mimic its signature. Thus an identification algorithm [67] must be used that is based on candidate particle characteristics to differentiate between true electron signal and background objects. In short, the electron identification algorithm is a likelihood fit based algorithm that allows us to select electrons with varying degrees of confidence represented by working points. The available working points for the electron ID are VeryLoose, Loose, Medium, and Tight. At present, an identification algorithm involving a Convolutional Neural Network (CNNs) is being explored to replace the current electron ID. This CNN shows an improvement in background

[1] Because in high pileup environments, the cell noise threshold $\sigma^{EM}_{Noise,cell}$ can adjust the significance threshold to be high enough so a non-negligible amount of signal is lost.

[2] Here the word electron is used to denote both electrons and positrons, as is convention

rejection from 1.7 to 5.5 times, depending on the kinematic details of the electron candidate [68].

6.0.4 Muon Reconstruction

The reliable reconstruction of muons is important for our analysis since one is used to define the Tau+μ (9.5.2) signal region. The muon is a Minimally Ionizing Particle (MIP) that has the ability to traverse the full ATLAS detector. And so, additional detector instrumentation has been developed to reconstruct muon tracks in conjunction with the Inner Detector (3.2) called the Muon Spectrometer (3.4). While muon tracks coming from the inner detector are reconstructed as described in section (6.0.1), Muon tracks are also reconstructed independently in the Muon Spectrometer by identifying straight line fits in one or multiple muon drift chambers [69][70]. These straight-line signatures are then combined via a fit of a curved path that roughly matches the track of a muon traversing a magnetic field across the muon stations. Information from the inner detector and calorimeters are then used to form muon track candidates. From here, muons can be reconstructed in 5 ways, that correspond to the sub-detectors used in their reconstruction process. These types are combined (CB), inside-out combined (IO), muon-spectrometer extrapolated (ME), segment-tagged (ST), and calorimeter-tagged (CT).

Muon reconstruction types

The different types are described shortly below, but more detail can be found in reference [70].

- **Combined** (**CB**) : Muons are identified by matching tracks in the muon spectrometer to tracks in the inner detector and performing a fit.
- **Inside − out combined**(**IO**) : Muons are reconstructed using an inside-out method similar to the one mentioned in section (6.0.1), tracks in the inner detector are extrapolated out to the muon spectrometer.
- **Muon − spectrometer extrapolated**(**ME**) : Muon tracks in the muon spectrometer cannot be matched to any tracks in the inner detector and so are extrapolated to the beam line.
- **Segment − tagged** (**ST**) : Muons are reconstructed by requiring that a track in the inner detector matches at least 1 track in the muon spectrometer with stringent matching criteria.
- **Calorimeter − tagged** (**CT**) : Muons are reconstructed by extrapolating tracks from the inner detector into the EM and Hadron calorimeters and searching for energy signatures consistent with muons.

μ Identification

Instead of a likelihood or neural network-based identification algorithm as is used in electron and tau identification, muon identification relies on certain kinematic cuts to select for high-quality muons. As is usual, muons are selected on a working point-based scheme. The selection working points are Loose, Medium, Tight, High-pT, and Low-pT and are designed to reject light hadrons or non-prompt muons

coming from the decay of bottom and charm quark decays. The Loose, Medium, and Tight, are standard and are defined to select muons with an increasing degree of confidence but come at the cost of reducing statistics. The High-pT and Low-pT working points are non-standard, so brief descriptions of the selections are below.

- **High $-$ $\mathbf{p_T}$ WP** : Created for W' and Z' searches[3], and requires that muons have a $p_t > 100$GeV and designed for the optimal rejection of poorly reconstructed tracks. Only CB and IO muons that pass the Medium WP are considered in this WP.
- **Low $-$ $\mathbf{p_T}$ WP** : Promptly created low energy muons often do not make it to the muon spectrometer and so are reconstructed by the IO method. This working point was created for analysis requiring low-energy muons for which the background from muons created by hadrons can be large.

6.0.5 Tau Reconstruction

Hadronically decaying taus are very important to this analysis, as they are the main decay product of the charged Higgs. There are many aspects to the reconstruction of tau jets, including their jet reconstruction method, vertex association, track classification process, and energy calibration. The following section describes briefly each part of the tau reconstruction process. Because tuning the tau identification algorithm was a major part of my thesis work, it is described in detail in chapter (7).

Tau Jet Reconstruction

Hadronically decaying taus manifest as jets, and so are reconstructed using the Anti-k_t algorithm (6.0.7) with a jet width of $R = 0.4$ [71]. Because taus decay to final states including neutrinos, it should be noted that only the visible portion of the tau decay products is used to perform reconstruction. Topo-clusters associated with the jet are reconstructed as in section (6.0.2) and calibrated using Local hadronic calibration (LC). Tau jets are later re-calibrated using the Tau Energy Scale (TES) as described in (6.0.5). Tau jet candidates must also have a $p_t > 5$ GeV and $|\eta| < 2.5$.

The Tau Jet Vertexing Algorithm (TJVA) algorithm

Because taus have a decay length of $c\tau = 87.03\mu m$ [72] there can be a discrepancy between the observed vertex and the true primary vertex the tau is associated with. The TauWG corrects for this discrepancy using a Tau Jet Vertex Association algorithm (TJVA) [73],[74] to identify the primary vertex of the tau decay. In short, after primary vertex candidates are created, this algorithm gathers all tracks associated with the tau candidate that lies within a cone of $\Delta R < 0.2$ and have a $p_t > 1$GeV, and selects the primary vertex candidate that has the largest $\Sigma p_t^{track\ i}$ to be the primary vertex of the tau. After defining a new vertex, the impact parameters and track characteristics, and topo-cluster associated with the tau are re-calculated with respect to the new primary vertex.

[3]These are additional hypothetical W and Z like bosons that come about by requiring the SM Lagrangian obey an additional SU(2) gauge symmetry.

Tau Track Classification

As shown by figure 8.3 hadronically decaying taus have a multitude of decay modes, each with a different number of charged and neutral pions in the decay. In order to better resolve the sub-structure of the tau jet the TauWG has created a tau track classifier. The ability to resolve the decay products of the tau and determine its decay modes was central to my qualification task shown in (8.2). The Tau Track Classifier is an RNN-based multi-class classification algorithm that is able to separate tau tracks into the following 4 types [71].

- Tau Tracks (TT): These are tracks originating from pions in the τ decay cone. These tracks are used to determine the net charge as well as to determine the number of charged pions in the decay that define its "prong-ness".
- Conversion Tracks (CT): These are tracks from electrons and positrons that are pair produced by photons in the detector.
- Isolation Tracks (IT): Tracks that likely originate from quark or gluon jets.
- Fake Tracks (FT): Tracks that are likely mis-reconstructed and or come from pile-up interactions.

Tau Jet Calibration

By default, tau jets are calibrated at the LC scale, but additional corrections to the Tau jet must be taken into account to obtain an accurate measurement of the tau energy. The LC calibration scheme for the tau does not account for some of its decay products not reaching the calorimeters, corrections from pile-up[4], and contributions from the underlying event, or from energy deposited outside of the reconstructed clusters [73]. The calibration of the tau energy to account for these effects is called the Tau Energy Scale calibration scheme or (TES). Energy corrections for the tau are applied dependent on the number of charged pions in the decay and the η coordinate of the tau candidate, and so takes place for 1 and 3 prong taus separately. The calibration process is described in detail in [73], [75].

τ Identification

Tuning the tau identification algorithm was a major part of my thesis work, and so is described in detail in chapter (7). A quick look at the specifics of the algorithm is here (7.1).

6.0.6 MET (E_T^{Miss}) Reconstruction

Because the initial transverse momentum of the protons that produce final state objects is very near 0, the vector sum of the individual components of these final state objects should also sum to 0[5]. Objects that do not interact with the ATLAS detector such as neutrinos or even dark matter, will not deposit their energy into its sub-detectors. This leads to an imbalance of initial and final state transverse momentum. This excess quantity is what we define as E_T^{miss} or MET.

[4] Signal from other pp collisions from either inside or outside the same bunch crossing
[5] This is due to simple momentum conservation.

E_T^{miss} is calculated by summing the p_t of each reconstructed object known as hard terms, as well as the p_t not associated with any reconstructed object called soft terms [76].

$$\Sigma E_T^{miss} = \Sigma p_t^{\mu} + \Sigma p_t^{e} + \Sigma p_t^{\gamma} + \Sigma p_t^{\tau} + \Sigma p_t^{Jets} + \Sigma p_t^{soft} \tag{6.2}$$

As described in section (9.2.7) MET in this analysis is calculated using the MET Maker tool.

6.0.7 Jet Reconstruction

Jets are a set of reconstructed particle objects whose momentum vectors lie within a cone structure [77]. This multi-particle object is created via quark confinement after the hard scatter of the partons in the pp collision. Quark confinement is an emergent feature of the strong force (4.3) because its strength increases along with the separation distance of any two quarks. In particle decays such as hadronic W decays ($W \rightarrow q\overline{q}$), where quarks are created with their component momenta in opposite directions, the energy between $q\overline{q}$ pairs forces hadrons out of the vacuum that are boosted into a cone-like structure in the direction of the original quarks. Jets in this analysis are reconstructed using the Anti-k_t algorithm [78] described below, and calibrated using the Jet Energy Scale (JES) detailed in [79].

The Anti-k_t Clustering Algorithm

The Anti-k_t clustering algorithm is named after the transverse particle momentum defined as $k_t = p_t$ used to characterize it. We begin with a list of track and topo-cluster 4 momenta called proto-jets, on which the clustering will take place [80].

Each proto-jet or pair of proto-jets is given a value that represents it's distance relative to the beam-line (d_{iB}) or each other (d_{ij}). These values are then placed into 2 independent arrays.

$$d_{iB} = \frac{1}{p_{ti}^2} \tag{6.3}$$

$$d_{ij} = min(\frac{1}{p_{ti}^2}, \frac{1}{p_{tj}^2})\frac{(y_i^2 - y_j^2)^2 + (\phi_i^2 - \phi_j^2)^2}{R^2} \tag{6.4}$$

In the equations above, p_{ti}, y_i, and ϕ_i are the transverse momentum, rapidity, and azimuth of object i respectively. R is a parameter analogous to the cone size parameter in the cone algorithm [77]. Using these two arrays, we find the smallest entry in the concatenation of both arrays and label it d_{min}. If d_{min} is an entry in d_{ij}, the i and j proto-jets are merged, and the algorithm resets. If d_{min} is an entry in d_{iB} then it is considered an independent jet entity and is removed from the list of proto-jets to consider for merging. This process continues until all proto-jets are merged to form independent jet objects.

6.0.8 b-Jet Reconstruction

As discussed in (6.0.7) quarks are can never exist in isolation due to properties of the strong force, so when b quarks are created, they hadronize into particles containing

a b-quark. Similar to the τ, b-quarks have a relatively long lifetime, and as such hadronize into particles that retain the long-lived property of the b. This causes the resulting jet, now referred to as a b-jet, to form a notable distance away from the primary vertex of the interaction called a "displaced vertex".

b-jet reconstruction begins at the trigger level, where a loose requirement on E_T dictated by the trigger menu is imposed by the L1 trigger (3.5.1). Candidates passing the selection criteria are then passed to the HL trigger (3.5.2) for further processing [81]. b-jet candidates are reconstructed as usual by the Anti-k_t algorithm [78], and their topo-clusters are reconstructed as described in section (6.0.2) [64].

b Identification

Before being passed to offline b-jet identification algorithms, bjet candidates must pass a pre-discrimination process at the trigger level [82]. If the b candidate passes these selection criteria, the output of these lower-level algorithms is then passed as input to the higher-level algorithms used for b identification. To properly select jets created from b-hadrons the b-tagging group [83] recommends the use of a Recurrent neural network b-tagger called the DL1r [84], which has been optimized to discriminate between b-jets, c-jets, light-jets[6], and τ-jets. The working point selection efficiencies for this algorithm do not have a naming scheme but are defined as 60%, 70%, 77%, and 85% selection working points.

[6]Here light jets are jets originating from u or d quarks.

Chapter 7

The Tau Identification Algorithm

The tau is often the decay product of theoretical particles such as those in 2HDMs ($H/h, A, H^{\pm}$), which if found will be direct evidence of physics beyond the Standard Model. Because Higgs bosons tend to couple strongly to heavy particles[1], taus represent a significant gateway into beyond standard model physics, and so our ability to accurately detect them is extremely important. Beginning in 2019, the ATLAS Tau Working Group has transitioned away from using Boosted Decision Trees (BDTs) to identify tau jets, and towards the use of more sophisticated algorithms such as RNNs [86]. At present, the TauWG uses 3 specialized Recurrent Neural Networks (RNNs) to identify hadronically decaying taus with 1, 2[2] or 3-prong signatures. This chapter serves to explain the work I did to re-tune the RNN with reprocessed Monte Carlo (MC) simulated data which culminated in an ATLAS PUB note [71] and describe the 2 prong TauID that I developed as part of my qualification task. After a summary of the network specifications in (7.1), I describe the RNN architecture in detail in section (7.2.1), the training data and object selection criteria in section (7.2.3), the network training variables in section (7.2.7), the final network performances in (7.2.10) and the 2 prong TauID in section (7.3).

7.1 The Tau ID: A Summary

The current tau identification algorithm is a set of 3 RNNs optimized to distinguish between Tau and quark/gluon-initiated jets with 1, 2, or 3 reconstructed prongs. These networks were trained with Keras [87] as a front end and Tensorflow [88] as a back end.

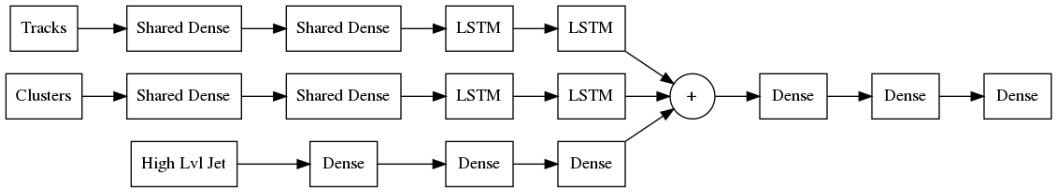

Figure 7.1: The RNN architecture used in the tau identification algorithms.

[1] The tau (τ) is the heaviest lepton in the standard model at a mass of 1.777 GeV [85]
[2] 2-prong jets are the result of incorrectly reconstructed 1-prong or 3-prong jets

These networks were trained using a supervised training method where true tau objects were given a classification label of 1, and QCD jets were given a label of 0. Training for these networks was performed by minimizing the binary cross-entropy function shown by equation 7.1 through gradient descent. In equation 7.1, y represents the true class value, and $\hat{y}$ is the RNN output score for the classified object.

$$\mathcal{L}_{\mathcal{BCE}} = -(y \log(\hat{y}) + (1 - y) \log(1 - \hat{y})) \tag{7.1}$$

The networks are trained for 100 epochs or until the loss function fails to improve after 10 epochs, whichever comes first. A Relu activation function is used between all hidden layers in figure 7.1 except the output layer. In the output layer, a sigmoid function is used in order for the network to return a classification likelihood of the object, near 0 for background-like (QCD jet) objects and near 1 for signal-like (τ jet) objects.

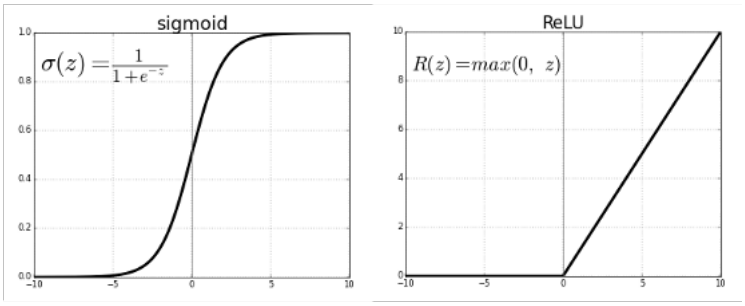

Figure 7.2: The Relu and sigmoid activation functions [89]

Due to computational limitations, the signal datasets are much smaller than the background datasets, in order to correct for this, class weights are given to each object class according to their p_t distributions multiplied by a beam spot weight detailed in (7.2.8). The training variables for each network are shown in (7.2.7) but in general, differ slightly depending on the prong number. All networks use track and cluster characteristics as well as high-level variables associated with the jet object.

7.2 The Tau ID: An In-Depth Look

During my time as a Ph.D. student, I worked extensively on the development of the tau identification algorithm. Disregarding my qualification task which gets its own section in another chapter (8.2.2), my contributions to the development of the TauID are, re-tuning the RNN algorithms by using reprocessed MC data and including new training variables, upgrading the code-base to allow for GPU[3] training, implementing and deploying new algorithms like Deepset/Particle Flow Neural Networks [90][91] (8), developing a code base to assess the impact of individual training variables on background rejection [92], parallelizing the hdf5 data creation process, and beginning the implementation of uproot [93] to the TauID workflow to shorten the data conversion pipeline. I feel I have helped to lay a strong foundation for the

[3]Graphics Processing Unit

development of future TauID algorithms via a heavily documented and easy-to-use code base and provided a tutorial for future users to draw from.

I have performed many intermediate trainings of the TauID in attempts to improve background rejection, but in this section, I describe the currently deployed TauIDs that I trained and that are mentioned in this ATLAS PUB note [71]. My work on re-tuning the TauIDs currently in use began in 2021 when the entirety of the Run 2 dataset was reprocessed to allow for better measurements with improved physics reconstruction algorithms. In order to maintain the performance of the TauID, it needed to be retrained on MC simulated data that was reconstructed using the same data reconstruction chain. Because of my experience with the TauID given my qualification task and other TauID re-tunings, I was recruited to re-tune the algorithm using reprocessed MC data created with improved tools.

7.2.1 The TauID Network Architecture (RNN)

As discussed in section (7.1), the TauID is a Recurrent Neural Network (RNN) (7.1). This network has 3 input branches that process individual Track and Cluster information, as well as High-level jet information[4]. RNNs were first developed for situations that involve processing an ordered sequence of data and are characterized by the Long Short Term Memory (LSTM) layer [94]. LSTM layers are able to retain the context of related objects and produce an output. Because the multiple tracks and topo-clusters associated with a jet can be represented as a sequence of data (7.2.9a), an RNN is a natural choice for a jet classification algorithm. But RNNs requires that we have a predetermined order in which we pass the tracks and clusters, which in theory could affect its performance.

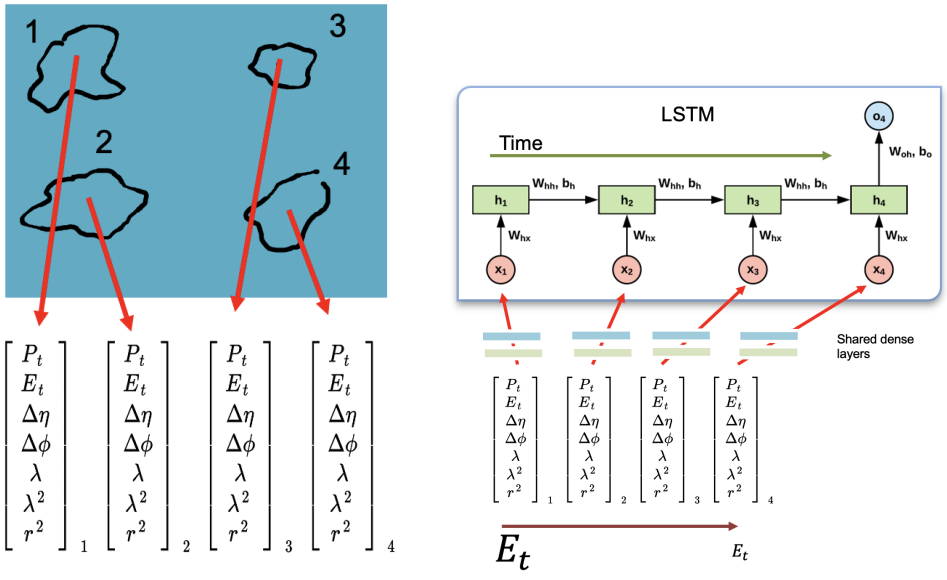

(a) (b)

Figure 7.3: (a) Reconstructed topo-clusters encoded into a sequence of arrays compatible with an RNN. (b) E_t ordered topo-clusters passed to an LSTM layer [95]

[4]These are defined as properties of the jet as a whole, these include variables like jet p_t, η, ϕ, etc.

Because there is no seemly significant physical reason to feed the track and cluster information to the networks in any particular order, the information is passed to the networks in the arbitrary order of decreasing transverse momentum P_t for tracks, and transverse energy E_t for topo-clusters. The shared dense layers in the network architecture also require that the length of the sequence passed to it be constant i.e. the number of jets and tracks to be processed is fixed. The RNN retains a maximum of 10 tracks and 6 topo-clusters, although it is capable of processing much more at any given time. In cases where a jet contains less than 10 tracks and 6 tracks and clusters, the network is passed "zero-padded" arrays, where the input vector has a value of 0 for each entry. Studies I performed on the dependence of the network's performance based on the number of tracks and clusters retained showed no meaningful difference in background rejection. Because the requirement that tracks and clusters be passed in a particular order does not have significance in a physics context, the TauWG has been in search of a network algorithm that is order agnostic. In my work in developing the TauID, I explored such an order agnostic network called a Deepset/Particle Flow Neural Network detailed in chapter (8).

7.2.2 Tau ID Training Environments

The computing resources used to train and evaluate these networks were NVidia GTX 1080 Ti GPUs located in the now-decommissioned Maverick-2 GPU cluster in the Texas Advanced Computing Center (TACC) at The University of Texas at Austin. The git repo containing the code based I developed to train the TauID is found here under the TauID_R22 branch, a full list of the packages used to train the R22 TauIDs can be found here.

7.2.3 Monte Carlo Training and Evaluation Samples

The signal and background xAOD data sets that I used to train and evaluate the TauID were produced via Monte Carlo simulation at an energy of 13TeV (mc20_13TeV). This data set represents reprocessed data containing true tau signal produced via $\gamma^* \rightarrow \tau\tau$ and QCD Di-jet[5] sample. The QCD background data was produced in p_t slices ranging from 15GeV to 3TeV.

7.2.4 Creation of the HDF5 datasets

The datasets mentioned in section (7.2.3) are in xAOD format, which is a .root file format with a tree structure that contains jet class objects. To train the networks, we must create a dataset in a format compatible with the Keras Neural Network API, which contains only the desired characteristics of the jets we would like to use for training. To do this the xAODs underwent a process called n-tuple flattening done by the THOR (Tau Harmonization and Optimization Resources) framework. After flattening, jet characteristics are stored in 1-dimensional arrays where they undergo the final selection cuts defined in (7.2.5) and converted to NumPy [96] objects stored in the HDF5[6] file format [97].

[5]Di-jets are simply events that result in 2 jets.
[6]Hierarchical Data Format 5

7.2.5 Signal and Background Selection Definitions

The selection criteria on jet objects is primarily on their reconstructed prong number to allow for separate training of TauID algorithms (1p, 2p, 3p). Additional selection criteria on the p_t and η of the jet objects are very similar to the original object selection of the RNN that was originally deployed [86], but notably I retrained the networks using the requirement that true taus have a truthParticleType=10. This selection removes non-isolated taus from heavy flavor hadron decays from our dataset, which were previously considered as good true taus. An additional change is that 1p, 2p, and 3p reconstructed jets have pt caps of $3.2TeV$, $3.0TeV$, and $2.6TeV$ respectively. This upper limit on the jet p_t ensures that signal and background samples have large enough statistics over the same pt spectrum to allow for proper class re-weighting as defined in section (7.2.8). The selections for the 1, 2, and 3 prong datasets are shown below.

1p Network	True τ signal	Di-Jet QCD background
p_t^{Reco}	$20GeV < p_t < 3.2TeV$	$20GeV < p_t < 3.2TeV$
truthParticleType	10	-
$\lvert\eta_{Reco}\rvert$	$< 2.5^*$	$< 2.5^*$
n_{prong}^{Reco}	1	1
Truth Prong	1	-
Truth Matched	$\lvert\eta\rvert, p_t$	-

2p Network	True τ signal	Di-Jet QCD background
p_t^{Reco}	$20GeV < p_t < 3.0TeV$	$20GeV < p_t < 3.0TeV$
truthParticleType	10	-
$\lvert\eta_{Reco}\rvert$	$< 2.5^*$	$< 2.5^*$
n_{prong}^{Reco}	2	2
Truth Prong	1 or 3	-
Truth Matched	$\lvert\eta\rvert, p_t$	-

3p Network	True τ signal	Di-Jet QCD background
p_t^{Reco}	$20GeV < p_t < 2.6TeV$	$20GeV < p_t < 2.6TeV$
truthParticleType	10	-
$\lvert\eta_{Reco}\rvert$	$< 2.5^*$	$< 2.5^*$
n_{prong}^{Reco}	3	3
Truth Prong	3	-
Truth Matched	$\lvert\eta\rvert, p_t$	-

Table 7.1: Selection criteria for signal and background jets used to train the 1, 2, and 3 prong RNN TauIDs. $^*\eta$ selection excludes the poorly instrumented crack region $1.37 < |\eta| < 1.57$

7.2.6 Training and Testing Sets

During the conversion from flattened N-tuples to HDF5s, the 1p, 2p, and 3p signal and background datasets were split further using a 50/50 ratio to create training and testing sets. These training and testing sets were created using a cut on their MC event number.

TRAIN_SEL="TauJets.mcEventNumber % 2 == 0"
TEST_SEL="TauJets.mcEventNumber % 2 == 1"

All jets with an even MC event number were placed into the training data set, and all jets with an odd MC event number were placed into a testing data set. The naming scheme of the HDF5 files used for training is shown below.

sig1P_test_%d.h5, bkg1P_test_%d.h5
sig1P_train_%d.h5, bkg1P_train_%d.h5

These HDF5 files were created using a "family driver", where multiple files with a maximum of 8GB are grouped to form a single dataset. The %d is used to indicate the index of the file in the family of files. At run time, TensorFlow uses 10% of the training set to validate the performance of the network as training is ongoing. Below is a table of the size of the training and testing datasets, where 1GB is approximately equal to 1 Million Jets.

Training Set			Test Set		
Network	Signal	Background	Network	Signal	Background
1p	5.2 GB	11.1 GB	1p	5.2 GB	11.1 GB
2p	.469 GB	13.9 GB	2p	.469 GB	13.9 GB
3p	1.4 GB	16.5 GB	3p	1.4 GB	16.5 GB

Table 7.2: Relative sizes of the datasets used to train the RNN TauIDs in GigaBytes (GB).

7.2.7 RNN TauID Input Variables

The tau identification networks use a range of high and low-level variables to classify jets. Low-level variables include track and cluster information from the associated jets such as the angular separation of the tracks from the center of the jet cone $d\eta, d\phi$ and the second moments of the radial and longitudinal distance of a cluster from the cluster center $r^2_{cluster}$ and $\lambda^2_{cluster}$. A full list of the variables used to train the 1p, 2p, and 3p networks are below. Notably, I performed the network training with additional variables deriving from a re-tuned Tau Jet Vertex Association algorithm (6.0.5) and created the documentation necessary to add new variables. The following new variables were added to the network with respect to the previous training, z0sinthetaTJVA, z0sinthetaSigTJVA, d0TJVA, d0SigTJVA, and pt_tau_log for both the track and cluster variable array. Which are re-tuned transverse z_0 and longitudinal d_0 impact parameters. A thorough description of the variables used to train the TauID can be found in appendix A.5.

Table 7.3: Training variables used for the 1p 2p and 3p networks.

Variable	1 prong	2 prong	3 prong
Jet Variables			
TauJets/centFrac	•	•	•
TauJets/etOverPtLeadTrk	•	•	•
TauJets/dRmax	•	•	•
TauJets/SumPtTrkFrac	•	•	•
TauJets/EMPOverTrkSysP	•	•	•
TauJets/ptRatioEflowApprox	•	•	•
TauJets/mEflowApprox	•	•	•
TauJets/pt_tau_log	•	•	•
TauJets/massTrkSys		•	•
TauJets/trFlightPathSig		•	•
Track Variables			
TauTracks/pt_log	•	•	•
TauTracks/pt_tau_log	•	•	•
TauTracks/dEta	•	•	•
TauTracks/dPhi	•	•	•
TauTracks/nInnermostPixelHits	•	•	•
TauTracks/nPixelHits	•	•	•
TauTracks/nSCTHits	•	•	•
TauTracks/z0sinthetaTJVA	•	•	•
TauTracks/z0sinthetaSigTJVA	•	•	•
TauTracks/d0TJVA	•	•	•
TauTracks/d0SigTJVA	•	•	•
Cluster Variables			
TauClusters/et_log	•	•	•
TauClusters/pt_tau_log	•	•	•
TauClusters/dEta	•	•	•
TauClusters/dPhi	•	•	•
TauClusters/SECOND_R	•	•	•
TauClusters/SECOND_LAMBDA	•	•	•
TauClusters/CENTER_LAMBDA	•	•	•

7.2.8 Re-weighting procedure

Jets are given a classification weight according to their p_t to reduce the bias that might arise from uneven statistics in signal and background datasets. Bins are obtained using 2 percentile slices[7] of the p_t distribution for background jets. The signal p_T distribution is binned using the resulting bin array. The ratio of Signal/Background distributions is taken. Weights are applied to individual background jets at training time according to the pt bin they fall into. Each signal jet is given a weight of 1. Each individual jet weight is also multiplied by the BeamSpotWeight to account for the difference in the beam spot width in data and simulated samples, although this has very little effect on performance.

$$Bkg\ p_t\ weight = \frac{S_i}{B_i} \times beamSpotWeight \tag{7.2}$$

$$Sig\ p_t\ weight = 1 \times beamSpotWeight \tag{7.3}$$

Here the index i is used to indicate the bin index of the $\frac{S_i}{B_i}$ histogram corresponding to the jet's p_t.

7.2.9 Score Flattening

Once the Tau ID networks were trained, I evaluated them on a test data set that contained $O(10^6)$ jets. In the evaluation process, jets are given a score from 0 to 1 to indicate their probability of being signal (τ) or background (QCD) jets. A score near 1 indicates a signal-like jet and a score near 0 indicates a background-like jet. These scores are called the raw scores.

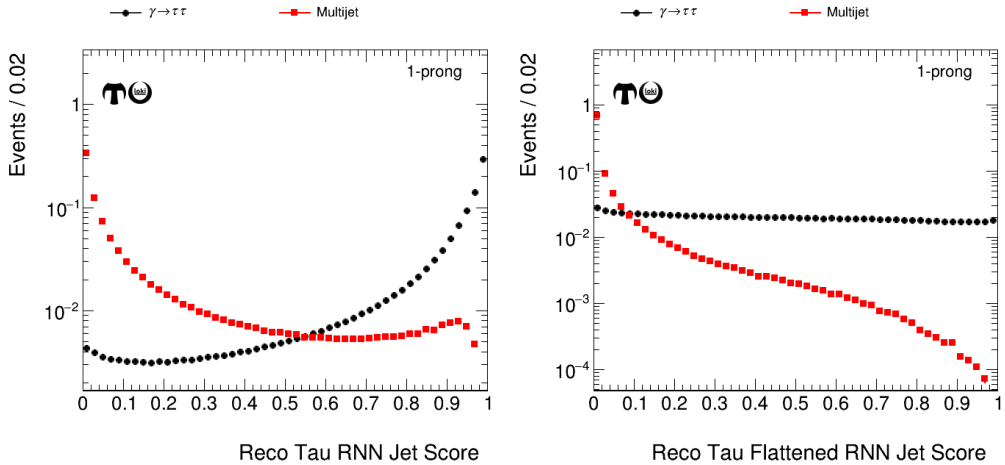

(a) (b)

Figure 7.4: (a) Example of raw output scores for 1 prong τ-jets given by the RNN TauID (b) Flattened scores for 1 prong τ-jets given by the RNN TauID

In order to obtain an unbiased sample of taus with respect to p_t and μ[8] for any given working point, the raw scores are transformed to be uniform across its range

[7] In the end, an array of 50 bins is obtained

[8] The value μ in this context is used to describe the number of pp collisions in the bunch crossing where this τ jet was produced.

from 0 to 1 in a process called score flattening. Score flattening is a process done by LOKI in which each jet score is transformed such that there are roughly the same number of jets per bin with an even p_t and μ spectrum. With a flat score distribution, we are able to choose a RNN score thresholds, at 95%, 85%, 75%, 60% or 45% of true reconstructed taus for a given signal sample. These selection efficiencies correspond to the **Tight, Medium, Loose** and **VeryLoose** selection working points for the TauID depending on the reconstructed prong number.

7.2.10 Tau Identification Performance

The plot below shows the rejection of fake tau candidates in the 1 and 3p networks. The results for the 2-prong network were not put into the public note as analysis groups focus mainly on the selection of correctly reconstructed 1 and 3-prong tau objects. A performance of the 2p Tau Identification (TauID) trained over a different dataset can be seen in section (8.3.2).

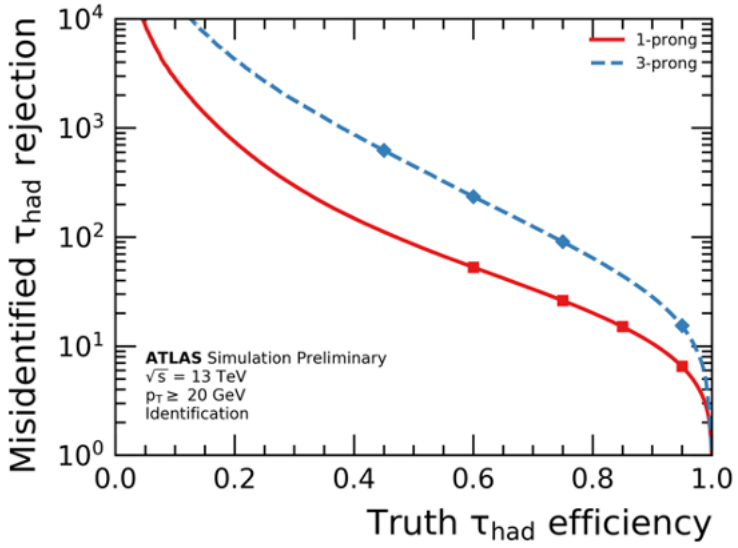

Figure 7.5: Background rejection vs signal efficiency for 1p , 3p TauIDs when evaluating jets with a $p_t >$ 20GeV, and trained on reprocessed Run2 samples

Working Point	.60	.75	.85	.95
1p Rejection	53.01	26.18	15.13	6.55

Working Point	.45	.60	.75	.95
3p Rejection	622.69	235.33	90.81	15.46

Table 7.4: Background rejection for VeryLoose, Loose, Medium, Tight and Very Tight working points for the 1p, 3p networks when evaluating jets with a $p_t >$ 20GeV, and trained on reprocessed Run2 samples

7.3 The 2p TauID

As part of my Qualification Task, I created and developed a 2 prong-specific TauID, that can reject fake tau candidates among jets with a mis-reconstructed prong number. Tau Jets mis-reconstructed to have 2 prongs represent a non-negligible amount of jets in MC simulated data, sometimes up to 27% for 3p taus as shown in figure (7.7). In the reconstruction process, 1p taus can have conversion tracks from electrons in its neutral pion decay reconstructed as a track belonging to a charged pion. In the 3-prong case, one of the 3 tracks in the jet can occupy the same space in the tracker and be disguised as a single track. And so, the figure (7.7) demonstrates a clear need to develop a specialized neural network to properly differentiate 2p jets as either signal or background. Before my qualification task, mis-reconstructed 2-prong objects were classified using the 3-prong TauID. I trained a 2p network that was able to show a significant increase in background rejection throughout the entire range of signal efficiency when compared to the 3-prong Inclusive Network.

7.3.1 2p Network Results RNN

The results of the specialized 2p RNN network trained for my qualification task are shown below. From this plot, we can see an improvement of a factor of up to about 2.5x in the region of signal efficiency used to define working points (.45, .60, .75, .95). This 2-prong network has since become a standard network used by the TauWG to classify mis-reconstructed tau jets.

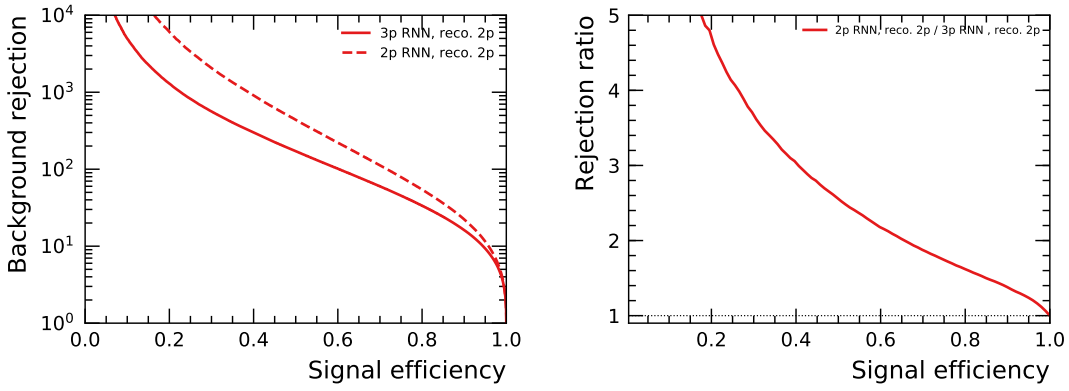

(a) (b)

Figure 7.6: (a) A comparison in the background rejection of 2-prong reconstructed taus when evaluated using a specialized 2p network and the default 3-prong TauID (b) The ratio of the rejection curves shown in (a).

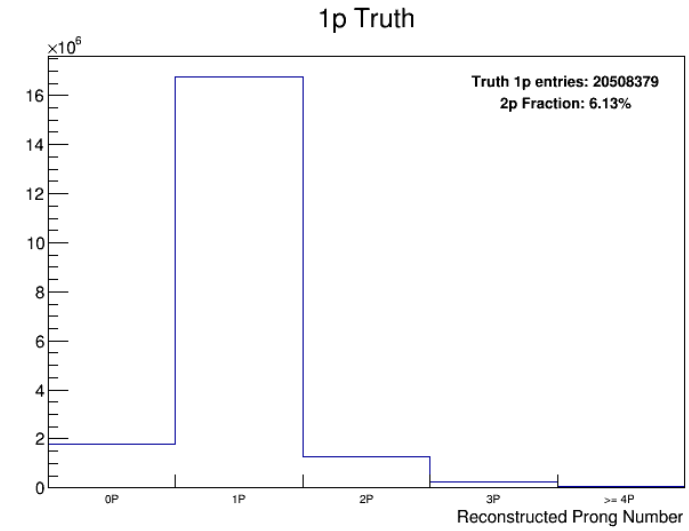

(a)

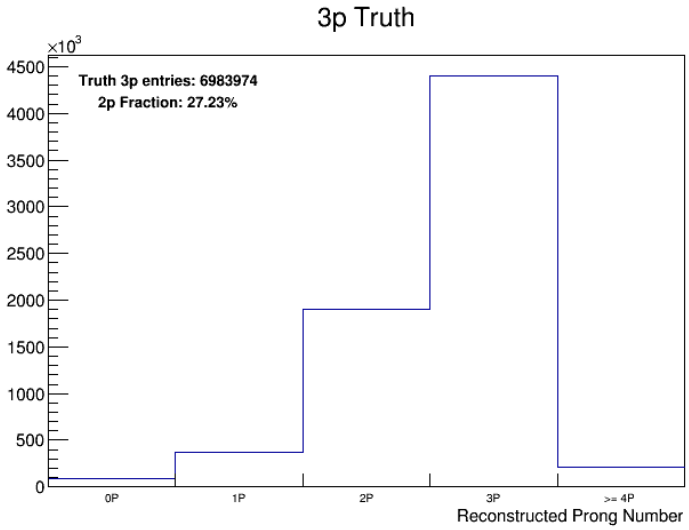

(b)

Figure 7.7: Distribution of the reconstructed prong number for (a) true 1 prong and (b) true 3 prong tau candidates created with $\gamma^* \to \tau\tau$ MC simulated data.

Chapter 8

The Deepset TauIDs And Other Experimental Networks

The RNN based TauID algorithm described in chapter 7 requires that we pass it track and cluster information in some predetermined order, which does not have meaning in a physics context. For this reason, the Tau Working Group (TauWG) has been in search of a network algorithm that is order agnostic. In my work in developing the TauID, I explored such an order agnostic network for use in the TauID referred to as a Deepset/Particle Flow Neural Network [90][91], and experimented with network architectures that included input from the Tau Track Classifier (6.0.5). In short, I found that Deepset based neural networks have the ability to retain similar performance to RNN based networks but take far less time to train (8.5). Tau Identification networks that make use of track classification variables also seem to perform much better than those that do not use them (8.3.2), although this is still the subject of study among members of the TauWG. In this chapter, I describe my contributions to ATLAS via the development of a Deepset based TauID with RNN Track Classification variables, and decay mode specific TauIDs with both Deepset and RNN based architectures. After an introduction to the Deepset architecture in section (8.1), I show the results of decay mode specific TauIDs I trained during my qualification task in section (8.2.4), and show a comparison of their performance when using Deepset vs RNN based architectures in section (8.2.5), finally in section (8.3.2) I show the performance of a Deepset based TauID with additional track information.

8.1 The Deepset Architecture

Particle Flow Networks [91] here referred to as Deepset Networks, are characterized by a SumLayer which applies a sum operation to the sequence of latent track and cluster arrays passed to it, converting them to a single 1-D array that is then processed by additional dense layers. Figure (8.1) demonstrates the sum operation applied to latent vectors of cluster information. These sum layers remove the condition of an ordered set of inputs required by an RNN.

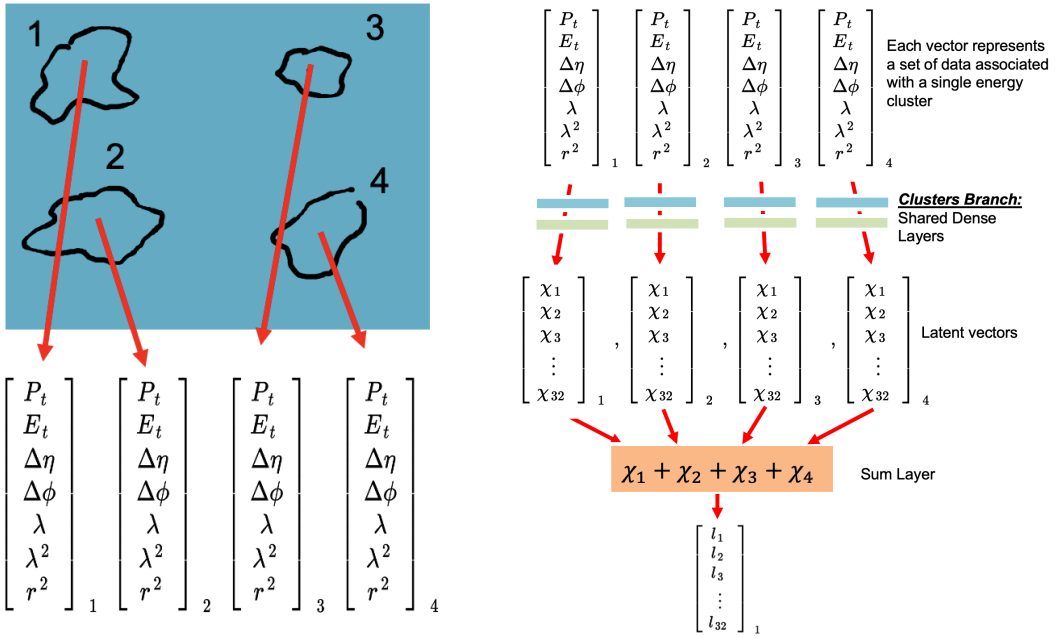

(a) (b)

Figure 8.1: (a) Reconstructed topo-clusters encoded into a sequence of arrays. (b) A sequence of arrays relating to topo-cluster information being acted upon by a SumLayer, effectively circumventing the order dependence of an RNN (7.2.9).

Because Deepset based networks can handle track and cluster information in an order agnostic fashion and could potentially perform similarly to an RNN, Deepset based architectures (8.2) are thought to be better physically motivated than RNNs (7.1). In my work, I found that Deepset based TauIDs can perform similarly to RNNs with the surprising benefit of a reduction in training time (8.2). The change I made to the original RNN architecture (7.1) to convert it to a Deepset based network was to replace the pair of LSTM[1] layers in the RNN with a SumLayer followed by two dense layers. The elimination of the LSTM layers significantly reduces the number of trainable parameters in the network, and leads to a reduction in the training time.

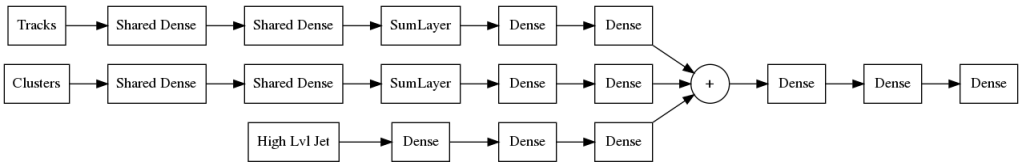

Figure 8.2: Deepset Tau Identification Architecture

8.2 Decay Mode Neural Nets

To become an ATLAS-qualified author I developed and tested decay mode specific tau identification algorithms to understand the possible benefits and drawbacks of using them over the inclusive prong-based networks detailed in section (7.1). In

[1]Long Short Term Memory

my studies, I tested both RNN and Deepset based neural networks and found that Deepset based TauIDs can perform similarly to RNNs while requiring much less time to train. This section serves to display the RNN-based results of my qualification task as a route to highlight my findings concerning the Deepset based TauIDs. A more detailed description of the studies I performed for my qualification task is shown in this ATLAS Internal Note [92].

8.2.1 Decay Mode Network Architectures

The RNN and Deepset based network architectures used to produce these results are the same as the ones displayed in section (7.1) and (8.1) of this thesis.

8.2.2 Tau Decay Modes And My Qualification Task

It is well known that tau's decay hadronically approximately 65% of the time [85]. These hadronic decays have a range of distinct signatures based on the number of charged ($\pi^{\pm}$) as well as neutral pions (π^0) in their decay. These distinct signatures are known as decay modes.

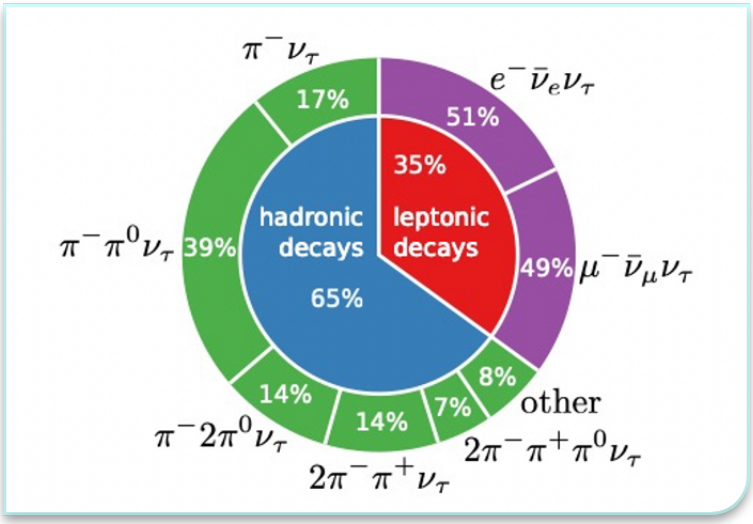

Figure 8.3: Hadronic and Leptonic Decay modes of the Tau [98]

In my qualification task, I explored whether decay mode specific tau identification algorithms for the following decay modes [2]: 1p0n, 1p1n 1pXn, 3p0n and 3pXn would improve background rejection when compared to their 1p and 3p "inclusive" network counterparts.

8.2.3 Decay Mode Net Training and Testing data sets

The data I used to train the decay mode and inclusive networks in this section was created in 2016 via pp collisions at a center of mass energy of 13TeV. The signal dataset was created via the process $\gamma^* \rightarrow \tau\overline{\tau}$ and the background jets were QCD-jets created in a Di-Jet process. These data sets were then prepared using the Tau

[2]Here 'p 'indicates the number of charged pions and 'n' indicates the number of neutral pions

Harmonization and Optimization Resources (THOR) framework, split according to their prong number or decay modes, and converted to HDF5 [97] to allow the datasets to interface with Keras in the same way as described in (7.2.4) but with different selection cuts on the jet objects to select jets belonging to a specific decay mode. See [92] for more details.

Network	Signal	Background	Network	Signal	Background
1p	3.6 GB	6.3 GB	3p	1.7 GB	11.2 GB
1p0n	830 MB	1.2 GB	3p0n	696 MB	5.3 GB
1p1n	2.2 GB	3.9 GB	3pXn	321MB	5.9 GB
1pXn	685 MB	1.4 GB	2p	653 MB	10.4 GB

Table 8.1: Relative sizes of training datasets in GigaBytes (GB) used to train the Decay mode specific and Inclusive data networks.

8.2.4 Inclusive vs Decay mode Networks

The performance comparisons between the RNN Decay Mode and RNN Inclusive Networks using raw jet scores are shown below.

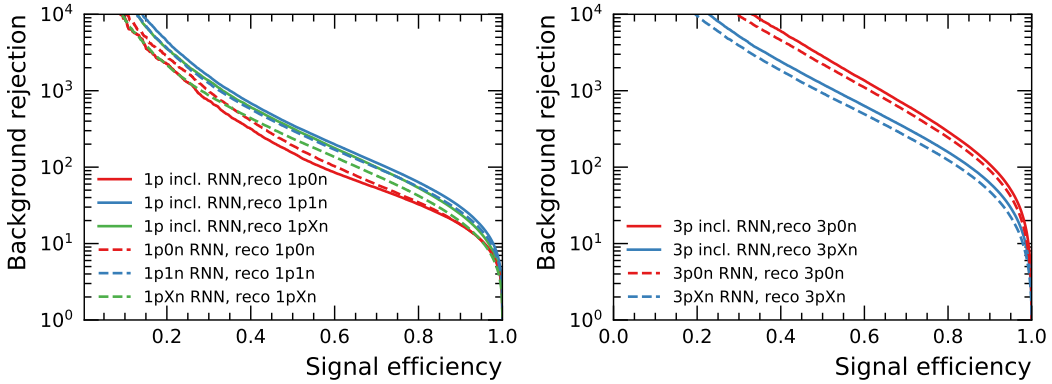

(a) (b)

Figure 8.4: A comparison of background rejection for (a) 1-prong and (b) 3-prong RNN Decay Mode vs Inclusive Networks when evaluating the same respective decay mode test datasets. Here "reco." indicates that the objects in the dataset were reconstructed with the corresponding decay mode.

In general, the Decay Mode Networks indicated by dashed lines, performed slightly worse than the Inclusive Networks, indicated by solid lines, when evaluating the same Decay Mode data set. In the 1-prong case, only the 1p0n net performed slightly better than the Inclusive Network. In the 3-prong case, none of the Decay Mode Networks performed better than the 3-prong inclusive nets.

8.2.5 RNN vs. Deepset, a pleasant surprise

Although Decay mode-specific TauIDs did not perform as expected, In my study I found that Deepest based TauIDs are able to retain similar performance when

compared to an RNN but with a drastically reduced training time. The number of hours needed to train these networks was reduced anywhere from 9 to 13 times. Given that the amount of time needed to train a network represents a significant bottleneck in testing neural networks for future use, the reduction in training time is notable. The performance of RNN Decay mode networks vs the Deepset Decay mode networks using raw scores is shown below. These networks were trained using a single node with 16 CPU processors, on an ATLAS Tier3 computing cluster located at The University of Texas at Arlington (UTA).

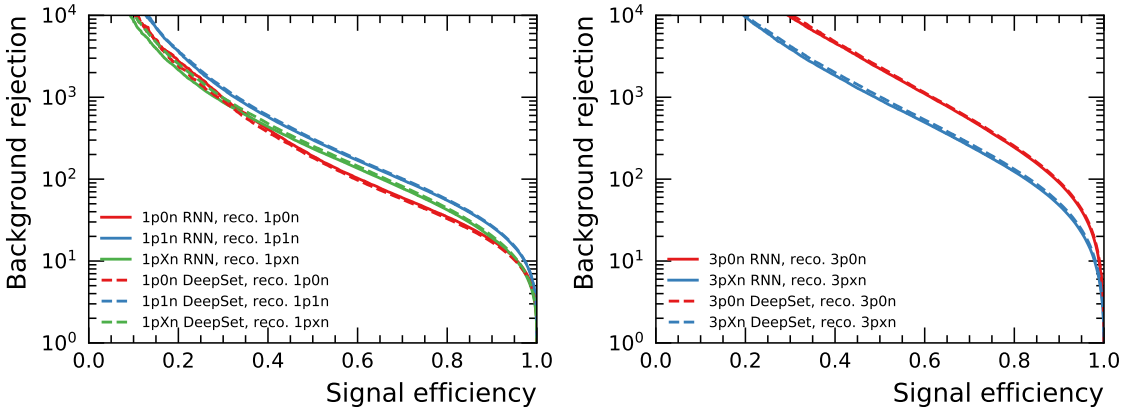

(a) (b)

Figure 8.5: A comparison in the background rejection of 1-prong (a) and 3-prong (b) decay mode neural networks evaluating their respective decay mode testing sets

Configuration	RNN	Deepset	Reduction Factor
1p0n	11.95 hrs	0.88 hrs	$\sim$ 13.5
1p1n	24.47 hrs	3.18 hrs	$\sim$ 7.69
1pXn	8.74 hrs	1.10 hrs	$\sim$ 7.94
3p0n	19.53 hrs	3.01 hrs	$\sim$ 6.48
3pXn	19.31 hrs	2.09 hrs	$\sim$ 9.23

Table 8.2: A table indicating the training time in hours (hrs) for the decay mode neural networks when trained with an RNN and a Deepset.

This knowledge allowed me to train several iterations of the TauID used for TauWG studies much faster than ordinarily allowed. I was also able to utilize the fast training speed of deepest based neural networks in the creation of a deepset-based fake factor estimation method, to estimate the number of fake taus in a given data region (10).

8.3 The Deepset Tau ID with Track RNN variables

While working in parallel to produce the RNN-based TauID shown in section (7.2.10), I worked on a Deepset based TauID that included track RNN scores from the Tau track classifier. The motivation behind the development of this network was an attempt to resurrect the studies I performed involving TauID algorithms that used

the output of a BDT-based tau track classifier which yielded a null result [92]. The belief was, that the TauID could potentially yield a higher background rejection if it takes advantage of an estimate of the probability of the track type passed to it. The network specifications of these Deepset based TauID with additional track score variables are the same as those shown in chapter 7, except that the p_t threshold used to select jet objects was lowered from 20 GeV to 15 GeV to potentially allow physics analysis groups to make use of low p_t Tau Jets. The $|\eta|$ selection now includes the crack region. And finally, the output of the RNN-based track classifier was used as input to the network. I developed and tested many iterations of these networks, as can be seen in internal ATLAS documentation and Indico meetings, but only the results of the highest-performing networks are shown here. In the case of the 2 and 3-prong networks, all RNN track outputs were used, and in the 1-prong network, only the Fake Track probability was excluded because a network trained without it yielded the highest background rejection.

Variable	1 prong	2 prong	3 prong
`TauTracks/chargedScoreRNN`	•	•	•
`TauTracks/isolationScoreRNN`	•	•	•
`TauTracks/conversionScoreRNN`	•	•	•
`TauTracks/fakeScoreRNN`		•	•

Table 8.3: Training variables used for the 1p 2p and 3p networks.

8.3.1 Equivalent Performance: Track (Deepset vs RNN) TauID

When performing a direct comparison between Deepset and RNN based TauIDs that contain Track RNN score variables as part of their input data. One can see that the Deepset based TauIDs retain equivalent performance to RNN based TauIDs. This performance comparison now shows a promising route in which to implement the more physically motivated Deepset/Particle Flow based network architecture.

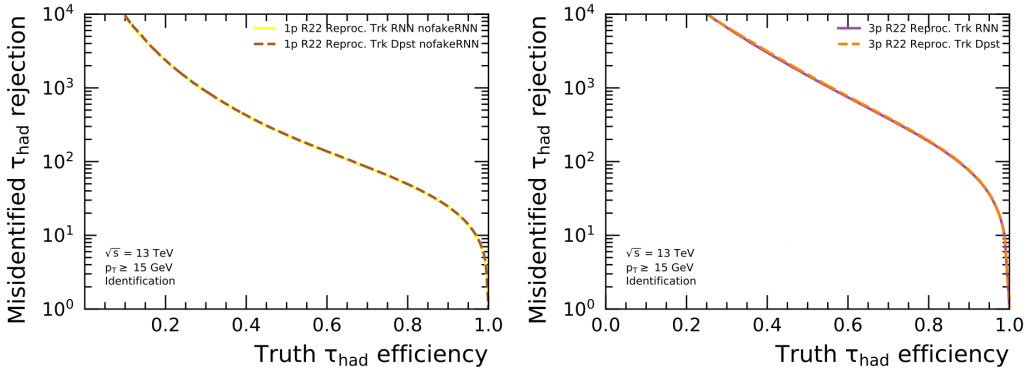

(a) (b)

Figure 8.6: Rejection of a (a) 1-prong and (b) 3-prong RNN based TauID **without** vs a Deepset based TauID trained with tau track RNN input variables.

8.3.2 Track Deepset TauID Performance

The results of the Track Deepset TauID when compared to the RNN-based TauID shown in section (7.2.10) evaluating jets with a $p_t > 15$GeV are shown below. By looking at table 8.4, one can see that networks including RNN Track score information see a 2 to 4 times improvement in background rejection. A surprising amount considering that previous studies involving a BDT track classifier yielded similar results to networks that did not utilize track classification scores.

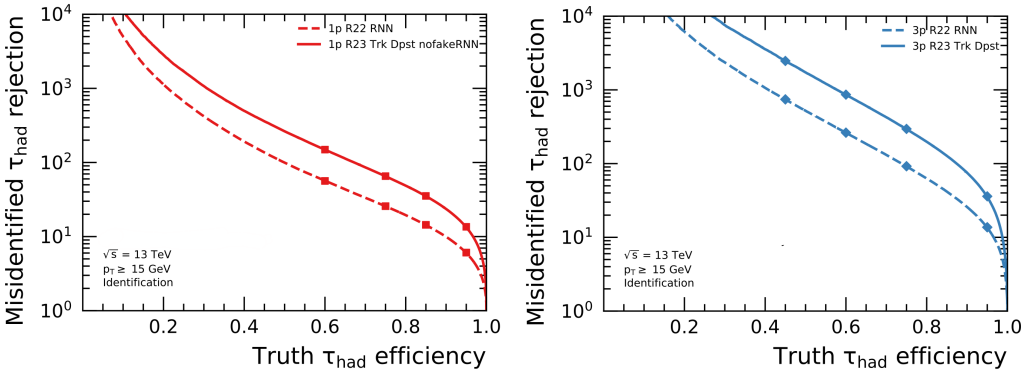

(a) (b)

(c)

Figure 8.7: Rejection of a (a) 1-prong and (b) 3-prong RNN based TauID **without** tau track RNN input variables v.s. a Deepset based network that **does** include tau track RNN input variables

After extensive testing and training iterations of networks involving the exclusion of combinations of Track RNN score variables, networks involving different permutations of Track RNN score information seemed to yield similar results (A.3). These Deepset based networks were then exported to other individuals in the TauWG to allow further testing using control regions of data where the projected rejection of the networks was not born out. At present studies are ongoing to understand the source of the improvement in background rejection, to reveal potential background sample bias, track mis-modeling that affects track input scores, etc.

Working Point	.60	.75	.85	.95
1p RNN	56.40	25.76	14.38	6.08
1p Trk Deepset	149.13	65.41	35.36	13.55
Improvement Factor	2.64	2.53	2.45	2.25

Working Point	.45	.60	.75	.95
2p RNN	143.36	54.02	21.39	4.32
2p Trk Deepset	400.49	155.30	60.82	9.58
Improvement Factor	2.79	2.87	2.84	2.21

Working Point	.45	.60	.75	.95
3p RNN	743.16	262.84	92.13	13.69
3p Trk Deepset	2468.40	861.51	295.43	35.98
Improvement Factor	3.32	3.27	3.20	2.62

Table 8.4: Background rejection improvement factors comparing 1 and 3 prong RNN-based networks that **don't** use Track RNN score variables and a Deepset based network that **does**.

8.3.3 Deepset TauID Training environment

The computing resources used to train and evaluate these networks ranged from Multiple GPU nodes in the now decommissioned Maverick-2 GPU cluster of the TACC Super-computing cluster located at UT Austin to a GPU cluster located on CERN's computing site.

Chapter 9

The $H^{\pm} \to \tau\nu$ analysis

As described in chapter 5, extensions to the standard model through 2 Higgs doublet models represent an attractive route by which to introduce new physics. With a rich phenomenology and wide ranging capabilities, 2HDMs fit into a multitude of Beyond Standard Model physics scenarios. This section details the search for charged Higgs bosons in a model-independent manner via $H^{\pm} \to \tau\nu$ in a mass range of 80GeV to 3000GeV, using $140.0 \pm .83 fb^{-1}$ of data collected by the ATLAS experiment in Run 2 of the LHC [54]. The particle object selection criteria are detailed in section (9.2), the definitions of signal and control regions in sections (9.3) and (9.7), background estimation methods in section (9.8), a description of the Parameterized Neural Network (PNN) [99] used to classify events in section (9.14), the data-sets used in the analysis in section (9.13), the statistical analysis procedure in section (9.15), and the final results of the analysis in section (9.26).

9.0.1 $H^{\pm} \to \tau\nu$ a summary

Three independent and combined signal regions are considered in this search, τ+Jets, τ+e, and τ+μ. In all cases, the τ in the event is required to decay hadronically where the accompanying final state object (Jets, e, μ) is produced by the hadronic or leptonic decay of the W boson in the event. Signal and background event discrimination is done using a Parameterized Neural Network (PNN) trained on Monte Carlo generated $H^{\pm}$ signal and SM background. Both MC and data control regions were evaluated by the PNN to validate its performance. The statistical analysis is performed on histograms of PNN output scores. The $H^{\pm}$ mass search range was set to be as broad as possible while taking into consideration the 95% exclusion limits set by the Large Electron Positron Collider (LEP) experiment [100] on charged Higgs bosons with a mass below 80GeV. The final results of this analysis are expected and observed 95% exclusion limits on $\mu = \sigma(pp \to tbH^{+}) \times \mathcal{B}(H^{+} \to \tau\nu)$ and $\mathcal{BF} = \mathcal{B}(t \to bH^{+}) \times \mathcal{B}(H^{+} \to \tau\nu)$ as a function of the charged Higgs mass placed on $140.0 \pm .83 fb^{-1}$ of data collected by ATLAS during Run2. Exclusion limits on μ span the entire $H^{\pm}$ mass range, while exclusion limits for $\mathcal{BF}$ are placed only for hypothesized $H^{\pm}$ masses below the top quark mass (80-160GeV). This analysis was done in a blinded manner, where the PNN score distributions of our observed data in our signal regions were not considered until all results on SM Asimov data were deemed to be understood and stable. This analysis is conducted in a model-independent manner, but the results are interpreted in a type-II 2HDM framework that is used in the habemus Minimal Super Symmetric model (hMSSM) [51].

9.1 $H^{\pm}$ Production

Due to the broad mass search range of the analysis, 80GeV - 3000GeV, three $H^{\pm}$ production modes must be considered. Each production mode has a distinct Feynman diagram that depends on the predicted mass of the $H^{\pm}$ relative to the top quark mass (172 GeV [72]). When the $H^{\pm}$ mass is predicted to be near 172GeV, diagrams interfere either constructively or destructively depending on the exact predicted $H^{\pm}$ mass. Three $H^{\pm}$ mass regions are defined according to which Feynman diagrams dominate in the production cross-section. These mass ranges are the

- Low mass range ($80GeV \leq m_{H^{\pm}} \leq 140GeV$)
- Intermediate mass range ($140GeV < m_{H^{\pm}} \leq 200GeV$)
- High mass mass range ($200GeV < m_{H^{\pm}} \leq 3000GeV$)

Figure 9.1 shows the leading order Feynman diagrams for each $H^{\pm}$ mass range.

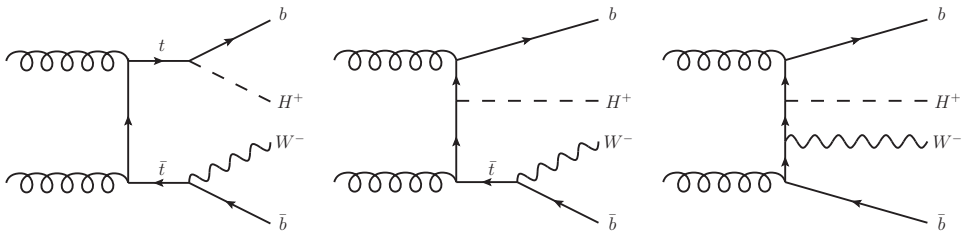

Figure 9.1: Leading-order Feynman diagrams contributing to the production cross-section of charged Higgs bosons: (a) double-resonant top-quark production dominating in the low mass regime and up to the top quark mass, (b) single-resonant top-quark production dominating in the intermediate mass regime with contributions from diagrams a and c, and (c) non-resonant top-quark production dominating in the high mass regime with contributions from b. [54]

9.2 Final State Particle Objects

The $H^{\pm}$ production modes shown in figure 9.1 allow us to construct a general list of the final state particle objects necessary to construct our signal regions. Our signal regions will require

Jets: At least 1 jet originating from the potential hadronic decay of the $W^{\pm}$ boson

b-jets: At least 1 b-jet, originating from the decay of the b quarks produced by decaying top quarks

τ-Jets: Exactly 1 Tau initiated jet, originating from the charged Higgs

Leptons (e,μ): Exactly 1 lepton, originating from the potential leptonic decay of the $W^{\pm}$ boson

MET: Large quantities of MET, originating from the neutrino produced in the $H^{\pm}$ and hadronic τ decay, and or leptonic decay of the $W^{\pm}$ boson, as well as from neutrinos produced in the accompanying jets.

9.2.1 Selections on final state particle objects

To ensure that the reconstruction quality of the particle objects we select remains high, we must apply certain kinematic and signal efficiency selections. These types of selections largely rely on trigger efficiencies, calorimeter resolution, detector acceptance, and algorithm performances. Signal efficiency working points defined by particle identification algorithms, like in the TauID (7.2.9) are used to select reconstructed particle objects with varying degrees of confidence. Particle objects that pass a tight selection working point are deemed to have been reconstructed correctly with a very high degree of certainty, where the degree of certainty drops as the working point selection becomes more loose. The final state physics objects of interest that require additional selections include jets, the visible component of the hadronically decaying taus, electrons, and muons. A summary of the selections applied to the particle objects used to define our signal regions is given by table 9.1.

	e	μ	τ $(1p, 3p)$	Jets
E_T	$> 20GeV$	–	–	–
p_t	$> 20GeV$	$> 25GeV$	$> 30GeV$	$> 25GeV$
η	$\|\eta\| < 2.47$	$\|\eta\| < 2.5$	$\|\eta\| < 2.3^*$	$\|\eta\| < 2.5$
$\|z_0 sin(\theta)\|$	$0.5mm$	$0.5mm$	–	–
$\|d_0/\sigma(d_0)\|$	< 5	< 3	–	–
WP Selection	LLHLoose, FCTight	LOOSE, PflowTight	JetRNNSigLoose†, JetRNNSigMedium	70% for b-jets

Table 9.1: Major selections applied to objects of interest. NOTE: Additional cuts for subsets of the mentioned objects are defined in their respective sections. $^*\eta$ indicates the exclusion of the crack region $1.37 < |\eta| < 1.52$. † Taus failing the JetRNNSigLoose working point are used to define the Anti-Tau control region.

A more detailed description of the selections on the physics objects used in this analysis is shown below.

9.2.2 Jet selections

The recommendations on how to select jet objects come from the JetETMiss working group [101]. These jets are reconstructed using the AntiKt algorithm [78] and calibrated using the Jet Energy Scale (JES) calibration scheme. Jets are required to have a $p_T > 25GeV$ and are required to have been detected with an eta coordinate between $|\eta| < 2.5$. Jets with a $p_T < 60GeV$ and an η coordinate $|\eta| < 2.4$ are required to have a JVT (Jet Vertex Tagger) score of $JVT > 0.50$ to select jets that come from the hard scatter vertex.

9.2.3 b-Jet selections

Jets initiated by b-quarks are selected using efficiency working points from a deep neural network-based identification algorithm called the DL1r b-jet tagger as recommended by the Flavor Tagging group [83]. b-jets used in the $H^\pm \to \tau\nu$ analysis are selected at a fixed working point efficiency of 70% per b-jet, and are required to pass the same selection criteria as the QCD jets above.

9.2.4 Taus (τ) jet selections

Taus candidates used in this analysis are required to decay hadronically, and selected using the TauSelectionTool[1] [102]. The tau candidates used in our signal regions are required to pass the medium working point detailed in section 7.1, and have a BDT-based electron veto applied to remove incorrectly reconstructed tau candidates. Tau jets are also required to have 1 or 3 reconstructed charged tracks and are required to have a visible component of transverse momentum $p_{Tvis} \geq 30GeV$ and an η coordinate of $|\eta| < 2.3$, excluding the crack region $1.37 < |\eta| < 1.52$. Tau candidates are reconstructed using the Anti-k_t algorithm and calibrated to the Tau Energy Scale (TES). Taus required to fail the loose identification working point are used to construct the anti-τ control region used to measure the number of fake taus making it into our signal regions (9.8.5). Only the leading[2] tau candidate in the event is stored for use in the analysis.

9.2.5 Electrons (e) selections

Electron objects are reconstructed as described in section (6.0.3), and are required to have a transverse energy $E_T > 20GeV$, a $p_t > 20GeV$ and located within the an η space of $|\eta| < 2.47$ (excluding the crack-region $1.37 < |\eta| < 1.52$). Additionally, the electron tracks are required to have transverse and longitudinal impact parameters of $|d_0/\sigma(d_0)| < 5$ and $|z_0 sin(\theta)| < 0.5$mm. Finally, we select electrons that pass the loose identification working point and tight isolation working points defined by the EGamma group recommendations [103][104]

9.2.6 Muons (μ) selections

Muons objects are reconstructed as described in section (6.0.4) and are selected using the MuonSelectionTool[3] [105]. Muons in this analysis must pass the loose identification and tight isolation working points defined by the Muon Working Group [106][104], and are required to have matching inner detector and Muon spectrometer tracks. Muons are required to have a $p_t > 25GeV$, $|\eta| < 2.5$, as well as to have inner detector tracks with the following impact parameter thresholds, $|z_0 sin(\theta)| <$ 0.5mm, $|d_0/\sigma(d_0)| < 3$, to remove unclassified muon candidates coming from pile-up interactions [107].

9.2.7 Missing Transverse Energy (E_T^{miss}) selections

MET is calculated via the METMaker [108] tool by considering the contributions of MET from muons, electrons, photons, hadronically decaying τ-leptons, and jets [76]. The METMaker tool performs its own overlap removal process independently of the procedure done for the other objects in the analysis. This process is described in detail in citations [109][76]. Cuts on the specific amount of E_T^{miss} we require are dependent on the search channel and their chosen MET trigger thresholds. These are shown below, in section 9.3.

[1] A tool used to perform simple selections on a set of tau properties at the preselection level

[2] Leading objects are defined to be the objects in the event that have the highest p_t. The object with the second highest p_t is referred to as the second leading, and so on.

[3] MuonSelectionTool is a tool used to select good quality muons for physics analysis[105]

9.2.8 Overlap Removal

Occasionally, our objects of interest have an overlap in the regions where they deposit their energy and momentum. To make an accurate assessment of the final state objects in our data sets, we must resolve them into independent signatures through a process called overlap removal. Overlap removal is the process of removing objects from our selections if they overlap significantly in η and ϕ space with other objects in the same event, as determined by some predefined criteria within the overlap removal tool itself. Overlap removal in this analysis is done using the Analysis Software Group (ASG) Overlap Removal Tool [110].

9.3 Signal Region Definitions: Tau+Jets, Tau+Lep

The **Tau + Jets** signal region, and the **Tau + Lep** signal region are defined by the hadronic or leptonic decay of the $W^{\pm}$ boson in our event. The **Tau + Jets** signal region is defined by the requirement that the $W^{\pm}$ boson in the event decays hadronically, $W^{\pm} \rightarrow q\overline{q}^{'}$, while the **Tau + Lep** channel requires that the $W^{\pm}$ boson decay leptonically, $W^{\pm} \rightarrow l\nu_l$. here ℓ is either an electron (e) or muon (μ). In both signal regions, the tau is required to decay hadronically.

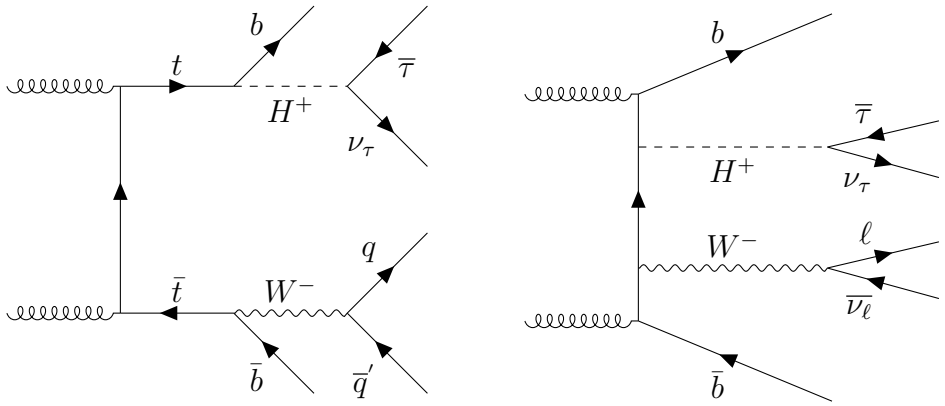

Figure 9.2: (a) A tree-level Feynman diagram representing double resonant top quark production where the top quarks decay into a charged Higgs boson and W boson, where the $W^{\pm} \rightarrow q\overline{q}^{'}$ defines the τ + Jets channel, and (b) non-resonant top quark production producing an H^+ where $W^{\pm} \rightarrow l\nu_l$ where $l = e, \mu$ defines the τ+Lep channel.

Figure 9.2 provides an example in the low mass $H^{\pm}$ regime where the distinction between the Tau+Jets and Tau+Lep channels can be understood. The primary difference between signal regions is the choice of trigger, a MET trigger is used for the Tau+Jets channels and a single lepton trigger for the Tau+Lep channel. Table 9.2 shows a summary of the set of selections used to define our signal regions, while a more full description of the selections is detailed below.

9.4 The Tau+Jets Channel

Along with the requirement that the $W^{\pm}$ in the event decays hadronically, events that enter the Tau+Jets signal region are required to pass a MET trigger. In the previous analysis, a tau+MET trigger was used to select events in the Tau+Jets signal region. Using a tau-dependent cut in conjunction with MET trigger introduced complications when estimating the uncertaintes on number of fake taus entering our signal regions, determined by our data-driven fake factor method (9.8.5). And so a MET trigger was chosen in lieu of a τ+MET trigger to eliminate the need to account for correlations of the trigger selection to fake taus in our fake factor estimations.

9.4.1 E_T^{miss} (MET) Trigger

The data used in this analysis were collected from 2015-2018 and have E_T^{miss} trigger thresholds of 70, 80, 90, or 110 GeV depending on the data-taking year. Because this analysis uses datasets collected throughout Run2, our E_T^{miss} requirement is set to $E_T^{miss} > 150GeV$ so that it never drops below the minimum MET threshold of the data collected in 2018. Additionally, the MET threshold is set so that we are in or near the plateau of the trigger efficiency curves shown in figure 9.3. Details on the corrections applied to the trigger efficiency are in section 9.8.2.

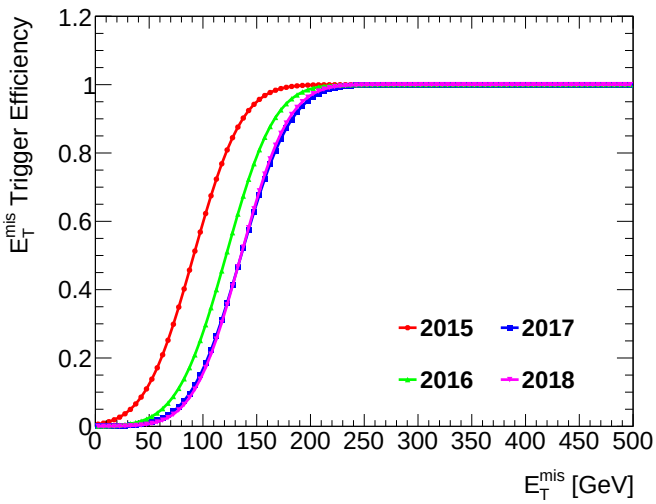

Figure 9.3: Trigger efficiency curves for data taken in the years 2015-2018, for the selection of a Tau candidate passing the Tight working point efficiency.[54]

9.4.2 Selections for the Tau+Jets SR

Events passing the MET trigger described in the section above require additional cuts on the objects within them to fully define the Tau+Jets signal region. Below is a full list of the selections used to define this region.

- Require events pass the E_T^{miss} trigger threshold corresponding to their data taking year.
- Remove events where any jet with a $p_t > 25GeV$ (τ or otherwise) fails the **LooseBad** working point.

- Require at least 1 τ candidate with a $p_t > 40GeV$ that passes the **JetRNNSigMedium** working point.
- Require 0 leptons (e or μ) passing the **Loose** selection working point, with $p_t > 20GeV$.
- Require at least 3 jets with $p_t > 25GeV$.
- Require at least 1 b-jet, by ensuring that at least 1 of the jets above passes the DL1r b-tagger 70% WP efficiency selection.
- Require $E_T^{miss} > 150GeV$.
- Require the transverse mass m_T of the highest p_t tau candidate has a value of $m_T > 50GeV$.
- Require that events are not in the Tau+Jets TTBar control region defined in section 9.7.2, for orthogonality reasons.

Here, the transverse mass m_T is defined as

$$m_T = \sqrt{2p_t^\tau E_T^{miss}(1 - cos(\Delta\phi_{\tau,E_T^{miss}}))} \tag{9.1}$$

where $\Delta\phi_{\tau,E_T^{miss}}$ is the azimuthal angle between the visible component of the p_t belonging to the τ candidate and the direction of the missing transverse momentum.

9.5 The Tau+Lep Channel

The Tau+Lep channel is composed of two individual channels, the Tau+Electron and Tau+Muon channels. Along with the requirement that the $W^\pm$ boson in the event decays leptonically, events that enter the the Tau+El and Tau+Mu signal regions are required to pass a single lepton trigger.

9.5.1 Single Lepton Trigger

The single lepton trigger used in this analysis is a logical OR combination of kinematic-based triggers and isolation working point requirements on the leptons. The kinematic-based trigger thresholds are E_t based in the case of electrons, and p_t based in the case of muons. The exact E_t/p_t trigger thresholds depend on the data taking year of the selected leptons and are fully defined in [111].

9.5.2 Selections for the Tau+Lep SR

The additional selections on the events required to fully define the the Tau+Lep channel are shown below.

- Remove events where any jet with a $p_t > 25GeV$ (τ or otherwise) fails the **Loose** working point.
- Require 1 (e, μ) lepton with a $p_t > 30GeV$, Also requires that it passes the *tight* identification criteria for its corresponding object in table 9.1, and is matched to the lepton passing the single-lepton trigger.
- Require at least 1 τ candidate with a $p_t > 30GeV$ that passes the **Medium** working point.

- Require the selected τ candidate to have an electric charge opposite of the selected lepton ($q_\tau * q_\ell = -1$)
- Require at least 1 b-jet with a $p_t > 25GeV$, defined by a jet passing the DL1r b-tagger 70% WP efficiency selection.
- Require $E_T^{miss} > 50GeV$.
- Require that events are not in the Tau+Lep TTBar control region defined in section 9.7.3, for orthogonality reasons.

It should be noted that the flavor of the required lepton defines the Tau+El or the Tau+Mu signal region.

9.6 Signal region and TTBar Control region Orthogonalization

The original definitions of our signal regions shown in table (9.2) included some overlap in the TTBar control regions used to re-weight our TTBar background (9.8.1). At the request of our editorial board, and in order to not introduce a source of bias that might arise in limit setting when data events are used to reweight our background statistics, our signal regions and TTBar control regions were made orthogonal by manually requiring that data events used in our TTBar control regions not be included in our signal regions and by adjusting the selections of the Tau+Jets and Tau+Lep TTBar control regions shown by table 9.7.14. This orthogonalization had a minimal effect on limits, but dropped the background statistics by (9.1%, 9.4%, 22%) for the ($\tau + e$, $\tau + \mu$, $\tau + jets$) signal regions respectively, while the signal statistics dropped by varying degrees depending on the mass of the $H^\pm$ generated in the dataset. In general $H^\pm$ signal regions with lower mass were most affected, where the % drop in $H^\pm$ signal statistics ranges from (10%-0%, 9%-0%, 24%-0%) in the ($\tau + e$, $\tau + \mu$, $\tau + jets$) signal regions.

Cut variable	SR TauJets	SR $\tau + e$	SR $\tau + \mu$
Trigger Req.	MET Trig.	Single Lep Trig.	Single Lep Trig.
$p_T(\tau_{hadvis})$	$> 40GeV$	$> 30GeV$	$> 30GeV$
p_T(lead-jet)	$> 25GeV$	$> 25GeV$	$> 25GeV$
WP Selection	JetRNNSigMedium for τ, **loose** for (e, μ)	JetRNNSigMedium for τ, **tight** for (e, μ)	JetRNNSigMedium for τ, **tight** for (e, μ)
$N_{b\text{-jet}}$	≥ 1	≥ 1	≥ 1
N_ℓ	0	$1e$	1μ
$p_T(\ell)$ (μ, e)	$> 20GeV$	$> 30GeV$	$> 30GeV$
$q(\tau_{hadvis}) * q(\ell)$ (μ, e)	$-$	-1	-1
N_{jet}	≥ 3	≥ 1	≥ 1
MET	$> 150GeV$	$> 50GeV$	$> 50GeV$
$m_T(\tau_{hadvis}, MET)$	> 50	$-$	$-$
N_{PV}	≥ 1	≥ 1	≥ 1
N_{tracks} $w.r.t$ PV	≥ 2	≥ 2	≥ 2
$Veto\ Event$	Jet $p_t \geq 20GeV$ fail **LooseBad** WP	Jet $p_t \geq 20GeV$ fail **LooseBad** WP	Jet $p_t \geq 20GeV$ fail **LooseBad** WP
Other	Logical Not $t\bar{t}$	Logical Not $t\bar{t}$	Logical Not $t\bar{t}$

Table 9.2: Cuts applied to the objects in the Tau+Jets, Tau+e and Tau+μ Signal regions. PV denotes primary vertices in the event. Further descriptions of the cuts applied for each signal region can be found in their respective sections, Tau+Jets 9.4, and Tau+Lep 9.5. The Logical Not $t\bar{t}$ is used to denote that an explicit selection to NOT include objected defined in the $t\bar{t}$ control region in order to make the signal regions orthogonal to the $t\bar{t}$ control region. Control regions are defined in section 9.7

9.7 Control/Validation Region Definitions

In order to validate the proportion of background in our signal regions, as well as to validate the trigger efficiency performance, the $H^{\pm} \rightarrow \tau\nu$ analysis has created 13 Control Region (CR)s in which to study these. These control regions are defined below. All regions are subject to basic event cleaning cuts.

9.7.1 E_T^{miss} (MET) Control Region

The MET control region is used to correct the trigger efficiency of the MC data via trigger efficiency scale factors described in section 9.8.2. This control region is defined by the following cuts

- Require 1 trigger matched electron, with a $p_t > 26GeV$ passing the **loose** identification criteria defined in 9.2.5.
- Require at least 1 τ jet with a $p_t > 30GeV$, passing the **JetRNNMedium** identification criteria defined in 9.2.4, and that has an opposite charge w.r.t the selected electron.
- Require at least 2 jets defined by the selection in 9.2.2 with a $p_t > 25GeV$
- Require at least 1 b-jet defined by section, by ensuring that at least 1 of the jets above passes the DL1r b-tagger 70% WP efficiency selection defined in 9.2.3.

9.7.2 TTBar Tau+Jets Control/Validation Region

The TTBar Tau+Jets control region is used to assess the modelling of the $\mathbf{t\bar{t}}$ background, and to derive the re-weighting factors for the $\mathbf{t\bar{t}}$ and W+Jets MC samples. This control region is very similar to the Tau+Jets signal region but with a few changes. This region is also used as a validation region for the MET Trigger efficiently detailed in section 9.8.2.

- Require that events pass the same selection as the Tau+Jets signal region, with the replacements below.
- Require $m_T < 100GeV$ in place of $m_T > 50GeV$.
- Require at least 2 b-jets, in place of $N_{b-jet} \geq 1$
- Do not require a $p_t > 25GeV$ for the QCD jets in the event.

9.7.3 TTBar Tau+Lep Control Region

The TTBar Tau+Lep control regions are defined for both the Tau+El and Tau+Mu signal regions, and to derive the re-weighting factors for the $\mathbf{t\bar{t}}$ and W+Jets MC samples. They are very similar to the Tau+Lep signal regions but with a few changes.

- Require that events pass the same selection as the Tau+Lep signal region, with the replacements below.
- Require $E_T^{miss} > 80GeV$ instead of $E_T^{miss} > 50GeV$.
- Require the transverse mass $m_T < 70GeV$.

- Require at least 2 QCD jets with a $p_t > 25GeV$ instead of 1.
- Require at least 2 b-jets, instead of $N_{bjet} \geq 1$.

9.7.4 b-Veto (e, μ) Control/Vaidation Regions

The $\mathbf{b-Veto}$ control regions are used to validate the W/Z+jets background events with true electrons/muons and fake tau candidates. These regions contain a high proportion of QCD jets faking τ candidates, and are used to validate the total number of fake tau candidates unintentionally passing into our Signal regions, see 9.8.5. These regions has the same event selection as the Tau+Lep signal region defined in table 9.2 except for a looser requirement that no b-jets are required. This region is also used as a validation region for the MET Trigger efficiently detailed in section 9.8.2.

- Require that events pass the same selection as the Tau+Lep signal region, with the replacements below.
- Require 0 b-jets, instead of ≥ 1.

9.7.5 b-Tag Control Region $(e + \mu)$

The $\mathbf{b-Tag}$ control region is used to validate the $t\bar{t}$ background. This region has the same event selection as the Tau+Lep signal region defined in table 9.2 with the following exceptions.

- Require the same selection as the Tau+Lep signal region, with the replacements below.
- Require 0 τ candidates.
- Require 2 leptons, in place of 1, where the second lepton is of the opposite flavor as the search channel (Tau+El or Tau+Mu). (eμ).
- Require that the 2 leptons in the event have opposite sign, $q(e) * q(\mu) = -1$

9.7.6 Anti-τ Control Region

The $\mathbf{Anti-\tau}$ control region is used to estimate the number of fake tau candidates that pass our tau selection criteria. This region is critical in the determination of Fake Factors defined in section 9.8.4, and is defined by applying additional cuts to a selected control region. In this analysis, these control regions include the MultiJet, W+Jets and the Inclusive control regions defined in sections 9.7.7, 9.7.8, 9.7.10.

- Require the events pass the same selection as a Control region of your choice.
- Require that selected τ candidates fail the **jetRNNSigLoose** working point criteria.
- Require the selected τ candidates have a **RNNJetScore** $>$ **0.01**.

The requirement that **RNNJetScore** $>$ **0.01** is to ensure that the anti-selected taus lie in a region with characteristics as similar as possible to the anti-selected taus in the signal region, thus providing an accurate measure of background contamination to the signal region.

9.7.7 Multi-Jet Control Region

The **Multi − Jet** control region is constructed in such a way that it contains a high proportion of Quark and Gluon initiated jets, and is used in conjunction with the W+Jets control region 9.7.8 to estimate the total number of QCD jets faking tau candidates that unintentionally pass into our Signal regions, see 9.8.5. This region is defined using the same selections as the Tau+Jets signal region, defined in section 9.4.2, but instead requires the following cuts

- Require selections identical to the Tau+Jets signal region 9.4.2, with the replacements below.
- Require 0 b tagged jets instead of ≥ 1.
- Require $E_T^{miss} < 80GeV$ instead of $E_T^{miss} > 150GeV$.
- Require the event to pass MultiJet triggers[4] in a logical OR combination.

9.7.8 W+Jets Control/Validation Region

The **W + Jets** control region is constructed in such a way that it contains a high proportion of quark initiated jets (due to the 67% branching fraction of $W^{\pm} \to q\bar{q}^{'}$) [85], and is used in conjunction with the MultiJet control region 9.7.7 to estimate the total number of jets faking tau candidates that unintentionally pass into our signal regions, see 9.8.5. This region is also used as a validation region for the MET Trigger efficiently detailed in section 9.8.2. The W+Jets control region is derived using the following cuts

- Remove events where any jet with a $p_t > 25GeV$ (τ or otherwise) fails the **LooseBad** working point.
- Require 1 electron passing the single lepton trigger.
- Require 0 b-tagged jets.
- Require at least 1 τ jet candidate.
- Require the selected electron have a transverse mass of $60GeV < m_T(\ell, E_T^{miss}) < 160GeV$.

Where the transverse mass is defined by equation 9.1.

9.7.9 Same Sign (e,μ) Control Region

The **Same Sign** $(\mathbf{e}, \mu)$ control regions are used to validate the heavy flavor Fake factors derived in section 9.8.5. These regions require the same set of cuts as the Tau+Lep channel, with the requirement that the selected lepton has a charge opposite to that of the selected τ.

- Require selections identical to the Tau+Lep signal region defined in section 9.5.2
- Require the selected lepton (e,μ) has the same sign as the selected τ $q(\tau) * q(\ell) = 1$.

[4]HLT 3j175, HLT 3j200, HLT 3j225, HLT 4j85, HLT 4j100, HLT 4j110, 747 HLT 4j120, HLT 5j60, HLT 5j70 L14J15, HLT 5j85 and HLT 5j85 L14J15

9.7.10 Inclusive Control Region

The **Inclusive** control region is a control region derived to allow for the estimation of Fake Factors for fake tau candidates originating from heavy flavor jets (c,b,s), see 9.8.5. The Inclusive control region is defined by the following cuts.

- Remove events where any jet with a $p_t > 25GeV$ (τ or otherwise) fails the **LooseBad** working point.
- Require at least 1 τ candidate with a $p_t > 30GeV$ passing the **JetRNNSigMedium** identification criteria.
- Require the selected tau candidates have 1 or 3 associated tracks, and have an η coordinate within $|\eta| < 2.5$ excluding the crack-region[5]

9.7.11 b-Veto MT100 Control/Validation Region

The $\mathbf{b-Veto\ MT100}$ control region is one of 3 regions used to validate the estimate of the number of quark and gluon-initiated jets produced by the Fake Factors derived in section 9.8.5. This validation region is very similar to the Tau+Jets signal region defined in section 9.4.2, but with a few differences. This region is also used as a validation region for the MET Trigger efficiently detailed in section 9.8.2.

- Require the events pass the same selection as the Tau+Jets signal region 9.4.2, but with the replacements below.
- Require 0 b-jets in place of ≥ 1.
- Require $m_T > 100GeV$ in place of $m_T > 50GeV$

9.7.12 Z-ee Control Region

The $\mathbf{Z-ee}$ control region is defined such that it contains a high proportion of electrons faking τ candidates, and is used to estimate the total number of electrons faking tau candidates that unintentionally pass into our Signal regions, see 9.8.5.

- Remove events where any jet with a $p_t > 25GeV$ (τ or otherwise) fails the **LooseBad** working point.
- Require 1 electron passing the single-electron trigger defined in section 9.5.
- Require 1 electron with $p_t > 30GeV$ passing the **tight** identification criteria and matched to the electron passing the single lepton trigger.
- Require 1 τ candidate with $p_t > 40GeV$, passing the **JetRNNSigMedium** working point.
- Require the selected τ candidate to have an electric charge opposite of the selected lepton ($q_\tau * q_\ell = -1$).
- Require at least 1 jet with a $p_t > 25GeV$.
- Require 0 b-tagged jets.
- Require 0 muons.
- Require the invariant mass of the (τ,e) system be between $80GeV$ and $110GeV$.

[5]The crack region is defined as the region of η space corresponding to $1.37 < |\eta| < 1.52$

9.7.13 Pre-Selection Control/Validation Region

The $\mathbf{Pre-Selection}$ region is defined as a set of broad initial cuts to the physics objects used in our analysis to reduce the size of our dataset after which additional cuts are applied. There are two pre-selection regions, for the Tau+Jets and Tau+Lep regions. The Tau+Jets pre-selection region is the Tau+Jets signal region (9.4.2), without the requirements on the number of b-jets and MET ($n_b^{jets} \geq 1$, $E_T^{Miss} > 150GeV$). This region is also used as a validation region for the MET Trigger efficiency detailed in section 9.8.2.

9.7.14 Summary of Control/Signal/Validation regions [111]

When applicable, units are in GeV and "Not TTBar$_{SR}$" means exclusion of events present also in the corresponding TTbar$_{SR}$ CR.

Cut	SR $\tau + Jets$	$t\bar{t}$	W+jets	b-veto	b-veto MT100
$p_t(\tau)$	> 40	> 40	> 40	> 40	> 40
p_t(lead-jet)	> 25	> 25	> 25	> 25	> 25
N_ℓ	0	0	0	0	0
N_{jet}	≥ 3	≥ 3	≥ 3	≥ 3	≥ 3
$N_{b\text{-jet}}$	≥ 1	≥ 2	0	0	0
MET	> 150	> 150	> 150	> 150	> 150
$m_T(\tau, MET)$	> 50	< 100	< 100	> 50	> 100
other	Not TTbar$_{\text{taujet}}$ CR				

Table 9.3: Regions without leptons in the final state.

Cut	SR $\tau + e$	$\tau + e$ b-veto	$\tau + e$ SS	$Z \to ee$	MET trigger
$p_t(\tau)$	> 30	> 30	> 30	> 30	–
$p_t(e)$	> 30	> 30	> 30	> 30	> 26
p_t(lead-jet)	> 25	> 25	> 25	> 25	> 25
$q(\tau) * q(e)$	-1	-1	1	-1	–
N_{jet}	≥ 1	≥ 1	≥ 1	≥ 1	≥ 2
$N_{b\text{-jet}}$	≥ 1	0	≥ 1	0	≥ 1
MET	> 50	> 50	> 50	> 50	–
other	Not TTbar$_{taulep}$	–	–	See caption	$p_t^{lead-jet} > 25$

Table 9.4: Regions with just electrons in the final state. In all cases, the electron must be trigger-matched, and it must pass a tight ID working point except in the MET trigger region. The $Z \to ee$ region has an additional cut on the mass of the $\tau + e$ system, as described in Sec. 9.7.12.

Cut	SR $\tau + \mu$	$\tau + \mu$ b-veto	$\tau + \mu$ SS	$t\bar{t}$, $\tau + \ell$	$e + \mu$ b-tag
$p_t(\tau)$	> 30	> 30	> 30	> 30	–
$p_t(e)$	–	–	–	> 30	> 30
$p_t(\mu)$	> 30	> 30	> 30	> 30	> 30
p_t(lead-jet)	> 25	> 25	> 25	> 25	> 25
$q(\tau) * q(\mu)$	-1	-1	1	-1	–
N_{jet}	≥ 1	≥ 1	≥ 1	≥ 2	≥ 1
$N_{b\text{-jet}}$	≥ 1	0	≥ 1	≥ 2	≥ 1
MET	> 50	> 50	> 50	> 80	> 50
other	Not TTbar$_{taulep}$	–	–	$m_T(\tau, E_T^{Miss}) < 70$	$q_e * q_\mu = -1$

Table 9.5: Regions with an e and or μ in the final state. In all cases, the electrons and/or muons must be trigger-matched. The $t\bar{t}$ requires exactly 1 electron or muon. The di-lepton region has a τ-veto and requires the leptons to have opposite sign.

9.8 Background Modeling and Validation

When determining the extent to which our background sources can contaminate our signal processes, we rely heavily on Monte Carlo generation. Much of the time, these MC simulations can reliably estimate the number of background processes we expect to see in the regions of phase space that are relevant for physics analysis. But occasionally, our lack of physics understanding and computational resources can cause a discrepancy in what our MC generators produce and is produced by nature. Thus, we as physicists must devise a way to properly account for our background processes in light of these discrepancies. The following sections describe the methods that are used by the $H^{\pm} \to \tau\nu$ analysis team to ameliorate the shortcomings of our Monte Carlo generators. The methods used in this analysis to estimate background sources are, the derivation of scale factors for the $t\bar{t}$ backgrounds in both signal regions, deriving scale factors for the triggers used, the validation of scale factors to correct for. the number of leptons faking tau candidates in our signal regions, and the use of Fake Factors to estimate the number QCD[6] jets faking taus and unintentionally making it into our signal regions.

9.8.1 TTBar and W+Jets Sample Re-Weighting

The TTBar and W+Jets backgrounds represent a significant portion of our background processes, and thus it is of the utmost importance that we model these properly. Unfortunately, the Monte Carlo generators used to produce these background samples do not perform well when simulating environments with a high number of jets. In order to improve the agreement between the MC and observed data for these backgrounds, the $H^{\pm} \to \tau\nu$ analysis team derives scale factors for the TTBar and W+Jets backgrounds. The derivation of these re-weighting factors is summarized below.

The re-weighting factors are defined as

$$R(x) = \frac{Data(x) - MC^{non-t\bar{t}/non-W+jets}(x)}{MC^{t\bar{t}/W+jets}(x)} \tag{9.2}$$

where x is the variable that is not modeled well by MC simulation.

TTBar Re-Weighting

The reweighing factors for the $t\bar{t}$ background in the Tau+Jets and Tau+Lep signal regions are derived using the **effective mass** of the objects in the TTBar Tau+Jets and TTBar Tau+Lep control regions defined in sections 9.7.2, 9.7.3 and equation 9.2. The effective mass of the objects in the control regions are defined as follows

$$TTBar_{taulep}: \quad m_{\text{eff}} = \sum_{\text{jets}} p_T^{\text{jets}} + p_T^{\tau} + p_T^{\text{leptons}} + E_T^{miss} \tag{9.3}$$

$$TTBar_{TauJets}: \quad m_{\text{eff}} = \sum_{\text{jets}} p_T^{\text{jets}} + p_T^{\tau} + E_T^{miss}. \tag{9.4}$$

[6]QCD jets are jets created by quarks

and are used to create binned distributions of the re-weighting factors defined by equation 9.2.

These distributions are then fit to a function of the form

$$f(x) = a + b(m_{\text{eff}} + 30) * e^{-cm_{\text{eff}}} \tag{9.5}$$

to allow for application to different binning schemes, and used to apply weights to the events with objects entering the distributions of E_T^{miss}, p_t^{τ} and n_{jets} in their respective signal regions. The effect of the application of these re-weighting factors on the MET distribution for the TTBar Tau+Jets control region is shown below.

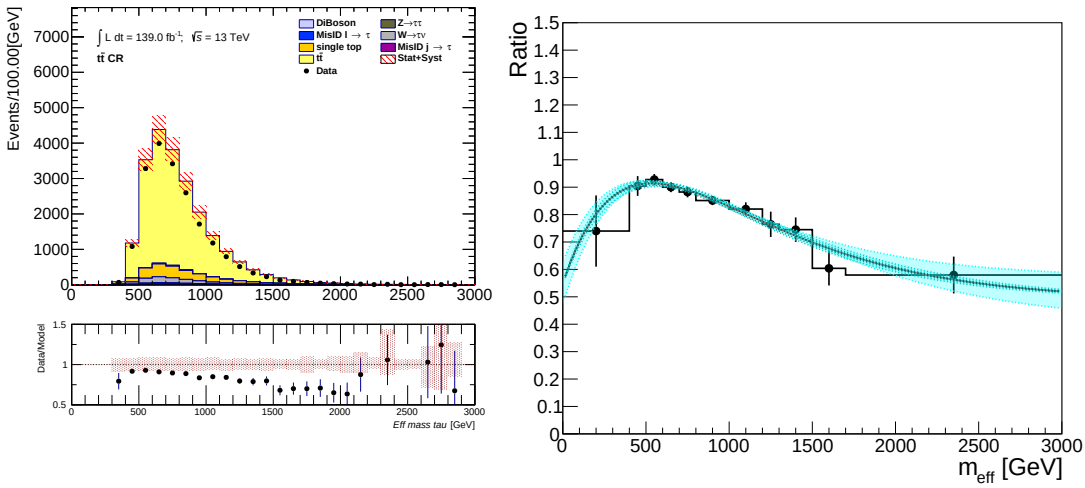

(a) (b)

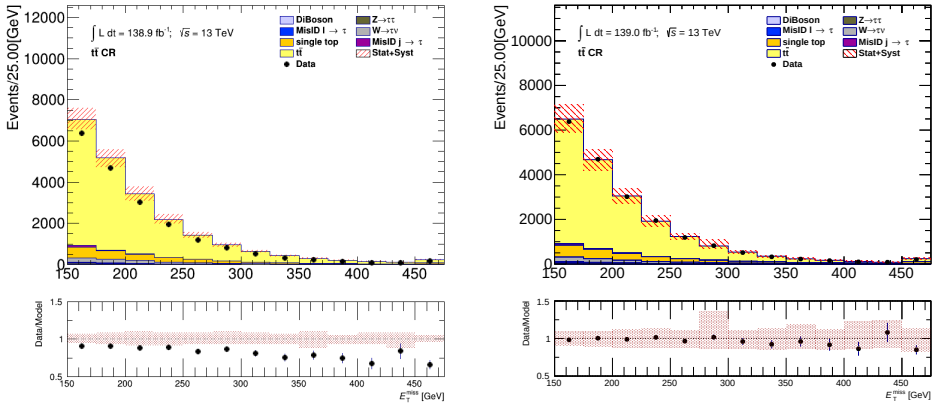

(c) (d)

Figure 9.4: [a] The distribution of the m_{eff} variable in the $\text{TTbar}_{\text{taujet}}$ control region before re-weighting factors are applied. [b] Re-weighting factors for the $\text{TTbar}_{\text{taujet}}$ control region with the fit applied (solid line) and error bands associated to the eigenvalues of the matrix error. [c] The distribution of E_T^{miss} of the $\text{TTbar}_{\text{taujet}}$ region before re-weighting factors are applied, [d] The distribution of E_T^{miss} of the $\text{TTbar}_{\text{taujet}}$ region after re-weighting factors are applied. The Monte Carlo samples now match the data within uncertainty bands.[54]

W+Jets Re-weighting

The re-weighting factors for the W+Jets background in both the Tau+Jets Lep signal regions are derived using the **jet multiplicity** of the jets in the W+Jets control region defined in section 9.7.8 and equation 9.2. The jet multiplicity, (N_{jets}) is simply defined as the total number of jets in the event. Binned distributions of the jet multiplicity are then fit to a polynomial function to allow application to distributions with other binning schemes. The polynomial function used in the fit is

$$f(N_{jets}) = a + b * N_{jets} + c * N_{jets}^2 + d * N_{jets}^3 \tag{9.6}$$

The derived re-weighting factors are obtained and are then applied to events entering the distributions of m_{eff} ,E_T^{miss}, p_t^τ and n_{jets} in their respective signal regions. The effect of the application of these re-weighting factors on the p_t^τ distribution for the W/Z Tau+Jets control region is shown below.

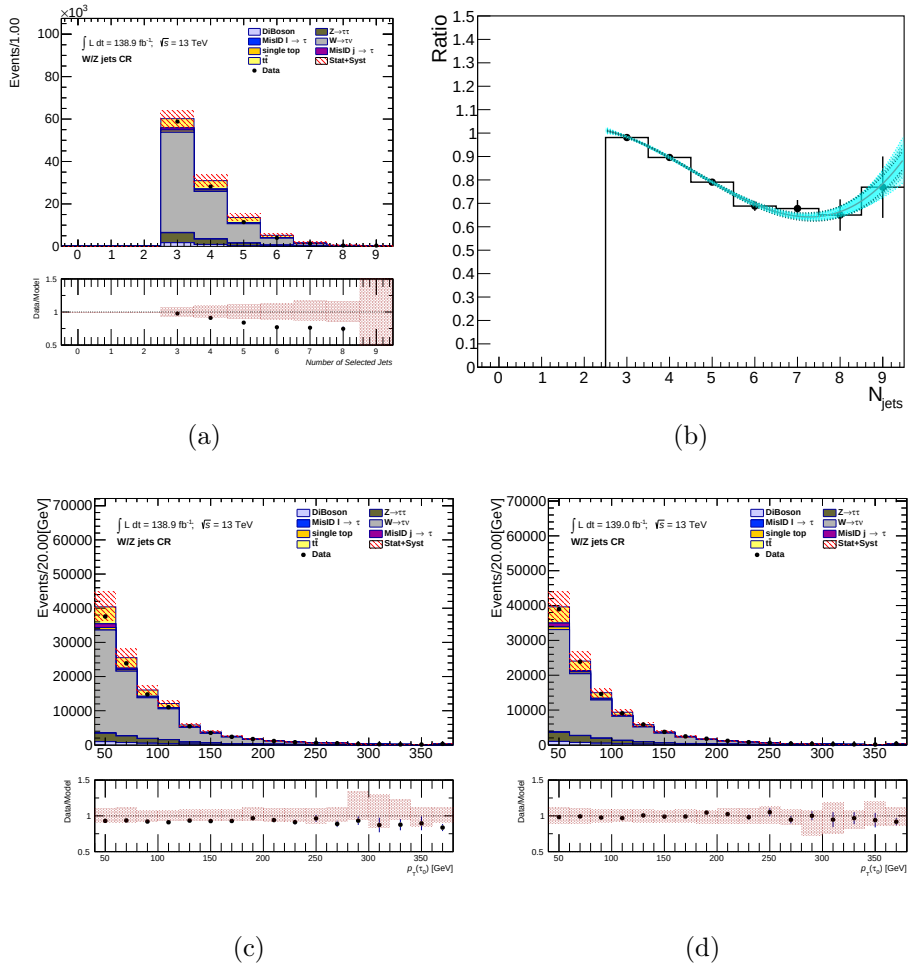

Figure 9.5: [a] The distribution of N_{jets} in W/Z+Jets CR of Tau+Jets channel before re-weighting procedure has been applied. [b] Distribution of re-weighting factors with the fit (solid line). [c] Original distribution of leading tau pt [d] distribution of leading tau pt after re-weighting procedure. [54]

9.8.2 Trigger Efficiency Scale Factors

Because the MET trigger efficiency is not modeled well by MC simulation, we must correct for the discrepancy in the trigger rate by applying a scale factor to the MET trigger selection in MC data. This is done by constructing a CR called the MET CR, defined in section 9.7.1, in which we determine scale factors to weight the MC of our analysis, so that it more closely aligns with observed data. These scale factors are derived for each trigger in each data-taking year (2015-2018), while considering 4 physics objects, and 2 kinematic situations. These objects are **tight** and **loose** τ objects, **medium** and **tight** electrons, events requiring at least 3 jets with a $p_t > 25GeV$ and events requiring at least 2 b-jets with a $p_t > 25GeV$.

To derive these scale factors, we first obtain binned histograms representing the trigger efficiency of MC and data in our control region, where we define the efficiency as the ratio of the number of selected objects in the MET CR with the additional MET trigger selection imposed and the number of selected objects in the MET CR without applying the MET trigger.

$$\epsilon = \frac{\text{event selection} + \text{chosen trigger}}{\text{event selection}} \tag{9.7}$$

The resulting histograms are then fit to an **error function** defined as

$$F(x) = 0.5\left[1 + erf\left(\frac{x - p_1}{p_2}\right)\right] \tag{9.8}$$

where p_1 and p_2 are free parameters that are allowed to float in order to obtain the best fit. The histogram is fit to equation 9.8 is performed to allow for the adjustment of the binning of the histograms where the scale factors will be applied.

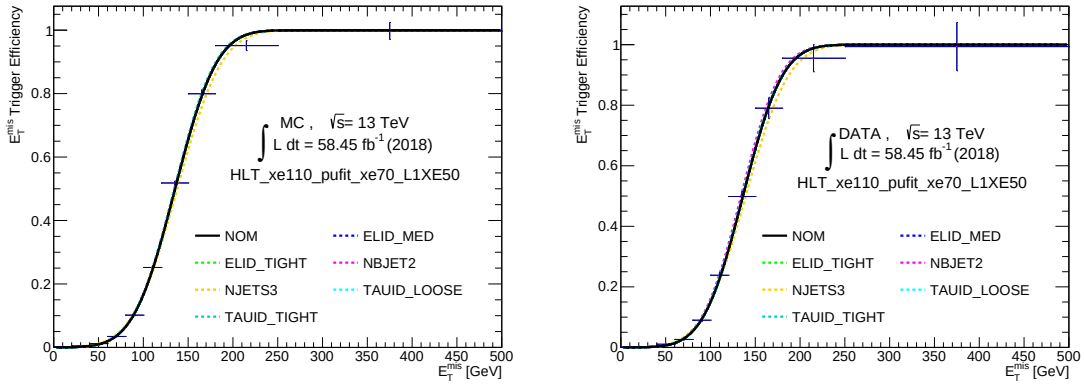

(a) (b)

Figure 9.6: Distributions of the MET trigger efficiency as a function of MET, fit with equation 9.8 for the different specified objects and kinematic situations using the MET control region. Here the 2018 trigger is shown. [54]

Following this treatment, the ratio of the MC and Data functions is taken to derive the scale factor function that will be applied to our MC.

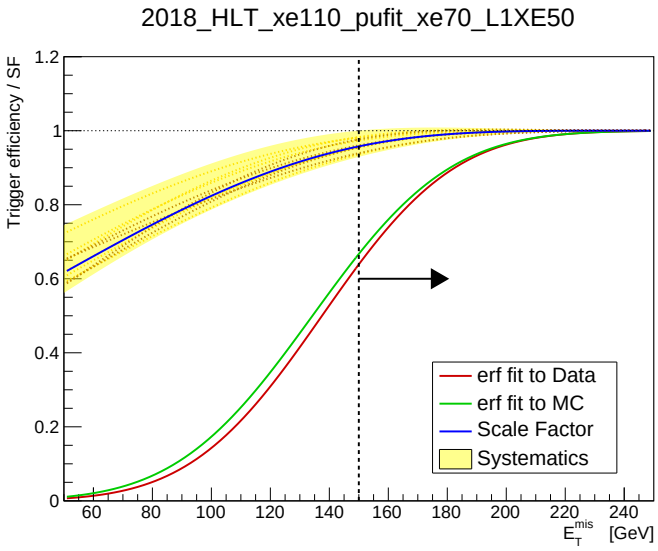

Figure 9.7: Ratio of NOMINAL functions shown in figure 9.6 used to derive the scale factors applied to MC objects. [54]

9.8.3 Misidentified Leptons faking τ candidates

Leptons can sometimes become misidentified as τ candidates, and make their way into our Tau+Lep signal regions. Because the mis-reconstruction rate of muons as taus is much lower than that of electrons faking taus, only fake tau background sources originating from electrons are considered in this analysis. Fortunately, these types of fakes are studied extensively by the E/Gamma working group, and provide scale factors to analysis groups to adjust their Monte Carlo samples to better agree with data. In order to validate these scale factors for our analysis, the $H^{\pm} \rightarrow \tau\nu$ analysis team has constructed a control region named the $Z \rightarrow ee$ control region defined in section 9.7.12 to perform these validations. The plots below show the agreement between MC-generated samples for the $Z \rightarrow ee$ control region and data samples for various kinematic variables. The agreement between MC and data was deemed to be satisfactory for this background source.

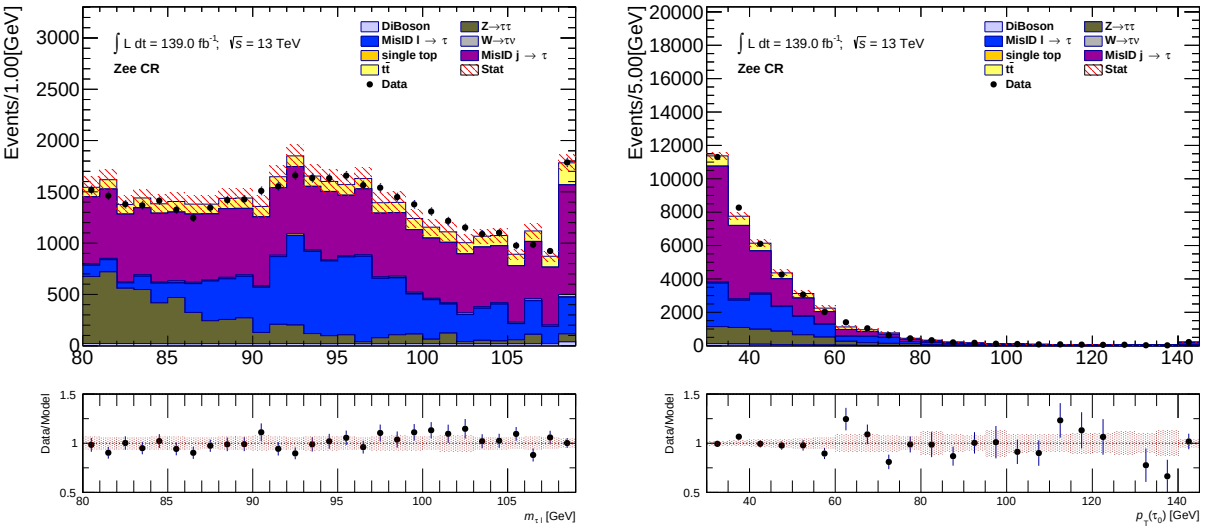

(a) (b)

Figure 9.8: Distributions of the [a] e-τ visible mass, [b] the p_t of the τ candidate in the $Z \to ee$ control region shown with the recommended $e \to \tau$ scale factors are applied. The $l \to \tau$ background includes all processes with e or μ reconstructed and identified as a τ that passes the **jetRNNSigMedium** working point. All other backgrounds correspond to events where the tau candidate is reconstructed correctly. [54]

9.8.4 Misidentified Jets faking τ candidates

Quark and gluon initiated jets that are mis-identified as τ candidates represent a significant background to our analysis. Unfortunately, backgrounds representing these so called "Fake" taus, are not modeled well by MC simulation and are not studied extensively by ATLAS working groups. We must therefore account for this background via the Fake Factor method described in section 9.8.5. In short, this is a data driven method used to estimate fake τ backgrounds in the p_t bins of the τ candidates of our signal regions. Fake factors are determined for 1 and 3 prong τ candidates in p_t bins ranging from $30 - 3000GeV$ and used to scale the MC background so that it agrees better with data. Fake factors are derived for the Tau+Jets and the Tau+Lep signal regions using a combination of the Fake Factors derived from the MultiJet and W+Jets control regions defined in sections 9.7.7, and 9.7.8, with the additional anti-τ selection defined in 9.7.6. These Fake Factors are validated using the b-veto (e, μ) and b-Veto MT100 control regions defined in sections 9.7.4 and 9.7.11. Fake factors for fake τ candidates coming from heavy flavor jets (c,b,s) are derived using the Inclusive control region defined in section 9.7.10 with the additional anti-τ selection, and validated using the b-Veto MT100 and Same Sign (e,μ) control regions defined in sections 9.7.4, 9.7.9.

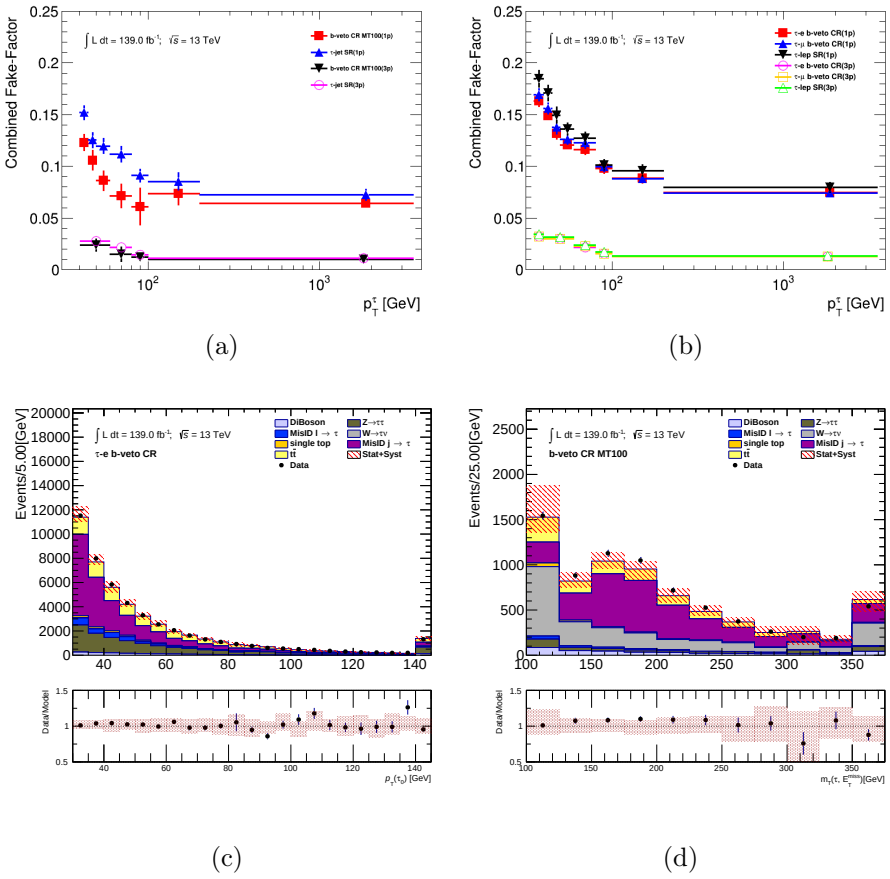

Figure 9.9: Combined fake factors for various regions including [a] τ+jets signal region and the [b] τ+lepton signal region. Distributions of [c] p_t^τ in the Tau+El b-veto region, and [d] m_T the b-Veto MT100 CR after application of combined fake factors. Error bars represent systematic uncertainties of the method. [54]

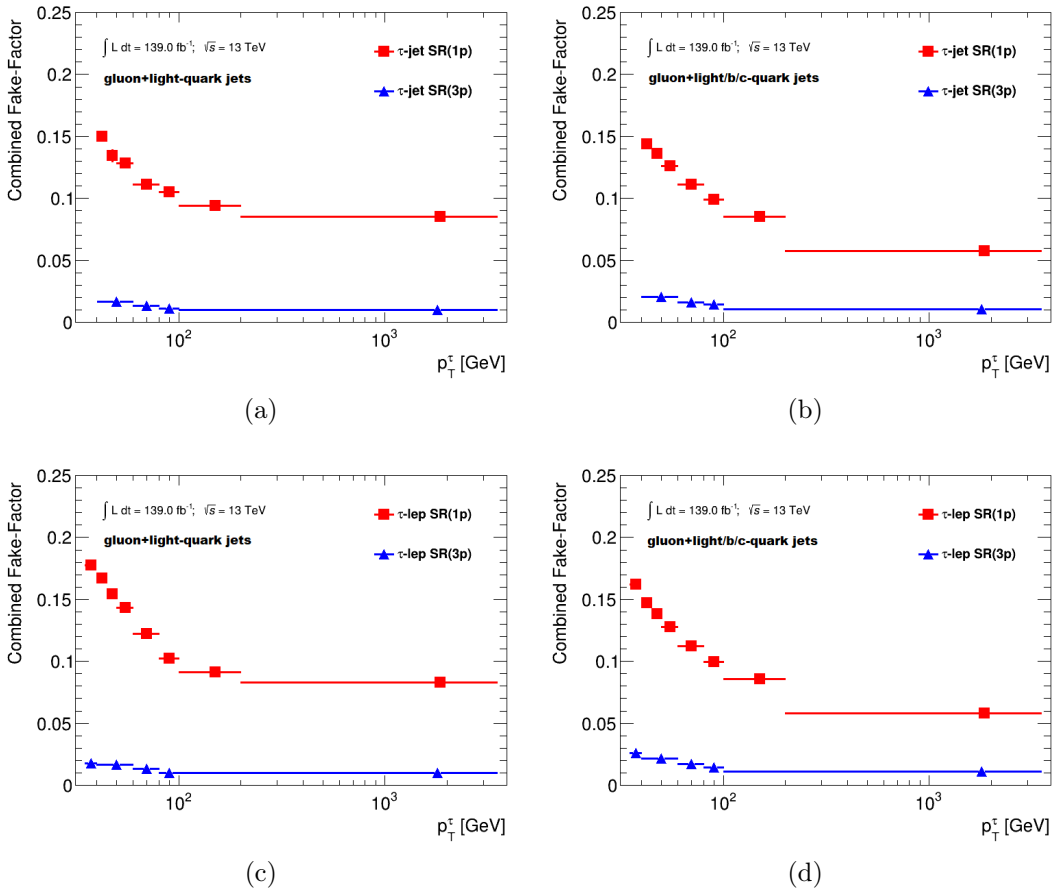

Figure 9.10: Combined fake-factors for 1 and 3 prong τ candidates, using [a][c] gluon+light-quark templates and [b][d] gluon+light/b/c-quark templates for the Tau+Jets and Tau+Lep signal regions. Error bars for $\mathrm{FF}^{\mathrm{gluon}}_{\mathrm{light}}$ represent uncertainties due to α_{MJ} fitting using template-fit method. [54]

9.8.5 The Fake Factor Method

The Fake Factor method is a data driven method used to estimate fake τ backgrounds in the p_t bins of the τ candidates of our signal regions. Fake Factors are determined for 1 and 3 prong τ candidates in p_t bins ranging from $30 - 3000GeV$ [7] using a template fit to the jet-width of the anti-τ candidates in the MultiJet (9.7.7) and W+Jets (9.7.8) control regions. The Fake Factor method is detailed extensively in citation [111], but is summarized below.

9.8.6 The MultiJet and W+Jets Fake Factors

Fake Factors are by definition the ratio of the number of fake $\tau_{had-vis}$ candidates in a given region that pass the τ selection, to the number of fake τ candidates that pass the anti-τ selection criteria 9.7.6 (Anti-Taus) in that same region.

$$FF = \frac{N_{\tau-id}}{N_{Anti-\tau-id}} \tag{9.9}$$

In order to account for the number of true-τ candidates making their way into the MJ and W+Jets control regions, the number of true taus ($N_{\tau-id}$) and anti-selected taus ($N_{anti-\tau}$) are adjusted before calculation of the Fake Factors through the following equations.

$$N_{\mathrm{CR}}^{\tau-\mathrm{id}} = N_{\mathrm{CR}}^{\tau-\mathrm{id}}(\mathrm{data}) - N_{\mathrm{CR}}^{\tau-\mathrm{id}}(\mathrm{MC}) \tag{9.10}$$

$$N_{\mathrm{CR,fakes}}^{\mathrm{anti}-\tau} = N_{\mathrm{CR}}^{\mathrm{anti}-\tau}(\mathrm{data}) - N_{\mathrm{CR,true}}^{\mathrm{anti}-\tau}(\mathrm{MC}) \tag{9.11}$$

In the MultiJet and W+Jets regions, the Fake Factors per p_t bin of the τ candidates can be measured outright by applying the tau and anti-tau selection criteria. This yields the FF_{MJ} and FF_{WJ} quantities shown in figure 9.11. It should be noted that combined fake factors defined as a linear combination of the MJ and W+Jets fake factors will be used to estimate the number of fake taus in our signal regions.

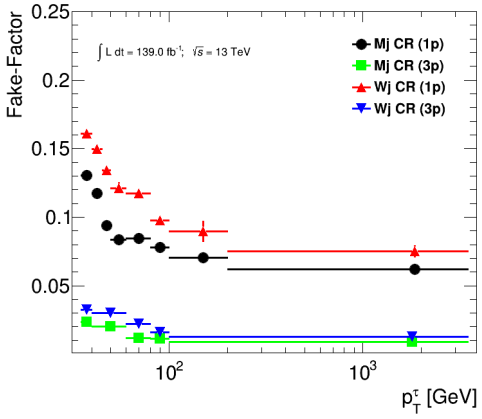

Figure 9.11: Fake Factors for the MultiJet and W+Jets control regions, binned in $\mathrm{p_T^\tau}$ bins for 1-prong and 3-prong τ candidates. The errors shown represent the statistical uncertainty. [54]

[7] The defined p_t bin edges for fake factors are: 30,35,40,45,50,60,80,3000

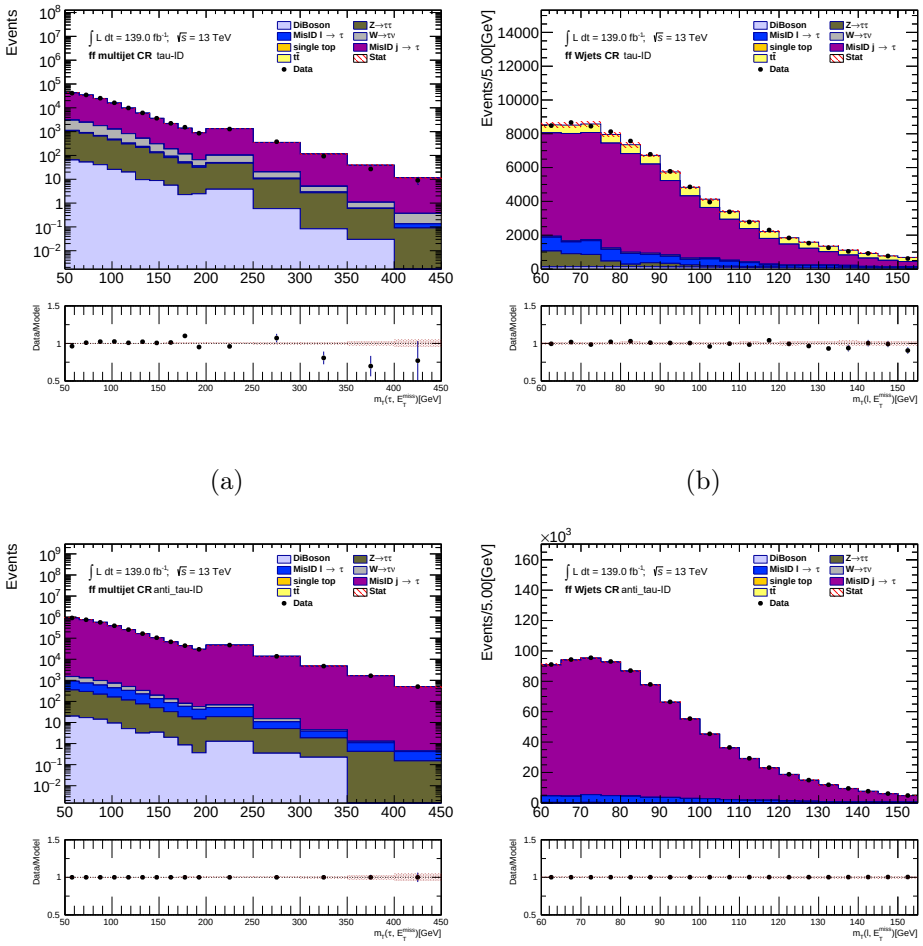

Figure 9.12: Transverse mass distributions for events passing the τ (top) and anti-τ identification criteria (bottom) in the multi-jet and the W+jets CR (right). [54]

9.8.7 Combined Fake Factors for signal regions FF_{SR}

The MultiJet and W+Jets regions were constructed to be dominant in gluon and quark initiated jets respectively. Since the Tau+Jets and Tau+Lep signal regions are expected to contain fakes of the same type, we can use the FF_{MJ} and FF_{WJ} Fake Factors to estimate the number of fake τ candidates in our signal regions, FF_{SR}. The Fake Factors for the signal regions are defined by the following equation.

$$\mathrm{FF_{SR}} = \alpha_{\mathrm{MJ}} \times \mathrm{FF_{MJ}} + (1 - \alpha_{\mathrm{MJ}}) \times \mathrm{FF}_{W+\mathrm{jets}}. \tag{9.12}$$

Where α_{MJ} can be estimated via a template fit method using the jet width distributions of the anti-taus in the MultiJet and W+Jets control regions.

Template Fit Method

The jet width, defined below

$$w_\tau = \frac{\sum\limits_{tracks} [p_T^{track} \times \Delta R(\tau, track)]}{\sum\limits_{tracks} [p_T^{track}]} \tag{9.13}$$

is used as a proxy variable to estimate the fraction of quark and gluon initiated jets f_q, f_g in the control regions of interest. Normalized distributions of w_τ that we call "templates" (Figure 10.1, left), are obtained for the MultiJet and W+Jets control regions for a given p_t bin we wish to derive a fake factor for. The content of the jet width bins for each distribution ($P_{\mathrm{bin}}^{\mathrm{Multi-Jet}}(x)$ and $P_{\mathrm{bin}}^{W+\mathrm{Jets}}(x)$) are then used to define the equation

$$P_{\mathrm{bin}}^{\alpha_{\mathrm{MJ}}}(x) = \alpha_{\mathrm{MJ}} \times P_{\mathrm{bin}}^{\mathrm{multi-jet}}(x) + (1 - \alpha_{\mathrm{MJ}}) \times P_{\mathrm{bin}}^{W+\mathrm{jets}}(x). \tag{9.14}$$

used to estimate the contributions of quark and gluon initiated jets for a given bin in the w_τ distribution of our signal region $P_{\mathrm{bin}}^{ROI}(x)$ (Figure 10.1, Middle).

A χ^2 fit is performed on the signal region distribution where one scans through the values of α_{MJ} until the value of χ^2 is minimized, (Figure 10.1, right). The function χ^2 to be minimized is

$$\chi^2_{\mathrm{bin}}\left(\alpha_{\mathrm{MJ}}\right) = \sum_{x=0}^{K+1} \frac{\left(P_{\mathrm{bin}}^{\alpha_{\mathrm{MJ}}}(x) - P_{\mathrm{bin}}^{\mathrm{ROI}}(x)\right)^2}{\left(\sigma_{\mathrm{bin}}^{\mathrm{template}}(x)\right)^2 + \left(\sigma_{\mathrm{bin}}^{\mathrm{ROI}}(x)\right)^2}, \tag{9.15}$$

here $\sigma_{\mathrm{bin}}(x)$ is the statistical uncertainty in a given bin and $K+1$ is the number of bins in the τ jet width template distribution (the number of degrees of freedom, or n.d.f.). The distribution of χ^2_{bin} is then a χ^2-function with K degrees of freedom, with a mean and a variance of K and $2K$. Once the minimal value of α_{MJ} is obtained, it is then plugged back into equation 9.12 to obtain the final Fake Factor. This procedure is performed for each pt bin in our fake factor production scheme, and for regions with 1 and 3 prong τ candidates.

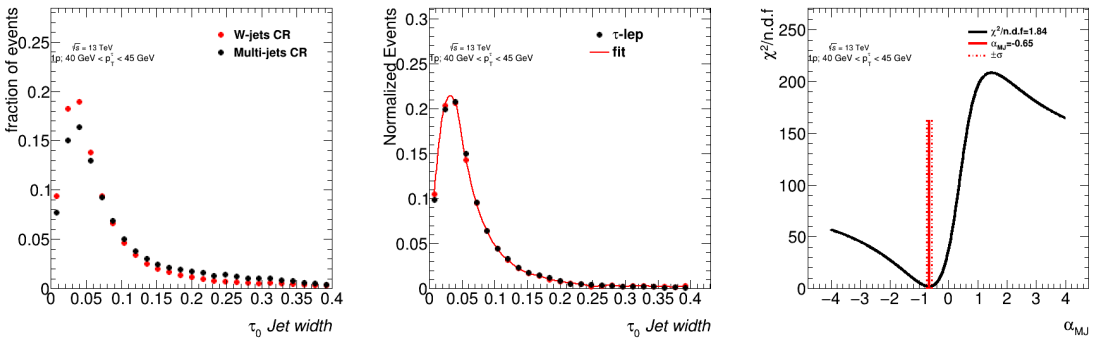

Figure 9.13: Estimation of α_{MJ} in the Tau+Lep signal region for 1-prong τ candidates with pt between $40GeV$ and $60GeV$. **Left** : Jet width templates for the MultiJet and W+Jets control regions for 1-prong taus. **Middle** : Distribution of jet width for the 1-prong Tau+Lep signal region fitted using the templates in (Left). **Right** : χ^2/ndf distribution fit as a function of α_{MJ} to the Tau+Lep jet width distribution. The error on α_{MJ} is defined by the band at $\chi^2_{\mathrm{min}}/\mathrm{ndf} + \sqrt{\frac{2}{\mathrm{ndf}}}$. [54]

9.9 Systematic Uncertainties

An accurate estimation of experimental and systematic uncertainties is crucial in any analysis. Assessing how well we can measure object properties, and the reconstruction of objects themselves plays a large role in determining the total number of events making it into our signal, background, control, and validation regions. This analysis required the use of many systematic uncertainties relating to each of the objects used (9.2.1). Many of these systematics follow standard recommendations from their corresponding working groups. This section gives a brief summary of a few systematic uncertainties implemented by the $H^{\pm} \to \tau\nu$ analysis team. A full list of the systematics used in this study and the object that they belong to is shown in Appendix A.7.

9.9.1 Detector related uncertainties

In order to be reconstructed, simulated particle objects must be propagated through a Geant4 model of the ATLAS detector. Ultimately the modeling capabilities of these objects depend on how well the sub-components of ATLAS can measure their properties. Contributions to systematic uncertainties due to instrumental effects, and reconstruction and identification of physics objects are called detector-related uncertainties. The impact of detector-related uncertainties for each of the physics objects contributing to the event yields of the Tau+Jets and Tau+Lep regions are obtained from the working groups that derived them. These uncertainties are then propagated through the Parameterized Neural Network where we take the percent difference in event yields for each variation as the $\pm 1\sigma$ error bars. The uncertainty coming from luminosity measurements are set to a flat 0.83%, as recommended by ATLAS working groups.

9.10 Effect of systematic uncertainties on final PNN distributions

The effect on the total yields for select TauJet systematics on the TTBar background making it into the Tau+Jets Signal region (9.4.2) after symmetrization are shown below. Plots here represent the effect of a given systematic on the PNN score distribution binned with the final binning scheme shown in appendix (A.11) and after (9.15.4) is performed. PNN bins are displayed with uniform binning for visibility of the bin content. The true bin content is preserved.

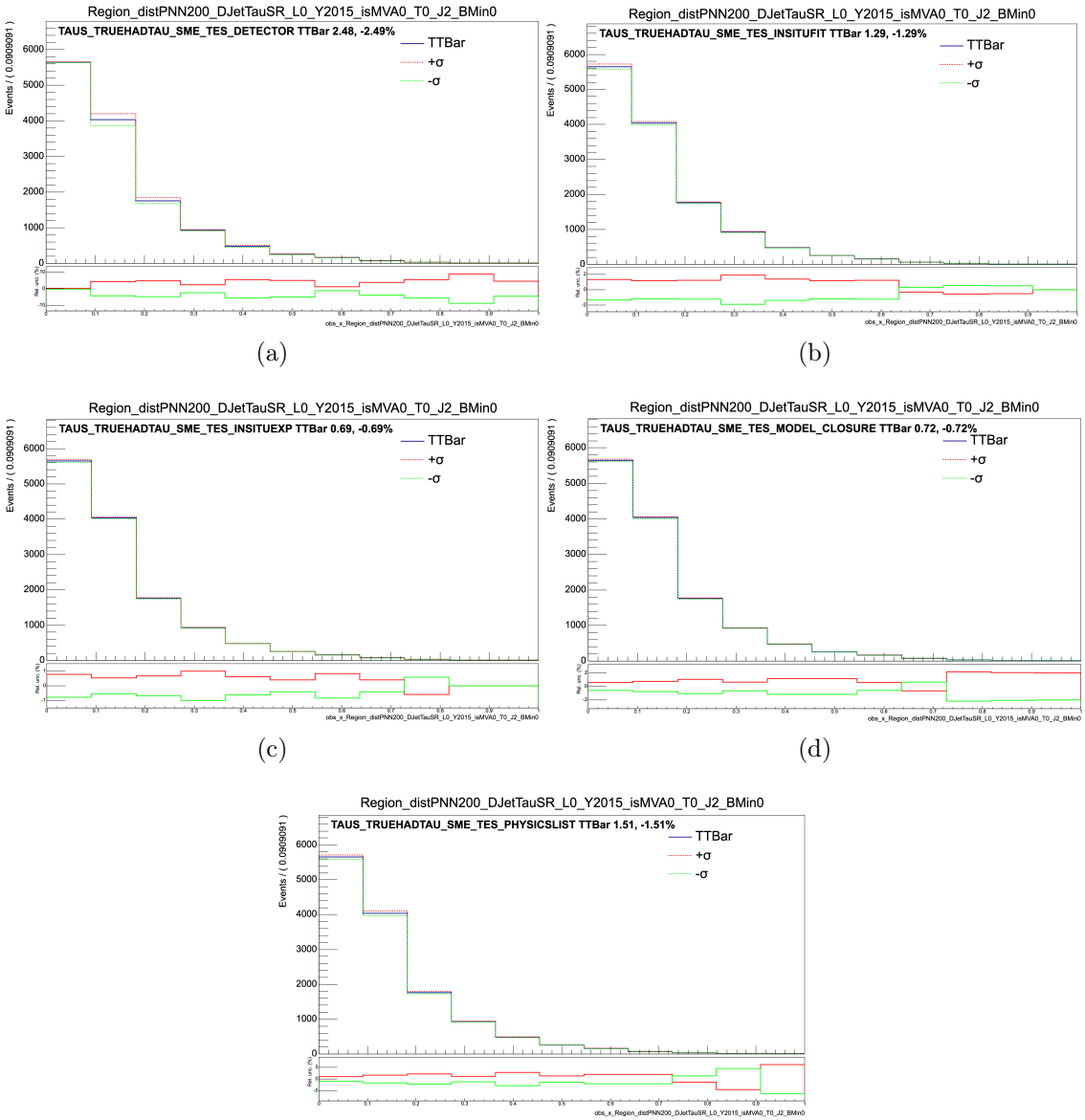

Figure 9.14: Systematic envelopes on of select τ related uncertainties in the TTbar background making it into the TauJets signal region after symmetrization is performed, and are displayed with a uniform bin width.

9.11 Fake Factor Uncertainties

The calculation of fake factors as defined in 9.8.5 required the $H^{\pm} \to \tau\nu$ analysis team to estimate the source of uncertainties on various steps of the calculation. Among these were a conservative uncertainty of 50% on the number of True MC taus used in our MC subtraction 9.10, an uncertainty from MC modeling of TauID scale factor at 5%, as well as systematic uncertainties in the calculation of the Fake factor fit parameter α_{MJ} (9.12) and fit method, and finally uncertainties on heavy flavor FakeFactor contributions and Smirnov transformations. These uncertainties are placed on the fake jet background QCD. Table 9.6 shows a summary of the effect on the total event yields for the Tau+Jets and Tau+Lep signal region from the different sources of FF uncertainties. A '•' icon in the shape column indicates that the uncertainty was propagated through to the PNN score envelopes differently bin by bin for a given $H^{\pm}$ mass hypothesis.

	τ+jets		τ+lepton	
Source of uncertainty	Effect on yield	Shape	Effect on yield	Shape
Fake factors: Statistical uncertainties	3.9%		3.2%	
Fake factors: True τ in the anti-τ CR	+3.4% -3.2%		+4% -4.3%	
Fake factors: τ RNN Identification SF	2.7%		2.7%	
Fake factors: α_{MJ} uncertainty	3.6%	•	1.9%	•
Fake factors: α_{MJ} fitting strategy	1.6%	•	2.8%	•
Fake factors: Smirnov transform	0%	•	0%	•
Fake factors: Heavy flavor jet fraction	5.9%	•	6.3%	•

Table 9.6: Effect on the shape variation and the yields of systematic uncertainties associated with the data-driven fake factor method, used to estimate the $j \to \tau$ background in the τ+jets and τ+lepton channel. [111]

9.11.1 Scale Systematic on W+Jets

The $H^{\pm} \to \tau\nu$ analysis uses a set of 6 scale systematics to account for the theoretical uncertainty on W+Jets processes concerning the QCD scale. This systematic is called wtaunu_scale_MUR. To build an envelope of a final scale systematic for our PNN score distributions, The up and down variations for this systematic are built according to the prescription here, where I loop through the bin content of the 6 scale variations to find the bin by bin maximum and minimum values of the scale variations, the maximum values of the set are used to build the up variation, and the minimum values of the set are used to build the down variation.

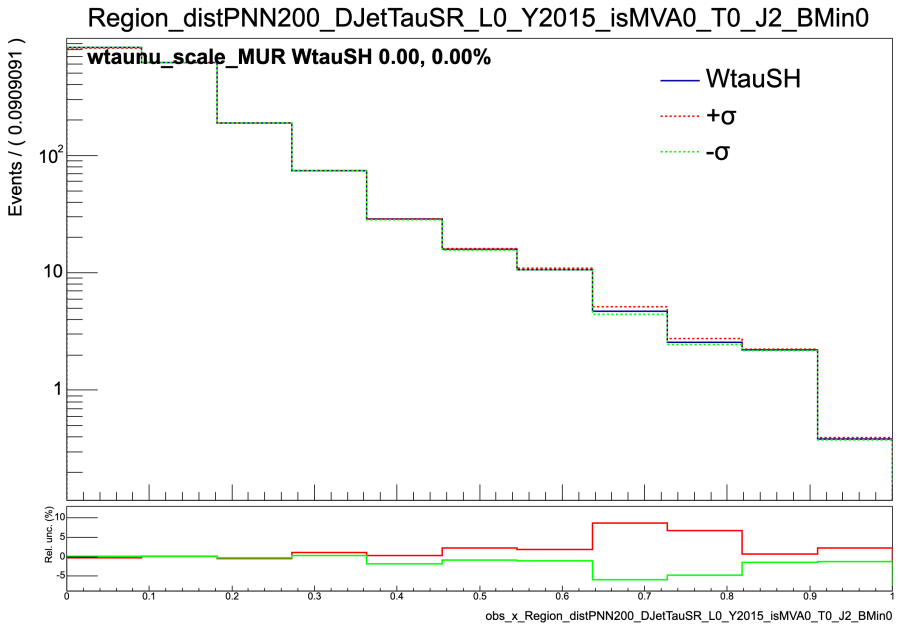

Figure 9.15: The systematic envelope for wtaunu_scale_MUR on the Wtaunu background of the TauJets PNN score when evaluated with the 200GeV $H^{\pm}$ mass hypothesis.

9.12 Impact of uncertainty types on Asimov limits

In order to understand the impact of the different sources of uncertainty on final observable $\mu = \sigma(pp \to tbH^+) \times \mathcal{B}(H^+ \to \tau\nu)$, I developed a code base that would include and exclude groups of systematics from our final fit. The impact of different sources of systematics on the final observable can be seen in table 9.7 where in general systematics reduce our sensitivity when compared to stat. only limits. These effects are larger in the low-mass region much more than in high mass. This is due to statistical limitations on signal efficiency at low mass that come as a result of region definitions. In summary, the total effect of all systematics on the arbitrary mass points 170GeV and 1000GeV show an impact of 75% and 15% respectively.

Source of systematic uncertainty	Impact on the expected limit (stat. only) in % $m_{H^+} = 170GeV$	$m_{H^+} = 1000GeV$
Experimental		
luminosity	5.44	0.02
trigger	5.62	0.01
tau	22.21	1.18
jet	15.38	0.52
electron	0.88	< 0.01
muon	1.01	0.02
met	35.08	0.03
SingleTop	26.71	0.41
Fake-factor method	12.05	1.06
Signal and background models		
$t\bar{t}$ modelling	15.55	0.17
W/Z+jets modelling	1.95	6.70
cross-sections ($W/Z/VV/t$)	3.45	0.44
H^+ signal modelling	2.60	< 0.01
All	75.34	15.06

Table 9.7: Impact of systematic uncertainties in percent on the expected 95% CL limit on $\sigma(pp \to tbH^+) \times \mathcal{B}(H^+ \to \tau\nu)$, for two H^+ mass hypotheses: 170GeV and 1000GeV in the combined channel. The impact is obtained by comparing the expected limit considering only statistical uncertainties (stat. only) with the expected limit when a certain set of systematic uncertainties is added in the limit-setting procedure. The row "All" is obtained by comparing the expected limits when all systematics are added in the limit setting procedure to when only statistical uncertainties are considered [111].

9.13 Data Samples

The following sections provide a description of how the data used in this analysis was simulated/collected, and what tools were used. In general, Monte Carlo (MC) data in this analysis was used to estimate background contributions, set expected limits, and understand the effects of systematic uncertainties. MC data was simulated using the ATLAS Geant4 model, and the same reconstruction chain as the observed data. The tools used to generate the MC data include MadGraph+aMC@NLO, Pythia8 v8.2.3, EvtGen v1.6.0, Herwig7 v7.0.4, Powheg-Box v2, MadSpin, and Sherpa 2.2.1. The observed data represents the full $140.0 \pm .83 fb^{-1}$ collected during Run 2 of the LHC. A full list of data samples used in this analysis can be found in the appendices of citation [111].

9.13.1 Signal Monte Carlo

The charged Higgs signal events $H^{\pm} \rightarrow \tau\nu$ were generated using **MadGraph5** according to the dominant Feynman diagrams of their mass range (Figure 9.1). These processes were generated with either Leading Order (LO) and or Next to Leading Order (NLO) diagrams depending on the availability of the tools at the time of production.

- Low mass $H^{\pm}$ signal events ($80GeV \leq m_{H^{\pm}} \leq 140GeV$) @ LO
- Intermediate mass $H^{\pm}$ signal events ($140GeV < m_{H^{\pm}} \leq 200GeV$) @ LO
- High mass $H^{\pm}$ signal events ($200GeV < m_{H^{\pm}} \leq 3000GeV$) @ NLO

All MadGraph output is then interfaced with Pythia8 v8.230 [112] to generate the subsequent hadron production. An event filter, described in table 9.8, is applied to the generated signal events to allow for maximal retention of signal events when forming our signal regions. The event filter is implemented such that the simulation of events is performed until the desired number of events passes our event filter. Additional cuts to reconstructed objects are applied post-event filter, and so some statistics are lost although not as much as when no event filter is applied. At the lowest, 95% of simulated events are retained after reconstruction cuts 9.2.1 are applied.

Variable	Tau+Lep SR	Tau+Jets SR
$p_{\mathrm{T}}(\tau)$	> 25 GeV	> 25 GeV
$\lvert\eta\rvert(\tau)$	< 2.5	< 2.5
p_{T} $(b-\text{quark})$	> 18 GeV	> 18 GeV
$\lvert\eta\rvert$ $(b-\text{quark})$	< 2.6	< 2.6
N_{jets} $(p_{\mathrm{t}} > 18, \lvert\eta\rvert < 2.6)$	$\geq 3(2)$ $\tau + e/\mu$	≥ 4
p_{t} $(e/\mu))$	> 25 GeV	–
$\lvert\eta\rvert$ (e/μ)	< 2.6	–
True $E_{\mathrm{T}}^{\mathrm{miss}}$	–	> 100 GeV

Table 9.8: Displayed are the cuts applied to generator level objects that form our the event filter for the Tau+Jets and Tau+Lep signal regions [54].

9.13.2 Background Monte Carlo

The sources of background to the $H^{\pm} \to \tau\nu$ process are simulated using the ATLAS Geant4 simulation package and reconstructed in the same way as the observed data. A number of event generators are used to generate background processes according to their nature. Overall, significant background contributions include, $t\bar{t}$, single top, W(Z)+Jets, and DiBoson processes. A list of backgrounds simulated and by which tools is shown in Table 9.9.

Background process	Generator & parton shower	Dataset number(s)	Cross section (in pb)
$t\bar{t}$ with at least one lepton ℓ	Powheg-Box v2 & Pythia8	410470	831.76
Single top-quark t-channel	Powheg-Box v2 & Pythia8	410658–9	70.43
Single top-quark s-channel		410644-5	3.35
Single top-quark Wt-channel		410646–9	79.25
$W(\ell\nu)$ + jets	Sherpa 2.2.1	364170–83 ($e\nu$) 364156–69 ($\mu\nu$) 364184–97 ($\tau\nu$)	2.0×10^4 2.0×10^4 2.0×10^4
$Z/\gamma^*(\ell\ell, \nu\nu)$ + jets	Sherpa 2.2.1	364114–27 (ee) 364100–13 ($\mu\mu$) 364128–41 ($\tau\tau$)	2.1×10^3 2.1×10^3 2.1×10^3
WW	Powheg-Box v2 & Pythia8 v8.210	36160x [x=0,6]	54.81
WZ		36160x [x=1,2,7,8,9]	26.45
ZZ		3616xy [xy=03,04,10,11]	8.41

Table 9.9: Table of background processes produced along with their generator, dataset numbers (DSIDs), and production cross sections σ. Here, ℓ refers to the three lepton flavours e, μ and τ. All background cross-sections are normalized to NNLO predictions, except for diboson events, where the NLO prediction is used. [54].

All background samples are weighted according to k factors defined as $k = \frac{\sigma_{LO}}{\sigma_{NLO}/\sigma_{NNLO}}$ so the amount of MC data generated matches the most recent theoretical predictions. In order to mimic pile-up effects and achieve similar conditions to the observed data, each of the background samples was subject to so-called "minimum bias" events where they underwent inelastic collisions generated by Pythia. These events were then weighted such that the average number of collisions per bunch crossing μ was in accordance with that of the observed data.

9.13.3 Observed Data

The observed events used in this analysis represent the full $140.0 \pm .83 fb^{-1}$ collected during Run 2 of the LHC. This data was collected with the ATLAS detector between 2015 and 2018, with the requirements that all ATLAS subsystems were fully operational, all data collected corresponds to a collision energy of $\sqrt{s} = 13TeV$, and from the Good Run Lists (GRLs) in Appendix A.2.

9.14 The Parameterized Neural Network

The $H^{\pm} \rightarrow \tau\nu$ analysis uses the output score from a set of PNNs [99] as a multivariate discriminant to distinguish between MC generated $H^{\pm}$ signal and background events. PNNs are a kind of neural network that allows for the classification of objects when one of the object classes can be represented by a smoothly varying parameter. Given that the predicted mass of the $H^{\pm}$ represents a smoothly varying parameter that spreads over a rather large range (80-3000GeV), the analysis team decided that the best approach would be to use a Parameterized Neural Network as opposed to training a dedicated neural network for each mass point in our search range. **4 PNN sets are trained for this analysis**, specific to the signal region and the prong-ness of the τ in the event. The 4 network sets are specific to the 1-prong Tau+jets, 1-prong Tau+Lep, 3-prong Tau+jets, and the 3-prong Tau+Lep. To retain enough training statistics, the 3-prong networks are trained using events that contain both 1 and 3-prong τ candidates, while the 1-prong networks are trained only with events containing 1-prong τ candidates. In the Tau+Lep networks, events from both the Tau+El and Tau+Mu channels are used in training to retain sufficient statistics in the training sets. The network performances were validated by evaluating the $\text{TTBar}_{TauJets}$ control region (9.7.2) with additional Tau+Jets selection for the Tau+Jets network, and the Di-lep b-tag (9.7.5), b-Veto (9.7.4) control regions with additional Tau+Lep selections for the Tau+Lep network.

9.14.1 PNN Architecture

The network architectures for the Tau+Jets and Tau+Lep signal regions differ. The highest-performing and final architectures for the networks were determined through hyperparameter optimization. The Tau+Jets PNNs used in the analysis are mass-parameterized neural networks with 4 hidden layers, 64 neurons in each layer, using a 10% dropout rate, 120 batch size, sigmoid activation function, and binary cross entropy loss function. The Tau+Lep PNNs used in the analysis are mass parameterized neural networks, with 3 hidden layers, 128 neurons in each layer, using a 10% dropout rate, 1024 batch size, Adam optimizer, LeakyRelu activation functions for each layer with a value $\alpha = 0.05$[8], and a binary cross entropy function as a loss function.

[8] α is defined to be the slope of the RELU (Rectified Linear Unit) function in the negative portion of the x-axis.

9.14.2 PNN Training

As mentioned in section 9.14, 4 network sets are trained for each signal region. These networks are trained on either exclusively 1-prong or 1 and 3-prong τ candidates. The networks were trained using the Keras and Tensorflow libraries, where Keras is used as the front end, and Tensorflow as a back end. This training was done using 32 unique signal data sets generated for each $H^{\pm}$ mass hypothesis, and 32 clones of background data. In order to remove any bias in network performance due to highly skewed data sets, the background events are weighted by a factor of $w = N_S^i/N_B^i$, where i is an $H^{\pm}$ mass, N_S^i and N_B^i are the number of signal and background events with a given a $H^{\pm}$ mass as a parameter respectively. For each mass hypothesis, the mass parameter in the input layer was set to match the $H^{\pm}$ mass hypothesis, and training would ensue using a k-fold method (9.14.3)[113], where $k = 5$. A batch size of 128 was also used in the training. The training dataset was then split 80/20 at runtime where 80% of the set was used to train, and 20% was used to validate the model in real-time. Parameterized networks can be trained on all of it's input parameter possibilities at once by attaching a mass hypothesis variable to the input dataset that acts as an input variable.

9.14.3 The k-Fold training method

When training and evaluating machine learning models, it is important to be able to reliably estimate its performance to be sure that its separation strength will hold in situations where it evaluates real data. The $H^{\pm} \to \tau\nu$ analysis team uses a k-fold training method, inspired by the k-Fold cross-validation method used to estimate the performance of a network by training and evaluating k-independent models using a single dataset [113]. We begin the k-Fold training method by randomizing the order of the events in our dataset and splitting it into k portions each with a roughly equal number of events.

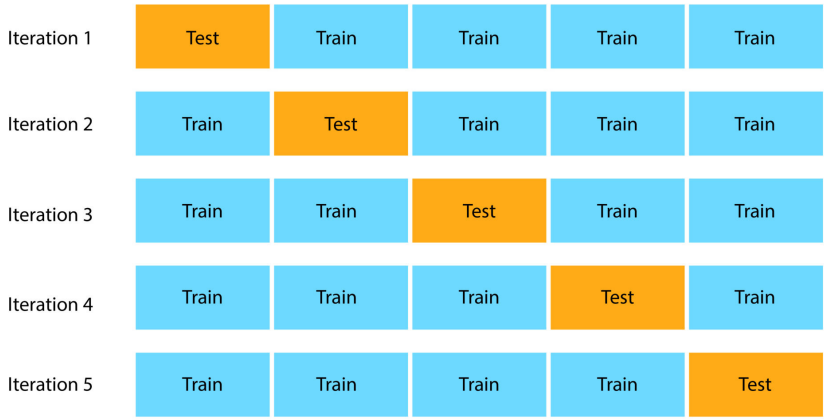

Figure 9.16: A visualization of the k-fold cross validation method where k=5. [114]

We obtain 'k' trained models by training the network on all k subsets except the first, all k subsets except the second, etc. Each trained model is the result of what is called a "fold" in the k-Fold method. Above is a table illustrating the process

of training and evaluating the networks. This analysis uses a 5-fold (k=5) PNN training framework to protect from overtraining and increase statistics for fitting. These 5 PNNs sets evaluate events by splitting them by their EventNumber%5 and passing them to the PNN with the corresponding 0-4 index.

9.14.4 PNN Training Variables

The input variables used to train the PNN networks are components of the 4-momentum of the tau, b-jets, and QCD-jets of the objects in the event. As well as the characteristics of the MET, the polarization of the τ objects in the event (Υ_τ), and the true charged Higgs mass parameter ($m^{H^+}_{truth}$) of the event. The variables used to train the Tau+Jets PNN and Tau+Lep PNN differ based on the number of objects available in the signal regions. i.e. the Tau+Jets region (9.4.2) requires at least 3 QCD jets be in its signal region, as opposed to the Tau+Lep (9.5.2) which requires at least 1. Although both signal regions require at least 1 τ jet and 1 $b-jet$, which leaves the possibility of more than 1 entering the signal regions, only the leading p_t jet is used at training and evaluation time. It should be noted that Υ_τ is only used to evaluate 1-prong networks. This is because of the powerful discriminating power of the variable in 1 prong tau cases

PNN input variable	τ+jets	τ+lepton
p_t^τ, η^τ , ϕ^τ, E^τ	•	•
p_t^ℓ, η^ℓ , ϕ^ℓ, E^ℓ		•
$p_t^{b\text{-jet}}$, $\eta^{b\text{-jet}}$, $\phi^{b\text{-jet}}$, $E^{b\text{-jet}}$	•	•
$p_t^{\text{jet-1}}$, $\eta^{\text{jet-1}}$, $\phi^{\text{jet-1}}$, $E^{\text{jet-1}}$	•	•
$p_t^{\text{jet-2}}$, $\eta^{\text{jet-2}}$, $\phi^{\text{jet-2}}$, $E^{\text{jet-2}}$	•	
$p_t^{\text{jet-3}}$, $\eta^{\text{jet-3}}$, $\phi^{\text{jet-3}}$	•	
$p_t^{\text{jet-2}}$	•	•
MET, $\Delta\phi_\tau^{MET}$	•	•
${\Upsilon_\tau}^a$	•	•
$m^{H^\pm}_{\text{truth}}$	•	•

[a] For 1-prong τ, only

Table 9.10: A table of the input variables used to train the PNN in the τ+jets and τ+lepton channels. Here, ℓ indicates the selected lepton (e or μ), jet-1,2,3 indicates leading, sub-leading and sub-sub-leading jets ordered in decreasing p_t. Because the physics object selection is different between signal regions, some objects like a second or 3rd QCD jet may not be available to the PNN. The variable Υ is related to the polarization of the τ-lepton and is only defined for 1-prong tau candidates.[54]

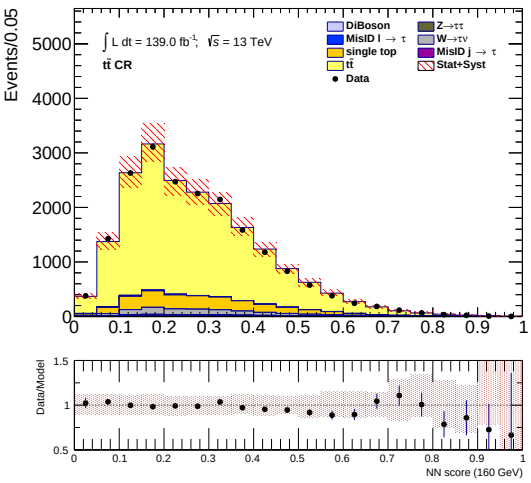

(a)

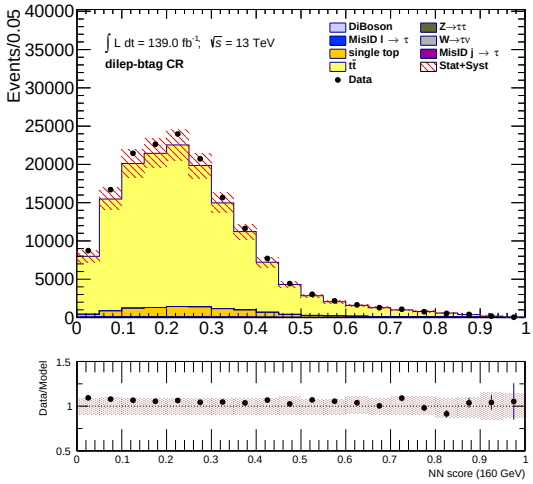

(b)

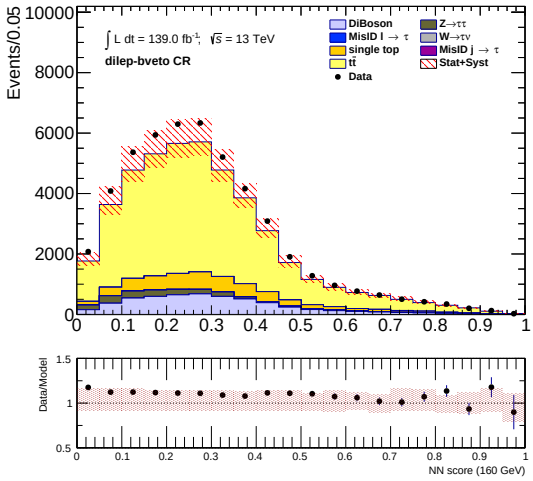

(c)

Figure 9.17: PNN score distributions of MC vs Data for various mass points and control regions. Events are evaluated with the 160GeV PNN mass parameter, in the [a] TTBar$_{TauJets}$ control region, [b] dilep b-tag control region for the Tau+Lep channel, [c] dilep b-veto control region for the Tau+Lep Network. The uncertainty bands in the ratio plots include both the statistical and systematic uncertainties of simulated events. [54]

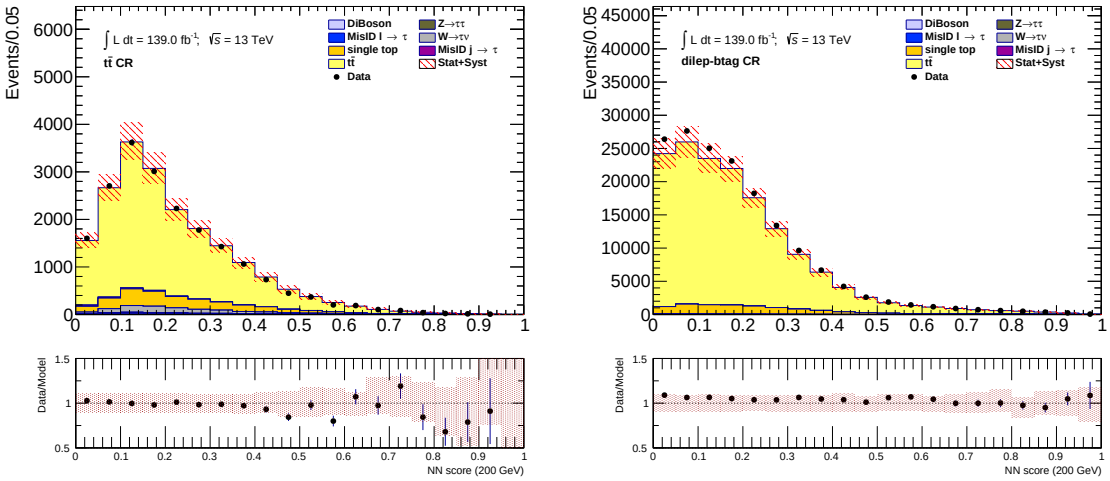

(a)

(b)

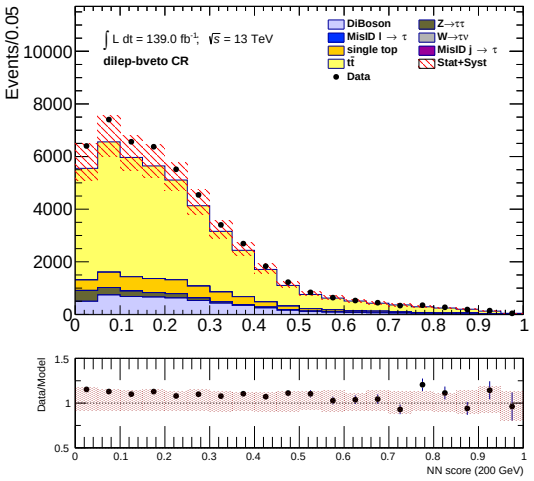

(c)

Figure 9.18: PNN score distributions of MC vs Data for various mass points and control regions. Events are evaluated with the 200GeV PNN mass parameter, in the [a] TTBar$_{TauJets}$ control region, [b] dilep b-tag control region for the Tau+Lep channel, [c] dilep b-veto control region for the Tau+Lep Network. The uncertainty bands in the ratio plots include both the statistical and systematic uncertainties of simulated events. [54]

9.15 Statistical Analysis

The following section contains details on the configuration of the analysis code base used to produce final results. The work contained within the section is largely my own and describes the binning scheme (9.15.2), the symmetrization (9.15.4), and pruning of systematics (9.15.5), fit procedure (9.15.6), and signal injection studies (9.15.8) I performed in the $H^{\pm} \rightarrow \tau\nu$ analysis.

9.15.1 Description of Fit Model

To perform statistical analysis I developed a custom branch of Workspace Maker to convert TH1F histograms of signal, background and systematic variations into RooWorkspaces, and fit the resulting PNN score distributions to Observed and Asimov data. The analysis procedure begins with a set of merged histogram files that contain charged Higgs signal, background, and systematic distributions for each charged Higgs mass hypothesis. This merged histogram set, is then split into individual files that contain only signal, background, and systematics for each charged Higgs mass hypothesis, 100, 200, 300 GeV, etc. They are then passed to Workspace Maker which identifies the relevant sample and their associated systematics and then converts them to RooWorkspaces after applying symmetrization, and pruning.

9.15.2 Binning Schemes

Histograms for signal, background, and their systematic distributions are rebinned from their original format of 1000 evenly spaced bins such that they will produce the best-expected limits while remaining statistically significant and allowing for the convergence of all fits on observed data. Through various trials on Asimov data, I found that a reverse log binning scheme with 14 logarithmic-ally spaced bins showed the best limit production for the Tau+Jets channel, and a hybrid of a reverse log binning scheme with 17 logarithmic-ally spaced bins for mass points above 140 GeV and the binning scheme used from the 2015 analysis[9] for mass points at and below 140 GeV showed the best limit production for the Tau+Lep channel. These were the final binning schemes used in the analysis. These bins are then merged from right to left, until each of the resulting bins has a minimum of 10 Asimov background entries, see (9.15.3). The reverse log binning schemes are defined as those which are produced by the following Python [115] code

$$bin_{arr} = (np.flipud(10 * *np.linspace(np.log10(0.1), np.log10(1.0), n_{bins})) * -1) + 1.0 + 0.1 \tag{9.16}$$

This equation results in a binning scheme that has "n_bins" evenly spaced bins in log space. The value "n_bins" was determined to be the optimal number of bins for a given channel through binning studies.

[9] Starting binning schemes for the Tau+Lep channel where the charged Higgs mass hypothesis is at or below 140 GeV is shown in Appendix A.11.

9.15.3 Minimum Number of Entries

As mentioned in (9.15.2), the minimum number of entries per bin was set to 10 for all channels. A minimum of 10 MC events per bin was chosen to allow for the convergence nuisance parameter pull fits for all mass points while having a minimal effect on our expected limits as seen below.

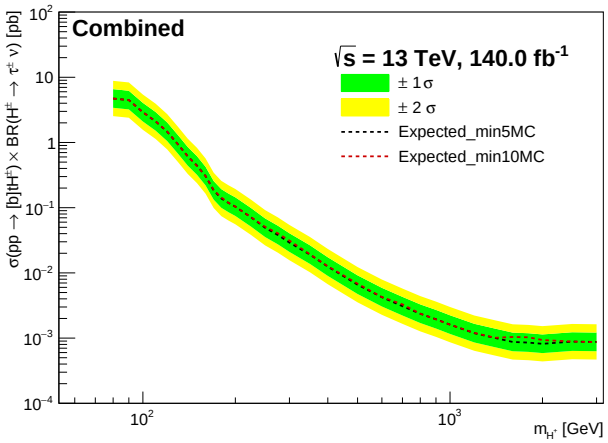

(a)

Figure 9.19: Expected 95% CL exclusion limits on (a) $\sigma(pp \to tbH^+) \times \mathcal{B}(H^+ \to \tau\nu)$ as a function of the charged Higgs boson mass in $140.0 fb^{-1}$ of pp collision data at $\sqrt{s} = 13$TeV, in the Combined channel. Here limits are presented in the cases where rebinning is done until a minimum of 5 MC (Black) and 10 MC (Red) events are in each bin. In the case of the 5MC events are required, one- and two-standard-deviation uncertainty bands are also shown.

9.15.4 Symmetrization

Four kinds of symmetrization are applied to the systematics in this analysis, these symmetrization procedures are applied to one-sided systematics for which either an up or down variation is missing, to systematics that are two-sided from the outset but symmetrized to yield the most conservative systematic envelope, or to systematics with two variations that are identical and need to be symmetrized to resolve nuisance parameter impact fit failures. Symmetrization method 1 is a standard reflection method used in WSMaker, symmetrization methods 2, 3 and 4 were written and integrated into the WSMaker framework by me.

- **Symmetrization method 1:** If a systematic variation is missing, the missing partner variation is set to be a reflection of the present distribution about the nominal distribution. This is the treatment reccomended by the Physics Modelling Group for the following 1 sided systematics:
  ttbar_PDF_X, MET_SoftTrk_ResoPara, MET_SoftTrk_ResoPerp, singletop_model_POWHEG_HERWIG7, ttbar_model_POWHEG_HERWIG7, singletop_DS, singletop_hdamp.
- **Symmetrization method 2:** If a systematic variation is missing, the missing partner variation is set to be 1% of the reflection of the present distribution

about the nominal distribution. It is used to construct a two sided systematic, required by workspace maker, such that it preserves its one sided systematic property but is not pruned unnecessarily. This treatment is applied to 2 systematics, w_sig_filter_effi_met and w_sig_filter_effi_int.

- **Symmetrization method 3:** This symmetrization method is also referred to as maxFullSym internally. For any two sided systematic, A bin by bin comparison of up and down systematic variations takes place where the smaller of the two variations is replaced with a reflection of the larger variation about nominal, yielding a conservative envelope. This treatment is applied to all systematics in the $H^{\pm} \rightarrow \tau\nu$ analysis, with the exception of those mentioned in Symmetrization method 1, 2, 4, rQCD_Heavy_Flavour_FF and wtaunu_scale_MUR. The later two systematics have no symmetrization applied, as symmetrization is specifically reccomended against, or are intrinsically one sided.
- **Symmetrization method 4:** This symmetrization method is applied to systematics with 2 variations that are identical, namely JET_JER_EffectiveNP_1-7 to resolve fit failures in the staged unblinding process. Here the down variation (both are identical) is set to be 1% of the reflection of the up variation about the nominal distribution.

9.15.5 Pruning

In the $H^{\pm} \rightarrow \tau\nu$ analysis pruning of systematics is done on a sample by sample basis where each shape and normalization contribution to a systematic variation for a given signal and background source is subject to a series of pruning functions of which specify a given criteria for pruning. If the systematic contribution fails to meet the criteria, they are "pruned" and are removed from contributing in the final fit. The pruning methods are shown in appendix (A.13).

9.15.6 Fit Procedure

An unconditional fit to Asimov \ Observed data is performed using the RooFit package within workspace maker when performing nominal \ Observed \ signal injection studies. Pre and post-fit plots, as well as pull and correlation plots are created while performing an unconditional binned likelihood fit to the data where mu is given an initial value of $\mu = 0.0$ and is allowed to float. Keeping the signal strength μ floating allows for the determination of the best-fit value of μ when performing our fit. Unconditional initial fits for pull plots were done where μ was set to have an initial value of $\mu = 0.01$ for most mass points where no complications were met. In unconditional initial pull fits where complications were met, μ was set to have an initial value of $\mu = 0.23333333$ or $\mu = 0.1$ to allow for fit convergence.

9.15.7 Limit setting procedure

Limits are set while considering either an individual or a simultaneous binned likelihood fit of PNN score distributions in the three signal regions (τ+jets, τ+electron, and τ+muon). The fit is performed using the RooFit package within workspace

maker, where the negative log-likelihood is minimized with respect to the signal strength parameter μ. The minimizer used by RooFit to perform limit setting is the Minuit2 minimizer set with a precision of 0.005, and target confidence level of 0.05, corresponding to a 95% confidence interval.

9.15.8 Signal Injection Studies

In order to verify the fitting machinery used to obtain nuisance parameter pull plots and exclusion limit plots, as well as to anticipate any potential problems with fits, I developed a code base to perform signal injection studies within the WSMaker framework. The complete set of signal distributions used to perform signal injection studies was done using a charged Higgs signal with masses of 130, 500, and 1000 GeV but for brevity, only the results of the 500 GeV signal injection are shown. In all cases, the signal was injected using the expected value for μ obtained after performing an Asomiv-only fit at a 95% confidence interval. The signal injected distribution was constructed by summing the individual background PNN score distributions along with a selected charged Higgs signal distribution scaled by the selected μ. The 500 GeV $H^+ \rightarrow \tau\nu$ signal was injected by adding the 500 GeV charged Higgs distribution scaled by $\mu = 0.0066$, which was selected to be equal to the median expected limit for the combined channel at 500GeV in this test iteration. The data distributions that were fit for each PNN mass hypothesis take the following form.

$$data_{PNN80} = Bkg_{PNN80} + Sig^{PNN80}_{500H^{\pm}} * \mu_{500}$$

$$\vdots$$

$$data_{PNN3000} = Bkg_{PNN3000} + Sig^{PNN3000}_{500H^{\pm}} * \mu_{500}$$

Figure 9.20: Equations explaining how the data distributions used in the signal injection studies were constructed.

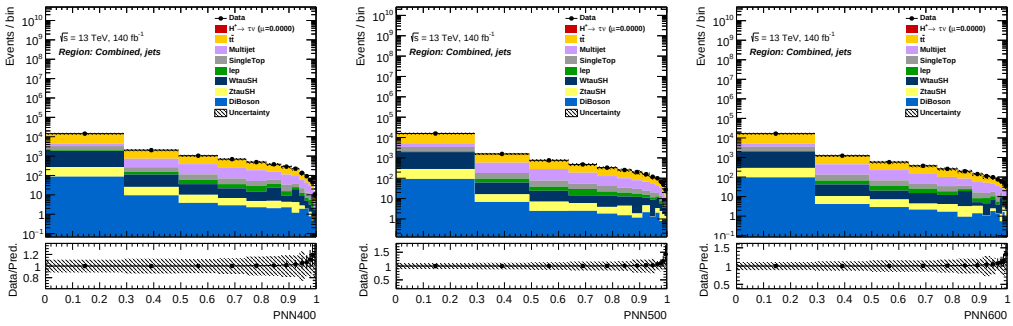

(a) TauJets PNN 400 (b) TauJets PNN 500 (c) TauJets PNN 600

Figure 9.21: PreFit Plots TauJets Signal Injection: 400-600

After the signal was injected, datasets were prepared for each PNN mass hypothesis and signal region, and fit for the combined channel. The fit was performed using the same fitting procedure as the nominal analysis. The pre-fit and post-fit plots

for each PNN mass hypothesis where the signal was injected can be seen below. Of particular interest in the post-fit plots is the value of μ in parenthesis. This value represents the best-fit mu value achieved by the fitting machinery.

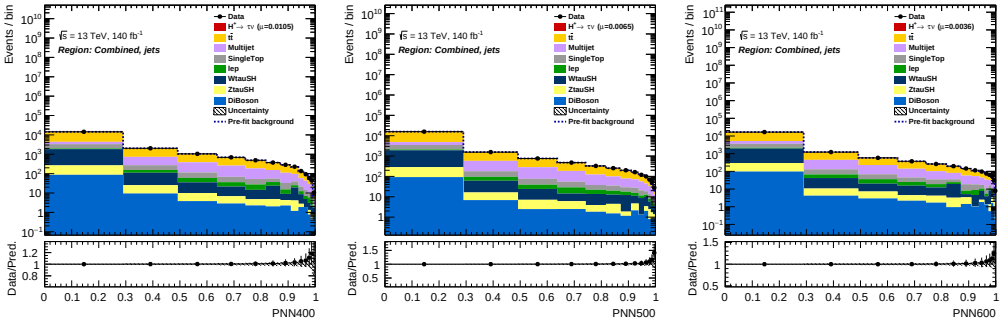

(a) TauJets PNN 400 (b) TauJets PNN 500 (c) TauJets PNN 600

Figure 9.22: PostFit Plots TauJets, Signal Injection: 400-600

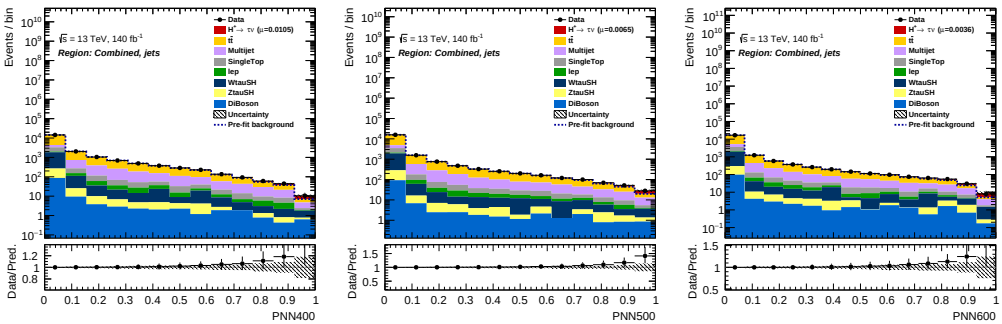

(a) TauJets PNN 400 (b) TauJets PNN 500 (c) TauJets PNN 600

Figure 9.23: PostFit Plots TauJets with uniform bin spacing, 500 GeV H+ Signal Injection: 400-600. Here the bin widths have been **displayed** as uniform to allow for a better presentation of the $H^{\pm}$ signal scaled to the converged upon mu value in the fit. Thus, these plots do not display accurate bin edges with respect to their axis.

After fitting was performed, one can observe that the best-fit value of μ for the 500 GeV post fit plot converges to the value of $\mu = 0.0065^{+0.0035}_{-0.0035}$, which very closely matches $\mu = 0.0066$ used to inject the signal, validating our fit machinary annd procedure.

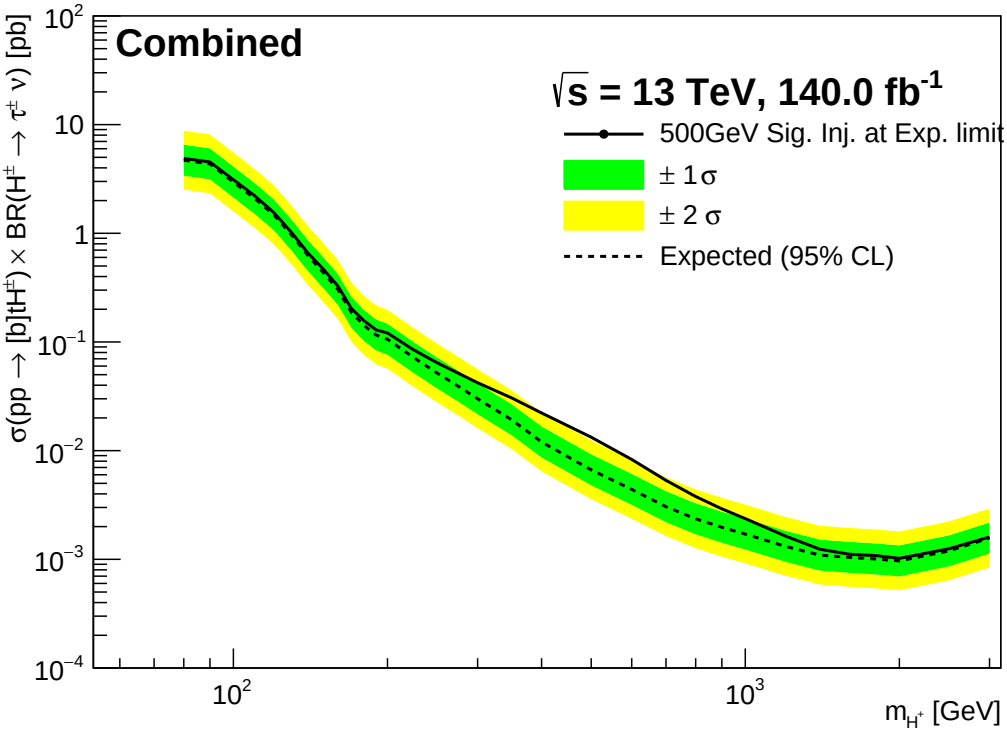

Figure 9.24: Expected 500 GeV H^+ Signal Injected 95% CL exclusion limits for $\sigma(pp \to tbH^+) \times \mathcal{B}(H^+ \to \tau\nu)$ and as a function of the charged Higgs boson mass in $140.0 fb^{-1}$ of pp collision data at $\sqrt{s} = 13$TeV, after a combination of the τ+jets and τ+lepton channels. In the case of the expected limits, one- and two-standard-deviation uncertainty bands are also shown.

9.16 Staged Unblinding: $36fb^{-1}H^{\pm} \to \tau\nu$ result

In order to make the analysis as robust as possible, the analysis team decided to perform a staged un-blinding process whereby we would reprocess the $36fb^{-1}$ data collected in 2015 and 2016 before running fits and unveiling our final result on the full run 2 dataset. Major differences between the analysis that took place in 2015-16 [116] include the improvement/addition/replacement of various systematics, changes in the binning of the histograms used in the final fits, and the use of a mass-parameterized neural network in place of a Boosted Decision tree as an MVA. Notable differences between NP ranking plots of the previous and reprocessed analysis results were determined to be due to changes in the processing of systematics and a change to a PNN. In conclusion, the results from the reprocessed unblinded 2015-2016 dataset were in agreement with the 2015-16 result [116].

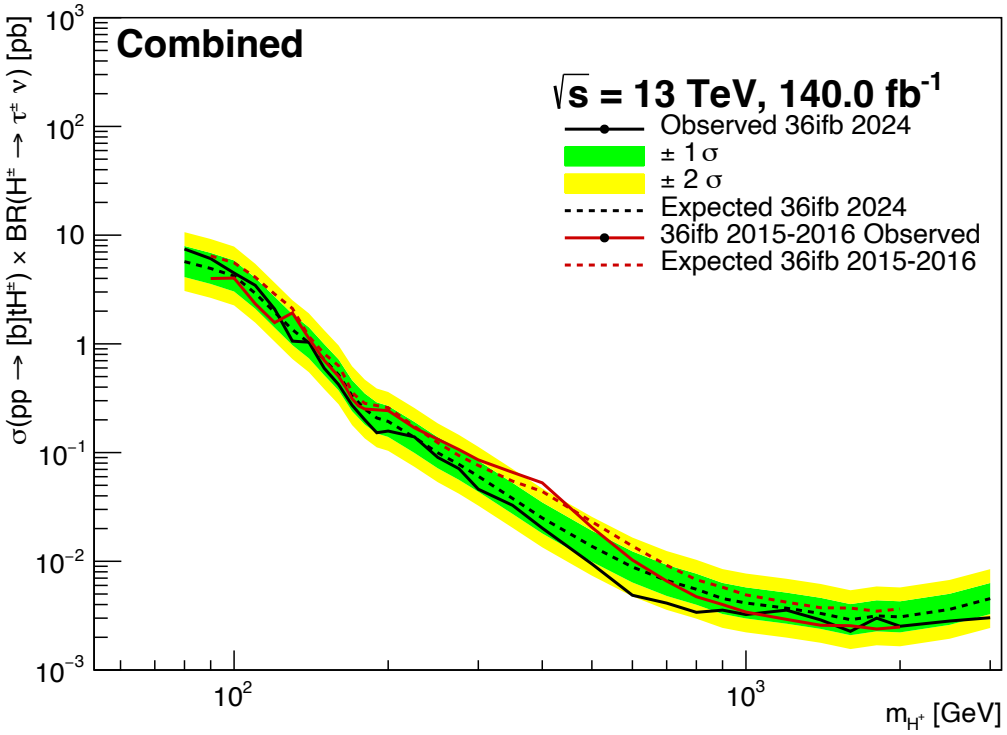

Figure 9.25: Observed and expected 95% CL exclusion limits on $\sigma(pp \to tbH^+) \times \mathcal{B}(H^+ \to \tau\nu)$ as a function of the charged Higgs boson mass in $36.1fb^{-1}$ of pp collision data at $\sqrt{s} = 13$ TeV, after combination of the τ+jets and τ+lepton channels. In the case of the expected limits for the 2024 $36fb^{-1}$ reprocessed result, one- and two-standard-deviation uncertainty bands are also shown. As a comparison, the Expected and Observed exclusion limits from the 2015-16 result are shown in red.

9.17 $140 fb^{-1}$ Results

Statistical analysis on the parameter of interest μ, defined as $\mu \equiv \sigma(pp \to tbH^+) \times \mathcal{B}(H^+ \to \tau\nu)$ was performed using a simultaneous binned likelihood fit on the individual and combined channels: $\tau + Jets$, $\tau + e$ and $\tau + \mu$. The test statistic $\tilde{q}_\mu$ [117] is used to test the compatibility of the data with the background-only and signal+background hypotheses. The test statistic is defined for different regions of best fit $\hat{\mu}$, and is computed from the profile likelihood ratios shown below:

$$\tilde{q}_\mu = \begin{cases} -2\ln\frac{\mathcal{L}(\mu,\hat{\hat{\theta}}(\mu))}{\mathcal{L}(0,\hat{\hat{\theta}}(0))}, & \hat{\mu} < 0 \\ -2\ln\frac{\mathcal{L}(\mu,\hat{\hat{\theta}}(\mu))}{\mathcal{L}(\hat{\mu},\hat{\theta})}, & 0 \leq \hat{\mu} \leq \mu \\ 0 & \hat{\mu} > \mu \end{cases} \tag{9.17}$$

In the above equations, the likelihood $\mathcal{L}(\hat{\mu}, \hat{\theta})$ is defined to be the multiplication of Poisson probability terms over all bins of the PNN score distributions in the channels that are included in the fit. Statistical and systematic uncertainties were taken into account via nuisance parameters defined by θ. In these equations, $\hat{\mu}$ and $\hat{\theta}$ are the values of the parameters that maximize the likelihood function, while $\hat{\hat{\theta}}(\mu)$ are the values of the nuisance parameters that maximize the likelihood function for a given value of the signal strength μ. Unconditional fits to Asimov and Observed data were performed to calculate 95% CL exclusion limits on μ using the CL_s method defined in [118]. Bins for the PNN score arrays for each mass hypothesis were chosen using a reverse log binning scheme, where by bins were collapsed from right to left such that each bin contained a minimum of 10 MC background events. These binning schemes were chosen to yield optimal exclusion limits in studies undergone using Asimov Data. Signal injection tests were performed where expected limits for the combined channel for the 130, 500, and 1000GeV mass hypothesis were injected to ensure proper convergence on mu (9.15.8)

After likelihood fits were performed on observed data, no excess above 2σ was observed in 95% CL exclusion limits on $\sigma(pp \to tbH^+) \times \mathcal{B}(H^+ \to \tau\nu)$ for any of the search regions in the analysis and are thus in agreement with SM predictions. Upper limits on the production on $\sigma(pp \to tbH^+) \times \mathcal{B}(H^+ \to \tau\nu)$ have been lowered to values between 4.5093pb for 80GeV and 4×10^{-4}pb for 3000GeV. The most significant excesses in this analysis are present for the 250 GeV $H^\pm$ mass hypothesis in the Combined and Tau+Jets Channel, with local excesses of 1.05σ and 1.82σ respectively. Full results for each of the individual signal regions can be found in Appendix A.8.

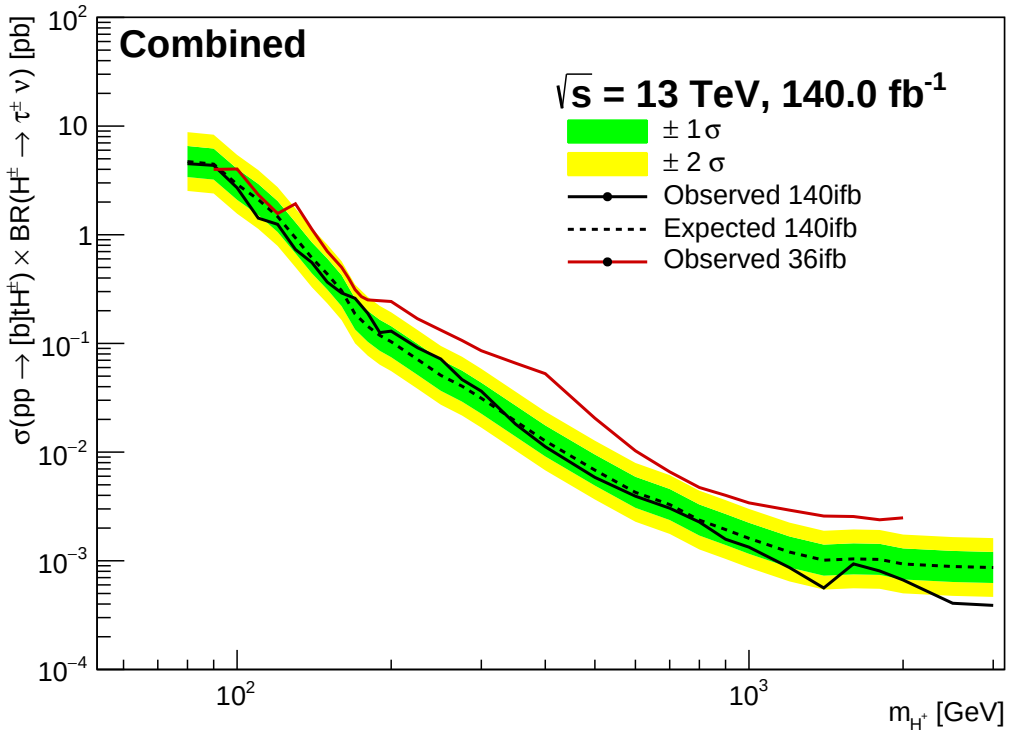

Figure 9.26: Observed (solid black) and expected (dashed-black) 95% CL exclusion limits on $\sigma(pp \to tbH^+) \times \mathcal{B}(H^+ \to \tau\nu)$ as a function of the charged Higgs boson mass in $140 fb^{-1}$ of pp collision data at $\sqrt{s} = 13$ TeV, after combination of the τ+jets and τ+lepton channels. In the case of the expected limits, one- and two-standard-deviation uncertainty bands are also shown. As a comparison, the observed results for the combined channel from the $36.1 fb^{-1}$ analysis [119] using 2015 and 2016 data are overlayed (red).

Mass	-2 Sigma	-1 Sigma	Expected	+1 Sigma	+2 Sigma	Observed
80	2.5299	3.3964	4.7136	6.5599	8.7940	4.5093
90	2.3964	3.2172	4.4649	6.2138	8.3301	4.3509
100	1.5623	2.0974	2.9108	4.0511	5.4307	2.7045
110	1.1324	1.5203	2.1099	2.9363	3.9363	1.4222
120	0.7888	1.0590	1.4696	2.0453	2.7419	1.2474
130	0.5031	0.6754	0.9373	1.3044	1.7487	0.7325
140	0.3287	0.4413	0.6124	0.8523	1.1426	0.5551
150	0.2338	0.3139	0.4357	0.6064	0.8129	0.3671
160	0.1641	0.2203	0.3057	0.4254	0.5703	0.2914
170	0.1002	0.1345	0.1867	0.2599	0.3484	0.2602
180	0.0771	0.1035	0.1437	0.2000	0.2680	0.1894
190	0.0637	0.0855	0.1186	0.1651	0.2214	0.1258
200	0.0556	0.0747	0.1036	0.1442	0.1933	0.1298
225	0.0383	0.0515	0.0714	0.0994	0.1332	0.0915
250	0.0273	0.0367	0.0509	0.0708	0.0949	0.0719
275	0.0217	0.0291	0.0405	0.0563	0.0755	0.0466
300	0.0168	0.0226	0.0313	0.0436	0.0584	0.0364
350	0.0103	0.0139	0.0193	0.0268	0.0360	0.0181
400	0.0068	0.0091	0.0127	0.0176	0.0236	0.0112
500	0.0037	0.0049	0.0068	0.0095	0.0127	0.0059
600	0.0023	0.0031	0.0043	0.0059	0.0080	0.0039
700	0.0018	0.0024	0.0033	0.0046	0.0061	0.0030
800	0.0013	0.0017	0.0024	0.0033	0.0044	0.0023
900	0.0010	0.0014	0.0019	0.0027	0.0036	0.0016
1000	0.0009	0.0012	0.0016	0.0022	0.0030	0.0013
1200	0.0006	0.0009	0.0012	0.0017	0.0022	0.0009
1400	0.0005	0.0007	0.0010	0.0014	0.0019	0.0006
1600	0.0006	0.0007	0.0010	0.0014	0.0019	0.0009
1800	0.0006	0.0007	0.0010	0.0014	0.0019	0.0008
2000	0.0005	0.0007	0.0009	0.0013	0.0017	0.0007
2500	0.0005	0.0006	0.0009	0.0012	0.0017	0.0004
3000	0.0005	0.0006	0.0009	0.0012	0.0016	0.0004

Table 9.11: 95% CL upper limits on $\sigma(pp \to tbH^+) \times \mathcal{B}(H^+ \to \tau\nu)$ in pb for Combined channel.

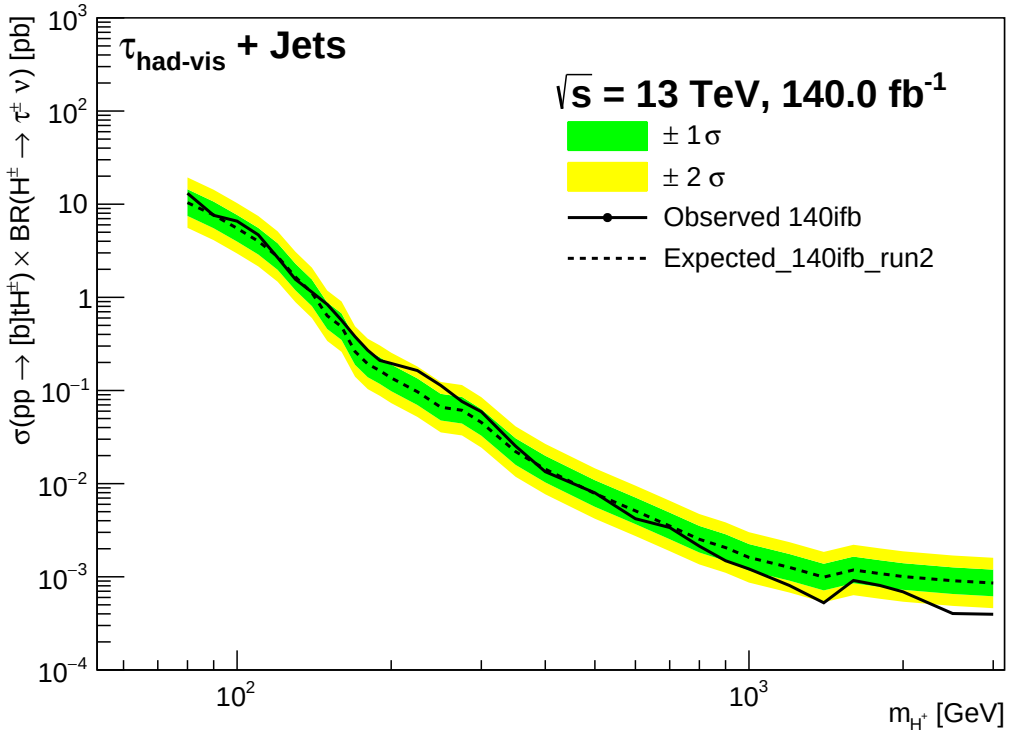

Figure 9.27: Observed and expected 95% CL exclusion limits on $\sigma(pp \to tbH^+) \times \mathcal{B}(H^+ \to \tau\nu)$ as a function of the charged Higgs boson mass in $140 fb^{-1}$ of pp collision data at $\sqrt{s} = 13$TeV, for the stand alone τ+jets channel. One- and two-standard-deviation uncertainty bands are shown for the expected limits.

Mass	-2 Sigma	-1 Sigma	Expected	+1 Sigma	+2 Sigma	Observed
80	5.5747	7.4841	10.3866	14.4551	19.3781	13.0952
90	4.1097	5.5173	7.6570	10.6563	14.2855	7.5935
100	2.9560	3.9685	5.5075	7.6649	10.2753	6.5773
110	2.1485	2.8843	4.0029	5.5709	7.4682	4.6890
120	1.4705	1.9742	2.7398	3.8131	5.1117	2.6736
130	0.8879	1.1921	1.6544	2.3024	3.0865	1.5611
140	0.5995	0.8049	1.1170	1.5546	2.0840	1.1378
150	0.3405	0.4571	0.6344	0.8829	1.1836	0.8403
160	0.2596	0.3486	0.4837	0.6732	0.9025	0.5672
170	0.1405	0.1887	0.2618	0.3644	0.4885	0.3784
180	0.1034	0.1388	0.1926	0.2681	0.3594	0.2701
190	0.0877	0.1177	0.1634	0.2274	0.3049	0.2104
200	0.0733	0.0984	0.1365	0.1900	0.2547	0.1952
225	0.0520	0.0699	0.0970	0.1350	0.1809	0.1637
250	0.0355	0.0477	0.0661	0.0920	0.1234	0.1133
275	0.0329	0.0442	0.0613	0.0854	0.1144	0.0762
300	0.0244	0.0327	0.0454	0.0632	0.0848	0.0592
350	0.0118	0.0159	0.0221	0.0307	0.0412	0.0253
400	0.0077	0.0103	0.0143	0.0199	0.0267	0.0134
500	0.0042	0.0056	0.0078	0.0109	0.0146	0.0080
600	0.0027	0.0037	0.0051	0.0071	0.0095	0.0042
700	0.0019	0.0025	0.0035	0.0049	0.0066	0.0034
800	0.0014	0.0018	0.0025	0.0035	0.0047	0.0021
900	0.0011	0.0015	0.0021	0.0029	0.0038	0.0015
1000	0.0009	0.0012	0.0016	0.0022	0.0030	0.0012
1200	0.0007	0.0009	0.0013	0.0018	0.0024	0.0008
1400	0.0005	0.0007	0.0010	0.0014	0.0019	0.0005
1600	0.0006	0.0009	0.0012	0.0016	0.0022	0.0009
1800	0.0006	0.0008	0.0011	0.0015	0.0020	0.0008
2000	0.0005	0.0007	0.0010	0.0014	0.0019	0.0007
2500	0.0005	0.0007	0.0009	0.0013	0.0017	0.0004
3000	0.0005	0.0006	0.0009	0.0012	0.0016	0.0004

Table 9.12: 95% CL upper limits on $\sigma(pp \to tbH^+) \times \mathcal{B}(H^+ \to \tau\nu)$ in pb for JetTau channel.

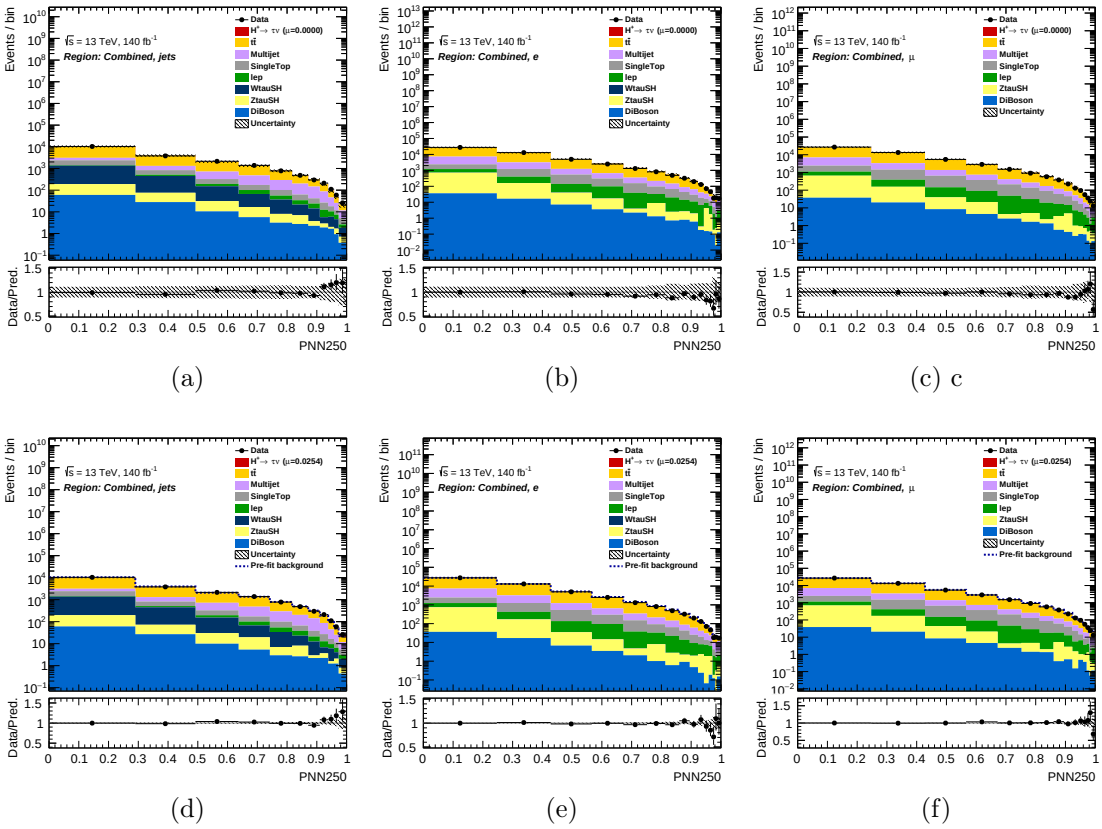

Figure 9.28: Prefit plots for the 250GeV mass hypothesis in the (a) TauJets, (b) TauEl, and (c) TauMu channel. Postfit plots for the 250GeV mass hypothesis in the (d) TauJets channel, (e) TauEl channel, (f) TauMu channel

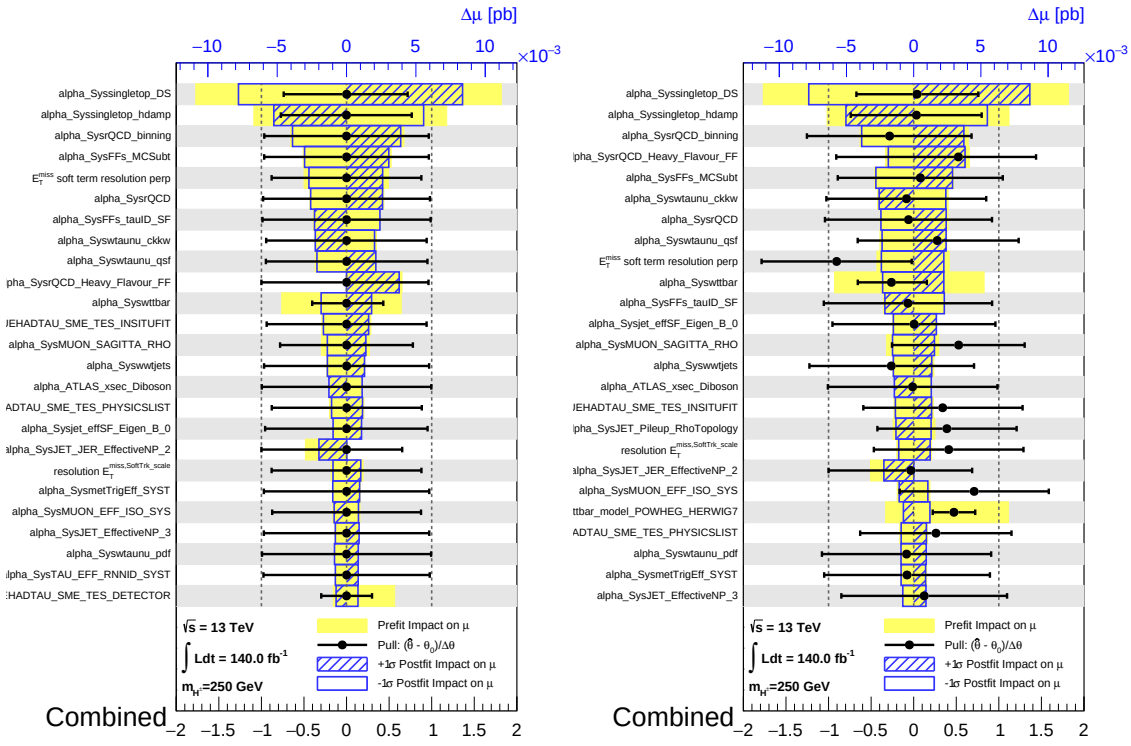

(a) a (b) b

Figure 9.29: Niusance parameter ranking plots for the Combined Channel 250GeV mass hypothesis for (a) Asimov and (b) Observed data for which the largest excess above expected was observed.

9.18 Interpretation

This analysis was conducted in a model-independent manner, but the results have been interpreted in the context of the hMSSM and the hMSSM- models. As seen in figure 9.30, the use of the full $140 fb^{-1}$ data set along with improved systematic estimations has allowed us to significantly drive down the exclusion limits on $\tan(\beta)$ when compared to the previous analysis result.

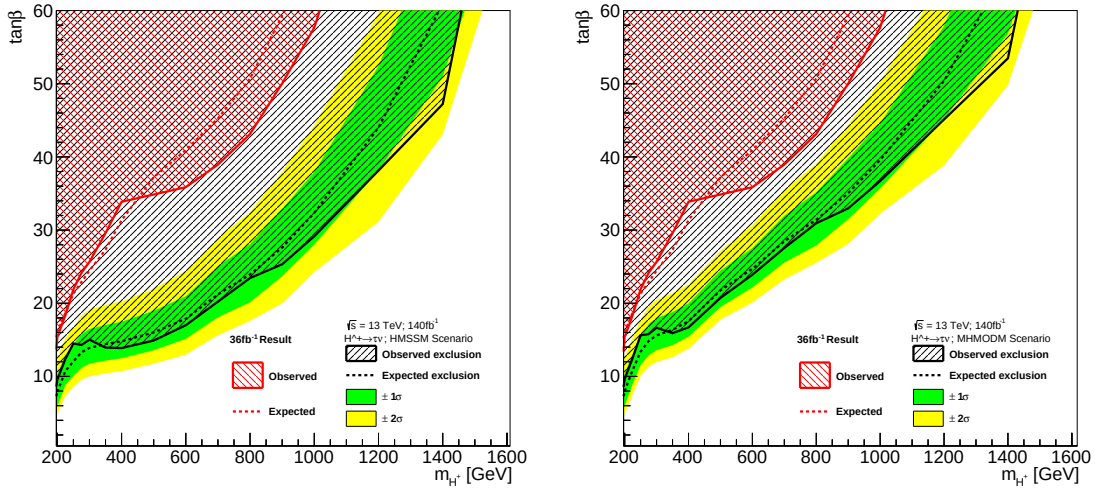

(a) a

(b) b

Figure 9.30: 95% CL exclusion limits on $\tan(\beta)$ as a function of $m_{H^\pm}$, shown in the context of (a) the hMSSM and (b) the m_h^{mod-} scenario of the hMSSM. The $\tan\beta$ regions considered for exclusion are $(0.5 \leq \tan\beta \leq 60)$. One- and two-standard-deviation uncertainty bands are shown for the expected limits of the $140 fb^{-1}$ analysis. The red curves shown are the observed and expected exclusion limits obtained using the $36.1 fb^{-1}$ dataset collected in 2015 and 2016 at $13TeV$ [119].

9.19 Conclusion

A search for charged Higgs bosons in a model-independent manner via $H^\pm \to \tau\nu$ in a mass range of 80GeV to 3000GeV, was performed using $140.0 \pm .83 fb^{-1}$ of data collected by the ATLAS experiment in Run 2 of the LHC. No significant excess above SM expected limits was observed. Exclusion limits on $\sigma(pp \to tbH^+) \times \mathcal{B}(H^+ \to \tau\nu)$ have been lowered to values between 4.5093pb for 80GeV and 4×10^{-4}pb for 3000GeV. Because of the $H^\pm$'s large branching fraction to $\tau\nu$, this analysis has been used as a benchmark to consider when proposing future charged Higgs searches. The lack of evidence for a charged Higgs in this decay channel thus indicates an even stronger constraint on the hMSSM model, making it less likely to be the over arching theory of our universe.

Chapter 10

Additional Studies

This section is dedicated to supplementary studies that I performed which did not fit the flow the main body of the thesis and so are shown here. The studies shown here are works in progress that either I or others on the $H^{\pm} \rightarrow \tau\nu$ analysis group will continue to develop.

10.1 The Deepset based Tau ID As A Region Classifier

Part of my contribution to the $H^{\pm} \rightarrow \tau\nu$ analysis was to attempt to improve fake factor estimation method for future iterations of the analysis by implementing a Particle Flow/Deepset based templates [90][91]. As described in section (9.8.5), estimating background contributions due to quark and gluon-initiated jets that appear in the signal region as fake-tau objects can be difficult because these fakes are not modeled well by simulation, and so a data-driven template fit model called the fake factor method must be applied to mitigate this lack of modeling.

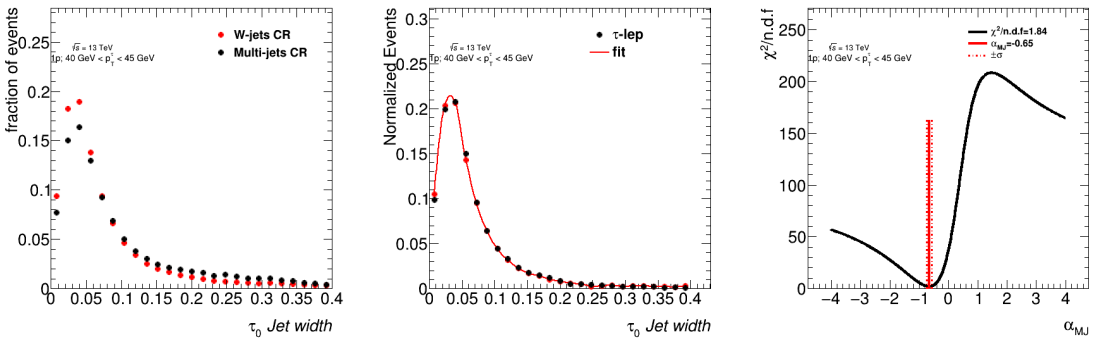

Figure 10.1: Estimation of α_{MJ} in the Tau+Lep signal region for 1-prong τ candidates with pt between $40GeV$ and $60GeV$. **Left** : Jet width templates for the MultiJet and W+Jets control regions for 1-prong taus. **Middle** : Distribution of jet width for the 1-prong Tau+Lep signal region fitted using the templates in (Left). **Right** : χ^2/ndf distribution fit as a function of α_{MJ} to the Tau+Lep jet width distribution. The error on α_{MJ} is defined by the band at $\chi^2_{\mathrm{min}}/\mathrm{ndf} + \sqrt{\frac{2}{\mathrm{ndf}}}$. [54]

In previous iterations of this analysis, the discriminating variable used in the calculation of the Fake factors has been the jet width, though the distinguishing power of this variable has not been optimal for the estimation of the Fake Tau Jet background contributions to the $H^+ \rightarrow \tau\nu$ signal region as seen in the figure above. Thus, a variable that provides a stronger distinguishing power was highly desired. Given the capability of the Deepset/Particle Flow TauID's (8.2.5) ability to distinguish between jet type objects, and with its accelerated training time, there was reason to believe the network would be very useful in classifying jets coming from the Multi-Jet and W+Jets control region used to extract these fake factors. In this study, the network scores for jets in the W+Jets and MultiJet control regions were used as template variables in the fake factor calculation. After preliminary trials using the Tau ID algorithm as a classifier for our 2 control regions, I found the network scores from the Deepest/Particle Flow Tau ID algorithm do seem to serve as a better template than the jet width for calculating fake factors. Further study is needed

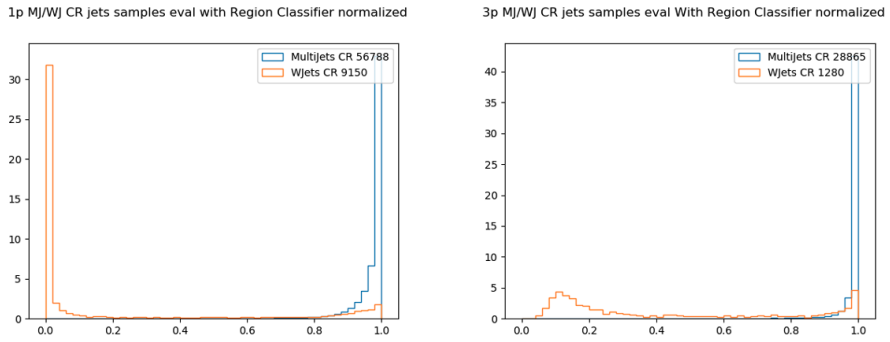

(a) (b)

Figure 10.2: Deepset/Particle Flow based TauID classification score for (a) 1 prong and (b) 3 prong jet objects in the Multi-Jet and W+Jets control regions

Appendix A

Appendices

A.1 Data Samples GRL

A.2 Good Run Lists

The data used in this analysis consists of events collected with all ATLAS subsystems operational that exist on the Good Run lists detailed below. This data sets represents $140 fb^{-}1$ of data from the entirety of Run2. The Good Run Lists (GRLs) used in this analysis are:

- data15_13TeV.periodAllYear_DetStatus-v89-pro21-02_Unknown_PHYS_StandardGRL_All_Good_25ns.xml
- data16_13TeV.periodAllYear_DetStatus-v89-pro21-01_DQDefects-00-02-04_PHYS_StandardGRL_All_Good_25ns.xml
- data17_13TeV.periodAllYear_DetStatus-v99-pro22-01_Unknown_PHYS_StandardGRL_All_Good_25ns_Triggerno17e33prim.xml
- data18_13TeV.periodAllYear_DetStatus-v102-pro22-04_Unknown_PHYS_StandardGRL_All_Good_25ns_Triggerno17e33prim.xml

A.3 TauID related results

This section shows supplementary plots relating to TauID studies, decay mode or otherwise

A.4 Decaymode net results

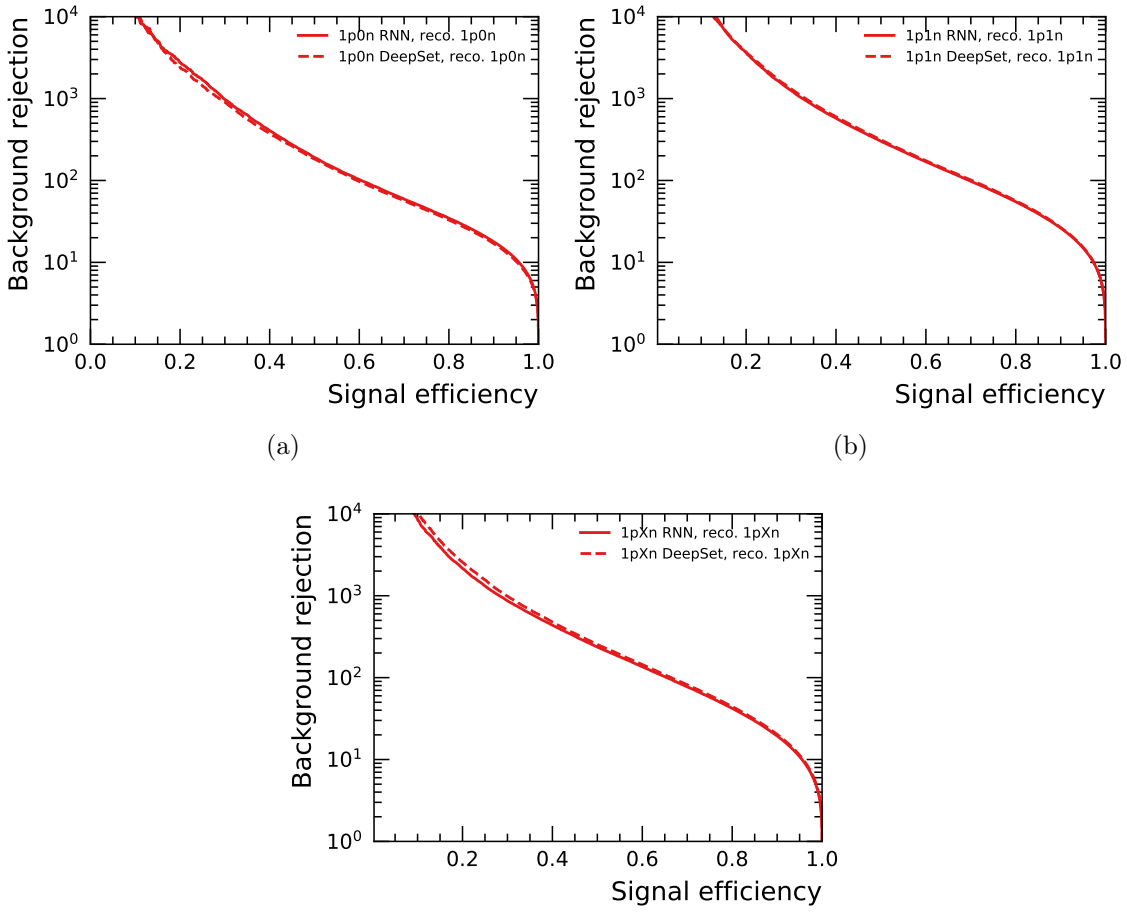

(a) (b)

(c)

Figure A.1: Performance of RNN vs Deepset based networks for 1p Decay mode networks trained during my qualification task

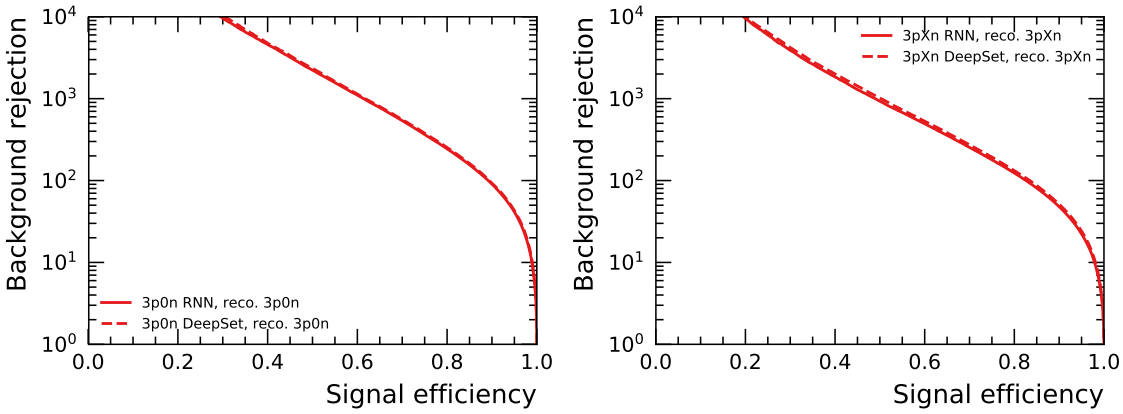

(a) (b)

Figure A.2: Performance of RNN vs Deepset based networks for 3p Decay mode networks trained during my qualification task

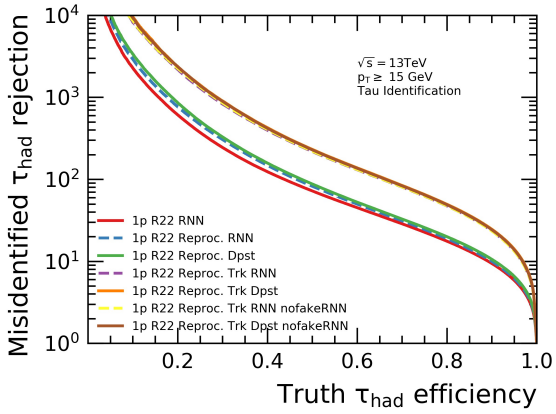

(a)

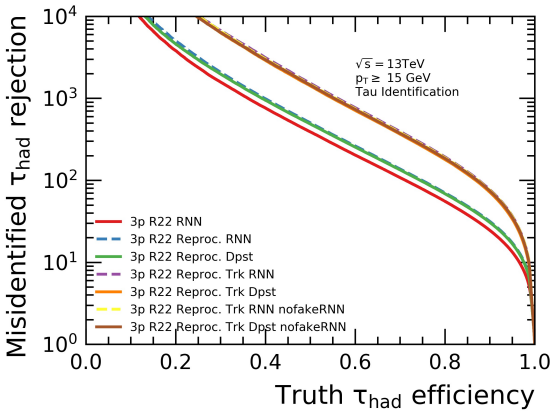

(b)

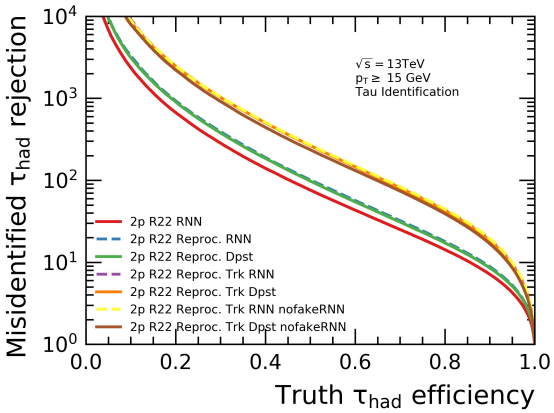

(c)

Figure A.3: Rejection curves for test iterations of a Deepset and RNN TauID that include track classification variables, a (a) 1-prong and (b) 3-prong, (c) 2-prong.

A.5 Tau ID Variable Descriptions [86][71]

A.5.1 High Level TauID Variable descriptions

High-Level Jet Variables
Central energy fraction ($cent\_frac$)**:** Fraction of transverse energy at EM scale deposited in the region $\Delta R < 0.1$ with respect to all energy deposited in $\Delta R < 0.2$ around the $\tau_{had-vis}$ candidate axis calculated by summing the energy deposited in all cells with a barycentre in these regions. The calorimeter cells are required to be part of a TopoCluster belonging to the $\tau_{had-vis}$ candidate.
Inverse momentum fraction of the leading track (etOverPtLeadTrk): The transverse energy sum, calibrated at the EM energy scale, deposited in all cells belonging to TopoClusters in the core region, divided by the transverse momentum of the highest-p_t core track of the $\tau_{had-vis}$ candidate.
Maximum track (dRmax): The maximum ΔR between a core track associated with the $\tau_{had-vis}$ candidate and the $\tau_{had-vis}$ direction.
Momentum fraction of isolation tracks (SumPtTrkFrac): Scalar sum of the p_t of isolation tracks associated with the $\tau_{had-vis}$ candidate divided by the sum of the pT of all the associated core and isolation tracks.
Ratio of EM energy and track momentum (EMPOverTrkSysP): Ratio of the sum of cluster energy deposited in the electromagnetic part of the TopoClusters (pre-sampler, first and second layers of the LAr calorimeter) to the sum of the momentum of core tracks. Clusters are calibrated at the LC energy scale.
Fraction of track-plus-EM-system pT (ptRatioEflowApprox): Ratio of the $\tau_{had-vis}$ p_t, estimated using the vector sum of core track momenta and up to two most energetic EM clusters in the core region to the calorimeter-only measurement of $\tau_{had-vis}$ p_t.
Mass of the track-plus-EM-system (mEflowApprox): Invariant mass of the system composed of the core tracks and up to two most energetic EM clusters in the core region, where EM cluster energy is the part of TopoCluster energy deposited in the presampler and first two layers of the LAr calorimeter, and the four-momentum of an EM cluster is calculated assuming zero mass and using TopoCluster seed direction.
Jet Momentum (pt_tau_log): The log_{10} of the momentum p_t, in GeV of the $\tau_{had-vis}$ candidate
Mass of the track system (massTrkSys): Invariant mass calculated from the sum of the four-momenta of all core and isolation tracks, assuming a pion mass for each track
Transverse flight path significance (trFlightPathSig): The decay length of the secondary vertex in the transverse plane, calculated with respect to the tau vertex, divided by its estimated uncertainty

A.5.2 Track TauID Variable descriptions

Track Variables:
Track momentum (pt_log): The Log_{10} of each associated jet track on the GeV scale
Jet Momentum (pt_tau_log): The Log_{10} on the GeV scale of the $\tau_{had-vis}$ candidate to correlate to each track
Angular distance in η (dEta): The angular distance of the track to the $\tau_{had-vis}$ candidate in η
Angular distance in ϕ (dPhi): The angular distance of the track to the $\tau_{had-vis}$ candidate in ϕ
Pixel hits to the innermost detector (nInnermostPixelHits): The number of hits on the track in the innermost Si pixel detector layer
Pixel hits to other detector layers (nPixelHits): The number of hits on the track in the Si pixel detector layers other than the innermost layer
Pixel Hits to Microstrip (nSCTHits): The number of hits on the track in the micro-strip detector layers
(z0sinthetaTJVA): The Longitudinal impact parameter z0 from the TauJet Vertexing Algorithm
(z0sinthetaSigTJVA): The significance of the longitudinal impact parameter z0 from the TauJet Vertexing Algorithm
(d0TJVA): The transverse impact parameter d0 from the TauJet Vertexing Algorithm
(d0SigTJVA): The significance of the transverse impact parameter d0 from the TauJet Vertexing Algorithm
(chargedScoreRNN): The output of the Track Classifier Neural Net that indicates the probability that a given track was produced by a charged particle.
(isolationScoreRNN): The output of the Track Classifier Neural Net that indicates the probability that a given track was in the isolation cone of the jet object.
(conversionScoreRNN): The output of the Track Classifier Neural Net indicates the probability that a given track was produced by pairs of charged leptons produced by pions in the jet cone.
(fakeScoreRNN): The output of the Track Classifier Neural Net that indicates the probability that a given track was a misidentified particle track.

A.5.3 Cluster TauID Variable descriptions

Cluster Variables:
Cluster energy (et_log): The Log_{10} of each associated jet cluster
Jet momentum (pt_tau_log): The Log_{10} on the GeV scale of the $\tau_{had-vis}$ candidate to correlate to each cluster
Angular distance in η (dEta): The angular distance of the cluster to the $\tau_{had-vis}$ candidate in η
Angular distance in ϕ (dPhi): The angular distance of the cluster to the $\tau_{had-vis}$ candidate in ϕ
Radial cluster extension (SECOND_R): Second moment of the radial distance of cluster cells from the cluster axis.
Longitudinal cluster extension (SECOND_LAMBDA): Second moment of the longitudinal distance of cluster cells from the cluster barycentre, along the cluster axis.
Cluster depth (CENTER_LAMBDA): The distance of the cluster barycentre from the calorimeter front face, determined along the cluster axis.

A.5.4 Decay mode Network Input Variables

Table A.1: Variables used to train the Inclusive and Decaymode networks for my Qualification Task.

Variable	1 prong	2 prong	3 prong
Jet Variables			
TauJets/centFrac	•	•	•
TauJets/etOverPtLeadTrk	•	•	•
TauJets/absipSigLeadTrk	•	•	•
TauJets/dRmax	•	•	•
TauJets/SumPtTrkFrac	•	•	•
TauJets/EMPOverTrkSysP	•	•	•
TauJets/ptRatioEflowApprox	•	•	•
TauJets/mEflowApprox	•	•	•
TauJets/ptIntermediateAxis	•	•	•
TauJets/massTrkSys		•	•
TauJets/trFlightPathSig		•	•
Track Variables			
TauTracks/pt_log	•	•	•
TauTracks/d0_abs_log	•	•	•
TauTracks/z0sinThetaTJVA_abs_log	•	•	•
TauTracks/pt_jetseed_log	•	•	•
TauTracks/dEta	•	•	•
TauTracks/dPhi	•	•	•
TauTracks/nInnermostPixelHits	•	•	•
TauTracks/nPixelHits	•	•	•
TauTracks/nSCTHits	•	•	•
Cluster Variables			
TauClusters/et_log	•	•	•
TauClusters/pt_jetseed_log	•	•	•
TauClusters/dEta	•	•	•
TauClusters/dPhi	•	•	•
TauClusters/SECOND_R	•	•	•
TauClusters/SECOND_LAMBDA	•	•	•
TauClusters/CENTER_LAMBDA	•	•	•
Additional vars used to train Track Class networks			
TauTracks_Isolation/BDT_score_1	•	•	•
TauTracks_Isolation/BDT_score_2	•	•	•
TauTracks_Charged/BDT_score_1	•	•	•
TauTracks_Charged/BDT_score_2	•	•	•

A.6 Systematic Used

A.7 Systematic List

A full list of the systematics used in this analysis and the particular object they belong to is listed below.

A.7.1 Luminosity

- SysATLAS_LUMI

A.7.2 Trigger Uncertainties

- SysEL_EFF_TRIGGER_TOTAL
- SysMUON_EFF_TRIG_SYS
- SysmetTrigEff_STAT
- SysmetTrigEff_SYST

A.7.3 Tau Uncertainties

- SysTAUS_TRUEHADTAU_SME_TES_DETECTOR
- SysTAUS_TRUEHADTAU_SME_TES_INSITUEXP
- SysTAUS_TRUEHADTAU_SME_TES_INSITUFIT
- SysTAUS_TRUEHADTAU_SME_TES_MODEL_CLOSURE
- SysTAUS_TRUEHADTAU_SME_TES_PHYSICSLIST
- SysTAU_EFF_ELEBDT_SYST
- SysTAU_EFF_RECO_TOTAL
- SysTAU_EFF_RNNID_HIGHPT
- SysTAU_EFF_RNNID_SYST

A.7.4 Jet Uncertainties

- SysJET_BJES_Response
- SysJET_EffectiveNP_1
- SysJET_EffectiveNP_2
- SysJET_EffectiveNP_3
- SysJET_EffectiveNP_4
- SysJET_EffectiveNP_5
- SysJET_EffectiveNP_6
- SysJET_EffectiveNP_7
- SysJET_EffectiveNP_8restTerm
- SysJET_EtaIntercalibration_Modelling
- SysJET_EtaIntercalibration_NonClosure_2018data
- SysJET_EtaIntercalibration_NonClosure_highE

- SysJET_EtaIntercalibration_NonClosure_negEta
- SysJET_EtaIntercalibration_NonClosure_posEta
- SysJET_EtaIntercalibration_TotalStat
- SysJET_Flavor_Composition
- SysJET_Flavor_Response
- SysJET_JER_EffectiveNP_1
- SysJET_JER_EffectiveNP_2
- SysJET_JER_EffectiveNP_3
- SysJET_JER_EffectiveNP_4
- SysJET_JER_EffectiveNP_5
- SysJET_JER_EffectiveNP_6
- SysJET_JER_EffectiveNP_7restTerm
- SysJET_Pileup_OffsetMu
- SysJET_Pileup_OffsetNPV
- SysJET_Pileup_PtTerm
- SysJET_Pileup_RhoTopology
- SysJET_SingleParticle_HighPt
- SysJET_TILECORR_Uncertainty
- Sysjet_effSF_Eigen_B_0
- Sysjet_effSF_Eigen_C_0
- Sysjet_effSF_Eigen_Light_0
- Sysjet_effSF_extrapolation
- Sysjet_effSF_extrapolation

A.7.5 Electron Uncertainties

- SysEG_SCALE_ALL
- SysEG_RESOLUTION_ALL
- SysEL_EFF_ID_TOTAL
- SysEL_EFF_ISO_TOTAL
- SysEL_EFF_RECO_TOTAL

A.7.6 Muon Uncertainties

- SysMUON_ID
- SysMUON_MS
- SysMUON_SAGITTA_RESBIAS
- SysMUON_EFF_ISO_STAT
- SysMUON_EFF_ISO_SYS
- SysMUON_EFF_RECO_STAT
- SysMUON_EFF_RECO_SYS
- SysMUON_EFF_TTVA_STAT

- SysMUON_EFF_TTVA_SYS
- SysMUON_SAGITTA_RHO
- SysMUON_SCALE

A.7.7 MET Uncertainties

- SysMET_SoftTrk_Scale
- SysMET_SoftTrk_ResoPerp
- SysMET_SoftTrk_ResoPara

A.7.8 SingleTop Uncertainties

- SysSingleTopNorm
- Syssingletop_model_POWHEG_HERWIG7
- Syssingletop_DS
- Syssingletop_hdamp

A.7.9 Fake Factor Uncertainties

- SysFFs_MCSubt
- SysFFs_tauID_SF
- SysrQCD
- SysrQCD_binning
- SysrQCD_Heavy_Flavour_FF

A.7.10 $t\bar{t}$ Modelling uncertainties

- Systtbar_ISR
- Systtbar_model_POWHEG_HERWIG7
- Systtbar_FSR
- Systtbar_PDF_1 through 30
- Syswttbar

A.7.11 W/Z+Jets Modelling Uncertainties

- Syswtaunu_ckkw
- Syswtaunu_qsf
- Syswwtjets
- Syswtaunu_scale_MUR05_MUF05
- Syswtaunu_scale_MUR05_MUF1
- Syswtaunu_scale_MUR1_MUF05
- Syswtaunu_scale_MUR1_MUF2
- Syswtaunu_scale_MUR2_MUF1
- Syswtaunu_scale_MUR2_MUF2

- Syswtaunu_pdf
- Syswtaunu_pdfset
- Syswtaunu_alphaS

A.7.12 Cross section Uncertainties

- ATLAS_xsec_W
- ATLAS_xsec_Z
- ATLAS_xsec_Diboson

A.7.13 H+ Signal uncertainties

- Sysw_sig_filter_effi_met
- Sysw_sig_filter_effi_int
- Sysw_sig_theory_pdf
- Sysw_sig_theory_scale
- Sysw_sig_filter_effi_int
- Sysw_sig_theory_pdf
- Sysw_sig_theory_scale

A.8 HTaunu Additional Results

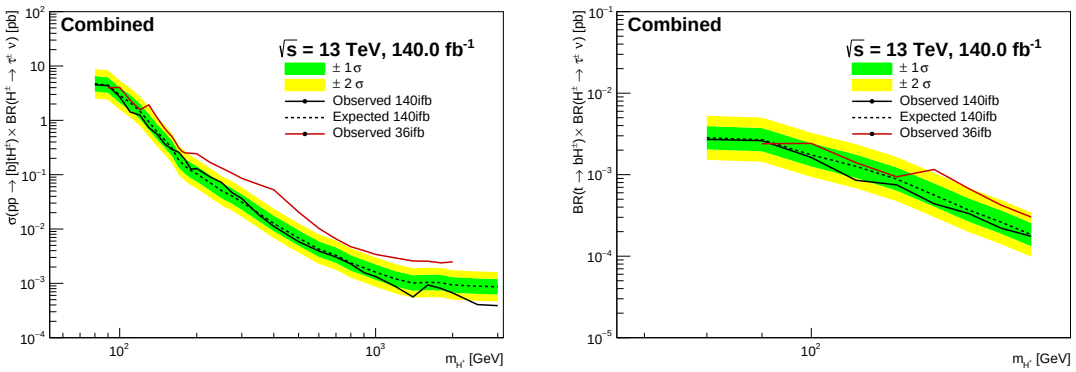

(a) (b)

Figure A.4: Observed and expected 95% CL exclusion limits on (a) $\sigma(pp \to tbH^+) \times \mathcal{B}(H^+ \to \tau\nu)$ and (b) $\mathcal{B}(t \to bH^+) \times \mathcal{B}(H^+ \to \tau\nu)$ as a function of the charged Higgs boson mass in $140 fb^{-1}$ of pp collision data at $\sqrt{s} = 13$ TeV, after combination of the τ+jets and τ+lepton channels (a). In the case of the expected limits, one- and two-standard-deviation uncertainty bands are also shown [54]. As a comparison, the Observed exclusion limits obtained with the dataset collected in 2015 and 2016 [116] are also shown in the combined limit plot.

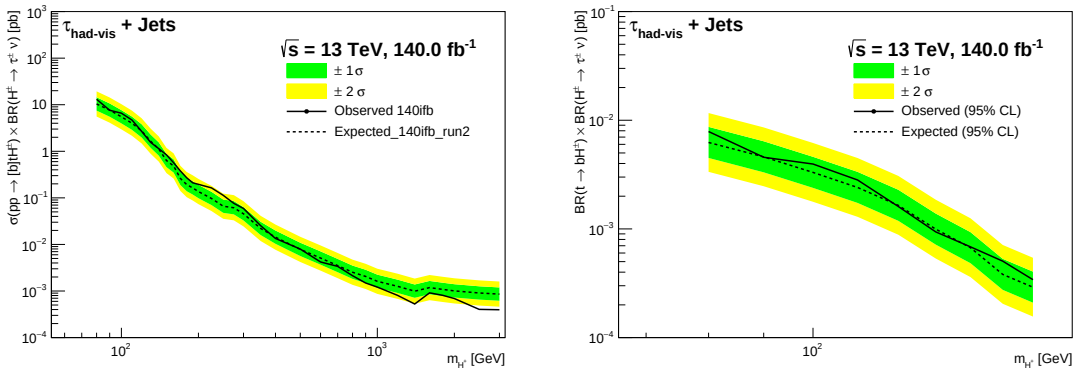

(a) (b)

Figure A.5: Observed and expected 95% CL exclusion limits on (a,c) $\sigma(pp \to tbH^+) \times \mathcal{B}(H^+ \to \tau\nu)$ and (b,d) $\mathcal{B}(t \to bH^+) \times \mathcal{B}(H^+ \to \tau\nu)$ as a function of the charged Higgs boson mass in $140 fb^{-1}$ of pp collision data at $\sqrt{s} = 13$ TeV for the τ+jets channel. In the case of the expected limits, one- and two-standard-deviation uncertainty bands are also shown. [54]

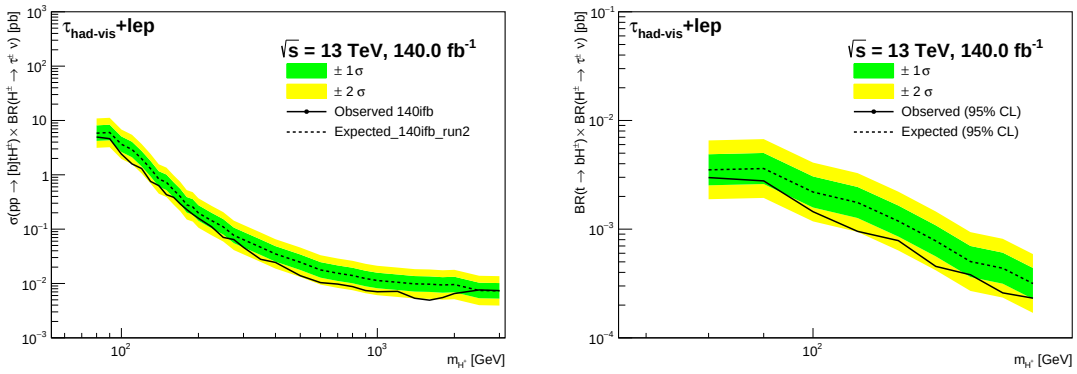

(a) (b)

Figure A.6: Observed and expected 95% CL exclusion limits on (a) $\sigma(pp \to tbH^+) \times \mathcal{B}(H^+ \to \tau\nu)$ and (b) $\mathcal{B}(t \to bH^+) \times \mathcal{B}(H^+ \to \tau\nu)$ as a function of the charged Higgs boson mass in $140 fb^{-1}$ of pp collision data at $\sqrt{s} = 13$ TeV, after combination of the τ+e and τ+μ channels. In the case of the expected limits, one- and two-standard-deviation uncertainty bands are also shown [54].

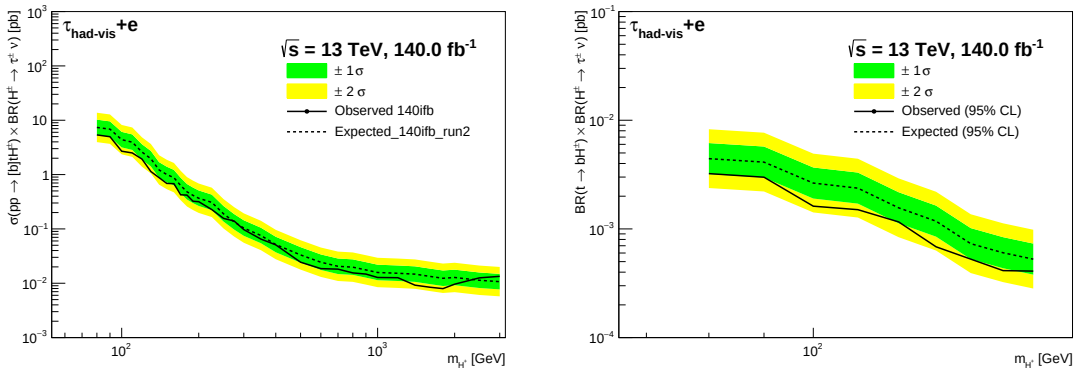

(a) (b)

Figure A.7: Observed and expected 95% CL exclusion limits on (a) $\sigma(pp \to tbH^+) \times \mathcal{B}(H^+ \to \tau\nu)$ and (b) $\mathcal{B}(t \to bH^+) \times \mathcal{B}(H^+ \to \tau\nu)$ as a function of the charged Higgs boson mass in $140 fb^{-1}$ of pp collision data at $\sqrt{s} = 13$ TeV, in the τ+e channel. In the case of the expected limits, one- and two-standard-deviation uncertainty bands are also shown [54].

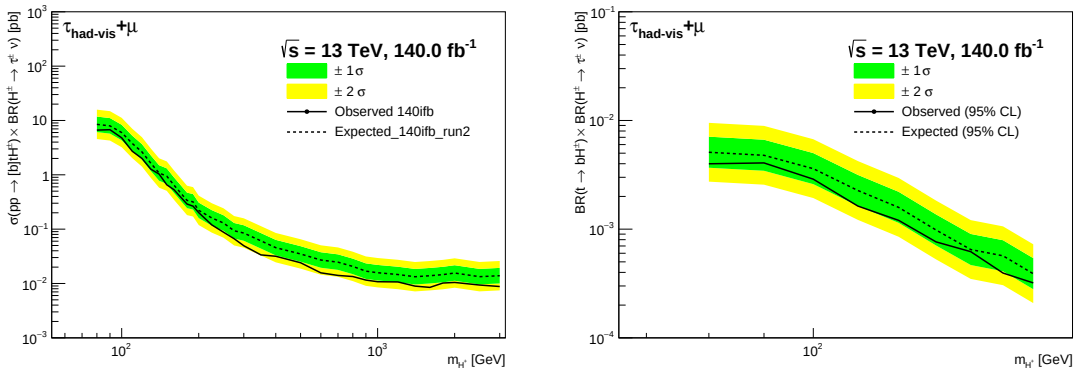

(a) (b)

Figure A.8: Observed and expected 95% CL exclusion limits on (a) $\sigma(pp \to tbH^+) \times \mathcal{B}(H^+ \to \tau\nu)$ and (b) $\mathcal{B}(t \to bH^+) \times \mathcal{B}(H^+ \to \tau\nu)$ as a function of the charged Higgs boson mass in $140 fb^{-1}$ of pp collision data at $\sqrt{s} = 13$ TeV, in the τ+μ channel. In the case of the expected limits, one- and two-standard-deviation uncertainty bands are also shown [54].

A.8.1 Cross Section Limit Tables

Mass	-2 Sigma	-1 Sigma	Expected	+1 Sigma	+2 Sigma	Observed
80	2.5299	3.3964	4.7136	6.5599	8.7940	4.5093
90	2.3964	3.2172	4.4649	6.2138	8.3301	4.3509
100	1.5623	2.0974	2.9108	4.0511	5.4307	2.7045
110	1.1324	1.5203	2.1099	2.9363	3.9363	1.4222
120	0.7888	1.0590	1.4696	2.0453	2.7419	1.2474
130	0.5031	0.6754	0.9373	1.3044	1.7487	0.7325
140	0.3287	0.4413	0.6124	0.8523	1.1426	0.5551
150	0.2338	0.3139	0.4357	0.6064	0.8129	0.3671
160	0.1641	0.2203	0.3057	0.4254	0.5703	0.2914
170	0.1002	0.1345	0.1867	0.2599	0.3484	0.2602
180	0.0771	0.1035	0.1437	0.2000	0.2680	0.1894
190	0.0637	0.0855	0.1186	0.1651	0.2214	0.1258
200	0.0556	0.0747	0.1036	0.1442	0.1933	0.1298
225	0.0383	0.0515	0.0714	0.0994	0.1332	0.0915
250	0.0273	0.0367	0.0509	0.0708	0.0949	0.0719
275	0.0217	0.0291	0.0405	0.0563	0.0755	0.0466
300	0.0168	0.0226	0.0313	0.0436	0.0584	0.0364
350	0.0103	0.0139	0.0193	0.0268	0.0360	0.0181
400	0.0068	0.0091	0.0127	0.0176	0.0236	0.0112
500	0.0037	0.0049	0.0068	0.0095	0.0127	0.0059
600	0.0023	0.0031	0.0043	0.0059	0.0080	0.0039
700	0.0018	0.0024	0.0033	0.0046	0.0061	0.0030
800	0.0013	0.0017	0.0024	0.0033	0.0044	0.0023
900	0.0010	0.0014	0.0019	0.0027	0.0036	0.0016
1000	0.0009	0.0012	0.0016	0.0022	0.0030	0.0013
1200	0.0006	0.0009	0.0012	0.0017	0.0022	0.0009
1400	0.0005	0.0007	0.0010	0.0014	0.0019	0.0006
1600	0.0006	0.0007	0.0010	0.0014	0.0019	0.0009
1800	0.0006	0.0007	0.0010	0.0014	0.0019	0.0008
2000	0.0005	0.0007	0.0009	0.0013	0.0017	0.0007
2500	0.0005	0.0006	0.0009	0.0012	0.0017	0.0004
3000	0.0005	0.0006	0.0009	0.0012	0.0016	0.0004

Table A.2: 95% CL upper limits on $\sigma(pp \rightarrow tbH^+) \times \mathcal{B}(H^+ \rightarrow \tau\nu)$ in pb for Combined channel.

Mass	-2 Sigma	-1 Sigma	Expected	+1 Sigma	+2 Sigma	Observed
80	3.1361	4.2102	5.8430	8.1317	10.9012	4.9602
90	3.2239	4.3280	6.0065	8.3593	11.2063	4.6244
100	1.9602	2.6316	3.6522	5.0828	6.8139	2.4079
110	1.5682	2.1053	2.9218	4.0663	5.4512	1.5871
120	1.0586	1.4212	1.9724	2.7450	3.6799	1.3045
130	0.6956	0.9339	1.2961	1.8038	2.4181	0.7555
140	0.4491	0.6029	0.8367	1.1645	1.5611	0.6325
150	0.3900	0.5235	0.7266	1.0112	1.3555	0.4310
160	0.2820	0.3786	0.5254	0.7313	0.9803	0.3855
170	0.2125	0.2852	0.3958	0.5509	0.7385	0.2897
180	0.1505	0.2020	0.2803	0.3902	0.5230	0.2295
190	0.1378	0.1849	0.2567	0.3572	0.4789	0.1881
200	0.1063	0.1427	0.1981	0.2757	0.3695	0.1586
225	0.0772	0.1037	0.1439	0.2002	0.2684	0.1109
250	0.0592	0.0794	0.1102	0.1534	0.2056	0.0705
275	0.0412	0.0553	0.0768	0.1068	0.1432	0.0643
300	0.0344	0.0461	0.0640	0.0891	0.1194	0.0462
350	0.0249	0.0335	0.0465	0.0647	0.0867	0.0278
400	0.0188	0.0252	0.0350	0.0487	0.0653	0.0244
500	0.0132	0.0177	0.0246	0.0342	0.0459	0.0139
600	0.0095	0.0128	0.0178	0.0247	0.0331	0.0104
700	0.0083	0.0111	0.0154	0.0215	0.0288	0.0097
800	0.0075	0.0101	0.0140	0.0195	0.0261	0.0088
900	0.0066	0.0089	0.0123	0.0171	0.0230	0.0074
1000	0.0061	0.0082	0.0113	0.0158	0.0212	0.0071
1200	0.0056	0.0076	0.0105	0.0146	0.0196	0.0072
1400	0.0053	0.0071	0.0098	0.0137	0.0184	0.0053
1600	0.0052	0.0070	0.0097	0.0135	0.0181	0.0049
1800	0.0050	0.0068	0.0094	0.0131	0.0175	0.0055
2000	0.0051	0.0069	0.0096	0.0133	0.0178	0.0065
2500	0.0040	0.0054	0.0074	0.0103	0.0139	0.0076
3000	0.0039	0.0053	0.0073	0.0102	0.0136	0.0074

Table A.3: 95% CL upper limits on $\sigma(pp \to tbH^+) \times \mathcal{B}(H^+ \to \tau\nu)$ in pb for LepTau channel.

Mass	-2 Sigma	-1 Sigma	Expected	+1 Sigma	+2 Sigma	Observed
80	5.5747	7.4841	10.3866	14.4551	19.3781	13.0952
90	4.1097	5.5173	7.6570	10.6563	14.2855	7.5935
100	2.9560	3.9685	5.5075	7.6649	10.2753	6.5773
110	2.1485	2.8843	4.0029	5.5709	7.4682	4.6890
120	1.4705	1.9742	2.7398	3.8131	5.1117	2.6736
130	0.8879	1.1921	1.6544	2.3024	3.0865	1.5611
140	0.5995	0.8049	1.1170	1.5546	2.0840	1.1378
150	0.3405	0.4571	0.6344	0.8829	1.1836	0.8403
160	0.2596	0.3486	0.4837	0.6732	0.9025	0.5672
170	0.1405	0.1887	0.2618	0.3644	0.4885	0.3784
180	0.1034	0.1388	0.1926	0.2681	0.3594	0.2701
190	0.0877	0.1177	0.1634	0.2274	0.3049	0.2104
200	0.0733	0.0984	0.1365	0.1900	0.2547	0.1952
225	0.0520	0.0699	0.0970	0.1350	0.1809	0.1637
250	0.0355	0.0477	0.0661	0.0920	0.1234	0.1133
275	0.0329	0.0442	0.0613	0.0854	0.1144	0.0762
300	0.0244	0.0327	0.0454	0.0632	0.0848	0.0592
350	0.0118	0.0159	0.0221	0.0307	0.0412	0.0253
400	0.0077	0.0103	0.0143	0.0199	0.0267	0.0134
500	0.0042	0.0056	0.0078	0.0109	0.0146	0.0080
600	0.0027	0.0037	0.0051	0.0071	0.0095	0.0042
700	0.0019	0.0025	0.0035	0.0049	0.0066	0.0034
800	0.0014	0.0018	0.0025	0.0035	0.0047	0.0021
900	0.0011	0.0015	0.0021	0.0029	0.0038	0.0015
1000	0.0009	0.0012	0.0016	0.0022	0.0030	0.0012
1200	0.0007	0.0009	0.0013	0.0018	0.0024	0.0008
1400	0.0005	0.0007	0.0010	0.0014	0.0019	0.0005
1600	0.0006	0.0009	0.0012	0.0016	0.0022	0.0009
1800	0.0006	0.0008	0.0011	0.0015	0.0020	0.0008
2000	0.0005	0.0007	0.0010	0.0014	0.0019	0.0007
2500	0.0005	0.0007	0.0009	0.0013	0.0017	0.0004
3000	0.0005	0.0006	0.0009	0.0012	0.0016	0.0004

Table A.4: 95% CL upper limits on $\sigma(pp \to tbH^+) \times \mathcal{B}(H^+ \to \tau\nu)$ in pb for JetTau channel.

Mass	-2 Sigma	-1 Sigma	Expected	+1 Sigma	+2 Sigma	Observed
80	3.9561	5.3111	7.3709	10.2581	13.7518	5.3685
90	3.6757	4.9346	6.8484	9.5309	12.7769	4.9761
100	2.3580	3.1656	4.3932	6.1141	8.1964	2.6929
110	2.1169	2.8419	3.9441	5.4890	7.3584	2.5005
120	1.3959	1.8740	2.6008	3.6195	4.8522	1.9302
130	1.0513	1.4114	1.9587	2.7259	3.6543	1.1385
140	0.6527	0.8763	1.2162	1.6925	2.2690	0.8771
150	0.5388	0.7233	1.0039	1.3971	1.8729	0.6876
160	0.4704	0.6315	0.8764	1.2196	1.6350	0.6802
170	0.3373	0.4528	0.6284	0.8746	1.1724	0.4244
180	0.2583	0.3468	0.4813	0.6698	0.8979	0.4191
190	0.2223	0.2985	0.4142	0.5765	0.7728	0.3228
200	0.1969	0.2643	0.3669	0.5106	0.6844	0.3171
225	0.1651	0.2216	0.3076	0.4281	0.5738	0.2268
250	0.1018	0.1366	0.1896	0.2639	0.3538	0.1562
275	0.0724	0.0972	0.1348	0.1877	0.2516	0.1397
300	0.0556	0.0746	0.1036	0.1442	0.1933	0.0971
350	0.0406	0.0545	0.0756	0.1052	0.1411	0.0650
400	0.0277	0.0371	0.0515	0.0717	0.0961	0.0508
500	0.0178	0.0239	0.0332	0.0462	0.0619	0.0244
600	0.0131	0.0176	0.0244	0.0339	0.0455	0.0186
700	0.0110	0.0148	0.0205	0.0285	0.0382	0.0182
800	0.0106	0.0142	0.0198	0.0275	0.0369	0.0155
900	0.0094	0.0127	0.0176	0.0245	0.0328	0.0148
1000	0.0085	0.0114	0.0158	0.0220	0.0294	0.0128
1200	0.0082	0.0110	0.0153	0.0212	0.0285	0.0127
1400	0.0079	0.0106	0.0147	0.0205	0.0274	0.0092
1600	0.0072	0.0096	0.0134	0.0186	0.0250	0.0085
1800	0.0066	0.0089	0.0123	0.0172	0.0230	0.0080
2000	0.0069	0.0092	0.0128	0.0178	0.0238	0.0096
2500	0.0061	0.0082	0.0113	0.0158	0.0212	0.0126
3000	0.0057	0.0077	0.0107	0.0149	0.0200	0.0134

Table A.5: 95% CL upper limits on $\sigma(pp \to tbH^+) \times \mathcal{B}(H^+ \to \tau\nu)$ in pb for ElTau channel.

Mass	-2 Sigma	-1 Sigma	Expected	+1 Sigma	+2 Sigma	Observed
80	4.5514	6.1103	8.4800	11.8017	15.8210	6.6454
90	4.2675	5.7291	7.9510	11.0655	14.8340	6.7667
100	3.2151	4.3163	5.9902	8.3367	11.1759	4.7949
110	2.0240	2.7172	3.7710	5.2482	7.0356	2.7120
120	1.4157	1.9006	2.6377	3.6709	4.9211	2.0042
130	0.8761	1.1762	1.6323	2.2717	3.0454	1.2696
140	0.5793	0.7778	1.0794	1.5022	2.0138	1.0320
150	0.5073	0.6811	0.9452	1.3155	1.7635	0.6561
160	0.3472	0.4661	0.6468	0.9002	1.2068	0.5326
170	0.2486	0.3338	0.4632	0.6447	0.8642	0.3890
180	0.1813	0.2434	0.3378	0.4702	0.6303	0.2899
190	0.1707	0.2292	0.3180	0.4426	0.5934	0.2650
200	0.1189	0.1596	0.2215	0.3082	0.4132	0.2014
225	0.0862	0.1158	0.1607	0.2236	0.2998	0.1197
250	0.0695	0.0933	0.1295	0.1803	0.2417	0.0878
275	0.0501	0.0673	0.0933	0.1299	0.1742	0.0666
300	0.0455	0.0611	0.0848	0.1180	0.1581	0.0495
350	0.0327	0.0439	0.0609	0.0847	0.1135	0.0336
400	0.0245	0.0329	0.0456	0.0635	0.0851	0.0317
500	0.0188	0.0252	0.0349	0.0486	0.0652	0.0241
600	0.0145	0.0195	0.0270	0.0376	0.0504	0.0157
700	0.0132	0.0178	0.0247	0.0344	0.0460	0.0141
800	0.0111	0.0148	0.0206	0.0287	0.0384	0.0134
900	0.0090	0.0121	0.0168	0.0234	0.0314	0.0115
1000	0.0085	0.0114	0.0158	0.0219	0.0294	0.0108
1200	0.0078	0.0105	0.0146	0.0204	0.0273	0.0107
1400	0.0071	0.0096	0.0133	0.0185	0.0248	0.0089
1600	0.0075	0.0100	0.0139	0.0193	0.0259	0.0085
1800	0.0078	0.0105	0.0146	0.0203	0.0272	0.0102
2000	0.0084	0.0112	0.0156	0.0217	0.0291	0.0104
2500	0.0072	0.0096	0.0133	0.0186	0.0249	0.0094
3000	0.0075	0.0100	0.0139	0.0194	0.0259	0.0088

Table A.6: 95% CL upper limits on $\sigma(pp \to tbH^+) \times \mathcal{B}(H^+ \to \tau\nu)$ in pb for MuTau channel.

A.9 Final Bin Arrays for Htaunu

A.10 Starting arrays for TauLep channel

These bins serve as a starting point for the TauLep (Tau+El and Tau+Mu) channel which are then collapsed requiring at minimum 10 MC events per bin.

- PNN80: $[0.0, 0.1, 0.2, 0.3, 0.4, 0.517, 0.621, 0.702, 0.766, 0.817, 0.856, 0.887, 1.0]$
- PNN90: $[0.0, 0.1, 0.2, 0.3, 0.4, 0.517, 0.621, 0.702, 0.766, 0.817, 0.856, 0.887, 1.0]$
- PNN100: $[0.0, 0.1, 0.2, 0.3, 0.4, 0.517, 0.621, 0.702, 0.766, 0.817, 0.856, 0.887, 1.0]$
- PNN110: $[0.0, 0.1, 0.2, 0.3, 0.4, 0.517, 0.621, 0.702, 0.766, 0.817, 0.856, 0.887, 1.0]$
- PNN120: $[0.0, 0.1, 0.2, 0.3, 0.4, 0.517, 0.621, 0.702, 0.766, 0.817, 0.856, 0.887, 1.0]$
- PNN130: $[0.0, 0.1, 0.2, 0.3, 0.4, 0.500, 0.627, 0.732, 0.807, 0.861, 0.900, 0.928, 1.0]$
- PNN140: $[0.0, 0.1, 0.2, 0.3, 0.4, 0.500, 0.627, 0.732, 0.807, 0.861, 0.900, 0.928, 1.0]$

A.11 Final Binning Arrays

Final Bin arrays for each channel after collapsing for a minimum of 10MC events are displayed below

Mass	N Bins	Final Bin Array
80	8	[0.0, 0.29, 0.492, 0.637, 0.742, 0.8170000000000001, 0.871, 0.91, 1.0]
90	9	[0.0, 0.29, 0.492, 0.637, 0.742, 0.8170000000000001, 0.871, 0.91, 0.9380000000000001, 1.0]
100	9	[0.0, 0.29, 0.492, 0.637, 0.742, 0.8170000000000001, 0.871, 0.91, 0.9380000000000001, 1.0]
110	9	[0.0, 0.29, 0.492, 0.637, 0.742, 0.8170000000000001, 0.871, 0.91, 0.9380000000000001, 1.0]
120	9	[0.0, 0.29, 0.492, 0.637, 0.742, 0.8170000000000001, 0.871, 0.91, 0.9380000000000001, 1.0]
130	10	[0.0, 0.29, 0.492, 0.637, 0.742, 0.8170000000000001, 0.871, 0.91, 0.9380000000000001, 0.9580000000000001, 1.0]
140	10	[0.0, 0.29, 0.492, 0.637, 0.742, 0.8170000000000001, 0.871, 0.91, 0.9380000000000001, 0.9580000000000001, 1.0]
150	10	[0.0, 0.29, 0.492, 0.637, 0.742, 0.8170000000000001, 0.871, 0.91, 0.9380000000000001, 0.9580000000000001, 1.0]
160	10	[0.0, 0.29, 0.492, 0.637, 0.742, 0.8170000000000001, 0.871, 0.91, 0.9380000000000001, 0.9580000000000001, 1.0]
170	10	[0.0, 0.29, 0.492, 0.637, 0.742, 0.8170000000000001, 0.871, 0.91, 0.9380000000000001, 0.9580000000000001, 1.0]
180	10	[0.0, 0.29, 0.492, 0.637, 0.742, 0.8170000000000001, 0.871, 0.91, 0.9380000000000001, 0.9580000000000001, 1.0]
190	11	[0.0, 0.29, 0.492, 0.637, 0.742, 0.8170000000000001, 0.871, 0.91, 0.9380000000000001, 0.9580000000000001, 0.973, 1.0]
200	11	[0.0, 0.29, 0.492, 0.637, 0.742, 0.8170000000000001, 0.871, 0.91, 0.9380000000000001, 0.9580000000000001, 0.973, 1.0]
225	11	[0.0, 0.29, 0.492, 0.637, 0.742, 0.8170000000000001, 0.871, 0.91, 0.9380000000000001, 0.9580000000000001, 0.973, 1.0]
250	11	[0.0, 0.29, 0.492, 0.637, 0.742, 0.8170000000000001, 0.871, 0.91, 0.9380000000000001, 0.9580000000000001, 0.973, 1.0]
275	11	[0.0, 0.29, 0.492, 0.637, 0.742, 0.8170000000000001, 0.871, 0.91, 0.9380000000000001, 0.9580000000000001, 0.973, 1.0]
300	11	[0.0, 0.29, 0.492, 0.637, 0.742, 0.8170000000000001, 0.871, 0.91, 0.9380000000000001, 0.9580000000000001, 0.973, 1.0]
350	12	[0.0, 0.29, 0.492, 0.637, 0.742, 0.8170000000000001, 0.871, 0.91, 0.9380000000000001, 0.9580000000000001, 0.973, 0.983, 1.0]
400	12	[0.0, 0.29, 0.492, 0.637, 0.742, 0.8170000000000001, 0.871, 0.91, 0.9380000000000001, 0.9580000000000001, 0.973, 0.983, 1.0]
500	13	[0.0, 0.29, 0.492, 0.637, 0.742, 0.8170000000000001, 0.871, 0.91, 0.9380000000000001, 0.9580000000000001, 0.973, 0.983, 0.991, 1.0]
600	13	[0.0, 0.29, 0.492, 0.637, 0.742, 0.8170000000000001, 0.871, 0.91, 0.9380000000000001, 0.9580000000000001, 0.973, 0.983, 0.991, 1.0]
700	13	[0.0, 0.29, 0.492, 0.637, 0.742, 0.8170000000000001, 0.871, 0.91, 0.9380000000000001, 0.9580000000000001, 0.973, 0.983, 0.991, 1.0]
800	14	[0.0, 0.29, 0.492, 0.637, 0.742, 0.8170000000000001, 0.871, 0.91, 0.9380000000000001, 0.9580000000000001, 0.973, 0.983, 0.991, 0.996, 1.0]
900	14	[0.0, 0.29, 0.492, 0.637, 0.742, 0.8170000000000001, 0.871, 0.91, 0.9380000000000001, 0.9580000000000001, 0.973, 0.983, 0.991, 0.996, 1.0]
1000	14	[0.0, 0.29, 0.492, 0.637, 0.742, 0.8170000000000001, 0.871, 0.91, 0.9380000000000001, 0.9580000000000001, 0.973, 0.983, 0.991, 0.996, 1.0]
1200	14	[0.0, 0.29, 0.492, 0.637, 0.742, 0.8170000000000001, 0.871, 0.91, 0.9380000000000001, 0.9580000000000001, 0.973, 0.983, 0.991, 0.996, 1.0]
1400	14	[0.0, 0.29, 0.492, 0.637, 0.742, 0.8170000000000001, 0.871, 0.91, 0.9380000000000001, 0.9580000000000001, 0.973, 0.983, 0.991, 0.996, 1.0]
1600	12	[0.0, 0.29, 0.492, 0.637, 0.742, 0.8170000000000001, 0.871, 0.91, 0.9380000000000001, 0.9580000000000001, 0.973, 0.991, 1.0]
1800	12	[0.0, 0.29, 0.492, 0.637, 0.742, 0.8170000000000001, 0.871, 0.91, 0.9380000000000001, 0.9580000000000001, 0.973, 0.991, 1.0]
2000	12	[0.0, 0.29, 0.492, 0.637, 0.742, 0.8170000000000001, 0.871, 0.91, 0.9380000000000001, 0.9580000000000001, 0.973, 0.991, 1.0]
2500	11	[0.0, 0.29, 0.492, 0.637, 0.742, 0.8170000000000001, 0.871, 0.91, 0.9380000000000001, 0.973, 0.991, 1.0]
3000	9	[0.0, 0.29, 0.492, 0.637, 0.742, 0.8170000000000001, 0.871, 0.9380000000000001, 0.983, 1.0]

Table A.7: Final Binnings JetTau

Mass	N Bins	Final Bin Array
80	12	[0.0, 0.1, 0.2, 0.3, 0.4, 0.517, 0.621, 0.7020000000000001, 0.766, 0.8170000000000001, 0.856, 0.887, 1.0]
90	12	[0.0, 0.1, 0.2, 0.3, 0.4, 0.517, 0.621, 0.7020000000000001, 0.766, 0.8170000000000001, 0.856, 0.887, 1.0]
100	12	[0.0, 0.1, 0.2, 0.3, 0.4, 0.517, 0.621, 0.7020000000000001, 0.766, 0.8170000000000001, 0.856, 0.887, 1.0]
110	12	[0.0, 0.1, 0.2, 0.3, 0.4, 0.517, 0.621, 0.7020000000000001, 0.766, 0.8170000000000001, 0.856, 0.887, 1.0]
120	12	[0.0, 0.1, 0.2, 0.3, 0.4, 0.517, 0.621, 0.7020000000000001, 0.766, 0.8170000000000001, 0.856, 0.887, 1.0]
130	12	[0.0, 0.1, 0.2, 0.3, 0.4, 0.5, 0.627, 0.732, 0.807, 0.861, 0.9, 0.928, 1.0]
140	12	[0.0, 0.1, 0.2, 0.3, 0.4, 0.5, 0.627, 0.732, 0.807, 0.861, 0.9, 0.928, 1.0]
150	13	[0.0, 0.247, 0.428, 0.5660000000000001, 0.672, 0.752, 0.8130000000000001, 0.86, 0.895, 0.923, 0.9430000000000001, 0.9590000000000001, 0.971, 1.0]
160	13	[0.0, 0.247, 0.428, 0.5660000000000001, 0.672, 0.752, 0.8130000000000001, 0.86, 0.895, 0.923, 0.9430000000000001, 0.9590000000000001, 0.971, 1.0]
170	14	[0.0, 0.247, 0.428, 0.5660000000000001, 0.672, 0.752, 0.8130000000000001, 0.86, 0.895, 0.923, 0.9430000000000001, 0.9590000000000001, 0.971, 0.98, 1.0]
180	14	[0.0, 0.247, 0.428, 0.5660000000000001, 0.672, 0.752, 0.8130000000000001, 0.86, 0.895, 0.923, 0.9430000000000001, 0.9590000000000001, 0.971, 0.98, 1.0]
190	14	[0.0, 0.247, 0.428, 0.5660000000000001, 0.672, 0.752, 0.8130000000000001, 0.86, 0.895, 0.923, 0.9430000000000001, 0.9590000000000001, 0.971, 0.98, 1.0]
200	15	[0.0, 0.247, 0.428, 0.5660000000000001, 0.672, 0.752, 0.8130000000000001, 0.86, 0.895, 0.923, 0.9430000000000001, 0.9590000000000001, 0.971, 0.98, 0.987, 1.0]
225	15	[0.0, 0.247, 0.428, 0.5660000000000001, 0.672, 0.752, 0.8130000000000001, 0.86, 0.895, 0.923, 0.9430000000000001, 0.9590000000000001, 0.971, 0.98, 0.987, 1.0]
250	15	[0.0, 0.247, 0.428, 0.5660000000000001, 0.672, 0.752, 0.8130000000000001, 0.86, 0.895, 0.923, 0.9430000000000001, 0.9590000000000001, 0.971, 0.98, 0.987, 1.0]
275	16	[0.0, 0.247, 0.428, 0.5660000000000001, 0.672, 0.752, 0.8130000000000001, 0.86, 0.895, 0.923, 0.9430000000000001, 0.9590000000000001, 0.971, 0.98, 0.987, 0.993, 1.0]
300	16	[0.0, 0.247, 0.428, 0.5660000000000001, 0.672, 0.752, 0.8130000000000001, 0.86, 0.895, 0.923, 0.9430000000000001, 0.9590000000000001, 0.971, 0.98, 0.987, 0.993, 1.0]
350	16	[0.0, 0.247, 0.428, 0.5660000000000001, 0.672, 0.752, 0.8130000000000001, 0.86, 0.895, 0.923, 0.9430000000000001, 0.9590000000000001, 0.971, 0.98, 0.987, 0.993, 1.0]
400	16	[0.0, 0.247, 0.428, 0.5660000000000001, 0.672, 0.752, 0.8130000000000001, 0.86, 0.895, 0.923, 0.9430000000000001, 0.9590000000000001, 0.971, 0.98, 0.987, 0.993, 1.0]
500	16	[0.0, 0.247, 0.428, 0.5660000000000001, 0.672, 0.752, 0.8130000000000001, 0.86, 0.895, 0.923, 0.9430000000000001, 0.9590000000000001, 0.971, 0.98, 0.987, 0.993, 1.0]
600	16	[0.0, 0.247, 0.428, 0.5660000000000001, 0.672, 0.752, 0.8130000000000001, 0.86, 0.895, 0.923, 0.9430000000000001, 0.9590000000000001, 0.971, 0.98, 0.987, 0.993, 1.0]
700	16	[0.0, 0.247, 0.428, 0.5660000000000001, 0.672, 0.752, 0.8130000000000001, 0.86, 0.895, 0.923, 0.9430000000000001, 0.9590000000000001, 0.971, 0.98, 0.987, 0.993, 1.0]
800	16	[0.0, 0.247, 0.428, 0.5660000000000001, 0.672, 0.752, 0.8130000000000001, 0.86, 0.895, 0.923, 0.9430000000000001, 0.9590000000000001, 0.971, 0.98, 0.987, 0.993, 1.0]
900	16	[0.0, 0.247, 0.428, 0.5660000000000001, 0.672, 0.752, 0.8130000000000001, 0.86, 0.895, 0.923, 0.9430000000000001, 0.9590000000000001, 0.971, 0.98, 0.987, 0.993, 1.0]
1000	16	[0.0, 0.247, 0.428, 0.5660000000000001, 0.672, 0.752, 0.8130000000000001, 0.86, 0.895, 0.923, 0.9430000000000001, 0.9590000000000001, 0.971, 0.98, 0.987, 0.993, 1.0]
1200	15	[0.0, 0.247, 0.428, 0.5660000000000001, 0.672, 0.752, 0.8130000000000001, 0.86, 0.895, 0.923, 0.9430000000000001, 0.9590000000000001, 0.971, 0.98, 0.993, 1.0]
1400	15	[0.0, 0.247, 0.428, 0.5660000000000001, 0.672, 0.752, 0.8130000000000001, 0.86, 0.895, 0.923, 0.9430000000000001, 0.9590000000000001, 0.971, 0.98, 0.993, 1.0]
1600	14	[0.0, 0.247, 0.428, 0.5660000000000001, 0.672, 0.752, 0.8130000000000001, 0.86, 0.895, 0.923, 0.9430000000000001, 0.9590000000000001, 0.98, 0.993, 1.0]
1800	14	[0.0, 0.247, 0.428, 0.5660000000000001, 0.672, 0.752, 0.8130000000000001, 0.86, 0.895, 0.923, 0.9430000000000001, 0.9590000000000001, 0.98, 0.993, 1.0]
2000	14	[0.0, 0.247, 0.428, 0.5660000000000001, 0.672, 0.752, 0.8130000000000001, 0.86, 0.895, 0.923, 0.9430000000000001, 0.9590000000000001, 0.98, 0.993, 1.0]
2500	12	[0.0, 0.247, 0.428, 0.5660000000000001, 0.672, 0.752, 0.8130000000000001, 0.86, 0.895, 0.9430000000000001, 0.971, 0.993, 1.0]
3000	12	[0.0, 0.247, 0.428, 0.5660000000000001, 0.672, 0.752, 0.8130000000000001, 0.86, 0.895, 0.9430000000000001, 0.971, 0.993, 1.0]

Table A.8: Final Binnings ElTau

Mass	N Bins	Final Bin Array
80	12	[0.0, 0.1, 0.2, 0.3, 0.4, 0.517, 0.621, 0.7020000000000001, 0.766, 0.8170000000000001, 0.856, 0.887, 1.0]
90	12	[0.0, 0.1, 0.2, 0.3, 0.4, 0.517, 0.621, 0.7020000000000001, 0.766, 0.8170000000000001, 0.856, 0.887, 1.0]
100	12	[0.0, 0.1, 0.2, 0.3, 0.4, 0.517, 0.621, 0.7020000000000001, 0.766, 0.8170000000000001, 0.856, 0.887, 1.0]
110	12	[0.0, 0.1, 0.2, 0.3, 0.4, 0.517, 0.621, 0.7020000000000001, 0.766, 0.8170000000000001, 0.856, 0.887, 1.0]
120	12	[0.0, 0.1, 0.2, 0.3, 0.4, 0.517, 0.621, 0.7020000000000001, 0.766, 0.8170000000000001, 0.856, 0.887, 1.0]
130	12	[0.0, 0.1, 0.2, 0.3, 0.4, 0.5, 0.627, 0.732, 0.807, 0.861, 0.9, 0.928, 1.0]
140	12	[0.0, 0.1, 0.2, 0.3, 0.4, 0.5, 0.627, 0.732, 0.807, 0.861, 0.9, 0.928, 1.0]
150	13	[0.0, 0.247, 0.428, 0.5660000000000001, 0.672, 0.752, 0.8130000000000001, 0.86, 0.895, 0.923, 0.9430000000000001, 0.9590000000000001, 0.971, 1.0]
160	14	[0.0, 0.247, 0.428, 0.5660000000000001, 0.672, 0.752, 0.8130000000000001, 0.86, 0.895, 0.923, 0.9430000000000001, 0.9590000000000001, 0.971, 0.98, 1.0]
170	14	[0.0, 0.247, 0.428, 0.5660000000000001, 0.672, 0.752, 0.8130000000000001, 0.86, 0.895, 0.923, 0.9430000000000001, 0.9590000000000001, 0.971, 0.98, 1.0]
180	14	[0.0, 0.247, 0.428, 0.5660000000000001, 0.672, 0.752, 0.8130000000000001, 0.86, 0.895, 0.923, 0.9430000000000001, 0.9590000000000001, 0.971, 0.98, 1.0]
190	14	[0.0, 0.247, 0.428, 0.5660000000000001, 0.672, 0.752, 0.8130000000000001, 0.86, 0.895, 0.923, 0.9430000000000001, 0.9590000000000001, 0.971, 0.98, 1.0]
200	15	[0.0, 0.247, 0.428, 0.5660000000000001, 0.672, 0.752, 0.8130000000000001, 0.86, 0.895, 0.923, 0.9430000000000001, 0.9590000000000001, 0.971, 0.98, 0.987, 1.0]
225	15	[0.0, 0.247, 0.428, 0.5660000000000001, 0.672, 0.752, 0.8130000000000001, 0.86, 0.895, 0.923, 0.9430000000000001, 0.9590000000000001, 0.971, 0.98, 0.987, 1.0]
250	15	[0.0, 0.247, 0.428, 0.5660000000000001, 0.672, 0.752, 0.8130000000000001, 0.86, 0.895, 0.923, 0.9430000000000001, 0.9590000000000001, 0.971, 0.98, 0.987, 1.0]
275	16	[0.0, 0.247, 0.428, 0.5660000000000001, 0.672, 0.752, 0.8130000000000001, 0.86, 0.895, 0.923, 0.9430000000000001, 0.9590000000000001, 0.971, 0.98, 0.987, 0.993, 1.0]
300	16	[0.0, 0.247, 0.428, 0.5660000000000001, 0.672, 0.752, 0.8130000000000001, 0.86, 0.895, 0.923, 0.9430000000000001, 0.9590000000000001, 0.971, 0.98, 0.987, 0.993, 1.0]
350	16	[0.0, 0.247, 0.428, 0.5660000000000001, 0.672, 0.752, 0.8130000000000001, 0.86, 0.895, 0.923, 0.9430000000000001, 0.9590000000000001, 0.971, 0.98, 0.987, 0.993, 1.0]
400	16	[0.0, 0.247, 0.428, 0.5660000000000001, 0.672, 0.752, 0.8130000000000001, 0.86, 0.895, 0.923, 0.9430000000000001, 0.9590000000000001, 0.971, 0.98, 0.987, 0.993, 1.0]
500	16	[0.0, 0.247, 0.428, 0.5660000000000001, 0.672, 0.752, 0.8130000000000001, 0.86, 0.895, 0.923, 0.9430000000000001, 0.9590000000000001, 0.971, 0.98, 0.987, 0.993, 1.0]
600	17	[0.0, 0.247, 0.428, 0.5660000000000001, 0.672, 0.752, 0.8130000000000001, 0.86, 0.895, 0.923, 0.9430000000000001, 0.9590000000000001, 0.971, 0.98, 0.987, 0.993, 0.997, 1.0]
700	17	[0.0, 0.247, 0.428, 0.5660000000000001, 0.672, 0.752, 0.8130000000000001, 0.86, 0.895, 0.923, 0.9430000000000001, 0.9590000000000001, 0.971, 0.98, 0.987, 0.993, 0.997, 1.0]
800	16	[0.0, 0.247, 0.428, 0.5660000000000001, 0.672, 0.752, 0.8130000000000001, 0.86, 0.895, 0.923, 0.9430000000000001, 0.9590000000000001, 0.971, 0.98, 0.987, 0.997, 1.0]
900	16	[0.0, 0.247, 0.428, 0.5660000000000001, 0.672, 0.752, 0.8130000000000001, 0.86, 0.895, 0.923, 0.9430000000000001, 0.9590000000000001, 0.971, 0.98, 0.987, 0.997, 1.0]
1000	16	[0.0, 0.247, 0.428, 0.5660000000000001, 0.672, 0.752, 0.8130000000000001, 0.86, 0.895, 0.923, 0.9430000000000001, 0.9590000000000001, 0.971, 0.98, 0.987, 0.997, 1.0]
1200	15	[0.0, 0.247, 0.428, 0.5660000000000001, 0.672, 0.752, 0.8130000000000001, 0.86, 0.895, 0.923, 0.9430000000000001, 0.9590000000000001, 0.971, 0.987, 0.997, 1.0]
1400	15	[0.0, 0.247, 0.428, 0.5660000000000001, 0.672, 0.752, 0.8130000000000001, 0.86, 0.895, 0.923, 0.9430000000000001, 0.9590000000000001, 0.971, 0.987, 0.997, 1.0]
1600	15	[0.0, 0.247, 0.428, 0.5660000000000001, 0.672, 0.752, 0.8130000000000001, 0.86, 0.895, 0.923, 0.9430000000000001, 0.9590000000000001, 0.971, 0.987, 0.997, 1.0]
1800	14	[0.0, 0.247, 0.428, 0.5660000000000001, 0.672, 0.752, 0.8130000000000001, 0.86, 0.895, 0.923, 0.9430000000000001, 0.9590000000000001, 0.98, 0.993, 1.0]
2000	14	[0.0, 0.247, 0.428, 0.5660000000000001, 0.672, 0.752, 0.8130000000000001, 0.86, 0.895, 0.923, 0.9430000000000001, 0.9590000000000001, 0.98, 0.993, 1.0]
2500	13	[0.0, 0.247, 0.428, 0.5660000000000001, 0.672, 0.752, 0.8130000000000001, 0.86, 0.895, 0.923, 0.9590000000000001, 0.98, 0.993, 1.0]
3000	11	[0.0, 0.247, 0.428, 0.5660000000000001, 0.672, 0.752, 0.8130000000000001, 0.895, 0.9430000000000001, 0.971, 0.993, 1.0]

Table A.9: Final Binnings MuTau

A.12 Statistical Methods

A.13 Pruning Methods

Systematic pruning methods within Workspace Maker are described below

Normalization contributions of a given systematic variation are subject to functions

- pruneSmallNormSysts(): Where if the values var_up OR var_down of the systematic variation, which is defined to be the absolute value of the ratio of the integrals of the up or down variation to its respective nominal distribution is less than .5% of the nominal distribution. Prune if

$$(sys.var\_up - 1) < .5\% || (sys.var\_do - 1) < .5\% \tag{A.1}$$

- pruneSameSignSysts(): Where if the product of the values $var\_up - 1$ and $var\_down - 1$ of a systematic variation are greater than or equal to 0, then the systematic is pruned. Since the up and down variations are defined as the absolute value of the ratio of the integrals of the up or down variation to its respective nominal distribution, the up variation is typically above 1 and the down variation is typically below 1. And so this pruning function is designed to remove systematics where the up AND down variations both have distributions that predominantly lie above or below their nominal distribution. Prune if

$$(sys.var\_up - 1) * (sys.var\_do - 1) >= 0 \tag{A.2}$$

Shape contributions of a given systematic variation are subject to the following pruning function

- pruneSmallShapeSysts(): Where at least 1 bin in the ratio of the up AND down variations of the systematic with respect to its nominal distribution is required to have a difference greater than .5%, If up AND down variations do not have at least 1 bin that has a variation larger than .5%, the systematic is pruned. Check for at least 1 bin in the up-AND-down variations

$$abs(varBin/nomBin - 1) > .5\% \tag{A.3}$$

  else prune systematic.

- pruneSmallShapeSysts_chi2_samesign(): (Only applies to smoothed histograms, and to background samples) Here, a chi-squared test is performed on the up and down variations with respect to their nominal distribution, and the maximum of these two fits is taken as a point of reference. A chi-squared test is then performed between the up and down variations with respect to each other. If the chi-squared value that comes as a result of the comparison between the up and down variations is less than the chi-squared value of the comparison between the up and down variations with respect to their nominal distribution, then the systematic is pruned.

A.14 Post-fit plots

A.14.1 Post Fit plots for JetTau Channel Observed

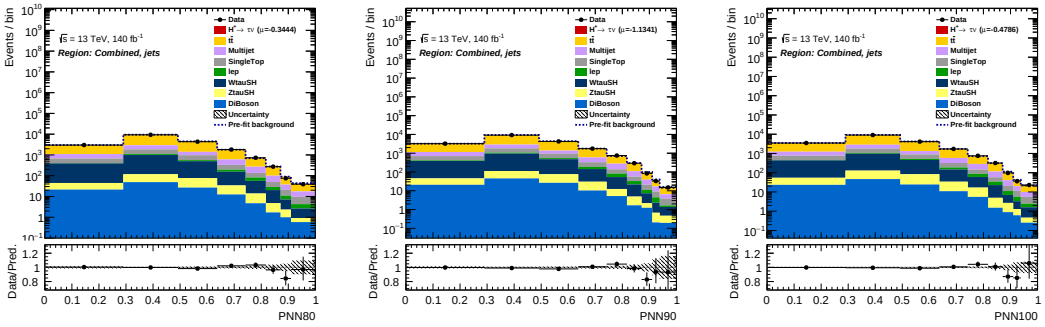

(a) JetTauSR PNN 80 PostFit (b) JetTauSR PNN 90 PostFit (c) JetTauSR PNN 100 PostFit

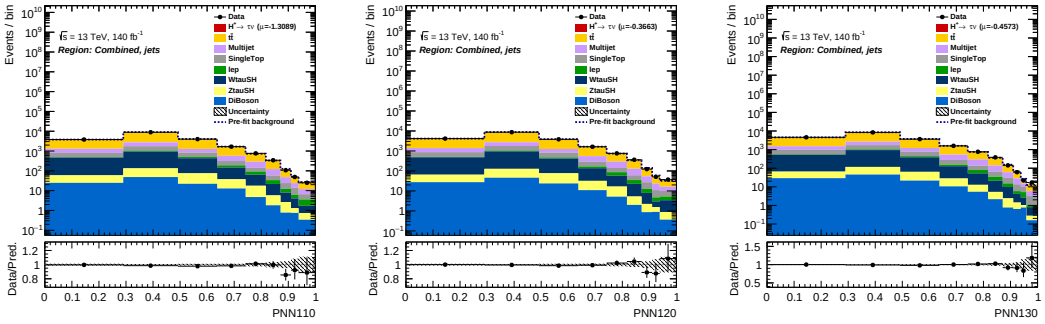

(d) JetTauSR PNN 110 PostFit (e) JetTauSR PNN 120 PostFit (f) JetTauSR PNN 130 PostFit

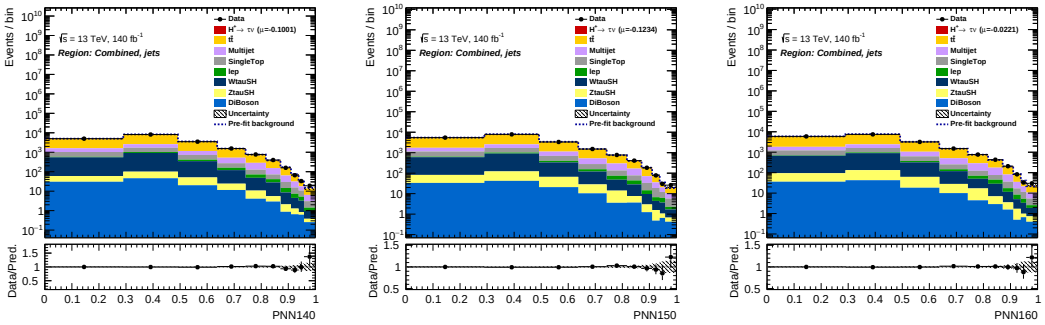

(g) JetTauSR PNN 140 PostFit (h) JetTauSR PNN 150 PostFit (i) JetTauSR PNN 160 PostFit

Figure A.9: PostFit Plots JetTauSR Observed: 80-160

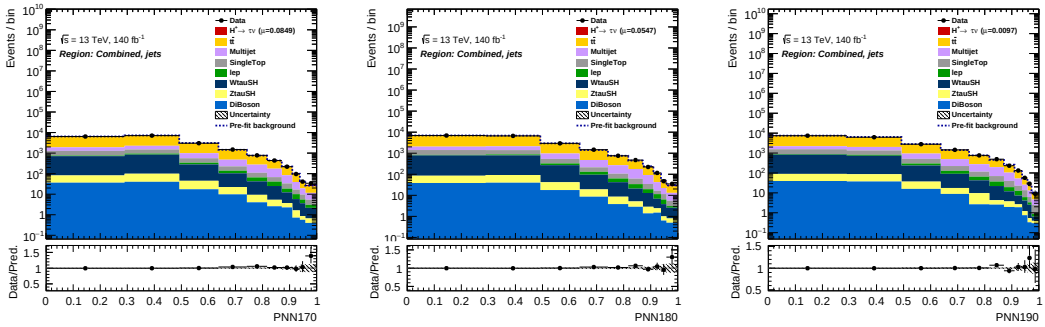

(a) JetTauSR PNN 170 PostFit (b) JetTauSR PNN 180 PostFit (c) JetTauSR PNN 190 PostFit

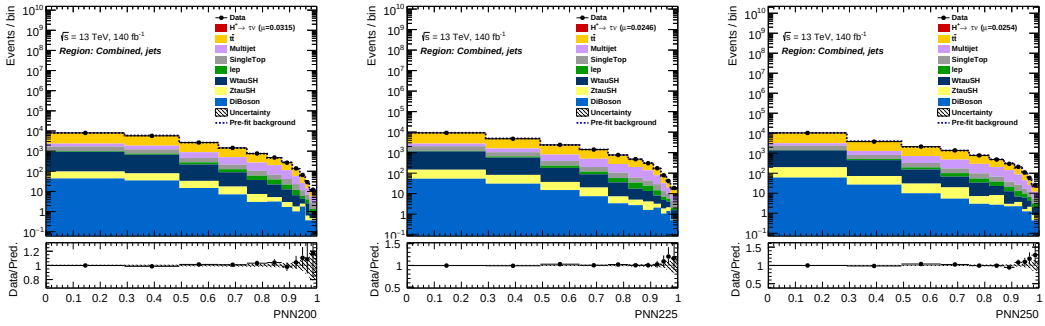

(d) JetTauSR PNN 200 PostFit (e) JetTauSR PNN 225 PostFit (f) JetTauSR PNN 250 PostFit

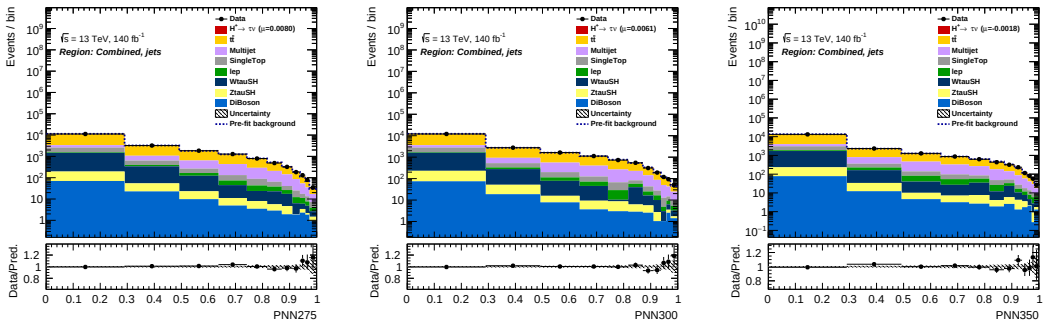

(g) JetTauSR PNN 275 PostFit (h) JetTauSR PNN 300 PostFit (i) JetTauSR PNN 350 PostFit

Figure A.10: PostFit Plots JetTauSR Observed: 170-350

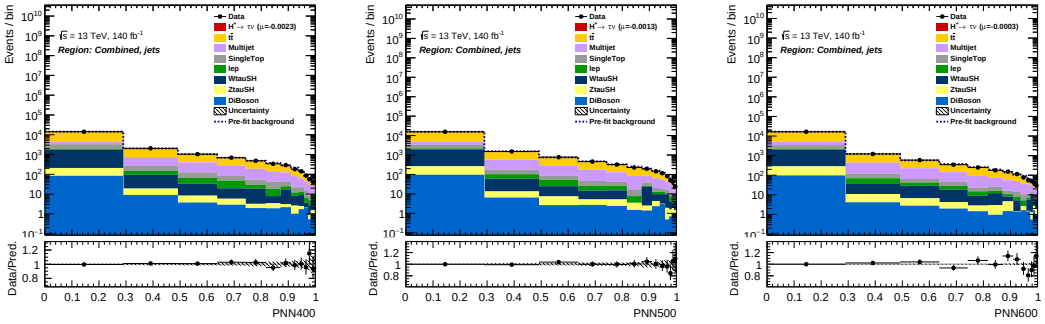

(a) JetTauSR PNN 400 PostFit (b) JetTauSR PNN 500 PostFit (c) JetTauSR PNN 600 PostFit

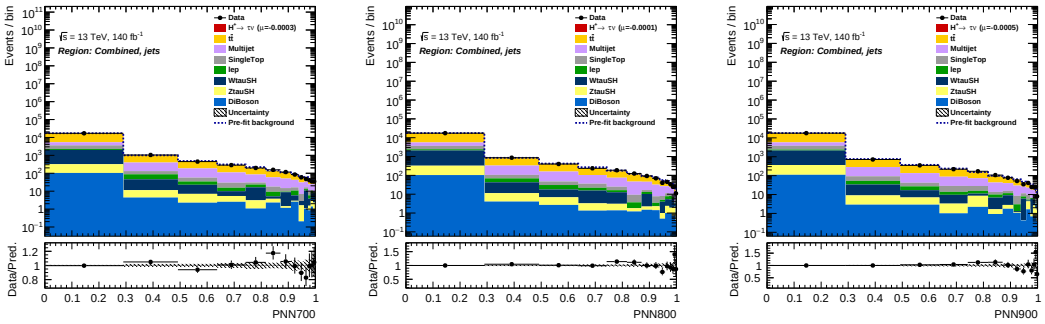

(d) JetTauSR PNN 700 PostFit (e) JetTauSR PNN 800 PostFit (f) JetTauSR PNN 900 PostFit

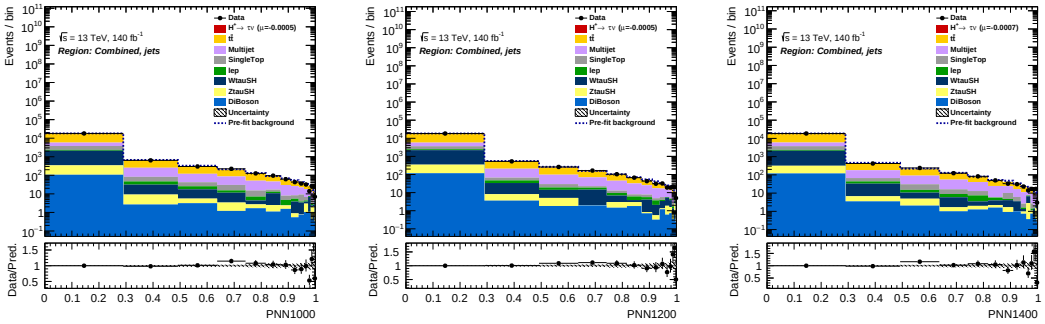

(g) JetTauSR PNN 1000 Post-Fit (h) JetTauSR PNN 1200 Post-Fit (i) JetTauSR PNN 1400 Post-Fit

Figure A.11: PostFit Plots JetTauSR Observed: 400-1400

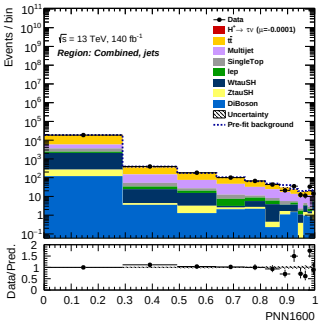

(a) JetTauSR PNN 1600 Post-Fit

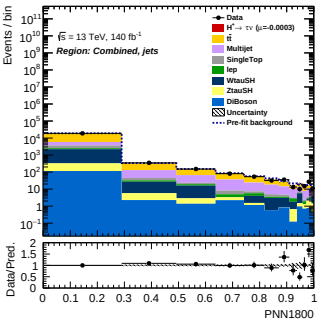

(b) JetTauSR PNN 1800 Post-Fit

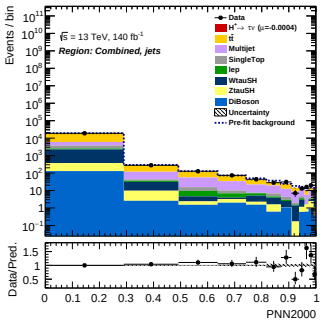

(c) JetTauSR PNN 2000 Post-Fit

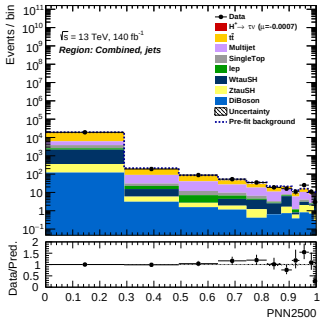

(d) JetTauSR PNN 2500 Post-Fit

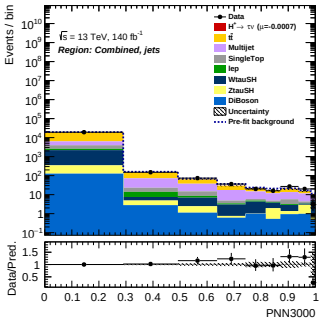

(e) JetTauSR PNN 3000 Post-Fit

Figure A.12: PostFit Plots JetTauSR Observed: 1600-3000

A.14.2 Post Fit plots for ElTau Channel Observed

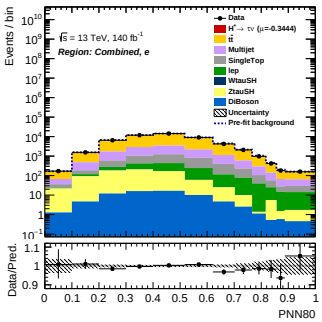

(a) ElTau PNN 80 PostFit

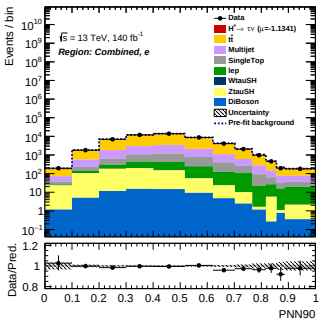

(b) ElTau PNN 90 PostFit

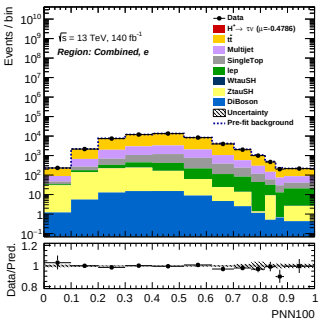

(c) ElTau PNN 100 PostFit

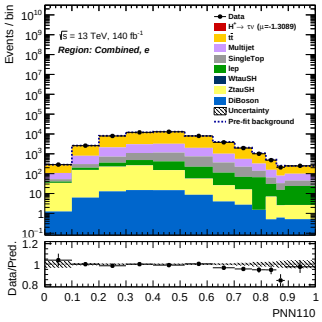

(d) ElTau PNN 110 PostFit

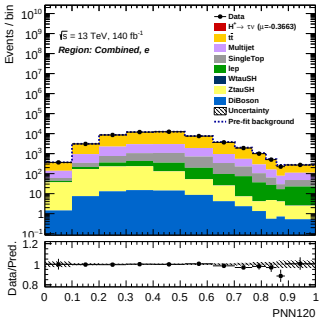

(e) ElTau PNN 120 PostFit

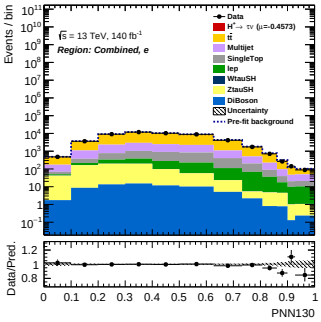

(f) ElTau PNN 130 PostFit

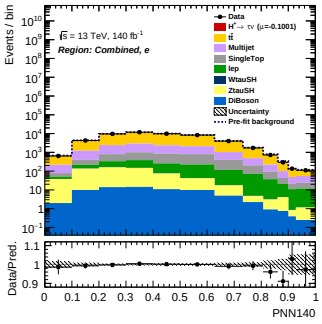

(g) ElTau PNN 140 PostFit

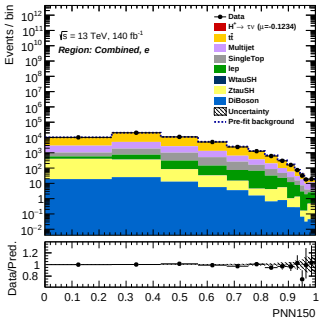

(h) ElTau PNN 150 PostFit

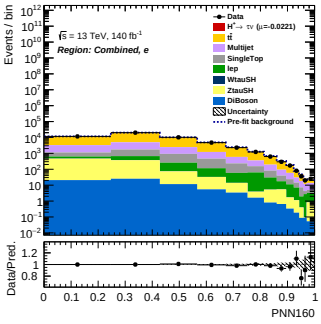

(i) ElTau PNN 160 PostFit

Figure A.13: PostFit Plots ElTau Observed: 80-160

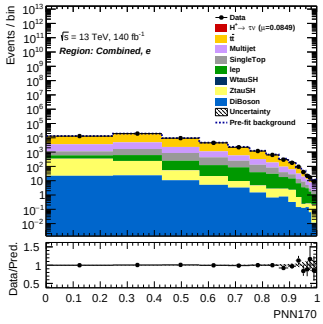

(a) ElTau PNN 170 PostFit

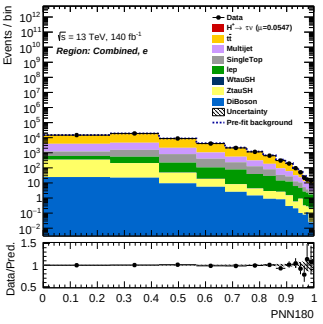

(b) ElTau PNN 180 PostFit

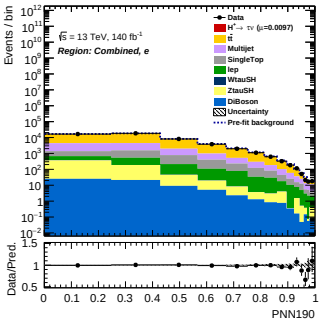

(c) ElTau PNN 190 PostFit

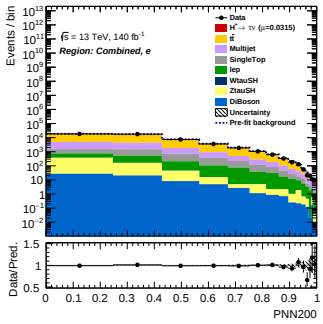

(d) ElTau PNN 200 PostFit

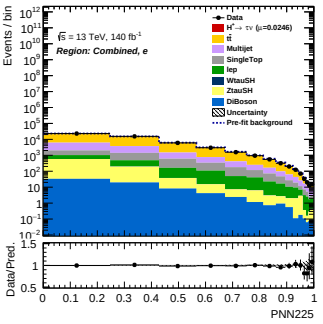

(e) ElTau PNN 225 PostFit

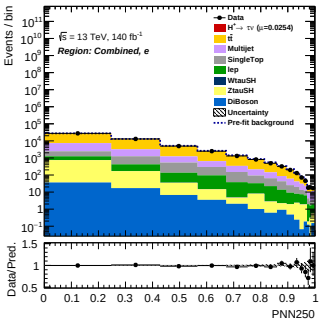

(f) ElTau PNN 250 PostFit

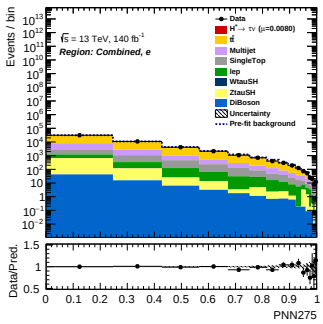

(g) ElTau PNN 275 PostFit

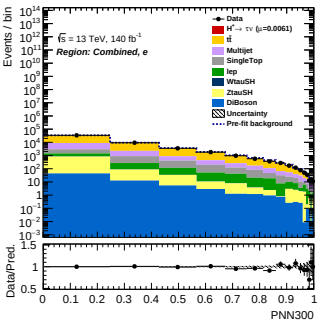

(h) ElTau PNN 300 PostFit

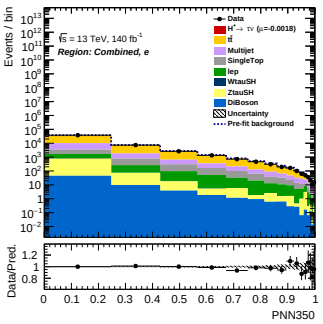

(i) ElTau PNN 350 PostFit

Figure A.14: PostFit Plots ElTau Observed: 170-350

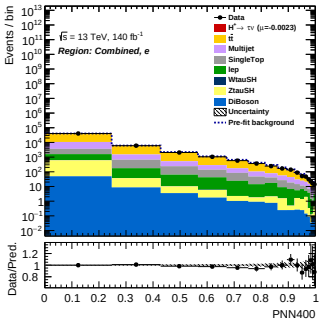

(a) ElTau PNN 400 PostFit

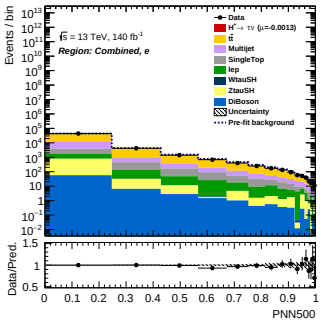

(b) ElTau PNN 500 PostFit

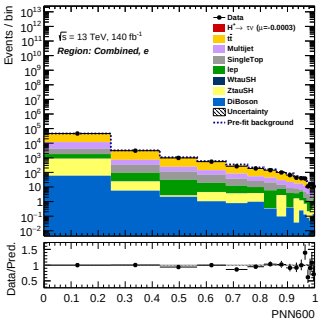

(c) ElTau PNN 600 PostFit

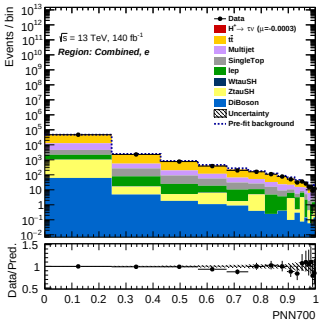

(d) ElTau PNN 700 PostFit

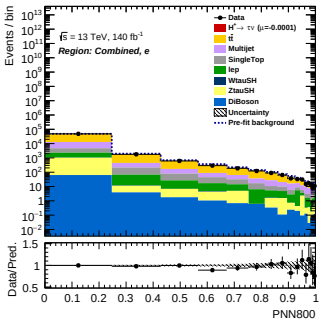

(e) ElTau PNN 800 PostFit

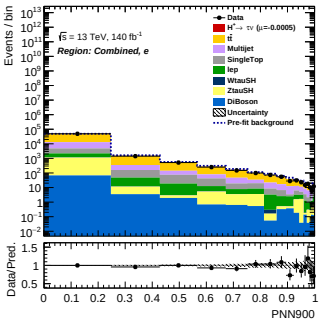

(f) ElTau PNN 900 PostFit

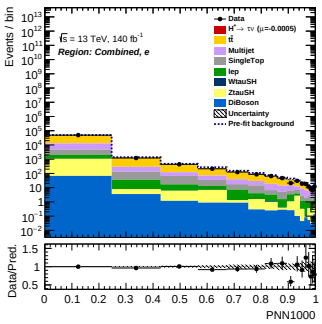

(g) ElTau PNN 1000 PostFit

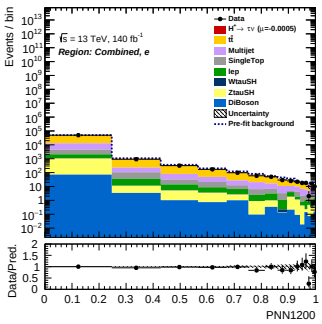

(h) ElTau PNN 1200 PostFit

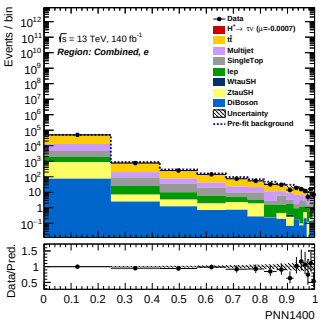

(i) ElTau PNN 1400 PostFit

Figure A.15: PostFit Plots ElTau Observed: 400-1400

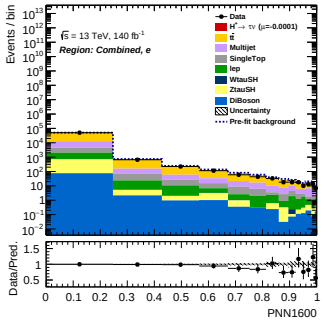

(a) ElTau PNN 1600 PostFit

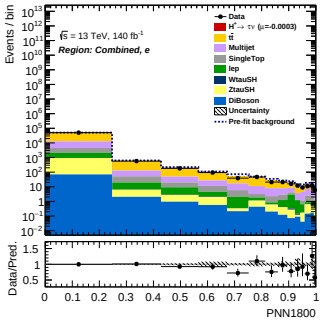

(b) ElTau PNN 1800 PostFit

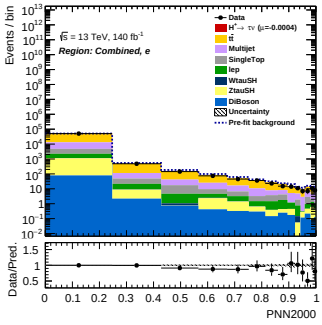

(c) ElTau PNN 2000 PostFit

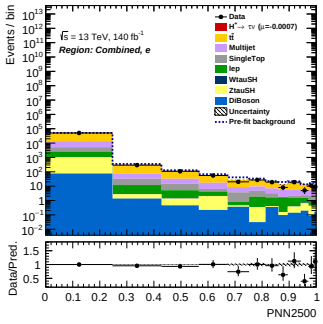

(d) ElTau PNN 2500 PostFit

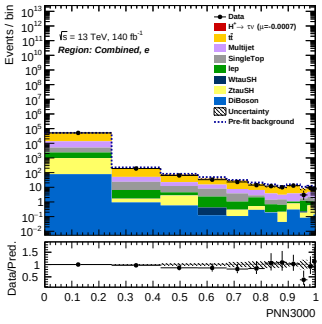

(e) ElTau PNN 3000 PostFit

Figure A.16: PostFit Plots ElTau Observed: 1600-3000

A.14.3 Post Fit plots for MuTau Channel Observed

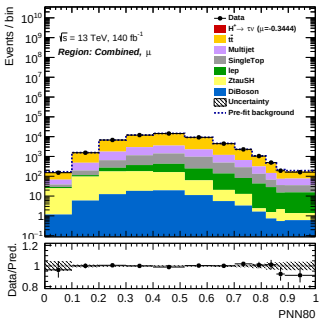

(a) MuTau PNN 80 PostFit

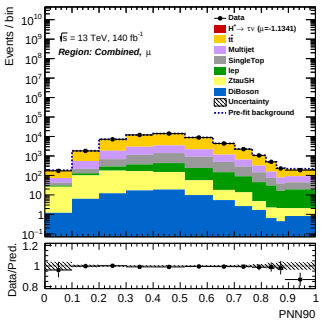

(b) MuTau PNN 90 PostFit

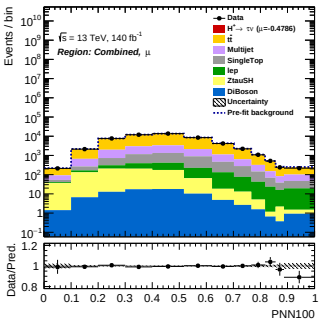

(c) MuTau PNN 100 PostFit

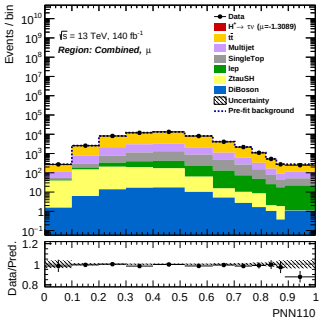

(d) MuTau PNN 110 PostFit

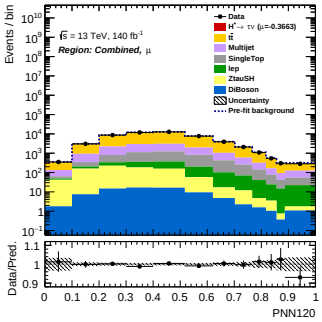

(e) MuTau PNN 120 PostFit

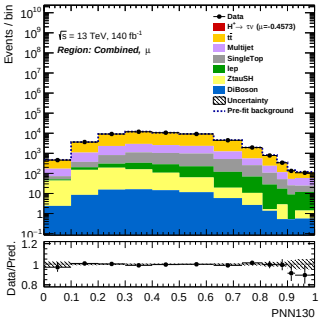

(f) MuTau PNN 130 PostFit

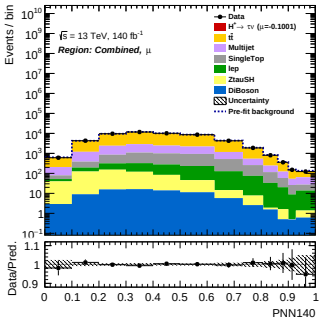

(g) MuTau PNN 140 PostFit

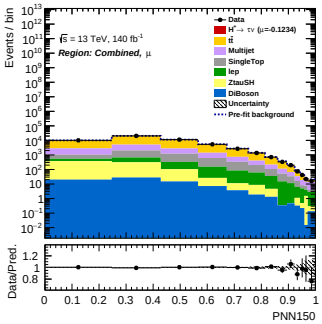

(h) MuTau PNN 150 PostFit

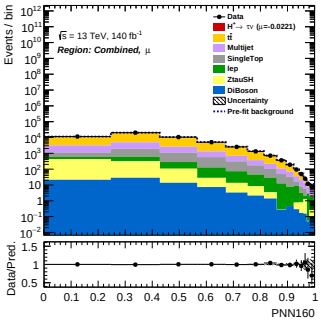

(i) MuTau PNN 160 PostFit

Figure A.17: PostFit Plots MuTau Observed: 80-160

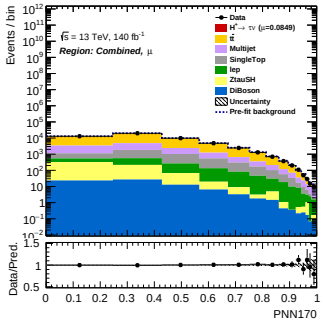

(a) MuTau PNN 170 PostFit

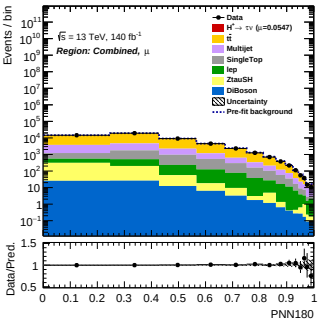

(b) MuTau PNN 180 PostFit

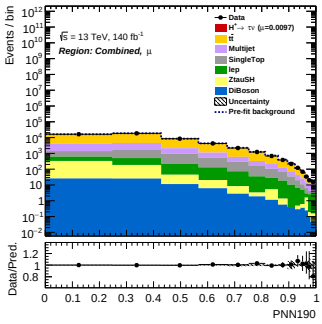

(c) MuTau PNN 190 PostFit

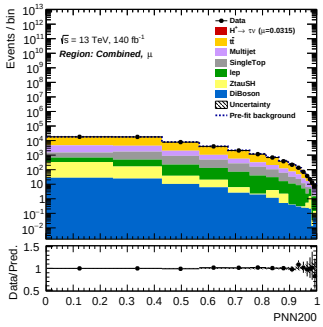

(d) MuTau PNN 200 PostFit

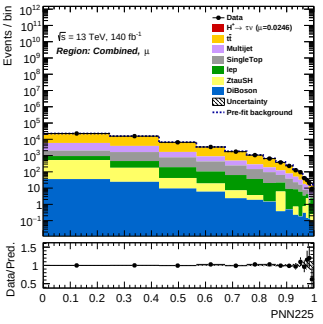

(e) MuTau PNN 225 PostFit

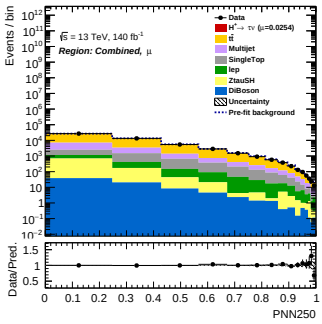

(f) MuTau PNN 250 PostFit

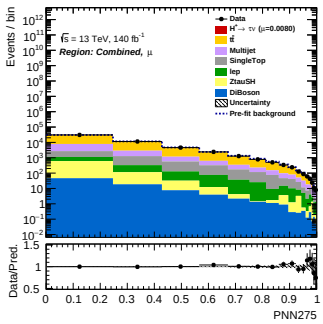

(g) MuTau PNN 275 PostFit

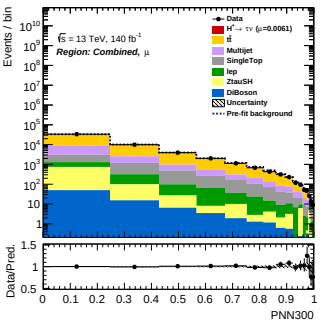

(h) MuTau PNN 300 PostFit

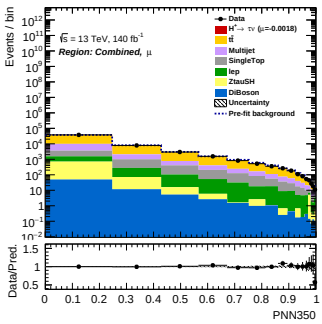

(i) MuTau PNN 350 PostFit

Figure A.18: PostFit Plots MuTau Observed: 170-350

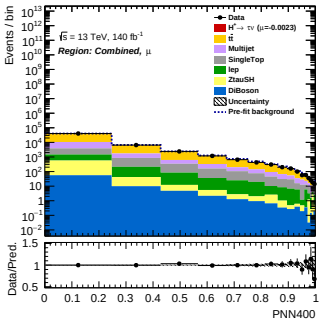

(a) MuTau PNN 400 PostFit

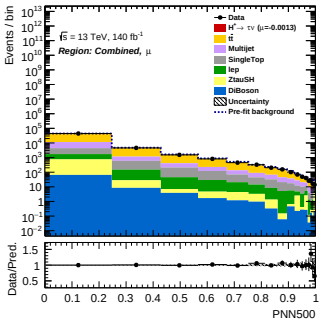

(b) MuTau PNN 500 PostFit

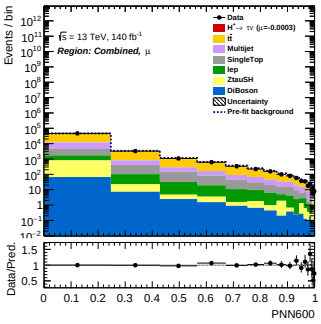

(c) MuTau PNN 600 PostFit

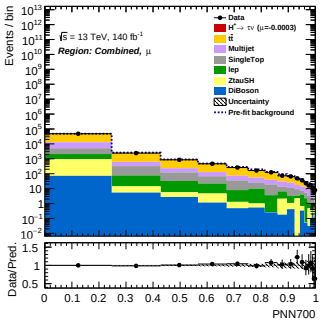

(d) MuTau PNN 700 PostFit

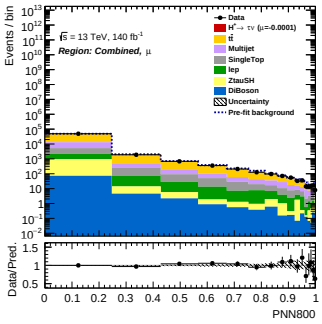

(e) MuTau PNN 800 PostFit

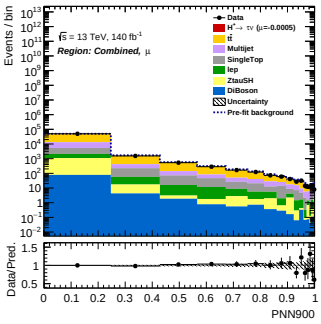

(f) MuTau PNN 900 PostFit

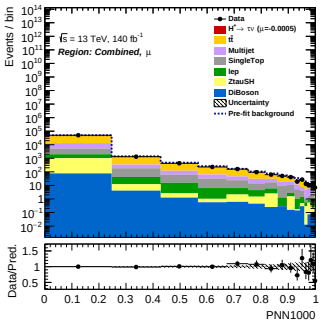

(g) MuTau PNN 1000 PostFit

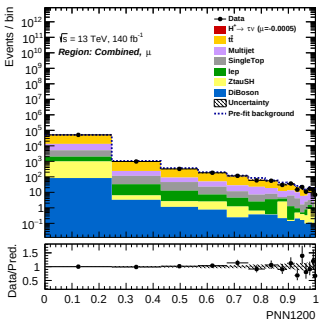

(h) MuTau PNN 1200 PostFit

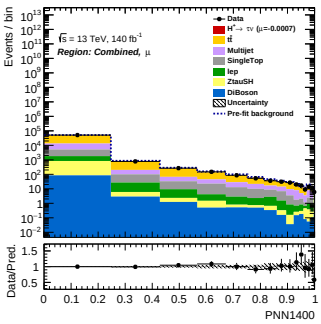

(i) MuTau PNN 1400 PostFit

Figure A.19: PostFit Plots MuTau Observed: 400-1400

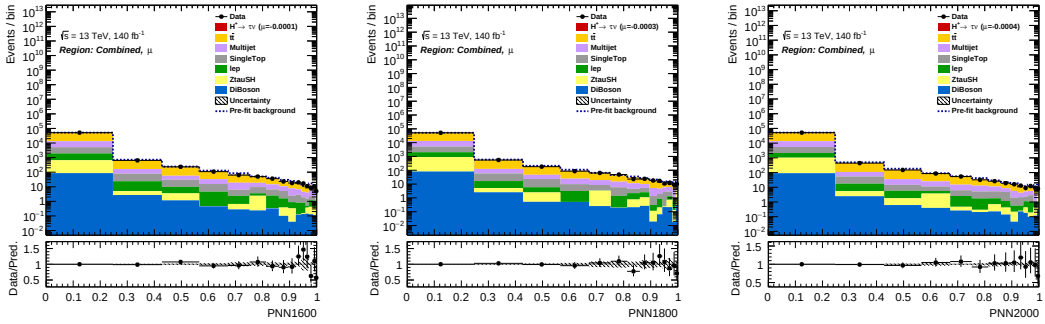

(a) MuTau PNN 1600 PostFit (b) MuTau PNN 1800 PostFit (c) MuTau PNN 2000 PostFit

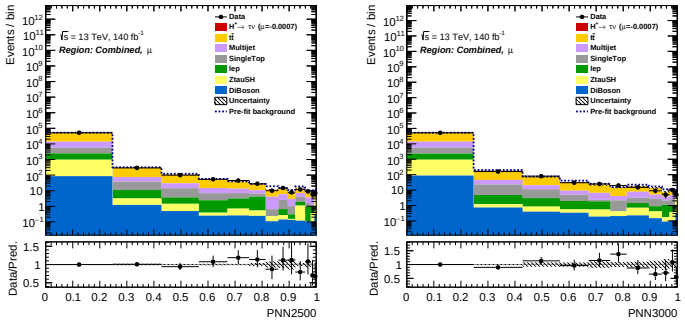

(d) MuTau PNN 2500 PostFit (e) MuTau PNN 3000 PostFit

Figure A.20: PostFit Plots MuTau Observed: 1600-3000

A.15 Nuisance Parameter Ranking Plots

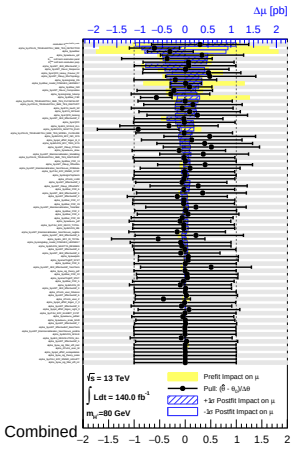

(a) Combined PNN 80 Pull

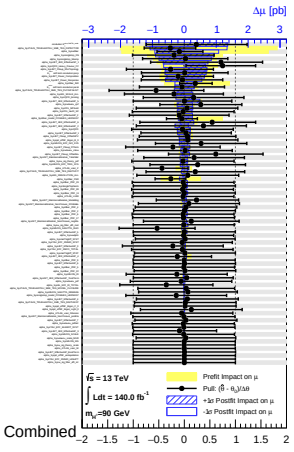

(b) Combined PNN 90 Pull

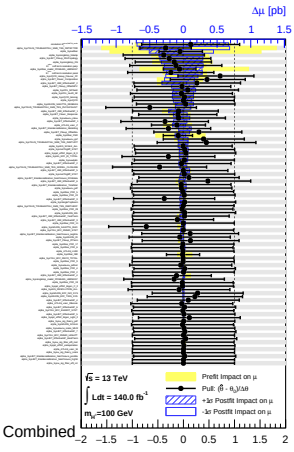

(c) Combined PNN 100 Pull

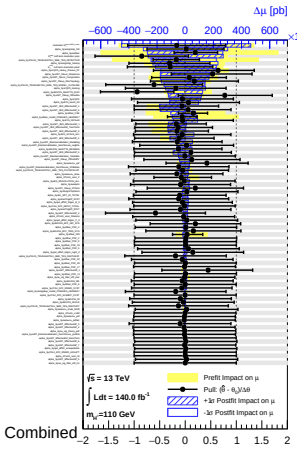

(d) Combined PNN 110 Pull

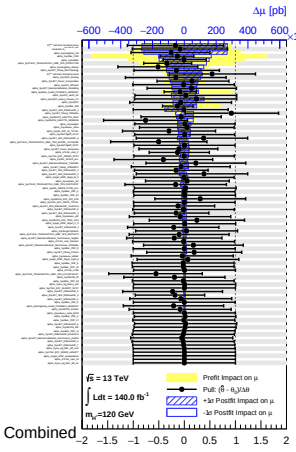

(e) Combined PNN 120 Pull

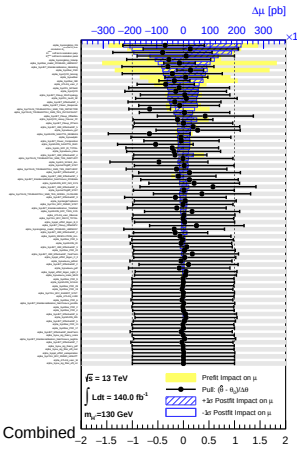

(f) Combined PNN 130 Pull

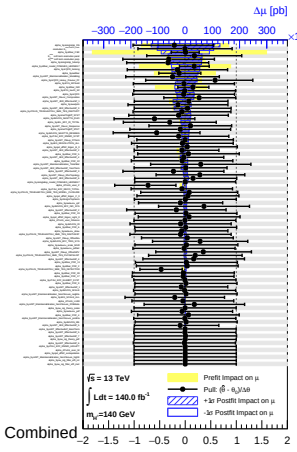

(g) Combined PNN 140 Pull

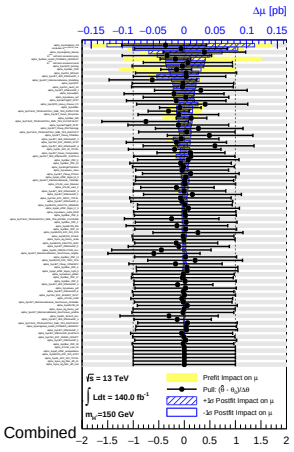

(h) Combined PNN 150 Pull

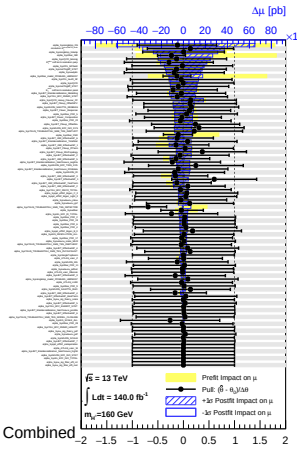

(i) Combined PNN 160 Pull

Figure A.21: Pull Plots Combined: 80-160 Observed

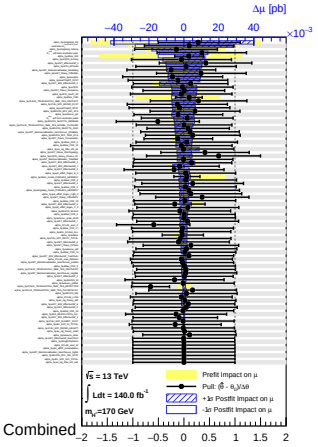

(a) Combined PNN 170 Pull

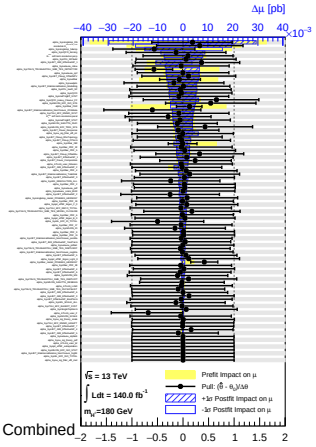

(b) Combined PNN 180 Pull

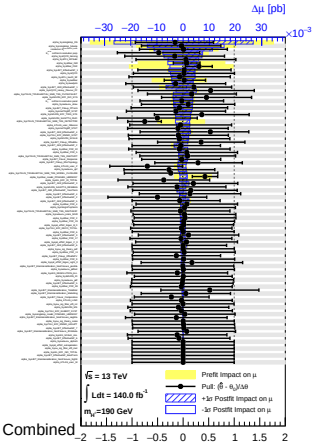

(c) Combined PNN 190 Pull

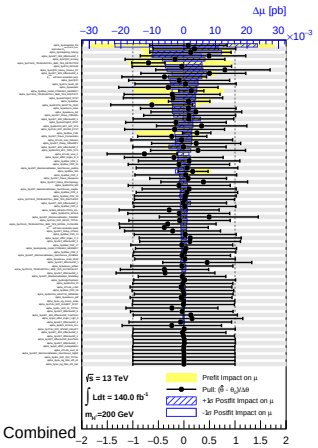

(d) Combined PNN 200 Pull

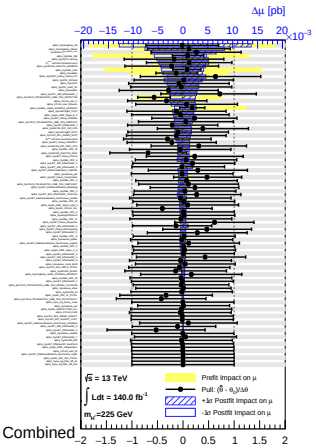

(e) Combined PNN 225 Pull

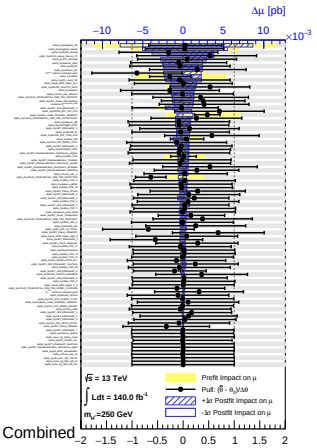

(f) Combined PNN 250 Pull

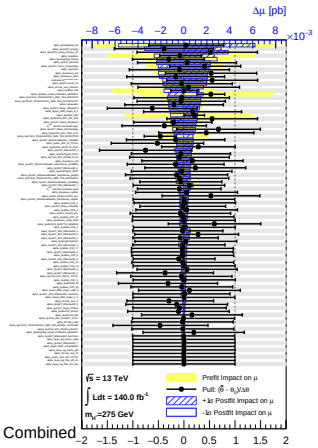

(g) Combined PNN 275 Pull

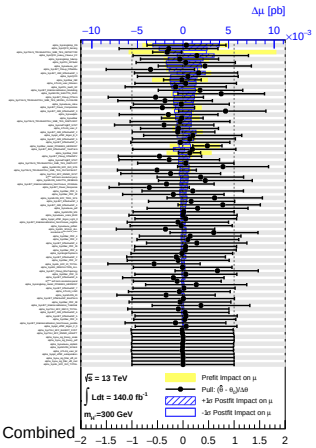

(h) Combined PNN 300 Pull

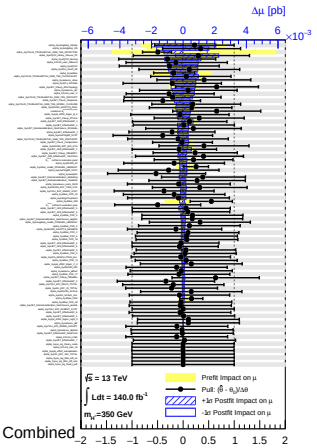

(i) Combined PNN 350 Pull

Figure A.22: Pull Plots Combined: 170-350 Observed

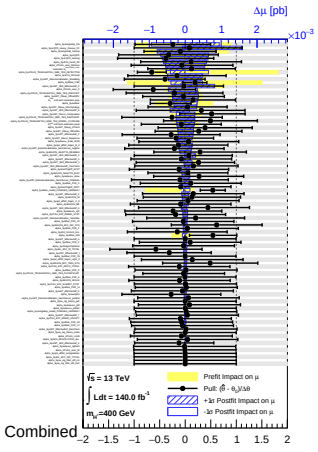

(a) Combined PNN 400 Pull

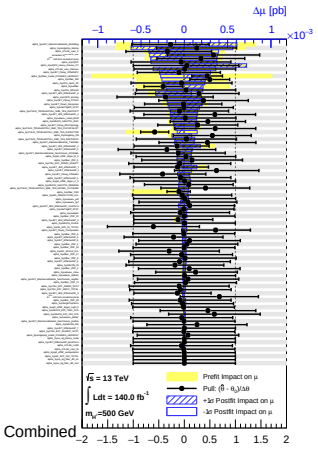

(b) Combined PNN 500 Pull

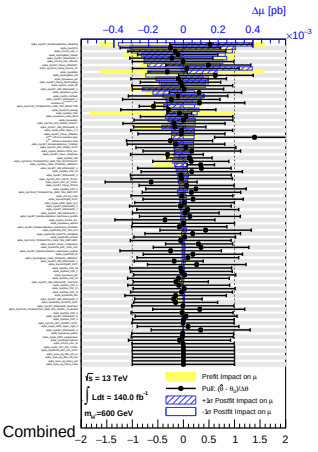

(c) Combined PNN 600 Pull

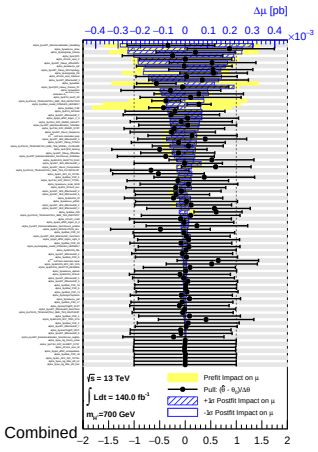

(d) Combined PNN 700 Pull

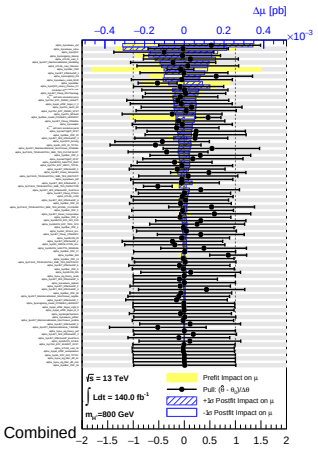

(e) Combined PNN 800 Pull

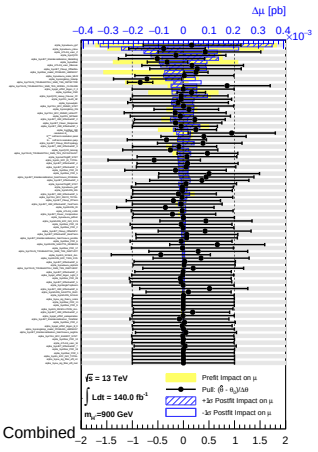

(f) Combined PNN 900 Pull

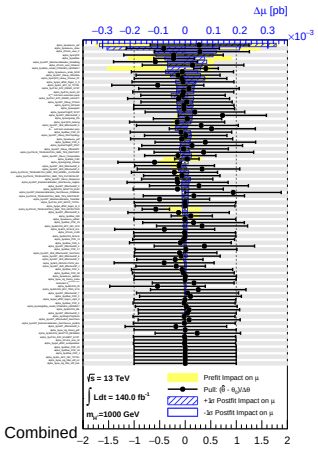

(g) Combined PNN 1000 Pull

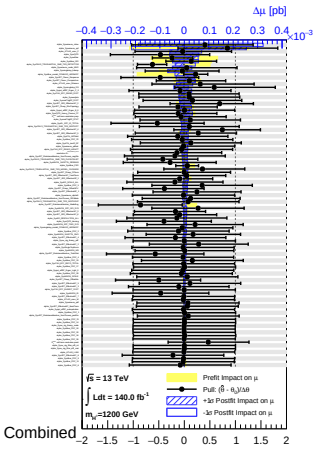

(h) Combined PNN 1200 Pull

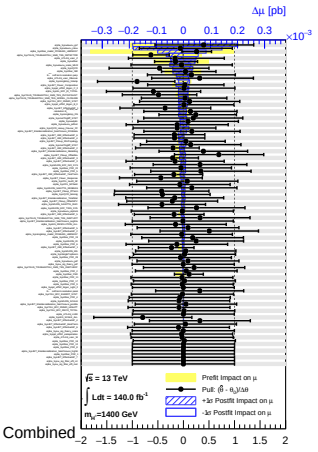

(i) Combined PNN 1400 Pull

Figure A.23: Pull Plots Combined: 400-1400 Observed

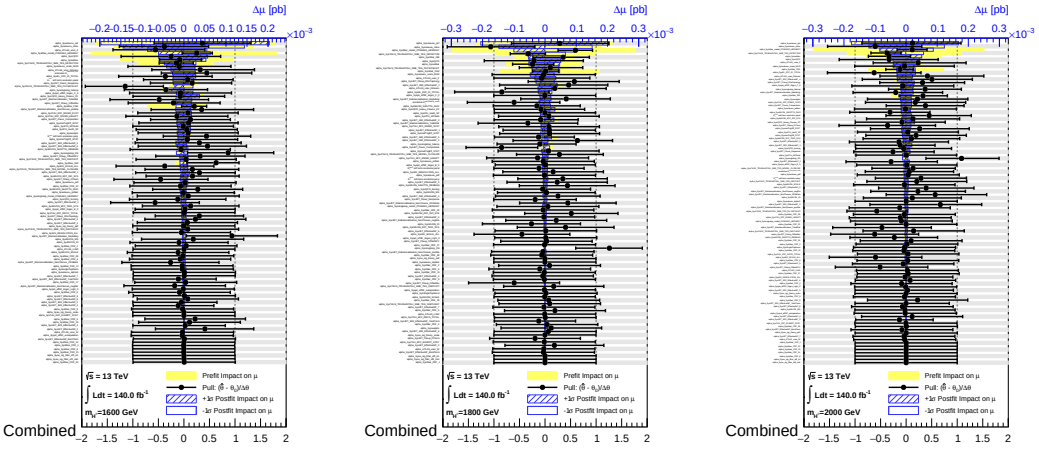

(a) Combined PNN 1600 Pull (b) Combined PNN 1800 Pull (c) Combined PNN 2000 Pull

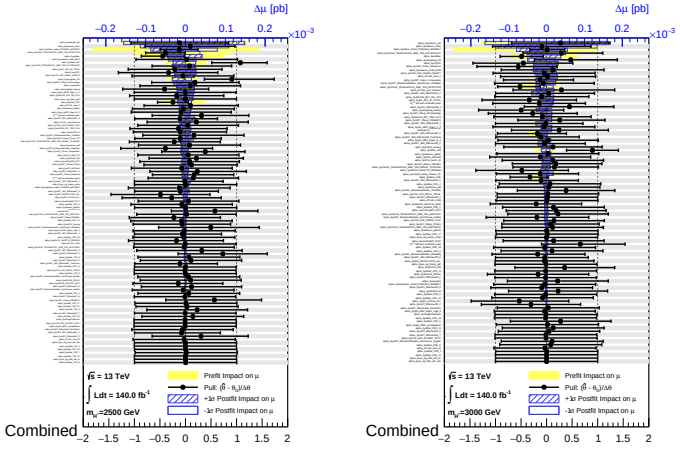

(d) Combined PNN 2500 Pull (e) Combined PNN 3000 Pull

Figure A.24: Pull Plots Combined: 1600-3000 Observed

Acronyms

2HDM 2 Higgs Doublet Model 23–25, 28, 37, 56

ALICE A Large Ion Collider Experiment 2

ATLAS A Torioidal LHC Apparatus 2, 4–6, 9, 12–14, 19, 23, 29, 31, 34, 37, 39

CMS Compact Muon Solenoid 2, 19

CR Control Region 65, 74

ECAL Electromagnetic Calorimeter 10, 11

FCAL Forward Calorimeters 10

FPGA Field Programmable Gate Array 13

GRL Good Run List 90

HCAL Hadronic Calorimeter 10, 11

HEC Hadronic End Cap Calorimeter 10

HLT High Level Trigger 12–14

ID Inner Detector 8

IP Interaction Point 7, 8

L1 Level 1 Trigger 12, 13

LEP Large Electron Positron Collider 56

LHC Large Hadron Collider 2, 6, 56, 109

LHCb Large Hadron Collider Beauty 2

LSTM Long Short Term Memory 39

MC Monte Carlo 37–39, 56, 71, 74, 77, 130

MET Missing Transverse Energy 13, 34, 57, 59–61, 65, IV

MIP Minimally Ionizing Particle 32

MSSM Minimal Super Symmetric Model 28

PNN Parameterized Neural Network 56, 90, 92

RNN Recurrent Neural Networks 37–42, 44–46, IV

ROI Region of Interest 13

SCT Silicon Microstrip Trackers 8, 29

SM Standard Model 23, 27, 28, 33, 56, 102, 109

SUSY Super Symmetry 27, 28

TauID Tau Identification 45, 48, 49, 51, 53

TRT Transition Radiation Tracker 8, 9, 29, 30

Bibliography

[1]L. R. Evans and P. Bryant, "LHC Machine", JINST **3**, This report is an abridged version of the LHC Design Report (CERN-2004-003), S08001 (2008).

[2]e. a. The ATLAS Collaboration, "The atlas experiment at the cern large hadron collider", Journal of Instrumentation **3**, S08003 (2008).

[3]e. a. The CMS Collaboration, "The CMS experiment at the CERN LHC", Journal of Instrumentation **3**, S08004 (2008).

[4]e. a. The ALICE Collaboration, "The ALICE experiment at the CERN LHC", Journal of Instrumentation **3**, S08002 (2008).

[5]e. a. The LHCb Collaboration, "The LHCb Detector at the LHC", Journal of Instrumentation **3**, S08005 (2008).

[6]CERN, *The_lhc_in_ints_geographic_location*, `https://cds.cern.ch/images/OPEN-PHO-CHART-2014-006-1/file?size=original`, [Online; accessed 05-May-2024], 2014.

[7]E. Lopienska, *Ccc-v2022*, `https://cds.cern.ch/images/CERN-GRAPHICS-2022-001-1`, [Online; accessed 23-April-2024], 2022.

[8]L. Arnaudon, P. Baudrenghien, M. Baylac, G. Bellodi, Y. Body, J. Borburgh, P. Bourquin, J. Broere, O. Brunner, L. Bruno, C. Carli, F. Caspers, S. M. Cousineau, Y. Cuvet, C. De Almeida Martins, T. Dobers, T. Fowler, R. Garoby, F. Gerigk, B. Goddard, K. Hanke, M. Hori, M. Jones, K. Kahle, W. Kalbreier, T. Kroyer, D. Küchler, A. M. Lombardi, L. A. López-Hernandez, M. Magistris, M. Martini, S. Maury, E. Page, M. Paoluzzi, M. Pasini, U. Raich, C. Rossi, J. P. Royer, E. Sargsyan, J. Serrano, R. Scrivens, M. Silari, M. Timmins, W. Venturini-Delsolaro, M. Vretenar, R. Wegner, W. Weterings, and T. Zickler, *Linac4 Technical Design Report*, tech. rep., revised version submitted on 2006-12-14 09:00:40 (CERN, Geneva, 2006).

[9]S. Albright, F. Antoniou, F. Asvesta, H. Bartosik, C. Bracco, and E. Renner, "New Longitudinal Beam Production Methods in the CERN Proton Synchrotron Booster", JACoW **IPAC'21**, 4130–4133 (2021).

[10]H. Bartosik and G. Rumolo, "Performance of the LHC injector chain after the upgrade and potential development", in Snowmass 2021 (Mar. 2022).

[11]T. A. collaboration, "Operation of the atlas trigger system in run 2", Journal of Instrumentation **15**, P10004 (2020).

[12]A. Team, "Diagram of an LHC dipole magnet. Schéma d'un aimant dipôle du LHC", `https://cds.cern.ch/record/40524`, 1999.

[13]J.-L. Caron, "LHC quadrupole cross section.", https://cds.cern.ch/record/841485, AC Collection. Legacy of AC. Pictures from 1992 to 2002., 1998.

[14]C. Degrande, R. Frederix, V. Hirschi, M. Ubiali, M. Wiesemann, and M. Zaro, "Accurate predictions for charged higgs production: closing the ...", Physics Letters B **772**, 87–92 (2017).

[15]J. Pequenao, "Computer generated image of the whole ATLAS detector", https://cds.cern.ch/record/1095924, 2008.

[16]A. R. BADEN, "Jets and kinematics in hadronic collisions", International Journal of Modern Physics A **13**, 1817–1845 (1998).

[17]I. Neutelings, *Cms coordinate system*, https://tikz.net/axis3d_cms/, [Online; accessed 07-May-2024], 2017.

[18]*ATLAS inner detector: Technical Design Report, 1*, Technical design report. ATLAS (CERN, Geneva, 1997).

[19]J. Pequenao, "Computer generated image of the ATLAS inner detector", https://cds.cern.ch/record/1095926, 2008.

[20]A. Vogel, *ATLAS Transition Radiation Tracker (TRT): Straw Tube Gaseous Detectors at High Rates*, tech. rep. (CERN, Geneva, 2013).

[21]"ATLAS liquid argon calorimeter: Technical design report", (1996).

[22]W. Lampl, C. Fabjan, and M. Aleksa, "Optimizing the energy measurement of the atlas electromagnetic calorimeter", (2006).

[23]*ATLAS tile calorimeter: Technical Design Report*, Technical design report. ATLAS (CERN, Geneva, 1996).

[24]J. Wotschack, *ATLAS Muon Chamber Construction Parameters for CSC, MDT, and RPC chambers*, tech. rep., Back-up document for the ATLAS Detector Paper (CERN, Geneva, 2008).

[25]G. Aad et al. (ATLAS), "Commissioning of the ATLAS Muon Spectrometer with Cosmic Rays. Commissioning of the ATLAS Muon Spectrometer with Cosmic Rays", Eur. Phys. J. C **70**, 875–916 (2010).

[26]*Trigger menu in 2018*, tech. rep., All figures including auxiliary figures are available at https://atlas.web.cern.ch/Atlas/GROUPS/PHYSICS/PUBNOTES/ATL-DAQ-PUB-2019-001 (CERN, Geneva, 2019).

[27]*Trigger Menu in 2017*, tech. rep., All figures including auxiliary figures are available at https://atlas.web.cern.ch/Atlas/GROUPS/PHYSICS/PUBNOTES/ATL-DAQ-PUB-2018-002 (CERN, Geneva, 2018).

[28]Y. Okumura (ATLAS), "Triggering in ATLAS in Run 2 and Run 3", PoS **EPS-HEP2021**, 788 (2022).

[29]G. Aad et al. (ATLAS), "Performance of the ATLAS Level-1 topological trigger in Run 2", Eur. Phys. J. C **82**, 7 (2022).

[30]Cush, *Standard model of elementary particles.svg*, `https://en.wikipedia.org/wiki/File:Standard_Model_of_Elementary_Particles.svg`, [Online; accessed 22-April-2024], 2019.

[31]C. S. Wu, E. Ambler, R. W. Hayward, D. D. Hoppes, and R. P. Hudson, "Experimental test of parity conservation in beta decay", Phys. Rev. **105**, 1413–1415 (1957).

[32]G. Aad, T. Abajyan, B. Abbott, J. Abdallah, S. Abdel Khalek, A. Abdelalim, O. Abdinov, R. Aben, B. Abi, M. Abolins, and et al., "Observation of a new particle in the search for the standard model higgs boson with the atlas detector at the lhc", Physics Letters B **716**, 1–29 (2012).

[33]e. a. The CMS Collaboration (CMS), "Observation of a new boson at a mass of 125 GeV with the CMS experiment at the LHC. Observation of a new boson at a mass of 125 GeV with the CMS experiment at the LHC", Phys. Lett. B **716**, 30–61 (2012).

[34]J. Ellis, M. K. Gaillard, and D. V. Nanopoulos, "A Historical Profile of the Higgs Boson", in *The standard theory of particle physics: Essays to celebrate CERN's 60th anniversary*, edited by L. Maiani and L. Rolandi (2016), pp. 255–274.

[35]D. Clowe, M. Bradač, A. H. Gonzalez, M. Markevitch, S. W. Randall, C. Jones, and D. Zaritsky, "A direct empirical proof of the existence of dark matter", The Astrophysical Journal **648**, L109–L113 (2006).

[36]S. P. MARTIN, "A supersymmetry primer", Advanced Series on Directions in High Energy Physics, 1–98 (1998).

[37]B. Abi, T. Albahri, S. Al-Kilani, D. Allspach, L. P. Alonzi, A. Anastasi, A. Anisenkov, F. Azfar, K. Badgley, S. Baeßler, I. Bailey, and e. a. Baranov (Muon $g-2$ Collaboration), "Measurement of the positive muon anomalous magnetic moment to 0.46 ppm", Phys. Rev. Lett. **126**, 141801 (2021).

[38]V. Khachatryan et al. (CMS), "Search for Lepton-Flavour-Violating Decays of the Higgs Boson", Phys. Lett. B **749**, 337–362 (2015).

[39]G. Aad et al. (ATLAS), "Searches for lepton-flavour-violating decays of the Higgs boson into $e\tau$ and $\mu\tau$ in $\sqrt{s} = 13$ TeV pp collisions with the ATLAS detector", JHEP **07**, 166 (2023).

[40]L. Collaboration, "Test of lepton universality in beauty-quark decays", Nature Physics **18**, 277–282 (2022).

[41]R. Aaij et al. (LHCb Collaboration), "Measurement of the ratios of branching fractions $\mathcal{R}(D^*)$ and $\mathcal{R}(D^0)$", Phys. Rev. Lett. **131**, 111802 (2023).

[42]J. P. Lees et al. (BaBar), "Evidence for an excess of $\bar{B} \to D^{(*)}\tau^-\bar{\nu}_\tau$ decays", Phys. Rev. Lett. **109**, 101802 (2012).

[43]M. Huschle et al. (Belle), "Measurement of the branching ratio of $\bar{B} \to D^{(*)}\tau^-\bar{\nu}_\tau$ relative to $\bar{B} \to D^{(*)}\ell^-\bar{\nu}_\ell$ decays with hadronic tagging at Belle", Phys. Rev. D **92**, 072014 (2015).

[44]R. Aaij, B. Adeva, M. Adinolfi, Z. Ajaltouni, S. Akar, J. Albrecht, F. Alessio, M. Alexander, A. Alfonso Albero, S. Ali, G. Alkhazov, P. Alvarez Cartelle, A. A. Alves, S. Amato, S. Amerio, Y. Amhis, L. An, L. Anderlini, G. Andreassi, M. Andreotti, J. E. Andrews, and e. a. Appleby (LHCb Collaboration), "Measurement of the ratio of the $B^0 \to D^{*-}\tau^+\nu_\tau$ and $B^0 \to D^{*-}\mu^+\nu_\mu$ branching fractions using three-prong τ-lepton decays", Phys. Rev. Lett. **120**, 171802 (2018).

[45]S. Iguro and K. Tobe, "$R(D^{(*)})$ in a general two Higgs doublet model", Nucl. Phys. B **925**, 560–606 (2017).

[46]A. Crivellin, C. Greub, and A. Kokulu, "Explaining $B \to D\tau\nu$, $B \to D^*\tau\nu$ and $B \to \tau\nu$ in a 2HDM of type III", Phys. Rev. D **86**, 054014 (2012).

[47]Y. Omura, E. Senaha, and K. Tobe, "τ- and μ-physics in a general two higgs doublet model with $\mu - \tau$ flavor violation", Phys. Rev. D **94**, 055019 (2016).

[48]M. Trodden, "Electroweak baryogenesis: A Brief review", in 33rd Rencontres de Moriond: Electroweak Interactions and Unified Theories (1998), pp. 471–480.

[49]A. G. Akeroyd, S. Moretti, and M. Song, "Slight excess at 130 GeV in search for a charged higgs boson decaying to a charm quark and a bottom quark at the large hadron collider", Journal of Physics G: Nuclear and Particle Physics **49**, 085004 (2022).

[50]H. E. Logan and D. MacLennan, "Charged Higgs phenomenology in the flipped two Higgs doublet model", Phys. Rev. D **81**, 075016 (2010).

[51]A. Djouadi, L. Maiani, G. Moreau, A. Polosa, J. Quevillon, and V. Riquer, "The post-Higgs MSSM scenario: Habemus MSSM?", Eur. Phys. J. C **73**, 2650 (2013).

[52]G. C. Branco, P. M. Ferreira, L. Lavoura, M. N. Rebelo, M. Sher, and J. P. Silva, "Theory and phenomenology of two-Higgs-doublet models", Physics Reports **516**, arXiv:1106.0034 [hep-ph], 1–102 (2012).

[53]V. Barger, J. L. Hewett, and R. J. N. Phillips, "New constraints on the charged higgs sector in two-higgs-doublet models", Phys. Rev. D **41**, 3421–3441 (1990).

[54]P. J. Klimek, B. O. Burghgrave, A. Kaczmarska, P. Bruckman De Renstrom, S. Bahrasemani, E. Parrish, M. Mlynarikova, M. Bahmani, M. K. Juzek, Z. K. Zak, L. Duval, E. Drechsler, H. Hadavand, D. Chakraborty, D. O'Neil, J. C. Cardenas Jr, and J. Adelman, *Search for charged Higgs bosons decaying via $H^\pm \to \tau^\pm\nu_\tau$ in the τ+jets and τ+lepton final states with 139 fb^{-1} of pp collision data recorded at $\sqrt{s} = 13$ TeV with the ATLAS experiment*, tech. rep., `https://cds.cern.ch/record/2777234` (CERN, Geneva, 2021).

[55]MonicaVazquezAcosta, *Yrhxs3$_b$r$_f$ig*34, `https://twiki.cern.ch/twiki/bin/view/LHCPhysics/LHCHWGCrossSectionsFigures?redirectedfrom=LHCPhysics.LHCHXSWGCrossSectionsFigures#H_cross_sections_plots_2HDM`, [Online; accessed 07-May-2024], 2014.

[56]*Summary plots for beyond Standard Model Higgs boson benchmarks for direct and indirect searches*, tech. rep., All figures including auxiliary figures are available at https://atlas.web.cern.ch/Atlas/GROUPS/PHYSICS/PUBNOTES/ATL-PHYS-PUB-2022-043 (CERN, Geneva, 2022).

[57]A. DJOUADI, "The anatomy of electroweak symmetry breaking tome ii: the higgs bosons in the minimal supersymmetric model", Physics Reports **459**, 1–241 (2008).

[58]A. Collaboration, *Athena*, https://doi.org/10.5281/zenodo.4772550, version 21.0.127, May 2021.

[59]M. Aaboud, G. Aad, B. Abbott, J. Abdallah, O. Abdinov, B. Abeloos, S. H. Abidi, O. S. AbouZeid, N. L. Abraham, H. Abramowicz, H. Abreu, R. Abreu, and e. a. Abulaiti, "Performance of the atlas track reconstruction algorithms in dense environments in lhc run 2", The European Physical Journal C **77**, 10.1140/epjc/s10052-017-5225-7 (2017).

[60]T. CP, *atlassoftwaredocs*, https://atlassoftwaredocs.web.cern.ch/trackingTutorial/, [Accessed: April 12, 2024], 2020.

[61]T. Cornelissen, M. Elsing, S. Fleischmann, W. Liebig, and E. Moyse, "Concepts, Design and Implementation of the ATLAS New Tracking (NEWT)", edited by A. Salzburger (2007).

[62]"Software Performance of the ATLAS Track Reconstruction for LHC Run 3", (2021).

[63]G. Aad et al. (ATLAS), "A neural network clustering algorithm for the ATLAS silicon pixel detector", JINST **9**, P09009 (2014).

[64]G. Aad, B. Abbott, J. Abdallah, O. Abdinov, R. Aben, M. Abolins, O. S. AbouZeid, H. Abramowicz, H. Abreu, R. Abreu, Y. Abulaiti, B. S. Acharya, L. Adamczyk, D. L. Adams, and e. a. Adelman, "Topological cell clustering in the atlas calorimeters and its performance in lhc run 1", The European Physical Journal C **77**, 10.1140/epjc/s10052-017-5004-5 (2017).

[65]T. Barillari et al. (ATLAS), "Local hadronic calibration", (2009).

[66]T. A. Collaboration, "Electron and photon performance measurements with the atlas detector using the 2015-2017 lhc proton-proton collision data", Journal of Instrumentation **14**, P12006 (2019).

[67]T. A. Collaboration, "Electron reconstruction and identification in the atlas experiment using the 2015 and 2016 lhc proton–proton collision data at $$\sqrt{s} = 13$$ $$\text {tev}$$", The European Physical Journal C **79**, 639 (2019).

[68]"Electron Identification with a Convolutional Neural Network in the ATLAS Experiment", (2023).

[69]G. Aad et al. (ATLAS), "Muon reconstruction performance of the ATLAS detector in proton–proton collision data at $\sqrt{s}$ =13 TeV", Eur. Phys. J. C **76**, 292 (2016).

[70]G. Aad et al. (ATLAS), "Muon reconstruction and identification efficiency in ATLAS using the full Run 2 *pp* collision data set at $\sqrt{s} = 13$ TeV", Eur. Phys. J. C **81**, 578 (2021).

[71]*Reconstruction, Identification, and Calibration of hadronically decaying tau leptons with the ATLAS detector for the LHC Run 3 and reprocessed Run 2 data*, tech. rep., All figures including auxiliary figures are available at

https://atlas.web.cern.ch/Atlas/GROUPS/PHYSICS/PUBNOTES/ATL-PHYS-PUB-2022-044 (CERN, Geneva, 2022).

[72]R. L. Workman et al. (Particle Data Group), "Review of Particle Physics", PTEP **2022**, 083C01 (2022).

[73]"Reconstruction, Energy Calibration, and Identification of Hadronically Decaying Tau Leptons in the ATLAS Experiment for Run-2 of the LHC", (2015).

[74]"Development of ATLAS Primary Vertex Reconstruction for LHC Run 3", (2019).

[75]G. Aad et al. (ATLAS), "Identification and energy calibration of hadronically decaying tau leptons with the ATLAS experiment in *pp* collisions at $\sqrt{s}$=8 TeV", Eur. Phys. J. C **75**, 303 (2015).

[76]*E_T^{miss} performance in the ATLAS detector using 2015-2016 LHC p-p collisions*, tech. rep., All figures including auxiliary figures are available at https://atlas.web.cern.ch/Atlas/GROUPS/PHYSICS/CONFNOTES/ATLAS-CONF-2018-023 (CERN, Geneva, 2018).

[77]S. D. Ellis and D. E. Soper, "Successive combination jet algorithm for hadron collisions", Physical Review D **48**, 3160–3166 (1993).

[78]M. Cacciari, G. P. Salam, and G. Soyez, "The anti-ktjet clustering algorithm", Journal of High Energy Physics **2008**, 063–063 (2008).

[79]G. Aad et al. (ATLAS), "Jet energy scale and resolution measured in proton–proton collisions at $\sqrt{s} = 13$ TeV with the ATLAS detector", Eur. Phys. J. C **81**, 689 (2021).

[80]M. Aaboud, G. Aad, B. Abbott, J. Abdallah, O. Abdinov, B. Abeloos, S. H. Abidi, O. S. AbouZeid, N. L. Abraham, H. Abramowicz, H. Abreu, R. Abreu, Y. Abulaiti, B. S. Acharya, S. Adachi, L. Adamczyk, J. Adelman, M. Adersberger, T. Adye, A. A. Affolder, T. Agatonovic-Jovin, and e. a. Agheorghiesei, "Jet reconstruction and performance using particle flow with the atlas detector", The European Physical Journal C **77**, 466 (2017).

[81]"Optimisation and performance studies of the ATLAS *b*-tagging algorithms for the 2017-18 LHC run", (2017).

[82]G. Aad et al. (ATLAS), "Configuration and performance of the ATLAS *b*-jet triggers in Run 2", Eur. Phys. J. C **81**, 1087 (2021).

[83]Flavour Tagging Group, *Tagger recommendations for release 21*, `https://twiki.cern.ch/twiki/bin/view/AtlasProtected/BTagTaggerRecommendationsRelease21`.

[84]"Identification of Jets Containing *b*-Hadrons with Recurrent Neural Networks at the ATLAS Experiment", (2017).

[85]R. L. Workman et al. (Particle Data Group), "Review of Particle Physics", PTEP **2022**, 083C01 (2022).

[86]*Identification of hadronic tau lepton decays using neural networks in the ATLAS experiment*, tech. rep., All figures including auxiliary figures are available at https://atlas.web.cern.ch/Atlas/GROUPS/PHYSICS/PUBNOTES/ATL-PHYS-PUB-2019-033 (CERN, Geneva, 2019).

[87]F. Chollet et al., *Keras*, https://keras.io, 2015.

[88]Martín Abadi, Ashish Agarwal, Paul Barham, Eugene Brevdo, Zhifeng Chen, Craig Citro, Greg S. Corrado, Andy Davis, Jeffrey Dean, Matthieu Devin, Sanjay Ghemawat, Ian Goodfellow, Andrew Harp, Geoffrey Irving, Michael Isard, Y. Jia, Rafal Jozefowicz, Lukasz Kaiser, Manjunath Kudlur, Josh Levenberg, Dandelion Mané, Rajat Monga, Sherry Moore, Derek Murray, Chris Olah, Mike Schuster, Jonathon Shlens, Benoit Steiner, Ilya Sutskever, Kunal Talwar, Paul Tucker, Vincent Vanhoucke, Vijay Vasudevan, Fernanda Viégas, Oriol Vinyals, Pete Warden, Martin Wattenberg, Martin Wicke, Yuan Yu, and Xiaoqiang Zheng, *TensorFlow: large-scale machine learning on heterogeneous systems*, Software available from tensorflow.org, 2015.

[89]s. SUGAR SHARMA, *1xxxia0jjvprhejhd4z893g*, https://miro.medium.com/v2/resize:fit:4800/format:webp/1*XxxiA0jJvPrHEJHD4z893g.png, [Online; accessed 22-April-2024], 2017.

[90]M. Zaheer, S. Kottur, S. Ravanbakhsh, B. Poczos, R. Salakhutdinov, and A. Smola, *Deep sets*, https://arxiv.org/abs/1703.06114, 2018.

[91]P. T. Komiske, E. M. Metodiev, and J. Thaler, "Energy flow networks: deep sets for particle jets", Journal of High Energy Physics **2019**, 10.1007/jhep01(2019)121 (2019).

[92]J. C. J. Cardenas, *Decay Mode Neural Networks for Tau Jet Classification in ATLAS*, tech. rep., https://cds.cern.ch/record/2744994 (CERN, Geneva, Nov. 2020).

[93]J. Pivarski, P. Das, C. Burr, D. Smirnov, M. Feickert, T. Gal, L. Kreczko, N. Smith, N. Biederbeck, O. Shadura, M. Proffitt, benkrikler, H. Dembinski, H. Schreiner, J. Rembser, M. R., C. Gu, Edoardo, E. Rodrigues, JMSchoeffmann, J. Rübenach, L. Koch, M. Peresano, N. Eich, R. Turra, and bfis, *Scikit-hep/uproot3: 3.14.4*, version 3.14.4, Feb. 2021.

[94]S. Hochreiter and J. Schmidhuber, "Long short-term memory", Neural computation **9**, 1735–80 (1997).

[95]M. Bayramov, *Rnn cell representation*, https://medium.com/@spyroot/shapegen-gran-generation-955d5b78e6d8, [Online; accessed 12-May-2024], 2021.

[96]C. R. Harris, K. J. Millman, S. J. van der Walt, R. Gommers, P. Virtanen, D. Cournapeau, E. Wieser, J. Taylor, S. Berg, N. J. Smith, R. Kern, M. Picus, S. Hoyer, M. H. van Kerkwijk, M. Brett, A. Haldane, J. F. del Río, M. Wiebe, P. Peterson, P. Gérard-Marchant, K. Sheppard, T. Reddy, W. Weckesser, H. Abbasi, C. Gohlke, and T. E. Oliphant, "Array programming with NumPy", Nature **585**, 357–362 (2020).

[97]A. Collette, T. Kluyver, T. A. Caswell, J. Tocknell, J. Kieffer, A. Scopatz, D. Dale, Chen, A. Jelenak, payno, juliagarriga, T. VINCENT, P. Sciarelli, V. Valls, S. Ghosh, U. K. Pedersen, jakirkham, M. Raspaud, A. Parsons, H. Abbasi, J. Readey, A. Paramonov, L. Chan, V. A. Solé, jialin, C. Danilevski, Y. Feng, G. A. Vaillant, M. Teichmann, and M. Brucher, *H5py/h5py: 3.2.1*, version 3.2.1, Mar. 2021.

[98]H. Nguyen, *Improving hadronic tau decay mode reconstruction at atlas using neural networks*, https://web.physik.uni-bonn.de/group/view.php?&group=1&lang=de&c=t&id=123, [Online; accessed 22-April-2024], 2020.

[99]P. Baldi, K. Cranmer, T. Faucett, P. Sadowski, and D. Whiteson, "Parameterized neural networks for high-energy physics", The European Physical Journal C **76**, 235 (2016).

[100]Aleph, Delphi, L3, O. Collaborations, and the LEP working group for Higgs boson searches, *Search for charged higgs bosons: combined results using lep data*, 2013.

[101]JetEtmiss Group, *Jet recommendations*, https://twiki.cern.ch/twiki/bin/view/AtlasProtected/JetEtmissRecommendationsR21.

[102]d. Dirk Duschinger David Kirchmeier, *Documentation for the tauselectiontool*, https://gitlab.cern.ch/atlas/athena/-/blob/21.2/PhysicsAnalysis/TauID/TauAnalysisTools/doc/README-TauSelectionTool.rst.

[103]Electron Gamma Working Group, *Egamma recommendations for release 21*, https://twiki.cern.ch/twiki/bin/view/AtlasProtected/EGammaRecommendationsR21.

[104]T. isolation and F. F. for electrons, *Isolationselectiontool for electrons*, https://twiki.cern.ch/twiki/bin/view/AtlasProtected/IsolationSelectionTool.

[105]T. A. Collaboration, *Muonselectiontool twiki*, https://twiki.cern.ch/twiki/bin/view/Atlas/MuonSelectionTool.

[106]MuonWorking Group, *Muon recommendations for release 21*, https://twiki.cern.ch/twiki/bin/view/Atlas/MuonSelectionToolR21.

[107]M. K. Bugge, S. Zambito, F. Sforza, D. Vannicola, F. Krieter, Z. Zheng, S. Rettie, S. Rosati, W. A. Leight, K. N. Barends, J. M. Keaveney, and S. Yacoob, *Muon Selection and Identification Working Points*, tech. rep. (CERN, Geneva, 2019).

[108]Jet ETMiss Working Group, *Usage of missing et in analyses*, https://twiki.cern.ch/twiki/bin/viewauth/AtlasProtected/METUtilities.

[109]*Performance of missing transverse momentum reconstruction for the ATLAS detector in the first proton-proton collisions at at* $\sqrt{s}$*= 13 TeV*, tech. rep., All figures including auxiliary figures are available at https://atlas.web.cern.ch/Atlas/GROUPS/PHYSICS/PUBNOTES/ATL-PHYS-PUB-2015-027 (CERN, Geneva, 2015).

[110]S. Steve Farrell, *Physicsanalysis/analysiscommon/associationutils - overlap removal tools*, https://gitlab.cern.ch/atlas/athena/tree/48a4143b865ebaf5490cd7be74b54a957cdd7d05/PhysicsAnalysis/AnalysisCommon/AssociationUtils.

[111]P. J. Klimek, B. O. Burghgrave, A. Kaczmarska, P. Bruckman De Renstrom, S. Bahrasemani, E. Parrish, M. Mlynarikova, M. Bahmani, M. K. Juzek, Z. K. Zak, L. Duval, E. Drechsler, H. Hadavand, D. Chakraborty, D. O'Neil, J. C. Cardenas Jr, and J. Adelman, *Search for charged Higgs bosons decaying via $H^{\pm} \to \tau^{\pm}\nu_{\tau}$ in the τ+jets and τ+lepton final states with 139 fb^{-1} of pp collision data recorded at $\sqrt{s} = 13$ TeV with the ATLAS experiment*, tech. rep. (CERN, Geneva, 2021).

[112]C. Bierlich et al., "A comprehensive guide to the physics and usage of PYTHIA 8.3", 10.21468/SciPostPhysCodeb.8 (2022).

[113]K. J. Max Kuhn, *Applied predictive modeling* (Springer, 2013).

[114]C. Y. Wijaya, *$1_x xxia0jjvprhejhd4z893g$*, https://cornellius.substack.com/p/cross-validation-to-improve-model, [Online; accessed 22-April-2024], 2023.

[115]G. Van Rossum and F. L. Drake Jr, *Python reference manual* (Centrum voor Wiskunde en Informatica Amsterdam, 1995).

[116]M. Aaboud, G. Aad, B. Abbott, O. Abdinov, B. Abeloos, D. K. Abhayasinghe, S. H. Abidi, O. S. AbouZeid, N. L. Abraham, H. Abramowicz, H. Abreu, Y. Abulaiti, B. S. Acharya, S. Adachi, and e. a. Adamczyk, "Search for charged higgs bosons decaying via $H^{\pm} \to \tau\nu$ in the τ+jets and τ+lepton final states with 36 fb-1 of pp collision data recorded at $\sqrt{s} = 13$ tev with the atlas experiment", Journal of High Energy Physics **2018**, 10.1007/jhep09(2018)139 (2018).

[117]G. Cowan, K. Cranmer, E. Gross, and O. Vitells, "Asymptotic formulae for likelihood-based tests of new physics", Eur. Phys. J. C **71**, [Erratum: Eur.Phys.J.C 73, 2501 (2013)], 1554 (2011).

[118]A. L. Read, "Presentation of search results: the cls technique", Journal of Physics G: Nuclear and Particle Physics **28**, 2693 (2002).

[119]M. Aaboud et al. (ATLAS), "Search for charged Higgs bosons decaying via $H^{\pm} \to \tau^{\pm}\nu_{\tau}$ in the τ+jets and τ+lepton final states with 36 fb^{-1} of pp collision data recorded at $\sqrt{s} = 13$ TeV with the ATLAS experiment", JHEP **09**, 139 (2018).